Measurement and Modelling of Human Sensory Feedback in Car Driving

This dissertation is submitted for the degree of

Doctor of Philosophy

January 2018

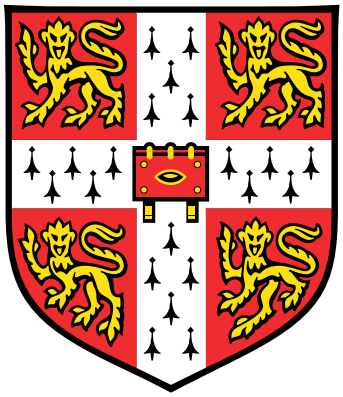

Christopher James Nash

Emmanuel College

Department of Engineering

University of Cambridge

Acknowledgements and declaration

Firstly, I would like to thank Dr. David Cole for his guidance and support over the course of my PhD. The project could never have been completed without his advice on the direction of the research, and his expertise has been invaluable in helping to overcome difficulties encountered during the work. I would like to express my gratitude to the engineers who helped me set up and run the experiments. Their useful suggestions during discussions of the experimental procedures and modelling work were always greatly appreciated. I am also incredibly grateful to the drivers for carrying out the experiments, offering highly informative feedback, and enduring the more stomach-churning trials without complaint. Finally, I wish to thank my family and friends. In particular thanks to my parents for their constant encouragement, and to Georgina Skinner for supporting me in countless ways over the last few years.

This work was funded by the UK Engineering and Physical Sciences Research Council (EPSRC), under studentship EP/P505445/1.

I hereby declare that except where specific reference is made to the work of others, the contents of this dissertation are original and have not been submitted in whole or in part for consideration for any other degree or qualification in this, or any other University. This dissertation is the result of my own work and includes nothing which is the outcome of work done in collaboration, except where specifically indicated in the text. This dissertation contains 68,648 words, 110 figures and 27 tables.

Christopher James Nash
January 2018

Abstract

With the growing complexity of vehicle control systems it is becoming increasingly important to understand the interaction between drivers and vehicles. Existing driver models do not adequately characterise limitations resulting from drivers' physical systems. In particular, sensory dynamics limit the ability of drivers to perceive the states of real or simulated vehicles. Therefore, the aim of this thesis is to understand the impact of sensory dynamics on the control performance of a human driver in real and virtual environments.

A new model of driver steering control is developed based on optimal control and state estimation theory, incorporating models of sensory dynamics, delays and noise. Some results are taken from published literature, however recent studies have shown that sensory delays and noise amplitudes may increase during an active control task such as driving. Therefore, a parameter identification procedure is used to fit the model predictions to measured steering responses of real drivers in a simulator. The model is found to fit measured results well under a variety of conditions.

An initial experiment is designed with the physical motion of the simulator matching the motion of the virtual vehicle at full scale. However, during more realistic manoeuvres the physical motion must be scaled or filtered, introducing conflicts between measurements from different sensory systems. Drivers are found to adapt to simple conflicts such as scaled motion, but they have difficulty adapting to more complicated motion filters.

The driver model is initially derived for linear vehicles with stochastic target and disturbance signals. In later chapters it is extended to account for transient targets and disturbances and vehicles with nonlinear tyres, and validated once again with experimental results. A series of simulations is used to demonstrate novel insights into how drivers use sensory information, and the resulting impact on control performance. The new model is also shown to predict difficulties real drivers have controlling unstable vehicles more reliably than existing driver models.

Supporting data is available at https://doi.org/10.17863/CAM.9741

Contents

List of figures

List of tables

Nomenclature

Roman letters

Upper case

$\mathbf{A}$	state matrix
$\hat{\mathbf{A}}$	linearised state matrix
A	nonlinear state function
$\mathbf{B}$	input matrix
B	'magic formula' tyre parameter
$\mathbf{C}$	output matrix
C	'magic formula' tyre parameter
C_f	front tyre cornering stiffness
C_r	rear tyre cornering stiffness
$\mathbf{D}$	feedthrough matrix
D	'magic formula' tyre parameter
E	expected value
E	'magic formula' tyre parameter
F	tyre force
$\mathbf{G}$	process noise matrix
G	steering ratio
$\mathbf{H}$	MIMO transfer function
H	transfer function
$\mathbf{I}$	identity matrix
I	moment of inertia
$\hat{I}$	sensory condition
J	controller cost function
$\mathbf{K}$	gain matrix
K	gain
$\mathbf{L}$	Kalman filter gain matrix
$\mathbf{M}$	matrix
M	equivalent signal magnitude
N	number of time steps
$\mathbf{P}$	state covariance matrix
P	probability
$\mathbf{Q}_\mathrm{KF}$	process noise covariance
$\mathbf{Q}_\mathrm{LQ}$	controller cost function matrix
$\mathbf{R}_\mathrm{KF}$	measurement noise covariance
$\mathbf{R}_\mathrm{LQ}$	controller cost function matrix
R	radius
$\mathbf{S}$	solution to LQR Riccati equation
S	power spectral density
$\hat{S}$	sensory observation
T	time constant
U	longitudinal velocity

V measurement noise RMS

W process noise RMS

$\mathbf{X}$ state trajectory

Lower case

a lateral acceleration

c constant

c damping ratio

e path-following error

f forcing function

j square root of -1

k time step index

k stiffness

l distance from axle to centre of mass

n time step index during controller prediction

s Laplace transform parameter

t time

$\boldsymbol{u}$ system input

$\boldsymbol{v}$ measurement noise

v lateral velocity

w process noise/white noise disturbance

$\hat{w}$ sensory weighting constant

$\boldsymbol{x}$ system states

$\hat{\boldsymbol{x}}$ state estimate

x Cartesian coordinate

$\boldsymbol{y}$ system output

y Cartesian coordinate

$\hat{y}$ equivalent lateral displacement

z vertical Cartesian coordinate

Greek letters

Upper case

Δ small change in value

$\boldsymbol{\Theta}$ MPC input matrix

$\boldsymbol{\Psi}$ MPC state matrix

Lower case

α slip angle

δ steering angle

$\hat{\delta}$ driver control action

ε weighted prediction error

ζ damping factor

η noise threshold

κ target path curvature

σ standard deviation

τ time delay

ϕ target path angle relative to vehicle

ψ yaw angle

$\hat{\psi}$ equivalent yaw angle

ω angular velocity/frequency

Numerals

$\mathbf{0}$ matrix of zeros

$\mathbf{1}$ matrix of ones

Subscripts

BJ Box–Jenkins

c continuous-time matrix

circ circle

DC dual control

exp	experiment
f	front tyre
ff	forcing function
HP	high-pass
Ia	type Ia afferent (muscle spindles)
Ib	type Ib afferent (GTOs)
II	type II afferent (muscle spindles)
KF	Kalman filter
L	linearisation point
LQ	linear quadratic regulator
m	maximum visual/vestibular delay
ma	lateral motion filter
mω	yaw motion filter
max	maximum
n	noise
nm	neuromuscular
nom	nominal
NP	no preview
OK	optokinetic influence
oto	otoliths
p	preview
R	reduced plant
r	rear tyre
ref	reference
s	sample time
SCC	semi-circular canals
sim	simulated
smr	simulator
STF	steering torque feedback
t	target
V	vehicle
ve	vestibular system
vi	visual system
$[i, j]$	containing i rows and j columns
(i, j)	ith row and jth column
$(i, :)$	entire ith row
$(:, j)$	entire jth column

Superscripts

T	transpose
$'$	internal model estimate
*	unit of filtered signal

Abbreviations

ADAS	advanced driver assistance systems
AN	additive noise
CAD	computer-aided design
CNS	central nervous system
CZW	coherence zone width
EEG	electroencephalography
EMG	electromyography
ESF	equivalent scaling factor
FEA	finite element analysis
FRO	focus of radial outflow
GMC	gain of mean coherence
GMO	gain of mean optimal
GTOs	Golgi tendon organs
GVS	galvanic vestibular stimulation
JND	just-noticeable difference
LQG	linear quadratic Gaussian

LQR	linear quadratic regulator
MAP	maximum a posteriori
MEG	magnetoencephalography
MLE	maximum likelihood estimation
MMSE	minimum mean-square error estimate
OZW	optimal zone width
PMC	point of mean coherence
PMO	point of mean optimal gain
PSD	power spectral density
RMS	root mean-square
SCCs	semi-circular canals
SDN	signal-dependent noise
SNR	signal-to-noise ratio
VAF	variance accounted for
VOR	vestibulo-ocular reflex

Chapter 1

Introduction

"I continuously go further and further learning about my own limitations, my body limitation, psychological limitations. It's a way of life for me."

— Ayrton Senna

1.1 Background and motivation

Over the last century the development of the motor car has revolutionised the way people travel, impacting on countless aspects of society. Today there are estimated to be over a billion cars on the road, and the number is expected to exceed two billion by 2030 [1]. The automotive industry has become a leading economic driver for many countries; in 2015 the UK automotive industry employed over 800,000 people and turned over more than £70 billion [2]. This has a significant environmental impact, with road transport currently accounting for around 16% of global CO_2 emissions [3], therefore increasing fuel efficiency and reducing emissions has become a top priority for vehicle manufacturers.

Developments in computing over the last few decades have fundamentally changed the way that vehicles are designed, tested and manufactured. Every component is analysed extensively using mathematical models and CAD and FEA packages, and vehicle systems are prototyped virtually long before any physical testing is carried out. Optimisation techniques are used with metrics which quantify objectives such as speed, safety and efficiency. However some less tangible objectives such as handling, ride comfort and aesthetics are harder to quantify and rely to some extent on subjective human judgements.

In spite of this ability to model and analyse vehicle systems in great detail, the role of the driver in the closed-loop driver-vehicle system is still poorly understood. Therefore, to assess the performance of the vehicle it is necessary to carry out extensive testing with real drivers, which is expensive and time-consuming. High-performance driving simulators are increasingly being used to test vehicles with a driver in the loop without requiring the manufacture of a prototype vehicle. However, simulators are only able to provide a limited

amount of physical motion feedback, and it is unclear how this affects the performance of the driver compared to a real vehicle. There is therefore significant motivation for understanding how drivers interact with vehicles in real and virtual environments.

Current trends in vehicle design are moving towards the development of autonomous vehicles, which has the potential to completely change the way that humans and vehicles interact [4]. However, before full autonomy is reached there are several stages of automation which must be passed through, in which the driver shares partial control of the vehicle [5]. In designing semi-autonomous vehicles it is of crucial importance to be able to predict how the driver will respond to any interventions by an automated vehicle system. Furthermore, human drivers are still likely to be on the roads for many decades, therefore even a fully autonomous vehicle must have an awareness of how to interact with vehicles controlled by human drivers.

1.2 Driver modelling

Driving a vehicle involves a wide range of information processing levels, from the high-level navigation task to the low-level control of vehicle speed and direction. The focus of this work is on the low-level control task, since this is where the interaction between driver and vehicle is most significant. Donges [6] considered the steering control task as the superposition of a target-following task (feedforward control) and a disturbance-rejection task (feedback control). Disturbances may act on the vehicle from sources such as wind gusts, uneven road surfaces and nonlinearities in the vehicle dynamics, or they may originate from the driver due to physiological constraints, noise and nonlinearities.

A simplified block diagram of the tasks involved in feedforward and feedback control of a vehicle is shown in Figure 1.1. The driver previews the upcoming road geometry using their visual system and then, using an internal model of the vehicle dynamics, plans a target trajectory combining path and speed profiles while also calculating corresponding feedforward control actions [7, 8]. Simultaneously, the driver senses the motion of the vehicle in relation to the target profiles and generates feedback control actions to reduce the effects of disturbances [8, 9]. Figure 1.1 assumes that feedback of vehicle motion is not used directly for generating the feedforward control action, however the feedback loop is able to correct for any discrepancies introduced by imperfections in the driver's feedforward control.

Modelling driver steering control mathematically has been a subject of research for several decades. Comprehensive reviews of early methods are provided by MacAdam [10] and Plöchl and Edelmann [11]. Recent research has focussed on the application of optimal

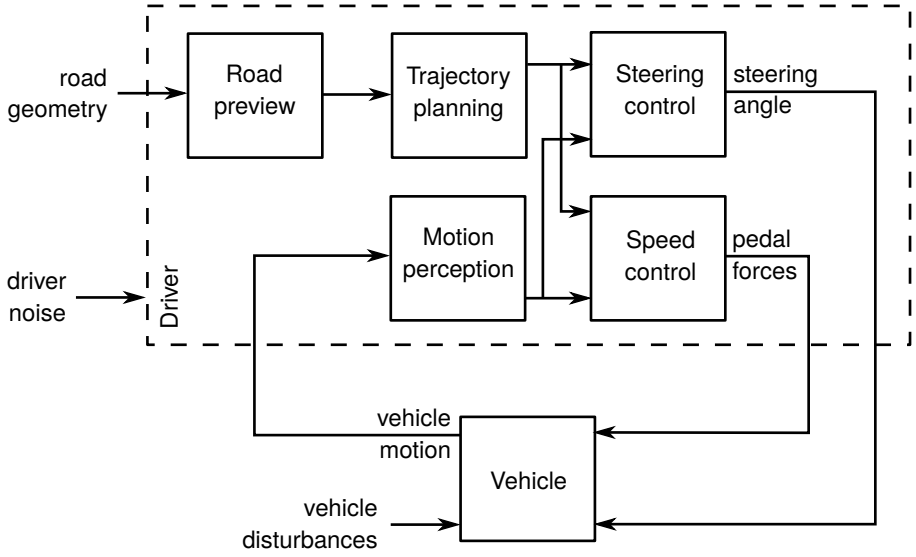

Figure 1.1: Block diagram of tasks carried out while driving. The driver perceives the motion of the vehicle and the upcoming road geometry, plans a desired trajectory, then calculates the required steering angle and pedal forces to follow this trajectory.

control theory, using model predictive or linear quadratic controllers that are able to preview the target path, as shown in Figure 1.2, and calculate an optimal sequence of control actions to follow this target [12–14]. This approach has been extended to include neuromuscular dynamics [15–18], and to the control of nonlinear vehicle dynamics [19–21]. Feedforward and feedback control are usually assumed to share a common objective function, however recent studies have synthesised independent feedforward and feedback controllers to examine the robustness of the driver's control strategy to disturbances [8, 9].

While driver steering control has a well-defined objective, to follow a target line and stay within road boundaries, the motivation for drivers' speed choice depends on the situation. During normal driving, drivers balance factors such as safety, comfort, journey time and control effort [22, 23]. Drivers have been found to decrease their speed to minimise their lateral acceleration in corners [24–26]. Road width has also been found to affect speed choice, with drivers adjusting their speed to remain within lane boundaries [27, 28]. In contrast, racing drivers aim to maximise their lateral acceleration within the limits of the tyres in order to minimise lap time [7, 8, 29]. In situations with heavy traffic, driver speed choice may also be dictated by the speed of other vehicles, aiming to maintain a safe distance behind the car in front [30, 31].

Despite these developments, most models assume the driver has full knowledge of the vehicle states, bypassing the motion perception block in Figure 1.1. No existing driver models are known which take full advantage of current understanding of human sensory dynamics. While this work is primarily focussed on driving of road vehicles, clear parallels

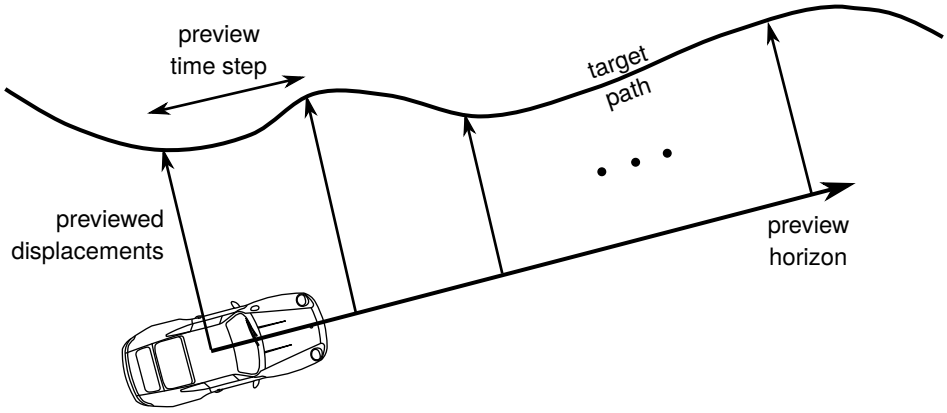

Figure 1.2: Preview model of drivers' perception of the upcoming target path, used for feedforward steering and speed control. The driver looks straight ahead and takes a series of measurements of the lateral displacement of the target path up to the preview horizon.

can be drawn with research into pilots in the aerospace industry. Sensory dynamics have been considered in greater detail in this field, and much of the existing research into human sensory dynamics has been carried out by aerospace engineers to understand human perception during control tasks. In particular, models incorporating the pilot's sensory dynamics have been used in conjunction with experiments carried out in flight simulators to understand how sensory information is used during real and simulated flight [32–40]. There is a significant opportunity to apply the techniques and outcomes from these studies to develop understanding of sensory perception during driving.

1.3 Research strategy

Mathematical modelling of vehicles generally begins with physical models of the separate vehicle components. The performance of each component can be investigated using physical testing, aided by sensors to measure variables such as stresses, accelerations and temperatures. Models of each subsystem can then be combined to give an understanding of the global performance of the whole vehicle. In contrast, the performance of the driver is primarily dependent on control calculations carried out in the brain. Techniques for measuring brain activity are currently crude and imprecise, therefore the driver is essentially a 'black box'. The only way to determine what is going on inside the driver's brain is to hypothesise a model, subject the driver and the model to the same inputs and compare the measured output from the driver with the prediction of the model.

It is important to be able to characterise the inputs to, and outputs from, the driver's brain accurately in order to develop models which simulate the control performance of the human driver. Measurements can generally only be taken once neural signals have passed

through the physical systems of the driver, so by incorporating accurate models of these systems measurements can be related more reliably to the driver's control actions. The control output of the driver is shaped by neuromuscular dynamics to give the steering angle and pedal forces, which can be measured easily. Various studies have developed models of a driver's neuromuscular dynamics to understand how the driver's control intention is shaped by physical limitations of the neuromuscular system [15–18].

Existing driver models have generally failed to characterise the inputs to the driver's brain accurately. It has been assumed that drivers have access to perfect measurements of the vehicle states and the upcoming road path. However, in reality the driver is only able to access a limited number of measurements taken by their sensory organs. Analogously to neuromuscular dynamics shaping the control output, the control inputs are shaped by the physical dynamics of the driver's sensory systems. There are also inherent delays in conduction and processing of sensory signals, and random noise which degrades the ability of the driver to perceive the true vehicle states. It is necessary to understand the limitations introduced by sensory dynamics in order to predict how a human driver will respond under different conditions.

Bigler [41] began the development of a driver model which considers sensory perception, incorporating results from studies of human sensory systems into a model of driver steering control. However, as discussed further in Chapter 2, human sensory systems do not necessarily perform the same during driving as they do during passive measurements. Studies from the aerospace industry have shown how system identification procedures can be used to identify models of human perception during active control tasks [32–40]. Therefore, the overall strategy for this research is to carry out experiments with human drivers, and use similar identification techniques to identify parameter values for a model of driver steering control which incorporates sensory dynamics, building on the model developed by Bigler [41].

1.4 Aim and objectives

The main aim of this work is:

> *to understand the impact of sensory dynamics on the control performance of a human driver in real and virtual environments.*

Achieving this aim requires the fulfilment of several objectives, which are to:

- Use relevant published research to assess current knowledge of the performance of human sensory systems.

- Develop a new driver model which accounts for the role of sensory dynamics, and validate this model with measurements from human drivers.
- Understand how drivers are affected by the limited physical motion feedback in a driving simulator.
- Determine whether drivers with different levels of experience use sensory information differently.
- Use the driver model to explore how sensory measurements are used during driving, and how they affect the performance of the driver.

1.5 Thesis structure

The remainder of this thesis is presented in seven chapters which describe the steps taken to achieve the aim and objectives defined in Section 1.4. A review of the literature on human sensory dynamics is presented in Chapter 2, to understand the state of the art in human sensory perception research and highlight key results which could be incorporated into a model of driver control behaviour. The initial development of a new model of driver steering control is described in Chapter 3, including an experiment carried out in a simulator with human drivers and an identification procedure used to fit the model prediction to experimental results.

The experiment described in Chapter 3 was designed so that the physical motion feedback could be replicated at full scale, to simulate a real driving task as closely as possible. To understand how drivers are affected by the limited physical motion usually available in a driving simulator, the performance of drivers with scaled or filtered physical motion is investigated in Chapter 4. The driver model developed in Chapters 3 and 4 is derived for a linear vehicle, using random target and disturbance signals with stationary statistical properties. To address these limitations, the response of drivers to transient target and disturbance signals is investigated in Chapter 5. The model is then extended to represent drivers' control of a vehicle with nonlinear tyres in Chapter 6.

The work described in Chapters 2 to 6 focuses on the development of a new driver model and validation of this model using experiments carried out by human drivers. Various simulations are carried out in Chapter 7 to investigate the predictions, applications and limitations of the new model. It is hoped that this will motivate further research into the role of sensory dynamics during driving. The main conclusions of the thesis and suggestions for further work are summarised in Chapter 8. A detailed summary of the new driver model, including a full mathematical derivation, is presented in Appendix A.

Chapter 2

Sensory perception literature review

When designing vehicle systems it is important to consider how the driver and vehicle interact. A survey of existing driver models in Chapter 1 shows that there is currently little understanding of the role of sensory dynamics in the driver-vehicle control task. A substantial amount of research has been carried out in the fields of biology and neuroscience to investigate human perception, cognition and action in various circumstances. In this chapter a review of the literature is carried out to consolidate information from previous studies which can be used when incorporating human sensory systems into the design of a driver model. Key results are highlighted from studies measuring sensory dynamics, delays and thresholds, and research into the integration of stimuli from different sensory systems. This review provides a basis for further study into sensory perception during driving. **An amended version of this chapter has been published as a journal paper [42].**

2.1 Introduction

Driving is one of many human sensorimotor tasks that involve perceiving stimuli in the surrounding environment and responding with a physical action [43]. The neurophysiological processes involved in such tasks are shown in Figure 2.1. A stimulus may excite various senses, which produce chemical signals characterised by the dynamics of the sensory receptors (explored in Section 2.2). Sensory signals are then transmitted through the nerves as electrical impulses caused by firing neurons, with the firing rate encoding a frequency-modulated signal [44]. Certain stimuli can elicit reflexive responses which bypass the brain by activating motor neurons emerging from the spinal cord [44].

There are physical and biochemical limitations to the speed with which each of the processes shown in boxes in Figure 2.1 can be carried out, therefore time delays are introduced into the sensorimotor system. These delays are discussed further in Section 2.3. In addition, noise is introduced due to nonlinearities in the receptor and neuromuscular

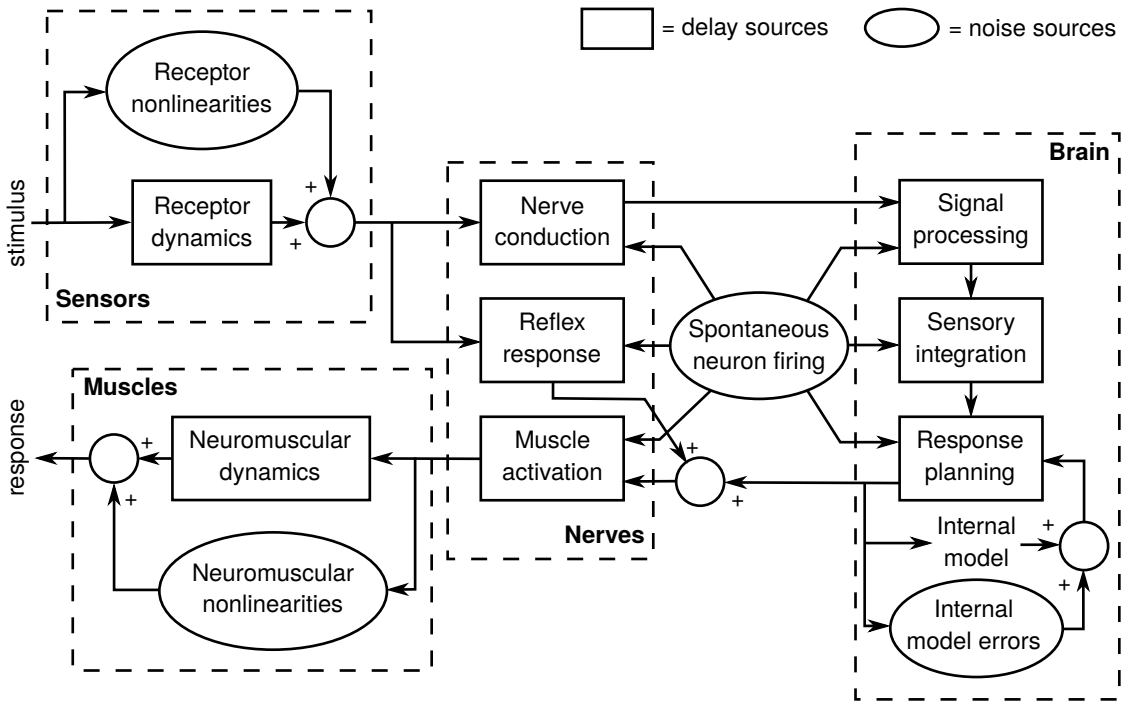

Figure 2.1: Diagram of the main processes carried out by the sensorimotor system to generate a physical response to a sensory stimulus. Processes which introduce time delays are shown by boxes, and sources of noise are shown by ovals.

dynamics, errors in the brain's internal models and spontaneous firing of neurons [45]. This means that humans are unable to measure stimuli with perfect accuracy or plan and execute an ideal response. It also results in thresholds below which stimuli cannot be perceived, as discussed in Section 2.4.

Once sensory signals are received in the brain, they are processed in the sensory cortex to extract information from the encoded signals transmitted through the nerves [46]. Information from different senses is integrated to form a single representation of the environment using internal models of the human body and the surrounding world [47, 48], as explained in Section 2.5. Based on this, a physical response to the perceived stimuli is planned. Signals required to activate the muscles are generated in the motor cortex, and fine-tuned in the cerebellum using feedback from the sensory measurements [46]. Signals are then transmitted along motor neurons which activate muscle fibres, causing them to contract. Physical responses are shaped by the dynamic properties of the activated muscles. In the context of driving, neuromuscular dynamics have been modelled for drivers' arms holding a steering wheel [15–17] and legs actuating a gas pedal [18].

An important feature of perception during driving tasks is that the stimuli perceived by the driver's sensory systems arise from the motion of the vehicle, which is controlled by the driver. This means that the driver is involved in an *active* closed-loop perception

and control task, as opposed to a passenger who is a *passive* observer [49]. The driver is able to anticipate future motion of the vehicle when integrating sensory measurements, as discussed in Section 2.5. During driving *multimodal* stimuli are perceived simultaneously by different senses in various axes, in contrast with *unimodal* stimuli which stimulate one sensor in a single axis. Care must be taken when relating results from investigations carried out in passive, unimodal conditions to models of active, multimodal control and perception. This is discussed in relation to sensory delays in Section 2.3 and thresholds in Section 2.4.

The scope of this review is broad and thus it is not possible to review every topic in great detail; each section could be extended significantly. However the aim of the review is to give an overview of key results from the literature, with particular focus on motivating and informing further development of driver models incorporating human sensory dynamics. Both steering and speed control are considered concurrently, since in many cases the sensory mechanisms discussed are relevant for both control tasks. The main findings of the review are summarised and discussed in Section 2.6. This review considerably extends earlier reviews by Bigler and Cole [41, 50].

2.2 Sensory dynamics

Various sensory systems are used by the driver to infer the state of the vehicle and its surroundings. The main senses used in the control of vehicle speed and direction are:

- *Visual:* The visual system is the only means the driver has of detecting the upcoming road geometry. It is also used to sense the motion of the vehicle relative to the surrounding environment.
- *Vestibular:* The vestibular organs are located within the inner ear, and they sense rotations and translations of the driver's head.
- *Somatosensors:* Somatosensors include a wide range of sensory organs which detect various states of the body, such as contact pressure, temperature and limb position. They include proprioceptors which detect joint angles and muscle lengths and tensions.

The following subsections give an overview of the published literature on these three sensory systems. Other senses such as hearing may also play a role but are not discussed.

2.2.1 Visual system

Visual perception is the subject of significant research activity in psychology, neuroscience and biology. There is still much to understand about how a human interprets the neural

signals received by the retina from a potentially complex three-dimensional visual scene containing objects that might be familiar or unfamiliar, and moving or stationary, with a moving or stationary observer. Detailed discussions of the processes involved in visual perception are presented in [51–56]. For the purpose of driver modelling it is not necessary or feasible to model all of these processes, therefore this review focuses on the most relevant results for modelling visual perception in a driving environment.

In the two-level model of vehicle control [6] the visual system is used in both the feedback task and the feedforward task. The feedback task involves using the visual system in combination with the vestibular and somatosensory systems to perceive the motion of the vehicle, which is used to respond to disturbances. In the feedforward task, the visual system views the geometry of the road ahead of the vehicle so that future control actions can be calculated. Higher levels of the driving task, not considered in this review, involve the visual system in perceiving additional information such as motion of other vehicles and pedestrians.

2.2.1.1 Perception of self-motion (feedback)

Visually-induced motion perception is typically caused by motion of the eyes relative to fixed surroundings, although illusory self-motion perception known as vection can be induced by moving surroundings [57]. Since vehicle motion is primarily planar, the role of the driver's visual system in perceiving self-motion is mainly concerned with three axes: longitudinal and lateral translations, and yaw (heading) rotations.

Various mechanisms have been suggested for visual motion perception. 'Optic flow' describes the velocity field created as points in the visual scene flow over the retina, along lines known as streamers [51, 52, 58]. Optic flow patterns while driving on straight and curved roads are shown by the dashed lines in Figure 2.2. For straight motion, the streamers all originate from a point directly in front of the observer known as the focus of radial outflow (FRO). This can be used as a visual cue to control the vehicle's heading direction, for example by aligning with the vanishing point at the end of a straight road [51]. For rotational motion the streamers are curved and the FRO does not exist, although the point on the horizon directly in front of the observer may still be used as a visual cue to heading direction [59]. However, Riemersma [60] suggested that the FRO and heading direction are too crude to play a role in car driving. Multi-level models of perception of motion from optic flow have been developed [61–63], however these descriptions do not lead easily to a simple relationship between vehicle motion and visually perceived motion, as they are dependent on the characteristics of the surroundings.

Alternatively, it has been proposed that humans measure the rate of change of vectors

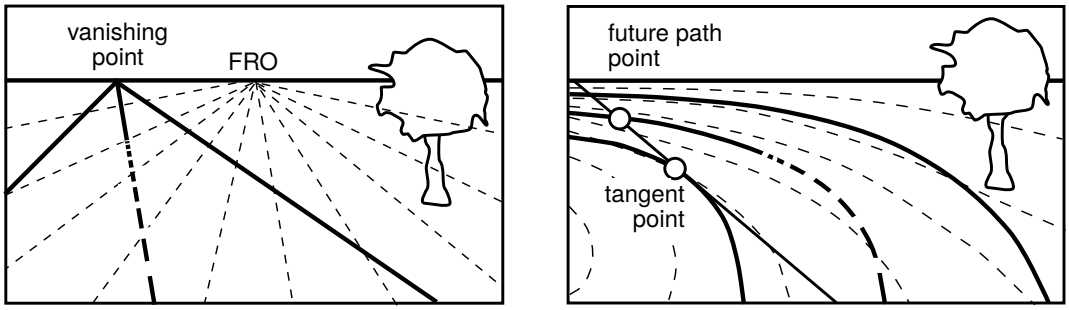

(a) Straight road **(b)** Curved road

Figure 2.2: Potential candidates for visual cues used while driving. Optic flow patterns are shown by dashed lines.

between themselves and specific objects in the visual field [64, 65]. This allows drivers to calculate the 'time-to-collision' with objects, which can be particularly useful when following a leading vehicle [31]. The distance and relative velocity of the objects can only be inferred with prior knowledge of the object's size or by comparison between two visually similar environments [65, 66]. The road edges and centre line have also been identified as key visual features used by drivers [60, 67].

Because of the variety of mechanisms involved in visual perception, it is difficult to say what constitutes the 'input' to the visual system. Optic flow models would suggest that velocities are measured, although the FRO can be used to measure heading direction (yaw angle), and translational displacements can be discriminated with reference to stationary features such as road markers. Gordon [65] used the unnatural appearance of the acceleration field to argue that accelerations and higher derivatives are not directly sensed by the visual system, therefore the most appropriate inputs to the feedback component of the driver's visual system are translational and angular velocities. Since displacements and angles can only be measured with respect to references such as road markers, they can be included within models of drivers' feedforward visual perception.

It is not clear from the mechanisms involved in visual perception whether perceived rotational and translational velocities depend on the frequency of the stimulus. A simple modelling approach is to assume unity gains between the actual and perceived velocities. Alternatively, the frequency response of the visual system could be estimated from sensory threshold measurements (see Section 2.4) [68, 69]. Riemersma [60] and Bigler [41] both measured thresholds of visual perception of lateral and yaw velocities, superimposed on a constant longitudinal velocity. Both studies presented subjects with a typical driving scene, with Riemersma [60] displaying edge lines for a straight road and Bigler [41] displaying a more realistic rendering of a straight road bordered by trees. Riemersma [60] found that lateral and yaw thresholds are independent of longitudinal speed. Bigler [41] measured

thresholds for stimuli of different frequencies, and analysing the results as in [68, 69] indicates that visual dynamics can be described by a low-pass filter:

$$H_{\mathrm{vi}}(s) = \frac{\omega_{\mathrm{vi}}}{s + \omega_{\mathrm{vi}}} \tag{2.1}$$

with lateral velocity or yaw angular velocity as inputs. The same cutoff frequency $\omega_{\mathrm{vi}} = 0.810$ rad/s fits the results for both lateral and yaw motion. A similar low-pass characteristic was also seen by Riemersma [60]. In the absence of direct measurements of nervous responses to sensory stimulation, this model inferred from sensory threshold data can be used to give some insight into the function of the visual system. However, further research is needed to validate this approach.

2.2.1.2 Perception of road geometry (feedforward)

One of the key characteristics of driving tasks is the ability of the driver to use their visual system to 'preview' the road ahead in order to carry out feedforward control. Studies have investigated the key features of road geometry which are perceived while driving, often using eye-tracking instrumentation to investigate where drivers look. On straight roads drivers generally focus near the FRO, while on curved roads drivers scan the geometry of the curve [70]. Many studies have found that drivers focus on the 'tangent point' on the inside of a bend [71–74], as shown in Figure 2.2. The angle between the vehicle heading and the tangent point can be used to estimate the road curvature [71] and required steering angle [73]. Other studies have suggested that drivers look at a point on the predicted vehicle path, the 'future path point' [75] as shown in Figure 2.2. There is no overwhelming evidence in favour of the tangent point over the future path point or other nearby points as a fixation point during driving [76–78].

Eye-tracking studies have found that drivers generally focus on a point around 1 to 2 s ahead of the vehicle on straight roads [6, 71], and that their gaze tends to move to an upcoming curve around 1 s before they steer in that direction [79, 80]. Drivers have also been found to make short 'look-ahead fixations', looking further along the road for short periods of time [81]. While eye-tracking instrumentation is useful for determining the gaze direction of a driver, Land and Lee [71] noted that it does not necessarily indicate where the driver is directing their attention, because the driver may be using their peripheral vision to gather information about road geometry away from the gaze point. To determine what information is needed by the driver, steering performance has been measured with only certain parts of the road visible [59, 82]. Performance was not degraded from the full visibility condition if drivers could see a near point 0.53 s ahead and a distant point 0.93 s ahead [82].

Steen et al. [83] reviewed many studies which proposed one, two or multi-point preview models, and concluded that a two-point preview model was the most realistic, with one point close to the driver and one more distant point. However, Sharp and Valtetsiotis [13] used a shift register to formulate a multi-point preview controller using visual information taken from a single preview point, suggesting that a human driver in a moving vehicle could use memory to construct a multi-point image of the road geometry from data sensed at one discrete point. The use of optimal control theory to calculate gains on previewed road geometry has shown that looking beyond a certain point results in diminishing returns [13, 14]. The point at which this occurs depends on the dynamic properties of the vehicle and the driver, and the amount of control effort applied by the driver.

2.2.2 Vestibular system

There is some disagreement in the literature as to the relative importance of the vestibular system in non-visual motion perception. Studies into thresholds of human motion perception in the dark generally assumed that the influence of the vestibular system is much larger than the somatosensors [68, 69, 84–87]. Motion perception thresholds for subjects with vestibular deficiencies have been found to be no different to normal subjects in some studies [88, 89], but much higher in others [90, 91]. The relative importance of the vestibular and somatosensory systems may depend on the precise nature of the stimuli, however the vestibular system is undoubtedly an important source of information for drivers.

The vestibular system consists of two sets of organs located in the inner ear: the semi-circular canals (SCCs) which sense rotational motion, and the otoliths which sense translational motion [46]. Many studies have investigated the function of the vestibular system in primates and humans, either directly by measuring electrical signals in the brain or indirectly by measuring the vestibulo-ocular reflex (VOR), a reflexive eye motion which uses vestibular information to compensate for head movements.

2.2.2.1 Otoliths

The otoliths are formed from small granular particles contained in a gelatinous membrane which is in turn connected to sensory cells via hairs called cilia. When subjected to translational acceleration, inertial forces on the otoliths deflect the cilia and excite the sensory cells [46]. Most mathematical models are based on empirical data from experiments carried out on humans and animals.

It is a natural extension of Einstein's equivalence principal [92] that the otoliths cannot discriminate between a translational acceleration and a change in orientation of the gravity

Table 2.1: Otolith model parameters. The gain K_{oto} has been adjusted to give comparable outputs, since the scaling of the perceived signal is arbitrary.

Study	K_{oto}	T_{oto1}	T_{oto2}	T_{oto3}
Young and Meiry [93]	0.4	13.2	5.33	0.66
Hosman [94]	0.4	1	0.5	0.016
Telban and Cardullo [95]	0.4	10	5	0.016
Soyka et al. [68]	0.0225	22.05	0.62	0.016

vector. Young and Meiry [93] developed an otolith model relating the perceived and actual specific forces (combination of inertial and gravitational accelerations). They proposed the transfer function:

$$H_{oto}(s) = K_{oto}\left[\frac{(1 + T_{oto1}s)}{(1 + T_{oto2}s)(1 + T_{oto3}s)}\right] \tag{2.2}$$

and identified values for the parameters, given in the first row of Table 2.1.

Fernandez and Goldberg [96] measured the afferent firing rate (AFR) in the brains of squirrel monkeys subjected to accelerations at various frequencies and magnitudes. They developed a model of the otoliths containing a fractional exponent, which is difficult to implement practically. Therefore Hosman [94] proposed a simplified version in the same form as Equation 2.2. Based on this and other research, Telban and Cardullo [95] suggested slightly modified parameter values. Soyka et al. [68] used a signal-in-noise model to find a transfer function for the otoliths which optimised the fit to sensory threshold measurements (see Section 2.4). Suggested otolith parameters from these studies are summarised in the remaining rows of Table 2.1. Bode plots of the otolith transfer function using the different parameters are compared in Figure 2.3. In general the otoliths exhibit a low-pass response. For a driving task, the mid-range frequencies (between 10^{-1} and 10^{1} rad/s) are the most important, and in this range the otolith response is roughly proportional to acceleration. There are differences in the details of the frequency responses measured in different studies, which highlights the difficulty in achieving repeatable results when using different subjects, equipment and methodologies.

2.2.2.2 Semi-circular canals

The SCCs consist of sets of three elliptical cavities which are each filled with fluid [46]. Angular motion about any axis causes the fluid to move within these cavities, causing deflections of small hairs which excite sensory cells. Early models of the SCCs were based on considerations of the physical dynamics of the organs. Steinhausen [97] used observations of motion within the SCCs of fish to develop the 'torsion-pendulum' model.

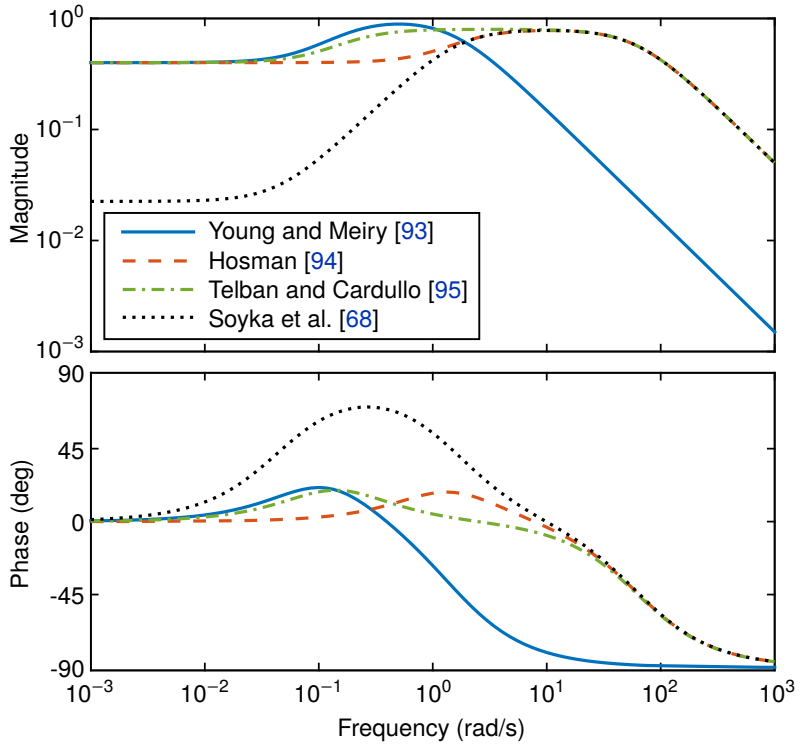

Figure 2.3: Bode plot for otolith transfer function (Equation 2.2) with parameters from different studies, given in Table 2.1. Input is acceleration.

Young and Oman [98] extended this model to include an additional 'adaptation' term T_{SCCa} to match trends seen in experimental results. Fernandez and Goldberg [45] added a lead term T_{SCC1}, giving the transfer function:

$$H_{\mathrm{SCC}}(s) = K_{\mathrm{SCC}} \left[\frac{T_{\mathrm{SCCa}} s}{(1 + T_{\mathrm{SCCa}} s)} \right] \left[\frac{(1 + T_{\mathrm{SCC1}} s)}{(1 + T_{\mathrm{SCC2}} s)(1 + T_{\mathrm{SCC3}} s)} \right] \tag{2.3}$$

which relates the perceived and actual angular acceleration.

Fernandez and Goldberg [45] measured the AFR of squirrel monkeys in response to angular accelerations of various amplitudes and frequencies. Hosman [94] suggested alternative parameter values based on results from the literature, neglecting the adaptation time constant T_{SCCa} since it lies outside the bandwidth of interest for driving tasks. Telban and Cardullo [95] reviewed several relevant studies and suggested slight modifications to the parameters of Equation 2.3. They also proposed a simplified transfer function for modelling purposes, which links angular *velocity* inputs (hence the s^2 term) to perceived outputs:

$$H_{\mathrm{SCC}}(s) = K_{\mathrm{SCC}} \left[\frac{T_{\mathrm{SCCa}} s^2}{(1 + T_{\mathrm{SCCa}} s)(1 + T_{\mathrm{SCC2}} s)} \right] \tag{2.4}$$

(there is a typographical error in [95], with s in the numerator instead of s^2). This transfer

Table 2.2: SCC model parameters. Parameters which the authors have suggested may be neglected are given in brackets. The gain K_{SCC} has been adjusted to give comparable outputs, since the scaling of the perceived signal is arbitrary.

Study	K_{SCC}	T_{SCCa}	T_{SCC1}	T_{SCC2}	T_{SCC3}
Fernandez and Goldberg [45]	5.73	80	0.049	5.70	0.005
Hosman [94]	5.73	(80)	0.110	5.90	0.005
Telban and Cardullo [95]	5.73	80	(0.060)	5.73	(0.005)
Soyka et al. [69]	2.2	(∞)	0.014	2.16	0.005

function neglects the short time constants T_{SCC1} and T_{SCC3}, which affect frequencies well above the range of normal head movements. Soyka et al. [69] optimised time constants to fit sensory threshold measurements using a signal-in-noise model. Similarly to Hosman [94], they neglected the adaptation time constant T_{SCCa}. SCC parameters found from various studies are summarised in Table 2.2. Bode plots of the SCC transfer function using the different parameters are compared in Figure 2.4. The key feature of the transfer function is roll-off at high and low frequencies, with zero response to constant angular acceleration. At mid-range frequencies the transfer functions have the characteristics of an integrator, hence why Telban and Cardullo [95] suggested the SCCs measure angular velocity rather than acceleration. The agreement between different studies is much higher than for the otoliths. This could be because they are based on similar models of the physical dynamics of the SCCs, although the transfer function found from sensory thresholds [69] also agrees well at mid-range frequencies.

2.2.3 Somatosensors

During driving the information provided by the visual and vestibular systems is complemented by the somatosensors [46]. A subset of these are known as proprioceptors, which sense motion and forces of the joints and muscles. These are particularly important in allowing the driver to sense the angle and torque of the steering wheel, which can allow experienced drivers to assess the contact between the tyre and the road. Proprioceptors are also used to sense the displacements and forces of the foot pedals. The following subsections discuss the properties of the muscle spindles, which measure muscle displacement, and the Golgi tendon organs (GTOs), which measure muscle force. Other somatosensors which may play a role include skin and joint receptors which give information on touch and joint angle [99, 100], and graviceptors which respond to the motion of fluid within the body [101]. While these can give the driver useful information, such as contact forces between the body and the seat [102], the nature of these stimuli means they are difficult to

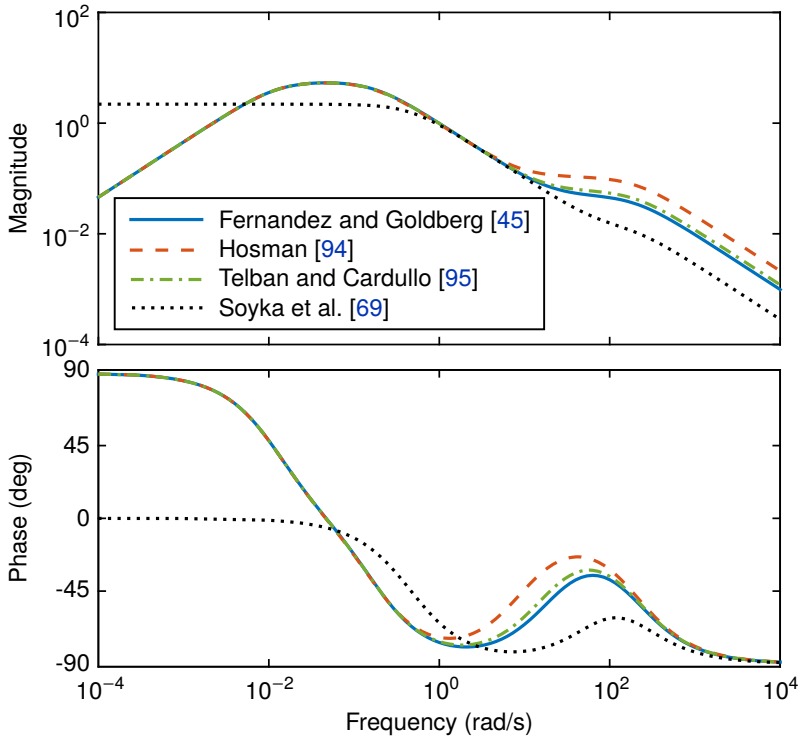

Figure 2.4: Bode plot for SCC transfer function (Equation 2.3) with parameters from different studies, given in Table 2.2. Input is angular acceleration.

measure and quantify, and therefore the existing literature does not lend itself to application within driver models.

2.2.3.1 Muscle spindles

Muscle spindles are sensors which detect the length and rate of change of length of the muscles. They produce two separate signals, one dependent on muscle velocity and length (type Ia afferent) and one dependent on muscle length only (type II afferent) [46]. An empirical linear model of the muscle spindle response, based on measurements taken in cats, was formulated by Poppele and Bowman [103], with the Ia and II afferent responses to muscle displacements given by:

$$H_{\mathrm{Ia}}(s) = \frac{s(s+0.44)(s+11.3)(s+44)}{(s+0.04)(s+0.816)} \tag{2.5}$$

$$H_{\mathrm{II}}(s) = \frac{(s+0.44)(s+11.3)}{(s+0.816)} \tag{2.6}$$

More complicated nonlinear models have also been developed which can predict the afferent responses accurately under a wide variety of conditions [104, 105].

2.2.3.2 Golgi tendon organs

GTOs respond to forces in the muscles. They share a nerve with the Ia afferent response of the muscle spindles, giving a response known as a type Ib afferent [46]. A linear model of the GTOs was first proposed by Houck and Simon [106], again based on measurements in cats. Their model was stated as a transfer function between muscle force and Ib afferent response by Prochazka [107]:

$$H_{\mathrm{Ib}}(s) = 333\frac{(s+0.15)(s+1.5)(s+16)}{(s+0.2)(s+2)(s+37)} \tag{2.7}$$

A nonlinear model of the GTOs has also been developed [108], and has been found to describe the static and dynamic properties of the GTOs accurately.

2.3 Time delays

As shown in Figure 2.1, there are various ways in which delays are introduced between sensory stimuli and the driver's control response. Delay sources include receptor dynamics, nerve conduction, neural processing and neuromuscular dynamics. Various techniques have been used in the literature to measure delays in human response to sensory stimulation. The simplest of these is to apply a stimulus and measure the time taken for a physical response (such as pressing a button) to be recorded. Some studies have used more sophisticated methods of applying stimuli, such as galvanic vestibular stimulation (GVS) which bypasses the vestibular organs by applying an electrical stimulus directly to the nerves [109]. Other methods have been used to detect responses at other points in the sensorimotor process, such as measuring the VOR to identify reflexive delays, using magnetoencephalography (MEG [110]) or electroencephalography (EEG) to measure electrical impulses within the brain, or using electromyography (EMG) to record electrical activity in the muscles.

When interpreting sensory time delays measured in different studies with various techniques, it is important to consider which of the delay components shown in Figure 2.1 are included in the measurement. The aim of this section is to use results from the literature to estimate the total delay between stimulus and response for each sensory system. However, it can be difficult to separate the effects of pure time delays from lags due to the dynamics of the sensors and muscles, and the time taken for signals to rise above noise levels [111]. Nevertheless, results from the literature can be used to find an approximate estimate of the time delays in human sensory systems.

EMG has been used to measure the response of the muscle spindles to applied muscle stretches, finding delays of 25–30 ms for the Ia afferent and 40 ms for the II afferent [112].

Bigler [41] combined these with measured nerve conduction delays [46, 113] to give delays of 34 ms and 48 ms for the Ia and II afferents. As the Ib afferent response of the GTOs shares the same nerve as the Ia muscle spindle response, the time delay for the Ib afferent may be the same as the Ia muscle spindle response. However these values do not include any neural processing time, so the total delays are likely to be larger.

Reaction times for drivers' responses to simulated wind gusts have been measured in a driving simulator [114]. Mean delays of 0.56 s without motion feedback and 0.44 s with motion feedback were found. These measurements encompass the complete process between stimulus application and physical response shown in Figure 2.1, including all delays, lags and noise. Therefore they can be considered as upper bounds for the delays in the visual system and combined visual-vestibular systems during driving. MEG has been used to record neural responses to visual stimuli and delays of 140–190 ms have been found [115, 116], although it is unclear how much neural processing is carried out before and after this response is measured. Vestibular reflex delays have been measured by actively stimulating vestibular nerves using GVS and measuring the latency to the onset of the VOR [117, 118]. Delays of 5–9 ms have been found, showing that the conduction of vestibular reflex signals is very fast.

There is a growing body of evidence, reviewed by Barnett-Cowan [119], that despite the very fast conduction of vestibular reflex signals, vestibular processing can take much longer than for other sensory signals. Vestibular delays have been found to be significantly longer than visual delays when measuring brain responses using EEG [120] or overall reaction times [121]. Impulses in the brain occurred 100 ms and 200 ms after visual and vestibular stimuli respectively, with a further 135 ms until a button was pressed in both cases. This gives visual and vestibular delays of 235 ms and 335 ms, however these delays may include the time taken for the stimuli to rise above threshold levels (as modelled by Soyka et al. [111]) so they could be overestimates [119].

Visual and vestibular delays measured by Barnett-Cowan et al. [120, 121] are significantly lower than those found in a driving simulator [114]. Furthermore, Barnett-Cowan et al. [120] measured larger vestibular delays than visual delays, whereas Wierwille et al. [114] found that adding vestibular stimuli significantly reduced the overall delay. This could indicate that sensory delays are dependent on the conditions in which the stimuli are applied. Delays due to nerve conduction and sensory and neuromuscular dynamics result from biochemical processes which are unlikely to depend significantly on the precise nature of the task. However, it is likely that neural processing time is affected by the complexity of the task and the presence of distracting information and stimuli. Studies have investigated the intermittent nature of cognitive processing [122, 123], which may play a part in increasing reaction times with increased mental load.

Rather than passively responding to stimuli, drivers actively control the motion of the vehicle. It is difficult to measure time delays during an active control task, as response times are affected by the closed-loop dynamics. Some insight can be gained by looking at studies which have identified visual and vestibular delays during closed-loop pilot control tasks [32–40]. In general vestibular delays have been found to be lower than visual delays, with vestibular delays from 0.05 to 0.23 s and visual delays from 0.18 to 0.32 s. These delays are consistent with the values measured in passive conditions, however due to the large variability in measurements it is difficult to say whether delays are longer in active or passive conditions. Delays have been found to increase in the presence of additional stimuli [37] and in real flight compared with a simulator [39]. This indicates that perceptual delays are higher during multimodal conditions.

2.4 Perception thresholds

Due to limits of human sensory organs and noise caused by spontaneous neuron firing, sensory systems have thresholds below which stimuli cannot be perceived. Perception thresholds are defined as the smallest stimulus which can be detected, and are commonly measured by asking subjects to distinguish something about the stimulus, such as its direction. In reality these thresholds are not precise, but a smooth transition from 0 to 100% probability of detection over a range of values. This cumulative probability distribution is known as a psychometric function [124], and is often modelled as a cumulative normal distribution. Variations on the 'up-down' method [125] are commonly used to measure perception thresholds, and depending on the method used the thresholds measured correspond to different probabilities of detection, generally between 65 and 80%.

The 'just noticeable difference' (JND) is defined as the smallest change in amplitude from a reference stimulus which is required before the difference between the two stimuli is noticed. From experiments on the perception of lifted masses, Weber [126] found that the JND in mass was proportional to the reference mass. This result has been found to be applicable for many perceptual systems, and has become known as 'Weber's law' with the constant of proportionality known as the 'Weber fraction'. Figure 2.5 shows how JNDs vary with stimulus intensity for a stimulus following Weber's law.

Most published measurements of perception thresholds were carried out under passive, unimodal conditions, meaning that subjects were exposed only to the one stimulus of interest and they did not perform any task other than perceiving the stimulus. However, during driving multiple senses are stimulated simultaneously in different axes, and the driver is carrying out an active control task. Groen et al. [127] defined the 'indifference

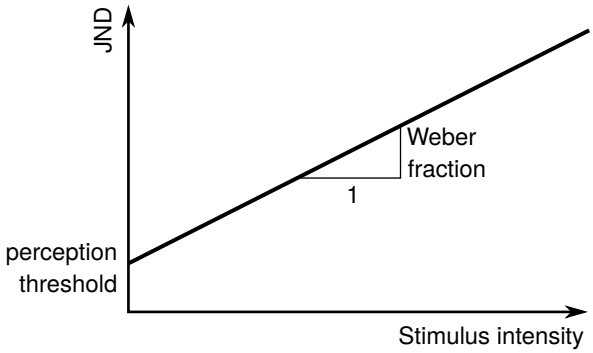

Figure 2.5: JNDs for a stimulus following Weber's law. Weber's law states that JNDs increase linearly with stimulus intensity. The constant of proportionality is known as the Weber fraction, and the y-intercept is the perception threshold.

threshold' as the threshold for perception of a stimulus in the presence of other congruent or incongruent stimuli. JNDs are a special case of indifference thresholds, when the background stimulus is in the same axis and modality as the stimulus which is being detected. Another special case of the indifference threshold is for congruent stimuli from two different sensory modalities (e.g. visual and vestibular systems), where the indifference threshold marks out a 'coherence zone' of stimuli which are perceived as consistent with each other.

2.4.1 Threshold models

The simplest model of sensory thresholds is a 'dead zone' where the perceived amplitude is zero. There are two possible methods for modelling this, as shown in Figure 2.6. Method 2 is the most applicable of these, as method 1 implies that the perceived amplitude would be smaller than the actual amplitude, even above the perception threshold. The dead zone model is useful for simplicity, however it assumes that the psychometric function is a step function, and it cannot be used directly to model JNDs.

Recent studies have suggested that sensory thresholds arise primarily as a result of noise in the sensory channels and the brain. Soyka et al. [68, 69] developed models of translational and rotational motion perception thresholds based on additive noise (AN) applied to the outputs of the otolith and SCC transfer functions. Perception thresholds were defined as the minimum stimulus amplitude required for the output to exceed the noise level. Both studies found good fits to experimental results, although the transfer functions had to be adjusted slightly from those found in the literature (see Section 2.2). This model predicts the frequency dependence of perception thresholds, and is valid for arbitrary motion inputs rather than solely sinusoidal motion. A similar principle was used by Bigler [41] to model JNDs as well as perception thresholds, by adding signal-dependent

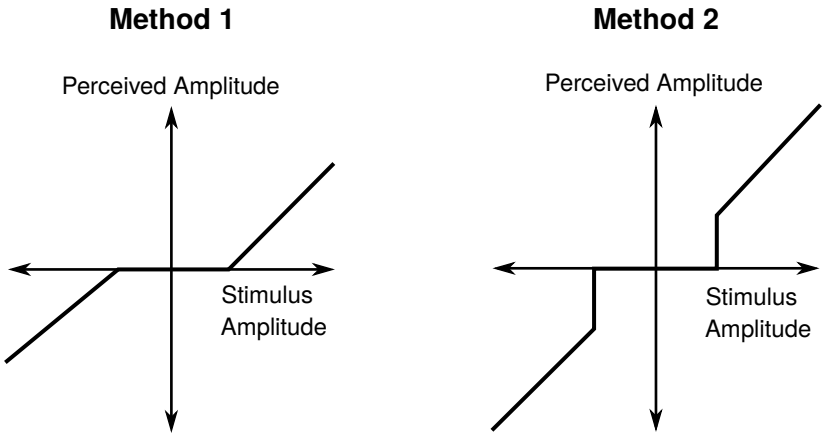

Figure 2.6: Two methods of modelling sensory thresholds as dead zones. In method 1 the perceived amplitude increases from zero after the threshold is reached, whereas in method 2 the perceived amplitude is equal to the stimulus amplitude above the threshold.

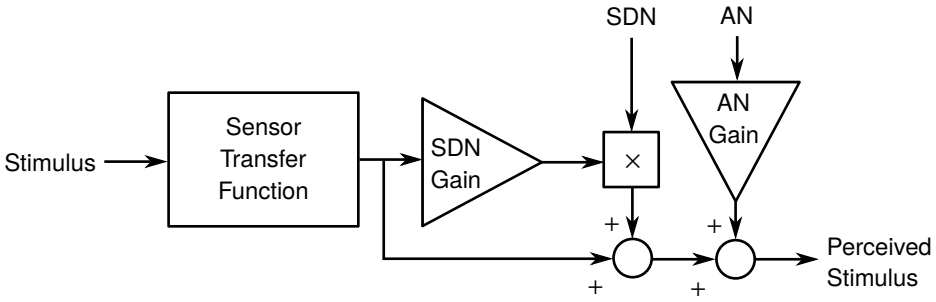

Figure 2.7: Sensor model incorporating additive and signal dependent noise [41]. Noise is added after the sensor transfer function to represent spontaneous neuron firing in the brain.

noise (SDN) as well as AN to the output of the sensor transfer function [128]. This sensor model is shown in Figure 2.7.

2.4.2 Passive threshold measurements

Thresholds and JNDs have been measured in passive conditions for a variety of stimuli. Soyka et al. [68, 69] showed that sensory thresholds could be predicted by finding when the output of the sensory transfer function rises above a specific noise amplitude, therefore this model can be used in reverse to infer noise amplitudes from sensory threshold measurements. In the following subsections noise amplitudes are found in this way for the different senses using sensory threshold measurements from the literature. These measurements have all been taken under passive unimodal conditions, therefore since thresholds have been found to increase under active or multimodal conditions (see Section 2.4.3) the noise amplitudes found in this section can be considered as lower bounds. For each sensory system, the signal-in-noise model of Soyka et al. [68, 69] is used to identify additive noise

amplitudes using two different transfer functions: (i) a published sensor transfer function from considerations of the sensory dynamics; and (ii) a sensor transfer function optimised to fit threshold data. It is unclear which of the two transfer functions is more appropriate for driver modelling. The parameters derived from sensory threshold measurements may describe the behaviour at low amplitudes better, however they may not completely match the dynamic behaviour of the sensory system. Noise amplitudes are given in units with a * symbol at the end, to indicate that the noise is added to the stimuli after filtering by the sensory transfer functions.

2.4.2.1 Visual thresholds

Various studies have measured perception thresholds and JNDs for the visual perception of self-motion. A driving simulator display was used by Bigler [41] to measure yaw angle and lateral displacement thresholds. The display was not calibrated to give full-scale visual feedback so the absolute values of the measured thresholds may not be at the correct scale, however the frequency response should not depend on the display scaling. The results are shown in Figure 2.8. The visual transfer function given in Equation 2.1 was used with the model of Soyka et al. [68, 69] to give predicted thresholds, shown by the solid lines in Figure 2.8. The model fits the thresholds very well, which is not surprising considering that the visual transfer function was found by fitting parameters to these results. The additive noise levels found are 0.0011 rad/s* for the yaw angular velocity and 0.032 m/s* for the lateral velocity. The measurements were also fitted to a simple model of the visual system dynamics, with unity transfer functions between actual and perceived yaw and lateral velocities. The fit using this model is shown by the dotted lines in Figure 2.8, and the noise values found are 0.0013 rad/s* for the yaw angular velocity and 0.035 m/s* for the lateral velocity. Visual JNDs have been measured for a range of yaw velocities, and Weber fractions of 7% [129], 10% [130] and 11% [131] have been found. No studies have been found which measure visual JNDs for lateral motion.

A few studies have investigated limits of visual perception of motion in the longitudinal direction. Reinterpretation of the data collected by Bremmer and Lappe [66] gives a longitudinal displacement JND of 450 mm, with a reference displacement of 4 m. This gives a Weber fraction of 10%, however extrapolating from measurements taken for this relatively short displacement of 4 m may be inaccurate. Monen and Brenner [132] determined the smallest step increase in forward velocity necessary for the difference to be perceived within half a second, and found a large Weber fraction of around 50%.

Thresholds of visual perception involved in feedforward control have not been measured explicitly. Authié and Mestre [133] measured JNDs in path curvature, finding a Weber

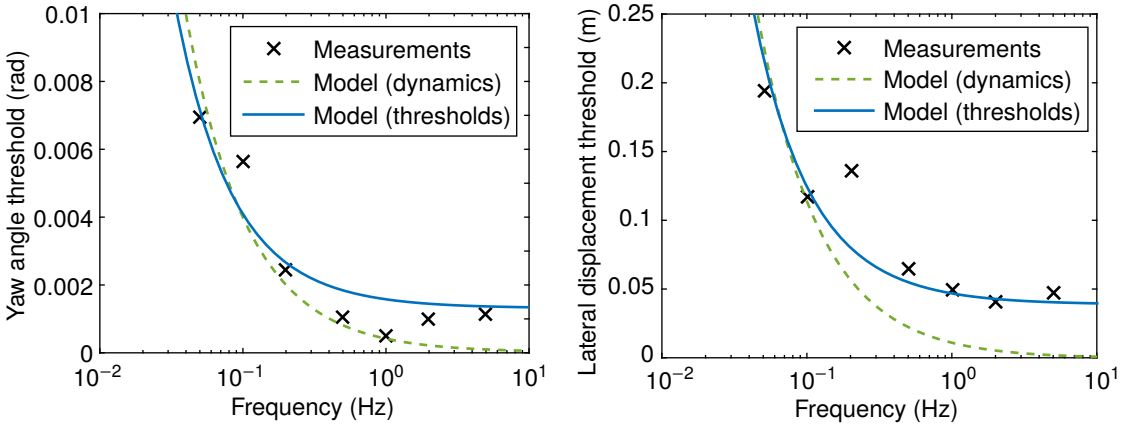

(a) Yaw thresholds

(b) Lateral thresholds

Figure 2.8: Visual feedback perception thresholds measured by Bigler [41], for sinusoidal yaw angles and lateral displacements superimposed on constant velocity forward motion.

fraction of approximately 11%. Bigler [41] used the results of Legge and Campbell [134], who found the angular resolution of the retina to be around 1.5 arcmin, to calculate additive and multiplicative noise variances for visual perception of road geometry. However these results were found by asking subjects to indicate when they could detect a change in position of a small dot, which is likely to be significantly easier than picking out the full road geometry from a complicated visual scene.

2.4.2.2 Otolith thresholds

Perception thresholds for translational accelerations in the horizontal plane have been measured extensively. Measurements have been taken in the longitudinal (x) and lateral (y) directions and the thresholds have been seen to be similar in both directions [84], therefore they are considered together in this section. Thresholds have also been measured in the vertical (z) direction [135], however this axis is not so relevant for the driver's control task.

The 'up-down' method [125] was used to measure thresholds in several studies, where participants were subjected to sinusoidal stimuli with amplitudes which changed for each trial [68, 84, 87]. Other studies used gradually increasing or decreasing motion amplitudes, and asked subjects to indicate when they started or stopped perceiving motion [137, 138]. Thresholds for decreasing amplitudes were found to be lower than for increasing amplitudes. It was thought that this was because the subjects were already 'tuned in' to the signal so were able to pick it out from the noise more easily. In all of these studies, the subjects were moved in only one axis at a time while seated in the dark, so they were focused on the acceleration stimulus without any other distractions.

Thresholds for the discrimination of the direction of sinusoidal accelerations in the

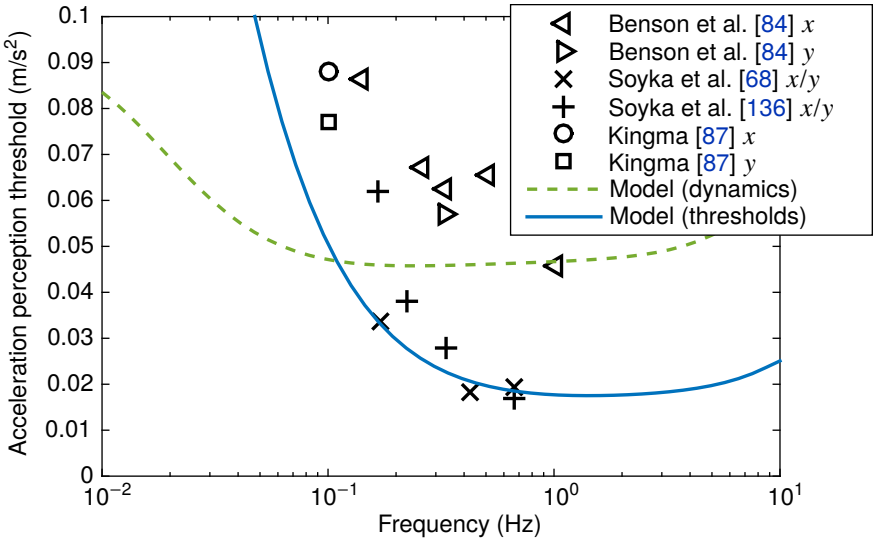

Figure 2.9: Lateral (y) and longitudinal (x) acceleration thresholds measured in several different studies, compared with models found from dynamics and thresholds of the otoliths.

horizontal plane from studies using the up-down method are combined in Figure 2.9. There is a large variability in results between different studies and even within each study, indicating that perception thresholds are sensitive to differences in experimental methods and participants. Predicted thresholds are also shown in Figure 2.9, found using the signal-in-noise model of Soyka et al. [68]. The transfer function given in Equation 2.2 was used with two different sets of parameters from Table 2.1. The dashed line shows the prediction using parameters suggested by Telban and Cardullo [95] from the dynamics of the otoliths and measurements of brain responses, and the solid line shows the prediction using parameters optimised by Soyka et al. [68] to fit measured thresholds. The 'threshold' model was fitted to the measurements of Soyka et al. [68] only, whereas the noise level for the 'dynamics' model was optimised to fit the whole data set. The noise levels found were 0.0377 m/s^2* for the dynamics model and 0.015 m/s^2* for the thresholds model. The thresholds model fits the results much better than the dynamics model, which predicts that thresholds plateau at a lower frequency than reality.

Naseri and Grant [139] measured JNDs for sinusoidal accelerations at 0.4 and 0.6 Hz with varying amplitudes. The results were found to fit Weber's law well, although a dependence on frequency was also seen. A Weber fraction of 5% was found for measurements taken at 0.4 Hz, whereas a value of 2% was found for measurements taken at 0.6 Hz.

2.4.2.3 Semi-circular canal thresholds

Various studies have measured thresholds for perception of angular velocity, using either the up-down method [69, 85, 86] or by gradually increasing or decreasing amplitudes [137,

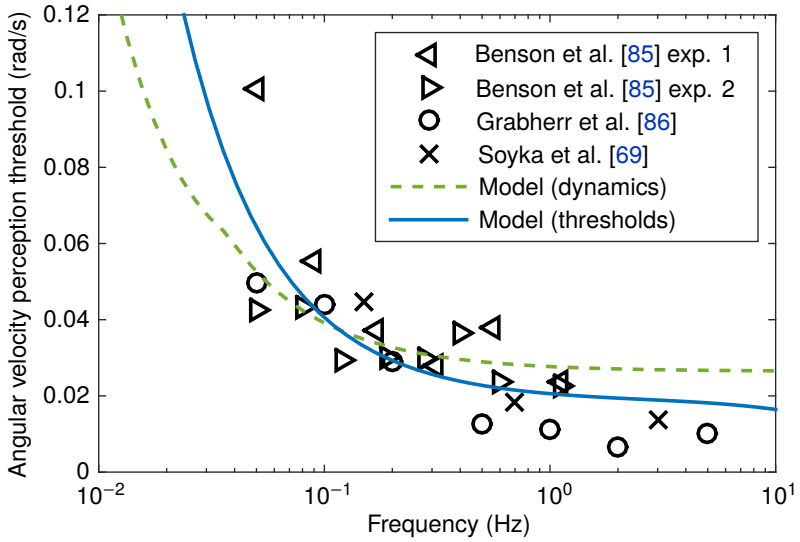

Figure 2.10: Yaw angular velocity thresholds measured in several different studies, compared with models found from the dynamics of the SCCs and from threshold measurements.

138], in a similar way to the otolith measurements. Measured thresholds from studies using the up-down method are compared in Figure 2.10. The data all follow a similar trend, with a fairly low amount of scatter compared to the otolith results. Predicted thresholds are also shown using the signal-in-noise model of Soyka et al. [69], based on the transfer function given in Equation 2.3. The solid line was found using parameters optimised by Soyka et al. [69] to fit threshold measurements, and the dotted line was found using the parameters suggested by Telban and Cardullo [95] for the SCCs, choosing the noise level to fit measured thresholds as well as possible. Both sets of SCC parameters are given in Table 2.2. The noise levels found were 0.025 rad/s* for the 'thresholds' model and 0.0231 rad/s* for the 'dynamics' model. Both models fit the results well, although the model optimised to fit threshold measurements matches more closely as expected.

JNDs for angular velocity perception have been measured by Mallery et al. [90] and dos Santos Buinhas et al. [130], finding Weber fractions of 3% and 13% respectively. The difference between these values may be a result of the fact that Mallery et al. [90] measured JNDs at larger amplitudes than dos Santos Buinhas et al. [130]. Mallery et al. [90] also found that the gradient (JND/amplitude) was higher at low amplitudes, and suggested a power law should be used rather than Weber's law. However it is debatable whether JNDs for the SCCs should follow a power law when most sensory systems follow Weber's law.

2.4.2.4 Somatosensor thresholds

Various studies have measured perception thresholds for the displacements of different limbs, however Bigler [41] is thought to be the first to have directly measured thresholds

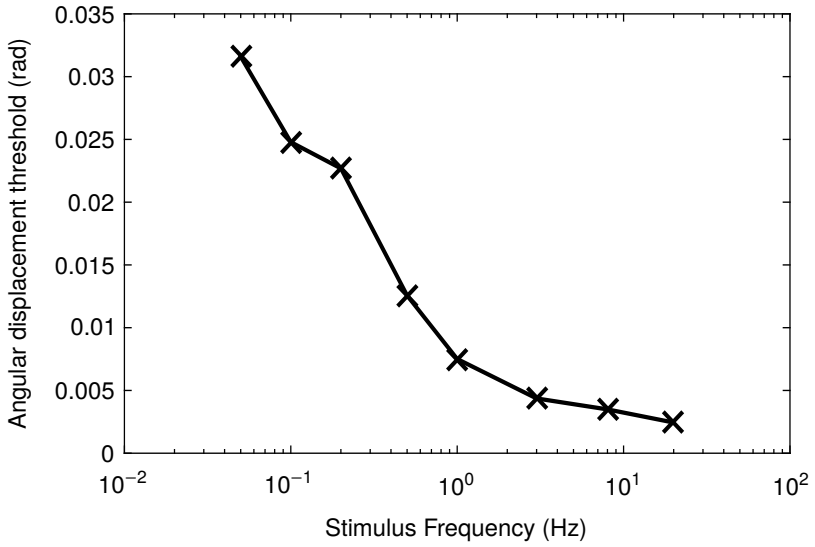

Figure 2.11: Thresholds for the perception of steering wheel angular displacement, measured by Bigler [41].

for the perception of steering wheel angle. The results are shown in Figure 2.11. These results cannot be used to find noise levels for the somatosensors without making some assumptions about the relationship between steering wheel displacement and the displacements, velocities and forces of the muscles, and further assumptions about the method used to integrate information from the Ia, Ib and II afferents. Further work is necessary to determine appropriate noise levels for the somatosensors.

Newberry et al. [140] measured JNDs in steering wheel angle, and reported a Weber fraction of 14%. However, this was achieved by fitting a line with zero perception threshold, and a better fit to the data can be achieved by including the effect of a non-zero threshold. This gives a good linear fit to the measurements, with a Weber fraction of 9.6% and a perception threshold of 0.006 rad. The stimulus profile and frequency was not reported by Newberry et al. [140], however the extrapolated perception threshold is similar to that measured by Bigler [41] for stimuli at 1 Hz (see Figure 2.11).

No studies are known to have directly measured perception thresholds for steering wheel force or torque. Steering wheel force JNDs were measured by Newberry et al. [140], and extrapolating from these measurements gives a perception threshold of 0.45 N and a Weber fraction of 9.6%. It is interesting to note that the Weber fraction found for the GTOs using this method matches the Weber fraction found for the muscle spindles almost exactly, suggesting that there may be a perceptual link between the two sensors. The GTO afferent and the primary muscle spindle afferent share the same nerve conduction path [46], so since JNDs are related to noise along the transmission path this could explain the similarity.

2.4.3 Active and multimodal thresholds

The studies summarised in Section 2.4.2 all measured thresholds of a single stimulus in isolation, during passive conditions where the subject was concentrating on the stimulus. However, sensory stimuli which occur during driving are very different to the stimuli applied in these controlled studies, so these results may not be directly applicable to driving tasks. Stimuli in driving tasks are perceived under active rather than passive conditions, and several stimuli are perceived simultaneously. Therefore the indifference threshold (threshold in the presence of other stimuli [127]) should determine the limits of perception during driving.

By asking subjects to perform a secondary control task in a separate motion axis, it has been found that increasing the mental load on subjects causes an increase in perception thresholds [137, 141]. Due to the equivalence of translational accelerations and shifts in the gravity vector the brain can easily be fooled into misinterpreting the two types of motion. Presenting subjects with visual cues simulating a translational acceleration while they were undergoing rotational motion caused thresholds for the rotation to increase by factors of 5 to 6 [142, 143]. During an active driving task thresholds increased by factors up to 4 for some subjects, but didn't change at all for others [143]. The participants whose thresholds did not increase during the active driving task reported higher levels of immersion in the simulation, indicating that immersion is linked to participants' ability to perceive the motion accurately.

Pitch and roll thresholds have been measured with masking vertical motion cues, finding a significant linear increase in pitch and roll thresholds with vertical motion amplitude [144, 145]. In contrast to these studies, Valente Pais et al. [146] found no significant effect of vertical motion amplitude on pitch rate thresholds. In this study the pitch and vertical motion were applied at the same frequency, which may have caused the motion cues to be perceived as coherent. Indifference thresholds for pitch rotation in the presence of longitudinal visual motion were found to have the same frequency response as the perception thresholds measured in passive conditions, but increased by a constant gain [127, 142]. This result has been used to hypothesise that the presence of additional sensory stimuli scales perception thresholds by a constant gain, without affecting the frequency response. This is consistent with the models of Soyka et al. [68, 69] and Bigler [41] (shown in Figure 2.7), where the threshold is placed after the sensory transfer function and the additional stimuli cause an increase in the noise level. Groen et al. [127] suggested that the increase in noise level is linearly dependent on the amplitude of the additional stimulus, which is equivalent to Weber's Law in the special case of the additional stimulus being in the same axis and modality as the measured stimulus.

Recent studies have used parameter identification methods to estimate threshold values during an active control task in the same axis, and thresholds in active conditions have been found to be around 1.6 times larger than thresholds measured in passive conditions [147, 148]. It is evident from the literature that various factors cause thresholds to increase from values measured in passive conditions, including mental load, the presence of other stimuli and carrying out an active control task. It therefore may not be appropriate to rely on passive threshold measurements to model sensory dynamics during an active driving task.

2.4.4 Coherence zones

The term 'coherence zone' was coined by van der Steen [149] to describe the range of amplitudes of inputs to two sensory systems (such as visual and vestibular systems) which are perceived as consistent with each other, as shown in Figure 2.12. The coherence zone can be defined in terms of the point of mean coherence (PMC), coherence zone width (CZW) and gain of mean coherence (GMC) as shown.

Coherence zones between the visual and vestibular systems have been measured at various amplitudes and frequencies [149–151]. The GMC was found to decrease with increasing stimulus amplitude, with subjects preferring larger vestibular motion than visual motion at small amplitudes and the opposite at larger amplitudes. Significant differences were found between values measured in different studies, highlighting that coherence

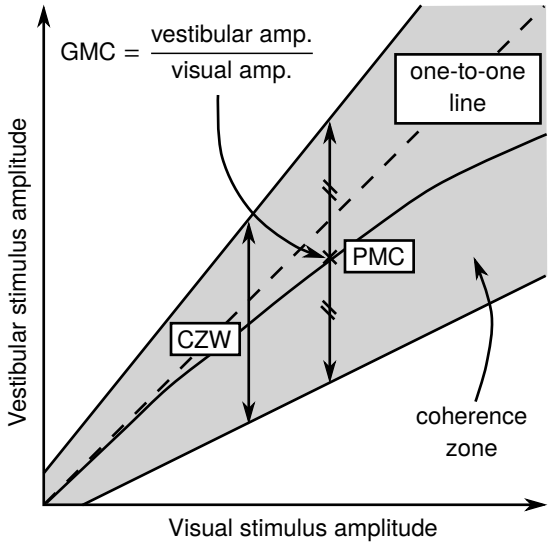

Figure 2.12: Coherence zone between visual and vestibular stimuli. The coherence zone width (CZW) is the difference between the upper and lower limits, and the point of mean coherence (PMC) is the point halfway between the limits. The gain of mean coherence (GMC) is defined as the ratio of the vestibular amplitude to the visual amplitude at the PMC, and represents the preferred gain between the visual and vestibular cues.

zones are highly dependent on experimental conditions. Contrary to results found for perception thresholds, coherence zones do not change significantly during an active control task [152]. This indicates that the perceptual mechanisms behind perception thresholds and coherence zones may not be directly linked. The concept of a coherence zone has been extended to the detection of heading direction [153] and phase differences [154, 155]. Jonik et al. [155] found that physical motion can lead visual motion by up to 22 deg without the difference being detected. This result was independent of the stimulus frequency, showing that humans can be considered as phase error detectors rather than time delay detectors.

Research has shown that, when asked to tune physical motion to match visual motion, subjects pick higher amplitudes when tuning downwards from high amplitude motion than when tuning upwards from low amplitude motion [156]. Correia Grácio et al. [157] defined the 'optimal zone' as the area between these upper and lower optima, and found that it lay within the coherence zone. Similar to the PMC, GMC and CZW for coherence zones, the optimal zone was defined in terms of the point of mean optimal gain (PMO), 'gain of mean optimal' (GMO) and optimal zone width (OZW). In contrast to coherence zone measurements, the OZW was found not to vary with amplitude or frequency, however the GMO was found to decrease at higher amplitudes and frequencies. The GMO was also found to be strongly affected by the field of view, resolution and depth of the visual scene, with more realistic scenes giving GMOs closer to unity [158].

Two approaches to modelling CZWs were compared by dos Santos Buinhas et al. [130], one matching the perceived intensity of the two stimuli and applying this to averaged JNDs, and one summing the JNDs for the two individual stimuli. Comparison of model predictions with experimental data showed that summing JNDs provides the best fit, explaining the results particularly well at lower amplitudes. dos Santos Buinhas et al. [130] suggested that PMCs could be modelled using Stevens' power functions of perceived stimulus intensity, however this method was not experimentally verified.

2.5 Sensory integration

The sensory systems described in Section 2.2 provide the central nervous system (CNS) with measurements which can be used to estimate vehicle states while driving. However, these measurements are shaped by the sensor dynamics, delayed (see Section 2.3) and also contain additive and signal-dependent noise (as described in Section 2.4). The CNS must therefore carry out sensory integration to give a single estimate of the vehicle states from the noisy, delayed, filtered information received from each of the sensors.

In a real-world driving scenario, the driver is presented with coherent sensory in-

formation. Any discrepancies between information from the different sensors is due to sensory noise, or incomplete information available to a particular sensor. However, in some situations the information presented to the different senses may be incoherent or biased, in which case the driver may use a different integration strategy. This is particularly relevant for motion in virtual environments, where the visual, vestibular and somatosensory information presented to the driver may not all accurately reflect the real-world stimuli. An overview of methods and results from investigations of sensory integration in a variety of virtual environments (not specific to driving) is given by Campos and Bülthoff [159]. The following subsections build on this, focusing on results which suggest how information from the sensory systems summarised in Section 2.2 may be integrated during driving.

2.5.1 Integration of coherent sensory measurements

The simplest model of sensory integration is a linear weighting of the estimates from different sensory systems [160]. Appropriate weightings can be identified from experiments, however the scope of models with fixed weightings is limited. For many sensory systems, the CNS has been found to integrate measurements using statistically optimal methods [161–169]. These methods are based on Bayes' theorem [170], which relates the *a posteriori* probability $\mathrm{P}(\hat{I} \mid \hat{S})$ of condition $\hat{I}$ given observation $\hat{S}$ to the probability $\mathrm{P}(\hat{S} \mid \hat{I})$ of observation $\hat{S}$ given condition $\hat{I}$, the *a priori* probability $\mathrm{P}(\hat{I})$, and the observation probability $\mathrm{P}(\hat{S})$ (which is usually assumed uniform):

$$\mathrm{P}(\hat{I} \mid \hat{S}) = \frac{\mathrm{P}(\hat{S} \mid \hat{I})\mathrm{P}(\hat{I})}{\mathrm{P}(\hat{S})} \tag{2.8}$$

Optimal integration of sensory cues involves choosing from the set of all possible conditions $\hat{I} = \{\hat{I}_i \mid i = 1, \ldots, N_{\hat{I}}\}$ the condition $\hat{I}_i$ which has the highest probability $\mathrm{P}(\hat{I}_i \mid \hat{S})$ based on the set of observations $\hat{S} = \{\hat{S}_i \mid i = 1, \ldots, N_{\hat{S}}\}$ from the different sensory channels. For a continuous set of possible conditions $\hat{I}$ a probability density function of $\mathrm{P}(\hat{I} \mid \hat{S})$ can be plotted. Equation 2.8 shows that $\mathrm{P}(\hat{I}_i \mid \hat{S})$ depends on an assumption about the probability distribution $\mathrm{P}(\hat{I})$ before the measurements are made, known as a 'prior'.

There are various ways in which the optimal value of $\hat{I}$ can be chosen, such as the 'maximum a posteriori' (MAP) estimate, the 'minimum mean square error estimate' (MMSE) and the 'maximum likelihood estimate' (MLE) [171, 172]. However, if the priors $\mathrm{P}(\hat{I})$ and $\mathrm{P}(\hat{S})$ are uniform and the probability distributions are symmetric these estimates are identical, and can found by maximising the likelihood function $\mathrm{P}(\hat{S} \mid \hat{I})$.

If the probability distributions of the sensory estimates $\hat{S}_i$ are all Gaussian, the MLE

$\hat{S}$ of a property is found by weighting each estimate in proportion to the inverse of its variance σ_i^2 [173]:

$$\hat{S} = \sum_i \hat{w}_i \hat{S}_i \qquad \text{with} \qquad \hat{w}_i = \frac{1/\sigma_i^2}{\sum_j (1/\sigma_j^2)} \tag{2.9}$$

The variance σ^2 of the combined estimate $\hat{S}$ is found from Equation 2.10 to be lower than the variances of the individual estimates from the different sensory systems:

$$\sigma^2 = \left(\sum_i \frac{1}{\sigma_i^2} \right)^{-1} \tag{2.10}$$

Oruç et al. [162] showed that a Gaussian prior can be included in the MLE analysis as an additional input, weighted by the inverse of its variance as usual. MacNeilage et al. [174] used this result to model the integration of visual and vestibular cues to disambiguate between an acceleration and a shift in the gravity vector, incorporating priors to model the assumptions that humans are normally in an upright position and that smaller accelerations are more likely than larger ones. Soyka et al. [175] measured off-centre yaw rotation thresholds and found that SCC and otolith signals were integrated, although the results suggested information from additional sensory systems may also have been used.

Near-optimal Bayesian integration of visual and vestibular information has been measured in several studies [164–169]. In contrast to these studies, de Winkel et al. [176] only found results that fit the MLE model for 3 out of 8 participants and Nesti et al. [177] found that combined visual-vestibular thresholds were higher than predicted by a MLE model. Butler et al. [178] found that participants exhibited optimal visual–vestibular integration 90% of the time with a stereoscopic visual display compared with 60% of the time with a binocular display. This suggests that the realism of the visual scene may affect whether or not visual and vestibular information is integrated optimally. Some studies have found that vestibular cues are weighted higher than visual cues [165, 166] while others have found that visual cues are weighted higher [167]. Prsa et al. [167] suggested that over-weighting of otolith signals and under-weighting of SCC signals may occur when vestibular cues are integrated with visual cues.

In order to develop effective and efficient control strategies for interacting with their surroundings, humans use their experience to develop internal models of themselves and the world around them [47]. They are able to use learning methods to adapt these models to changes in the environment [48] such as astronauts entering microgravity [179]. Using an internal model, a recursive state estimator can be used to provide new *a priori* estimates at

each time step to give improved estimates of the system states. A common implementation of this method is the Kalman filter [180, 181]. It is assumed that the observer has an internal model of the system given in state-space form:

$$\begin{aligned} \boldsymbol{x}(k+1) &= \mathbf{A}\boldsymbol{x}(k) + \mathbf{B}\boldsymbol{u}(k) + \boldsymbol{w}(k) \\ \boldsymbol{y}(k) &= \mathbf{C}\boldsymbol{x}(k) + \boldsymbol{v}(k) \end{aligned} \tag{2.11}$$

The main difference between a driver and a passenger is that the driver has knowledge of the inputs $\boldsymbol{u}$, although they are perturbed by process noise $\boldsymbol{w}$. Both driver and passenger measure the outputs $\boldsymbol{y}$, which are perturbed by measurement noise $\boldsymbol{v}$. The new estimate of the states $\hat{\boldsymbol{x}}(k+1)$ is predicted by propagating the current input $\boldsymbol{u}(k)$ and state estimate $\hat{\boldsymbol{x}}(k)$ through the internal model of the system. A correction is then added based on the error between the previous estimated output $\mathbf{C}\hat{\boldsymbol{x}}(k)$ and measured output $\boldsymbol{y}(k)$, weighted by the 'Kalman gain' $\mathbf{K}(k)$:

$$\hat{\boldsymbol{x}}(k+1) = \mathbf{A}\hat{\boldsymbol{x}}(k) + \mathbf{B}\boldsymbol{u}(k) + \mathbf{K}(k)\left\{\boldsymbol{y}(k) - \mathbf{C}\hat{\boldsymbol{x}}(k)\right\} \tag{2.12}$$

The time-varying Kalman gain $\mathbf{K}(k)$ is calculated to give a statistically optimal minimum-variance estimate, weighting the estimates based on the covariances of the Gaussian noise $\boldsymbol{w}$ and $\boldsymbol{v}$. If the covariances are time-invariant, a steady-state linear filter can be found to give the optimal state estimate for the system. Various studies have proposed models of visual-vestibular integration based on Kalman filters [182–184] and Kalman filters have also been used to model estimation of vehicle states for pilots [185] and drivers [41].

One implication of MLE models of human sensory integration is that the observer must have access to estimates of the noise variance for each sensory channel. Ernst and Bülthoff [186] suggested that the variance could be determined by looking at the responses over a population of independent neurons. Several studies have attempted to build realistic neural models to describe this behaviour [187–189], and they have found that a close approximation to MLE can be achieved in such a way. Fetsch et al. [166] studied the integration of visual and vestibular cues to heading angle in humans and monkeys with varying reliability of the visual cues. They found that both humans and monkeys were able to dynamically re-weight the cues between trials, indicating that they were able to measure the reliability of each cue.

2.5.2 Integration of biased sensory measurements

While MLE is an optimal method of combining measurements from noisy sensory channels with the same mean, if the signals are biased such that their means are no longer coherent,

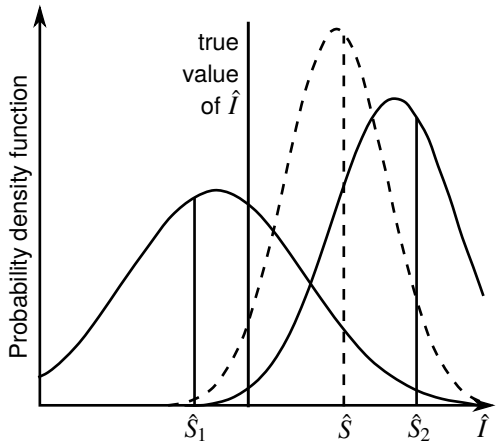

Figure 2.13: Maximum likelihood integration of two biased sensory channels. Probability distributions of the sensors $\hat{S}_1$ and $\hat{S}_2$ (solid lines) are both biased, and using MLE causes this bias to carry through to the combined estimate (dashed line).

using MLE will cause the bias to carry through into the 'optimal' sensory estimate as seen in Figure 2.13 [190]. There will always be differences between measurements $\hat{S}_i$ from noisy sensory channels, however it is impossible to separate the effects of stochastic variations about the mean from bias in the sensory channels without prior knowledge of the bias. The CNS may integrate biased sensory measurements using the MLE method if conflicts are small [165, 191, 192] or if the conflicting information is presented in different motion axes [193]. de Winkel et al. [194] found that over half of subjects integrated visual and physical heading information regardless of the size of the bias. However other studies have found evidence of various strategies for reducing bias in perceived signals [195–198].

When presented with two different sensory cues, the CNS must decide whether or not they are coherent (originating from the same source). If they are coherent, differences between them are a result of stochastic variations and the cues can be combined using MLE. If not, the cues should be treated separately, treating the situation as a 'cue conflict'. Körding et al. [195] proposed a model using Bayes' rule to decide whether or not two cues are coherent based on a prior describing the likelihood of the cues coming from the same source. The model was validated using experimental results, however Seilheimer et al. [163] noted that Körding et al. [195] did not vary the reliability of the cues, so it is unclear whether the model is valid in all cases. A similar Bayesian model incorporating priors was proposed by Knill [199]. They found that the weight applied to a cue shrunk as the size of the conflict increased, but it did not decrease to zero. However other studies have found that under some circumstances humans will 'veto' a cue that does not fit with the other sensory measurements [196, 200].

Ghahramani et al. [201] proposed an additional stage of 'cue calibration' before cues

are fully integrated, where the difference between the estimates is reduced. The values of estimates $\hat{S}_1$ and $\hat{S}_2$ are calibrated by adding $\Delta\hat{S}_1$ and $\Delta\hat{S}_2$, given by:

$$\begin{aligned} \Delta\hat{S}_1 &= c_1(\hat{S}_2 - \hat{S}_1) \\ \Delta\hat{S}_2 &= c_2(\hat{S}_1 - \hat{S}_2) \end{aligned} \tag{2.13}$$

This improves internal consistency [197], ensuring that the estimates from different sensory systems agree with each other, although it doesn't necessarily improve external accuracy (the overall accuracy of the CNS's combined estimate). If $c_1 + c_2 = 1$, calibration achieves full internal consistency by adjusting both estimates to the same value, otherwise the reduction in the difference between estimates is smaller. Several studies have shown that vision dominates the other senses under certain conditions [161, 202], so a model of 'visual capture' has been proposed [161, 186]. In this model the non-visual sensory estimate adapts to equal the visual estimate, giving $c_i = 0$ for the visual channel and $c_i = 1$ for the other channel. Alternatively, Ghahramani et al. [201] proposed that calibration may be based on reliability, with each calibration constant c_i proportional to the variance σ_i^2 of the sensory estimate $\hat{S}_i$. Burge et al. [197] tested this model in an experiment on visual-haptic estimation of slant, and reported strong evidence in favour of this reliability-based cue calibration.

Reliability-based calibration does not make physical sense as a method for reducing sensory bias, however, as the reliability of a cue is independent of its bias [190]. A sensory estimate could have low variance (high reliability) and high bias, or a high variance (low reliability) but low bias. For example, in Figure 2.13 the cue with the higher variance has the lower bias. Evidence opposing reliability-based calibration was found by Girshick and Banks [200], who showed that the vetoed cue was not necessarily the cue with the highest variance. Fixed-ratio calibration (with constants c_i learned from past experience) was found to fit measurements better than reliability-based calibration by Zaidel et al. [198], who also explained how erroneous indications of reliability-based calibration could appear using the methods of Burge et al. [197].

Linear cue calibration has been observed for conflicting visual and vestibular measurements in several studies although, as with coherent measurements, there is disagreement about which sense is more highly weighted. Visual dominance was found by Rader et al. [203], whereas the vestibular system was found to dominate by Harris et al. [204]. Ohmi [205] found that visual cues dominated when conflicts were small but vestibular cues dominated when conflicts were large. Zacharias and Young [206] found that vestibular cues dominated visual cues at higher frequencies, so the dominant sensory system may depend on the frequency content of the motion.

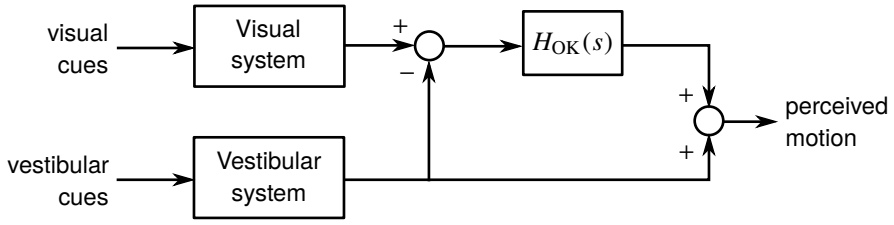

Figure 2.14: Model of the 'optokinetic influence' proposed by van der Steen [149]

Experimental studies have shown that when a consistent conflict is observed between the visual and vestibular systems, the perceived motion will eventually drift towards the visual estimate [207]. van der Steen [149] proposed a model of the 'optokinetic influence', where the visual estimate attracts the vestibular estimate over a transient period due to the onset of visual self-motion (vection). This is modelled by passing the difference between the visual and vestibular estimates through a low-pass filter given by:

$$H_{OK}(s) = \frac{1}{1 + \omega_{OK} s} \tag{2.14}$$

giving the optokinetic influence which is then added to the vestibular output as shown in Figure 2.14. An implication of this model is that pre-filtering the vestibular cues by the inverse of the vestibular dynamics, or conversely pre-filtering the visual cues by the vestibular dynamics, should cause the visual and vestibular cues to be perceived as coherent even though they differ substantially. Wentink et al. [208] tested this hypothesis using subjective feedback from experiments in a simulator, and found that pre-filtering the vestibular cues by the inverse of the vestibular dynamics did indeed result in coherent perception. However pre-filtering the visual cues by the vestibular dynamics produced cues which were perceived as coherent for only half the motion conditions.

Zacharias [209] developed a detailed empirical model of visual-vestibular integration under cue-conflict conditions, shown in Figure 2.15. Borah et al. [182] developed an adaptive version of this model, multiplying the visual estimate by the gain K and combining it with the vestibular estimate using a Kalman filter. Telban and Cardullo [95] extended the model of Zacharias [209], using some of the modifications suggested by Borah et al. [182] and including the optokinetic influence modelled by van der Steen [149], and showed that latencies measured in previous studies on humans could be predicted. However, further validation work is needed to determine whether this model is more generally applicable. Wright et al. [210] subjected participants to conflicting visual and vestibular motion in the vertical axis with a realistic visual display. The results were found to be incompatible with linear weighting conflict models and the more complicated model of Zacharias [209], as for high visual amplitudes visual perception was found to dominate, independent of the

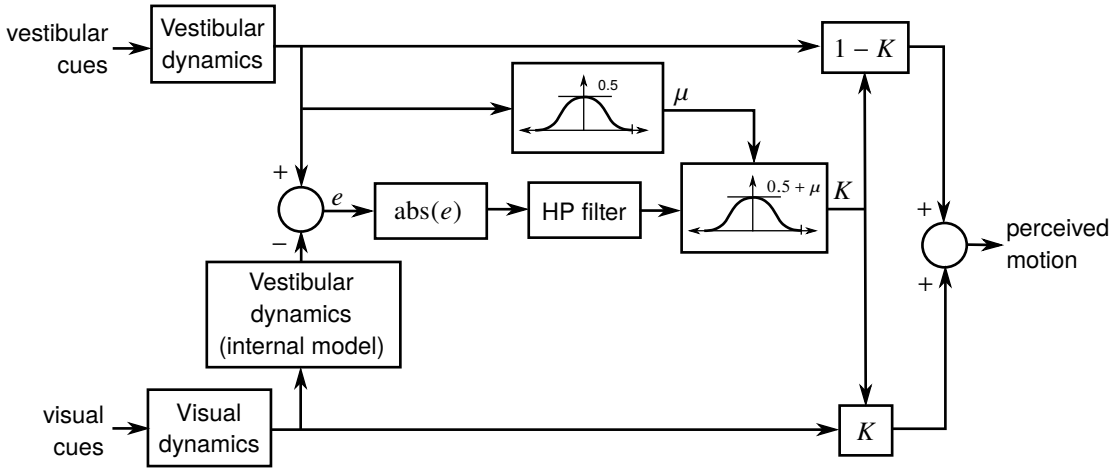

Figure 2.15: Visual-vestibular integration model proposed by Zacharias [209], adapted from [95]. Visual measurements are filtered through an internal model of the vestibular dynamics, subtracted from the vestibular measurements and passed through a high-pass filter to resolve steady-state conflicts. Cues are weighted by K, which varies between 0 and 1 based on cosine-bell weighting functions. Large conflicts drive K to 0, vetoing the visual cue. Small conflicts give K between 0.5 and 1, based on the magnitude of the visual cue.

vestibular amplitude. More research is clearly needed to understand how humans integrate biased sensory estimates in different conditions.

2.6 Discussion

Key results from the literature on human sensory dynamics are presented in Sections 2.2 to 2.5. In this section these results are summarised and discussed with a view to understanding and modelling driver steering and speed control. Results for the human sensory systems which are most relevant to driver modelling are summarised in Table 2.3. Transfer functions are presented which have either been found from models of the sensory dynamics and measurements of brain activity or inferred from sensory threshold measurements. Using the transfer functions found from sensory threshold data may give more accurate results near the limits of perception, however they may not capture all of the dynamic behaviour of the sensory system.

Noise magnitudes have been inferred from sensory threshold measurements using the signal-in-noise model of Soyka et al. [68, 69]. These were found from passive threshold measurements taken for one sensory stimulus at a time, however thresholds have been found to increase in active conditions and in the presence of other sensory stimuli by factors between 1.5 and 6 [137, 141–145, 147, 148]. Therefore the noise values shown in Table 2.3 should be considered as lower bounds. Most sensory systems have been found

Table 2.3: Summary of sensory system results from the literature. Noise amplitudes are given in units with a * symbol at the end, to indicate that the noise is added to the stimuli filtered by the sensory transfer functions.

		From sensory dynamics		From perception thresholds		Weber fraction	Sensor delay
System	**Input**	**Transfer function**	**Noise**	**Transfer function**	**Noise**	**(%)**	**(ms)**
Visual feedback	Yaw angular velocity	1	0.0013 (rad/s*)	$\frac{0.810}{s+0.810}$	0.0011 (rad/s*)	7–11	100–560
Visual feedback	Lateral velocity	1	0.035 (m/s*)	$\frac{0.810}{s+0.810}$	0.032 (m/s*)	7–11	100–560
Visual feedback	Longitudinal velocity	1	–	–	–	10-50	100–560
Visual feedforward	Target path	Preview model	–	–	–	11	100–560
Otoliths	Acceleration	$\frac{0.4(1+10s)}{(1+5s)(1+0.016s)}$	0.038 (m/s^2*)	$\frac{0.0225(1+22.05s)}{(1+0.62s)(1+0.016s)}$	0.015 (m/s^2*)	2–5	5–440
SCCs	Angular velocity	$\frac{5.73(80s^2)}{(1+80s)(1+5.73s)}$	0.023 (rad/s*)	$\frac{2.2s(1+0.014s)}{(1+2.16s)(1+0.005s)}$	0.025 (rad/s*)	3–13	5–440
Muscle spindles (type Ia)	Arm muscle displacement	$\frac{s(s+0.44)(s+11.3)(s+44)}{(s+0.04)(s+0.816)}$	–	–	–	10	> 34
Muscle spindles (type II)	Arm muscle displacement	$\frac{(s+0.44)(s+11.3)}{(s+0.816)}$	–	–	–	10	> 48
GTOs	Arm muscle force	$\frac{333(s+0.15)(s+1.5)(s+16)}{(s+0.2)(s+2)(s+37)}$	–	–	–	10	> 34

to approximate Weber's law, with JNDs increasing with stimulus amplitude, therefore Weber fractions have been included in Table 2.3. Increases in sensory noise with stimulus amplitude can be modelled by including signal-dependent noise [41, 128].

Estimates of sensor delays are also given in Table 2.3 for each system, comprising of all components of the time delay between stimulus application and physical response. However, there is still some uncertainty about the precise values, as it is thought that delays in neural processing may be dependent on the exact nature of the stimuli and the task being carried out. It is unclear whether delays increase or decrease during active conditions, however they have been found to increase with additional stimuli in multimodal conditions [37, 39].

For many types of stimuli, coherent sensory information has been found to be integrated in a statistically optimal fashion [161–169]. Humans build up internal models of themselves and their surroundings [47, 48] and a Kalman filter can be used to model optimal sensory integration using internal models [180–185]. For incoherent sensory information, when conflicting information is presented to the different sensory channels, sensory integration is less well understood. A variety of models have been proposed, however no overwhelming evidence has been found in favour of any of them. Consideration of how humans integrate incoherent or biased sensory measurements may be important when studying drivers in virtual environments, however in normal driving sensory measurements are coherent.

Since sensory parameters have been found to change under active or multimodal conditions, it may not be appropriate to apply the results shown in Table 2.3 directly to a driver model. It is very difficult to measure sensory parameters directly during realistic driving conditions. However, by developing a model of driver control behaviour incorporating sensory dynamics, parametric identification methods could be used to gain some insight into the performance of sensory systems while driving. Procedures for parameter identification have been developed [211, 212] and used to identify models of drivers [213, 214] and pilots [32–40].

It is hoped that the information presented in this literature review will inform and motivate future researchers to consider the influence of sensory dynamics in driving tasks. The differences highlighted between active and passive measurements indicate that it is not always appropriate to apply results from the sensory perception literature directly to driver models. However, identification methods have been used in recent aerospace studies to investigate perception during active control tasks, and there is clear scope for applying similar techniques to studying drivers. The danger in such an approach is that identification of a large number of sensory parameters may become infeasible. Therefore care must be taken to increase the complexity of sensory models slowly, and use carefully designed experiments to isolate different features of sensory perception during driving. This review

should serve as a guide for potential areas of investigation, and a reference to compare with new results.

2.7 Conclusion

The results summarised in this literature review give an insight into various different sensory systems, and how they can be used to model driver control behaviour. Sensory transfer functions have been studied extensively, and there is little disagreement between different studies. Sensory integration is reasonably well understood under normal conditions, however there is no consensus on how humans integrate conflicting sensory information. Studies have shown that sensory thresholds increase under active and multimodal conditions, but further research is necessary to determine how and why this happens. Time delays also increase during multimodal conditions, however it is not clear whether they vary during active control tasks. There is a great deal of scope for improving the available knowledge on human sensory perception during active control tasks, so future research should focus in this area. It is hoped that the information in this review will motivate the development of more sophisticated driver steering and speed control models which take account of the driver's sensory dynamics.

Chapter 3

Driver model development and identification

Existing models of driver steering control do not consider the driver's sensory dynamics. Many aspects of human sensory perception have been researched extensively, as reviewed in Chapter 2. Therefore, a new driver model is proposed incorporating sensory transfer functions, noise and delays. An experiment was carried out in a driving simulator, aiming to replicate a real-world driving scenario with no motion scaling. The results of this experiment are used to identify parameter values for the new driver model, and the new model is found to describe the results of the experiment well. While some parameter values vary depending on the experimental conditions, a fixed-parameter model is still able to provide a good approximation to the measured results. The identified parameter values are compared with results from the literature and are found to be physically plausible, supporting the hypothesis that driver steering control can be predicted using models of human perception and control mechanisms.

3.1 Introduction

As discussed in Chapter 1, there is significant motivation for developing driver models which allow quantitative analysis and optimisation of the driver-vehicle system without relying on track testing and subjective driver feedback. Various models of driver steering control exist, as reviewed by MacAdam [10] and Plöchl and Edelmann [11], however few of these consider the driver's sensory dynamics. The role of sensory dynamics during driving can be explained within the 'two-level' model proposed by Donges [6]. In this model a feedforward controller observes the road ahead, plans a trajectory for the vehicle and calculates the required steering inputs, while a feedback controller corrects for disturbances about this planned trajectory. The feedforward controller operates based on inputs from the visual system alone, as modelled by optimal 'preview' controllers [13, 14]. The feedback task involves using estimates of the vehicle states to correct for disturbances around the planned path. Drivers cannot know all the vehicle states with complete accuracy, but

instead take noisy, filtered, delayed measurements of different sensory variables and use these to estimate the information required to control the vehicle [43]. The main sensory systems used for the feedback task are the visual, vestibular and somatosensory systems.

A review of published literature relevant to sensory dynamics in driving tasks is presented in Chapter 2, and the results of this can be used to assist with the design of a new driver model incorporating sensory dynamics. The new model builds on the work of Bigler [41], who used measurements from the literature to develop a driver steering control model incorporating sensory dynamics, noise and delays. However, the predictions of the model developed by Bigler [41] matched experimental results poorly. Recent studies have shown that sensory thresholds increase significantly during an active control task [143, 147, 148] and in the presence of additional sensory stimuli [127, 142–145]. An active control task such as driving requires attention to be shared between the task itself and the perception of concurrent sensory stimuli, in contrast with passive measurements where the subject is concentrating solely on one sensory stimulus. Therefore, to understand how sensory systems are used during driving an identification procedure should be used to fit the model to measurements from an active driving control task, rather than using passive measurements from previous studies.

The aim of this work is to develop a new model of driver steering control which uses models of the underlying physical processes involved in drivers' perception and control. The derivation of this new model is presented in Section 3.2. Preliminary analysis of this model was carried out previously [215], using results from an experiment in a flight simulator [36] to validate the modelling approach for an aeroplane control task. The design of a new experiment is described in Section 3.3, following similar procedures to Zaal et al. [36] to measure steering control behaviour in a driving simulator. An identification procedure described in Section 3.4 is used to find parameter values to fit the data from the experiment, giving the results presented in Section 3.5. The findings are discussed in Section 3.6 and the main conclusions are summarised in Section 3.7.

3.2 New driver steering control model

A new parametric driver steering control model is derived in this section, incorporating human sensory dynamics. The model is built around an optimal control strategy, hypothesising that on average drivers achieve close to the best possible performance within the limitations of their sensory and motor systems. Driving a vehicle is a complicated task involving many physical and neural processes, so various simplifying assumptions and omissions are made to allow a more reliable analysis. These assumptions can be relaxed in

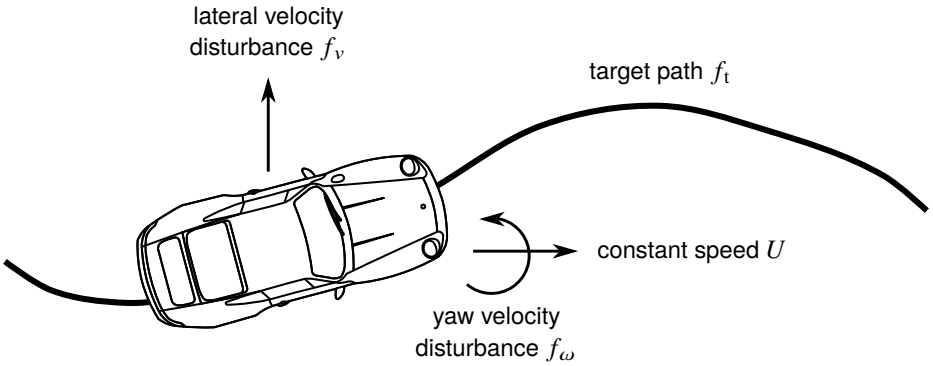

Figure 3.1: Summary of steering task described by new parametric driver model. The driver follows a target path f_t while compensating for disturbances f_v and f_ω.

the future once more is known about the role of sensory dynamics in the core driving task. The scope of the model does not extend to speed choice or control, therefore only vehicles travelling at constant longitudinal speed are considered. However, the principles behind this model could be extended to include variable-speed vehicles. The task of trajectory planning and optimisation is also not modelled; the driver is assumed to follow a given target path of negligible thickness. This limitation could be overcome by cascading a trajectory planning model which calculates a desired trajectory based on the road geometry [7, 8] with the steering control model which attempts to follow this trajectory. To reduce the computational effort involved in simulating the model and provide efficient mathematical solutions for the controller, linear dynamics are used to model the driver-vehicle system. Tyre friction characteristics are not considered, and the yaw angle of the vehicle is assumed to be small. These assumptions are addressed in later chapters.

The steering task described by the model is shown in Figure 3.1, combining the feedforward and feedback tasks described by the two-level model [6]. The feedforward task involves following the target path f_t, and the feedback task involves compensating for random disturbances f_v and f_ω. These disturbances may come from a variety of sources such as wind gusts, vehicle nonlinearities and driver noise, however they can be modelled as additive disturbances referred to the vehicle lateral velocity v and yaw velocity ω. The target and disturbance signals f_t, f_v and f_ω are collectively known as forcing functions, as under controlled conditions they can be synthesised artificially in order to identify different loops of the driver-vehicle control system [36]. It is assumed that the aim of the driver is to minimise the tracking error between the vehicle lateral displacement and the target path.

The structure of the new parametric model is shown in Figure 3.2. The plant describes the system controlled by the driver, including models of the vehicle dynamics and the driver's neuromuscular dynamics and sensory systems. The driver's control strategy follows the linear quadratic Gaussian (LQG) framework, combining a linear quadratic

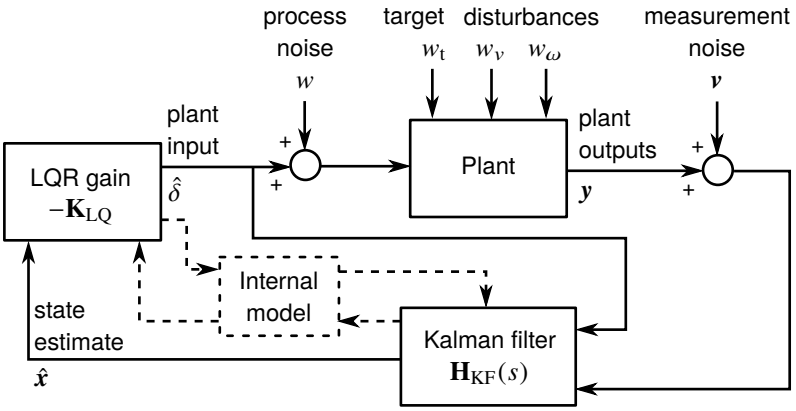

Figure 3.2: Structure of new driver steering control model. Target and disturbance signals are input as white noise w_t, w_v and w_ω, then filtered in the plant. The plant input $\hat{\delta}$ and outputs $\boldsymbol{y}$ are perturbed with process and measurement noise w and $\boldsymbol{v}$, so a Kalman filter estimates the plant states $\hat{\boldsymbol{x}}$. An LQR controller computes an optimal plant input $\hat{\delta}$.

regulator (LQR) with a Kalman filter to give statistically optimal control actions and state estimates based on the driver's internal model of the plant. Previous studies have used an LQR controller to model driver steering control while following a target path [13, 14], hypothesising that an experienced driver will learn to steer in an approximately optimal fashion. Various studies have found evidence that humans combine visual and vestibular information optimally [164–169], and humans have been found to use internal models to assist with various motor control tasks [47, 48]. A Kalman filter uses an internal model to achieve optimal state estimation in the presence of additive white noise [181]. Sections 3.2.1 to 3.2.4 describe the various components of the new driver model, and a full mathematical derivation of the complete model is presented in Appendix A.

3.2.1 Plant

The plant describing the dynamics of the system controlled by the driver is shown in Figure 3.3. It is assumed that the driver's internal model is a perfect representation of the true plant. The plant input $\hat{\delta}$ plus process noise w is filtered by the driver's neuromuscular dynamics, giving the steering angle δ. Forcing functions f_t, f_v and f_ω are generated by filtering white noise plant inputs w_t, w_v and w_ω, and added to the vehicle's lateral velocity v and angular velocity ω. The driver previews the upcoming target f_t, with measurements delayed by a visual delay τ_{vi} to give perceived displacements $\boldsymbol{e}_{vi}$. The vehicle lateral acceleration is sensed through the otoliths and the angular velocity is sensed through the semi-circular canals (SCCs), with a vestibular delay of τ_{ve} in both cases, giving perceived lateral acceleration a_{ve} and angular velocity ω_{ve}. The plant is modelled in discrete time with sample time T_s, allowing the delays to be implemented explicitly using a shift register [16].

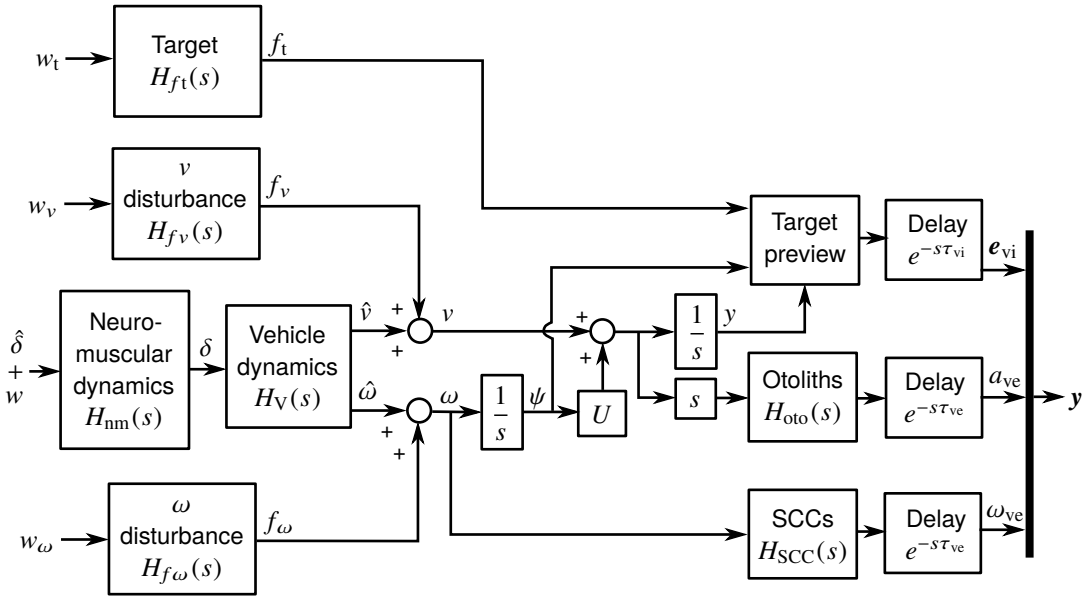

Figure 3.3: Structure of plant in new driver model. The plant describes the dynamics controlled by the driver, including the vehicle dynamics, driver's neuromuscular and sensory dynamics, and target and disturbance filters.

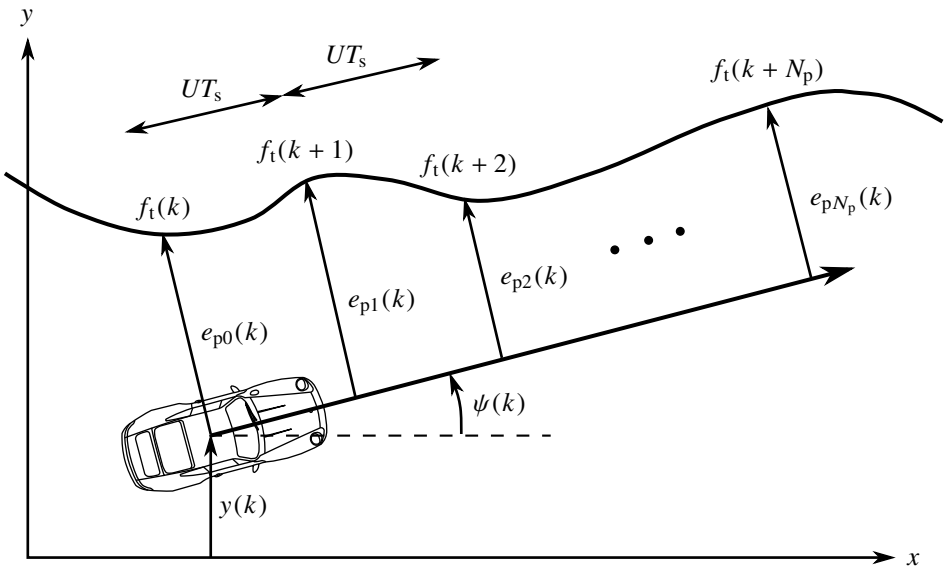

Figure 3.4: Preview model of driver's visual system. The driver measures lateral displacements of the target path relative to a line projected forward from the vehicle. Measurements are taken at intervals of UT_s up to a prediction horizon $N_p = T_p/T_s$ time steps ahead.

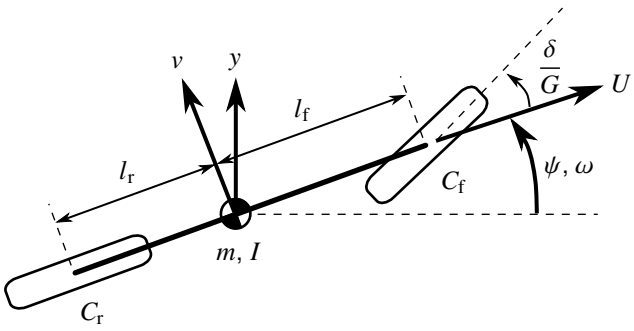

Figure 3.5: Single-track model of lateral vehicle dynamics. The front and rear tyre pairs are each represented as a single tyre, with constant cornering stiffnesses C_f and C_r.

A 'preview' model is used to describe the driver's visual perception of the upcoming target path [13, 14]. The driver previews future values of the target path up to the preview horizon T_p as shown in Figure 3.4. The previewed displacements $e_{\mathrm{p}n}(k)$ for $n = 0, 1, \ldots, N_\mathrm{p}$, where $N_\mathrm{p} = T_\mathrm{p}/T_\mathrm{s}$, are given by:

$$e_{\mathrm{p}n}(k) = f_\mathrm{t}(k+n) - y(k) - nUT_\mathrm{s}\psi(k) \tag{3.1}$$

assuming small yaw angles ψ. The vehicle is chosen for simplicity to be a two degree-of-freedom single-track model moving at constant speed, as shown in Figure 3.5, with continuous-time state-space equations:

$$\begin{Bmatrix} \dfrac{\mathrm{d}\hat{v}}{\mathrm{d}t} \\ \dfrac{\mathrm{d}\hat{\omega}}{\mathrm{d}t} \end{Bmatrix} = \begin{bmatrix} \dfrac{-(C_\mathrm{f}+C_\mathrm{r})}{Um} & \dfrac{-(l_\mathrm{f}C_\mathrm{f}-l_\mathrm{r}C_\mathrm{r})}{Um} - U \\ \dfrac{-(l_\mathrm{f}C_\mathrm{f}-l_\mathrm{r}C_\mathrm{r})}{UI} & \dfrac{-(l_\mathrm{f}^2C_\mathrm{f}+l_\mathrm{r}^2C_\mathrm{r})}{UI} \end{bmatrix} \begin{Bmatrix} \hat{v} \\ \hat{\omega} \end{Bmatrix} + \begin{bmatrix} \dfrac{C_\mathrm{f}}{mG} \\ \dfrac{l_\mathrm{f}C_\mathrm{f}}{IG} \end{bmatrix} \delta(t) \tag{3.2}$$

The vehicle dynamics are discretised using a zero-order-hold method.

3.2.2 LQR controller

For a time-invariant linear plant an LQR controller can be calculated, consisting of a gain vector $\mathbf{K}_\mathrm{LQ}$ which acts on the plant states to give an optimal plant input $\hat{\delta}$, which minimises a cost function J. Additive white noise does not affect the optimal solution, so the white noise plant inputs w, w_t, w_v and w_ω can be ignored. The cost function incorporates costs on the tracking error $e_{\mathrm{p}0}$ and the plant input $\hat{\delta}$, weighted by q_e and q_δ:

$$J = \sum_{k=0}^{\infty} \left\{ q_e e_{\mathrm{p}0}(k)^2 + q_\delta \hat{\delta}(k)^2 \right\} \tag{3.3}$$

Previous studies have included costs on yaw angle error [13, 14], and it is also possible to include additional terms such as steering velocity in the cost function. However for simplicity only two costs are included. The optimal solution only depends on the relative weightings, therefore q_e is set to 1 m^{-2}. As the steering cost is placed on $\hat{\delta}$ rather than δ, the cost on steering inputs is shaped by the neuromuscular transfer function $H_{\mathrm{nm}}(s)$. The optimal gain $\mathbf{K}_{\mathrm{LQ}}$ can be found using the Matlab function *dlqr*.

3.2.3 Kalman filter

The LQR gain $\mathbf{K}_{\mathrm{LQ}}$ multiplies the plant states $\boldsymbol{x}(k)$ to give an optimal plant input $\hat{\delta}$. However, the driver only has access to measurements of the plant outputs, perturbed by process and measurement noise w and $\boldsymbol{v}$. Therefore, a Kalman filter is used to compute an optimal estimate of the plant states based on the computed plant input $\hat{\delta}$ and noisy measurements of the plant outputs [181]. The noise covariance matrices $\mathbf{Q}_{\mathrm{KF}}$ and $\mathbf{R}_{\mathrm{KF}}$ are given by:

$$\begin{aligned} \mathbf{Q}_{\mathrm{KF}} &= \mathrm{diag}\left(\begin{bmatrix} W^2 & W_v^2 & W_\omega^2 & W_{\mathrm{t}}^2 \end{bmatrix}\right) \\ \mathbf{R}_{\mathrm{KF}} &= \mathrm{diag}\left(\begin{bmatrix} V_{\mathrm{p}}^2 \times \mathbf{1}_{(1,\,N_{\mathrm{p}}+1)} & V_a^2 & V_\omega^2 \end{bmatrix}\right) \end{aligned} \tag{3.4}$$

where W^2, W_v^2, W_ω^2 and W_{t}^2 are the variances of the process noise w and the disturbance and target white noise inputs w_v, w_ω and w_{t}; V_{p}^2, V_a^2, and V_ω^2 are the variances of the measurement noise added to the plant outputs $\boldsymbol{e}_{\mathrm{vi}}$, a_{ve}, and ω_{ve}; and $\mathbf{1}_{(1,\,N_{\mathrm{p}}+1)}$ represents a column vector of $(N_{\mathrm{p}}+1)$ ones.

This model assumes that the measurement noise has the same variance for all previewed target path displacements $\boldsymbol{e}_{\mathrm{vi}}$. Previous studies have accounted for an increase in noise with distance from the observer and eccentricity from the gaze direction [41], however there is a lack of research into how drivers view the geometry of an upcoming target path. The assumption of constant measurement noise V_{p} across all previewed displacements, while clearly a simplification, was not found to affect the fit to experimental results significantly. A time-invariant Kalman filter $\mathbf{H}_{\mathrm{KF}}(s)$ can be calculated for this system using the Matlab function *kalman*. The state estimate $\hat{\boldsymbol{x}}$ can then be found from:

$$\hat{\boldsymbol{x}}(s) = \mathbf{H}_{\mathrm{KF}}(s)\begin{Bmatrix} \hat{\delta}(s) & \boldsymbol{y}(s) \end{Bmatrix}^{\mathrm{T}} \tag{3.5}$$

3.2.4 Model transfer functions and parameters

As explained in Section 3.1, previous studies reviewed in Chapter 2 have shown that measurements taken in passive conditions may not be applicable to active control tasks

such as driving [137, 141–145, 147, 148]. Therefore, most of the parameters of the model are found using an identification procedure to fit to experimental results. However, the forms of some of the transfer functions can be fixed using results from the literature. Models of the vestibular system are taken from [95]:

$$H_{\mathrm{SCC}}(s) = \frac{458.4s^2}{(80s+1)(5.73s+1)} \tag{3.6}$$

$$H_{\mathrm{oto}}(s) = \frac{0.4(10s+1)}{(5s+1)(0.016s+1)} \tag{3.7}$$

Drivers' neuromuscular dynamics are approximated by a second-order filter [15, 216]:

$$H_{\mathrm{nm}}(s) = \frac{\omega_{\mathrm{nm}}^2}{s^2 + 2\zeta_{\mathrm{nm}}\omega_{\mathrm{nm}}s + \omega_{\mathrm{nm}}^2} \tag{3.8}$$

Pick and Cole [15] studied drivers' neuromuscular dynamics by applying torque disturbances to a steering wheel and found values of $\omega_{\mathrm{nm}} = 5.65$ rad/s and $\zeta_{\mathrm{nm}} = 0.43$ for drivers with relaxed arms and $\omega_{\mathrm{nm}} = 23.2$ rad/s and $\zeta_{\mathrm{nm}} = 0.24$ with tensed arms. It is unclear which of these is more appropriate for driver steering modelling, as drivers' arms may be partially tensed, therefore ω_{nm} and ζ_{nm} are identified to fit experimental data.

The values of some of the remaining parameters, such as the vehicle dynamics and the spectra and amplitudes of the forcing functions, are given by the experimental conditions. However various other parameters values must be identified, including the steering cost weight q_δ, preview time T_{p}, the visual and vestibular delays τ_{vi} and τ_{ve}, noise amplitudes W, V_a, V_ω and V_{p}, and neuromuscular parameters ω_{nm} and ζ_{nm}.

If the driver previews the upcoming target path they should be able to compensate for their internal latencies to follow the target without any delay. However, preliminary analysis of the experimental results showed that the drivers sometimes steered earlier than expected, as if they were following a 'shifted' version of the target f_{t}. This could be because the drivers aligned a different part of the car with the target than the centre of mass. An additional time constant T_{t} is therefore included to model this effect, such that the driver attempts to follow $f_t(t - T_{\mathrm{t}})$ rather than $f_t(t)$. In total there are eleven parameters which are neither determined by the experimental conditions nor fixed using results from the literature, and these are found using an identification procedure to fit experimental data.

3.3 Steering control experiment

A new model of driver steering behaviour based on the dynamics of human sensory systems is presented in Section 3.2. To investigate how sensory information is used during driving,

an experiment was carried out to provide data which can be used to identify values for the parameters of this model. A similar parameter identification procedure has previously been carried out in [215] to fit the model to an experiment carried out by pilots in a flight simulator [36]. The new experiment was designed following similar principles to measure driver steering control in a combined target-following and disturbance-rejection task.

The experiment was carried out in a driving simulator, rather than a real vehicle on a test track, due to the control that this allows over the experimental set-up. Driving simulators have limited available travel, so the vehicle motion is usually scaled down or filtered to fit within these physical limitations. This results in a conflict between the information perceived by the visual and vestibular systems. There is some disagreement in the literature as to how sensory conflicts are perceived by humans (see Chapter 2). Therefore, to ensure the drivers used their sensory systems in the simulator in the same way as they would in a real vehicle, the vehicle motion was designed to fit within the simulator limits without any scaling or filtering.

3.3.1 Steering control task

The steering control task carried out in the experiment was the same as the task described by the model in Section 3.2 (shown in Figure 3.1). The vehicle moved at constant longitudinal speed U and the drivers were asked to follow a target lateral displacement f_t as closely as possible. Disturbances f_v and f_ω were added to the lateral velocity and yaw angular velocity of the vehicle as shown in Figure 3.3. The target and disturbance forcing function signals f_t, f_v and f_ω were generated by filtering Gaussian white noise to match the assumptions made in the driver model. White noise signals w_t, w_v and w_ω were generated in discrete time by choosing random numbers from a zero-mean normal distribution. The variances W_t^2, W_v^2 and W_ω^2 of these signals were adjusted between trials, as discussed in Section 3.3.3.

The forcing functions were tuned during preliminary testing to ensure that the amplitudes were as large as possible without exceeding the simulator limits, and that a large range of frequencies was included without becoming uncomfortable for the driver. The spectrum of the target forcing function f_t was chosen by combining a high-pass filter, to attenuate low frequencies and ensure that the target path was within the simulator limits, with a low-pass filter to restrict the bandwidth of the target. The filters were chosen to have 40 dB/dec roll-off at high and low frequencies, with upper and lower cutoff frequencies of 2 rad/s and 0.1 rad/s:

$$H_{ft}(s) = \left(\frac{s}{s+0.1}\right)^2 \left(\frac{2}{s+2}\right)^2 \tag{3.9}$$

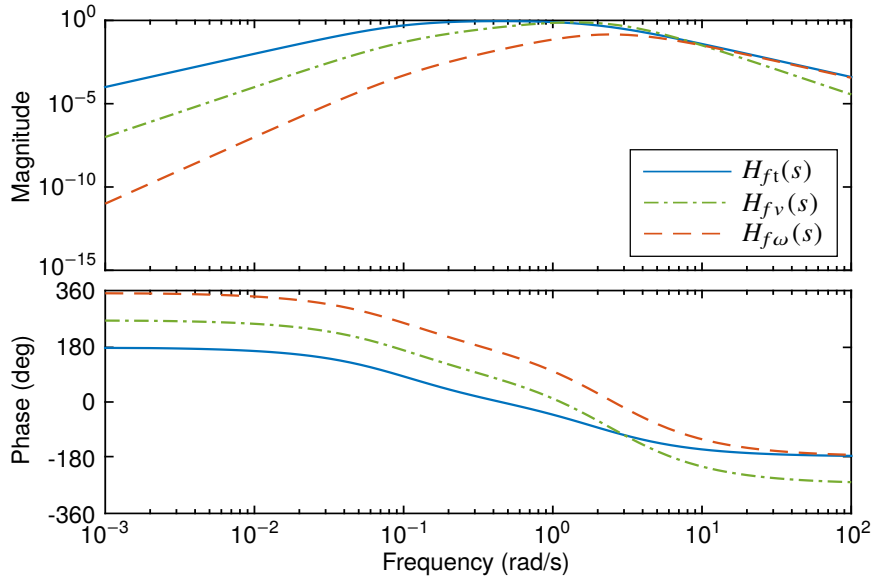

Figure 3.6: Bode diagram of the forcing functions used in the experiment, for $U = 10$ m/s

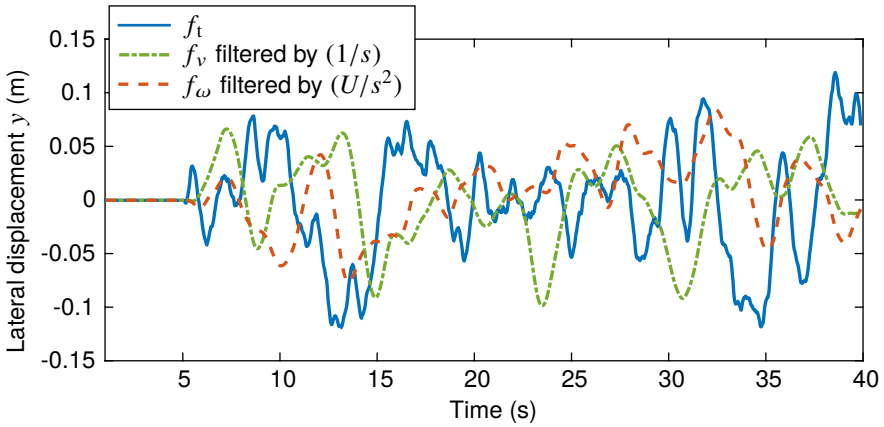

Figure 3.7: First 40 s of the forcing functions used in trial A7. Disturbance forcing functions have been filtered to show their effect on the vehicle lateral displacement.

The spectrum of f_v was chosen so that, in the absence of any steering, the vehicle's lateral displacement y would have the same spectrum as f_t. This was achieved by multiplying $H_{ft}(s)$ by s, however this resulted in large-amplitude high-frequency components which caused very large velocities and accelerations. Therefore, the spectrum was multiplied by an additional low-pass filter with cutoff frequency 3 rad/s:

$$H_{fv}(s) = s\left(\frac{3}{s+3}\right)^2 H_{ft}(s) \tag{3.10}$$

The spectrum of f_ω was chosen similarly, multiplying $H_{ft}(s)$ by s^2/U so that the lateral displacement due to f_ω was the same as f_t, and multiplying by a low-pass filter with cutoff

frequency 3 rad/s to reduce the amplitude of high frequencies:

$$H_{f\omega}(s) = \left(\frac{s^2}{U}\right)\left(\frac{3}{s+3}\right)^2 H_{ft}(s) \tag{3.11}$$

Bode diagrams for each of the forcing function filters are plotted in Figure 3.6, and time-domain examples of the forcing functions used in one of the trials are shown in Figure 3.7.

3.3.2 Simulation conditions

A moving-base driving simulator was used for the experiment, with a high-fidelity visual display and a motion platform which applied physical feedback to the driver. To confirm that the bandwidth of the simulator is sufficiently high to provide an accurate recreation of the desired motion signals at the required frequencies, the spectra of the demanded and measured simulator motion are calculated using a discrete Fourier transform and plotted in Figure 3.8. The spectra are seen to be similar for all frequencies with significant motion amplitudes. The lateral and yaw motion applied to the driver was not scaled or filtered in any way during the experiment. No longitudinal motion was used, however since humans

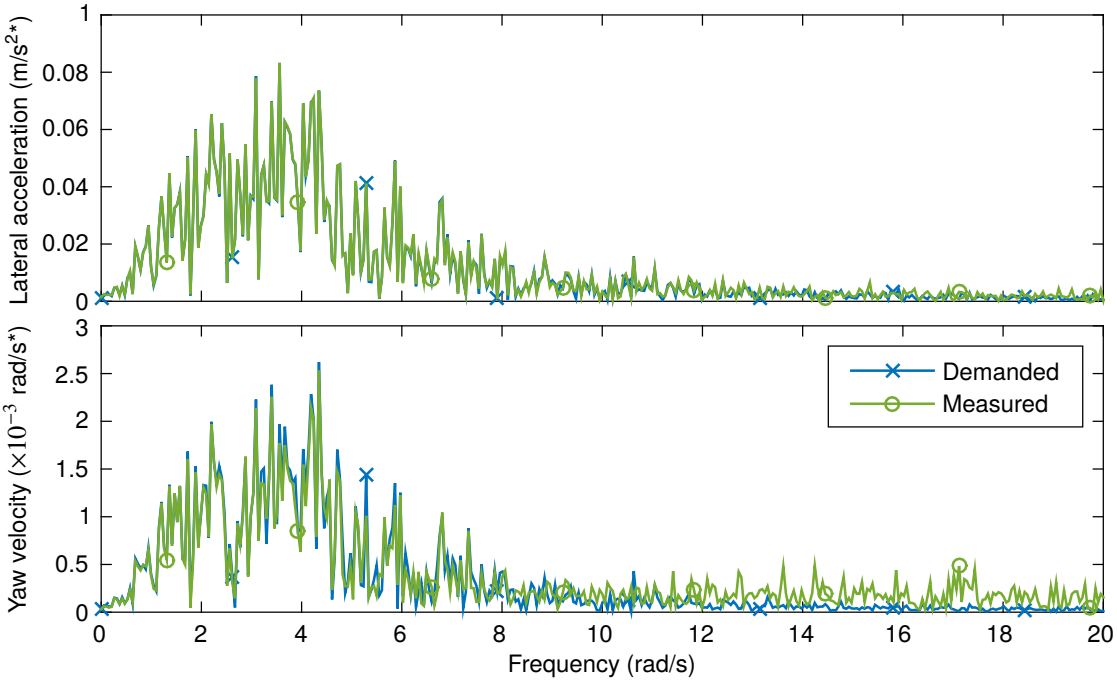

Figure 3.8: Comparison of demanded and measured simulator motion. The lateral acceleration and yaw angular velocity for trial A7, driver 1 have been passed through the vestibular dynamics to give the spectra of the perceived signals.

Table 3.1: Vehicle parameter values used in experiment

Parameter	Mass m	Length l_f	Length l_r	Cornering stiffness C_f	Cornering stiffness C_r	Moment of inertia I	Steering ratio G	Speed U
Units	kg	m	m	kN/rad	kN/rad	kgm^2	–	m/s
Base (B) vehicle	650	1.85	1.65	100	230	450	10	–
Slow (S) vehicle	650	1.85	1.65	100	230	450	30	10
Fast (F) vehicle	650	1.85	1.65	100	230	450	150	40
Fast (F*) vehicle	650	1.85	1.65	100	230	450	30	40

cannot detect constant velocities the visual and physical motion was perceived as coherent. Simulated engine noise was played to mask the sounds of the motion platform.

The vehicle used in the experiment was the single-track model shown in Figure 3.5, with dynamics given in Equation 3.2. Suitable parameter values were identified by fitting the lateral and yaw responses of the single-track model to data from a high-accuracy nonlinear vehicle model, using a least-squares method with the same steering input to both models. A consequence of the difference in model complexity is that not all of the identified parameter values of the single-track vehicle model are close to the corresponding parameter values of the high-accuracy model. However, comments from the drivers during the experiment confirmed that the identified single-track vehicle model gave a realistic steering response. The identified parameter values are summarised as the 'base' vehicle in Table 3.1. For the experiment, two different vehicle speeds were chosen, a 'fast' vehicle with $U = 40$ m/s and a 'slow' vehicle with $U = 10$ m/s, which gives larger amplitudes of yaw motion without exceeding the lateral displacement limits of the simulator. Due to the small size of the target displacements, the steering ratio G was increased for both vehicles to reduce the sensitivity of the vehicle to steering inputs. An amended fast vehicle (F*), with a smaller steering ratio, is also included in Table 3.1 for use in later chapters.

In the experiment of Zaal et al. [36], the visual display used by the pilots consisted of a screen which showed a line representing the target aeroplane pitch angle and a cross-hair showing the actual pitch angle. This display did not give the pilots any information about future values of the target angle. In contrast, drivers are usually able to see the road ahead of them, previewing the upcoming target path as shown in Figure 3.4. This allows them to compensate for delays in the visual feedback loop by planning steering actions in advance. Two types of visual display were designed for the experiment, one which allowed the driver to preview the upcoming target path in order to replicate a more realistic driving scenario, and one without preview to allow delays in the visual system to be investigated. Examples of the two displays are shown in Figure 3.9. In both cases the vehicle moved along a

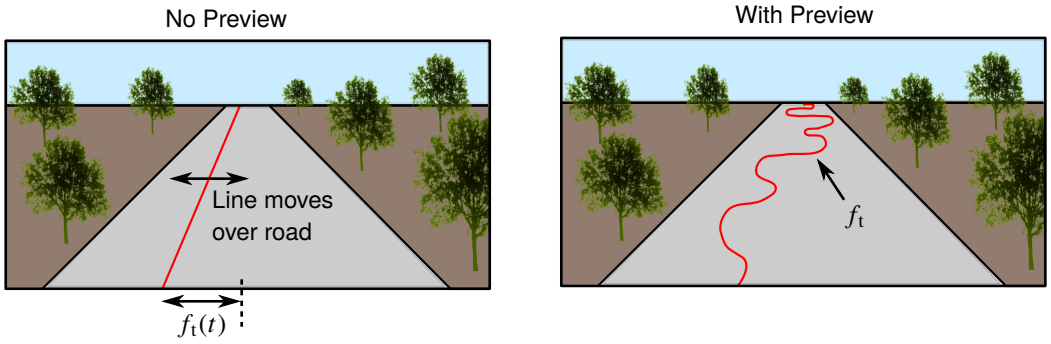

Figure 3.9: Visual display examples, with and without preview. Note that the simulator display was much higher fidelity than these examples.

straight road, with objects such as trees and buildings next to the road for use as visual cues to speed and depth. In the 'no preview' case, a straight target line moved laterally across the road, with the lateral displacement of each point on this line equal to $f_t(t)$ at time t. This allowed the driver to see the current value of f_t without any information about future values of the target. In the preview case the target line was fixed to the road, allowing the driver to see the upcoming target.

In a real vehicle, lateral forces generated by the tyres on the front axle are communicated to the driver through torque at the steering wheel, and this can give the driver useful information about the vehicle states. The new driver model does not currently take account of steering torque feedback, therefore the steering system was modelled as parallel spring and damper, with transfer function:

$$H_{\mathrm{STF}}(s) = \mathsf{k}_{\mathrm{STF}} + \mathsf{c}_{\mathrm{STF}} s \tag{3.12}$$

between steering angle and resistive torque. This provided some resistance to steering, however it didn't give the driver any information about the vehicle states. The stiffness $\mathsf{k}_{\mathrm{STF}}$ was set to 8 Nm/rad and the damping coefficient $\mathsf{c}_{\mathrm{STF}}$ to 1 Nms/rad. Drivers' perception of more sophisticated torque feedback can be investigated in the future and incorporated into the driver model.

3.3.3 Experiment procedure and trials

The experiment consisted of fourteen trials, with a range of conditions designed to explore different aspects of the driver's control strategy. The conditions are summarised in Table 3.2. Various forcing function combinations were tested with the slow and fast vehicles, with or without preview. For trials with no target (marked **0** in the preview column) the 'preview' and 'no preview' models are equivalent. There were five test subjects in total, all male

Table 3.2: Experimental conditions for each trial

	Forcing function amplitudes				
Trial	W_t (m*)	W_v (m/s*)	W_ω (rad/s*)	**Vehicle**	**Preview**
A1	1.58	0	0	F	✗
A2	1.58	0	0	F	✓
A3	0	1.58	0	F	**0**
A4	0	0	1.58	F	**0**
A5	0	1.11	1.11	F	**0**
A6	0.79	0.79	0.79	F	✗
A7	0.79	0.79	0.79	F	✓
A8	1.58	0	0	S	✗
A9	1.58	0	0	S	✓
A10	0	1.58	0	S	**0**
A11	0	0	1.58	S	**0**
A12	0	1.11	1.11	S	**0**
A13	1.11	1.11	1.11	S	✗
A14	1.11	1.11	1.11	S	✓

and aged between 24 and 30. All five drivers possessed driving licences and had at least six years experience driving cars on public roads. Drivers 1–4 all had a small amount of experience driving in a simulator. Driver 5 was a professional test driver with a great deal of experience driving simulated and real cars. Reaction times [217] and sensory thresholds [87] have been found to increase with age, therefore the small age range of the subjects allows measured differences to be linked to driving experience. However, the identified parameter values may be lower than values expected for older drivers.

Practice runs of several of the trials were carried out before the experiment to familiarise the drivers with the steering task and the different disturbances and vehicle models. During the experiment the order of the trials was randomised. Before the experiment began each subject was told how the conditions may vary between the trials, however in order to avoid biasing their expectations they were not told anything about the specific conditions of each trial.

3.4 Identification procedure

An identification procedure can be used to find values for the parameters of the new driver model presented in Section 3.2 which give the best possible fit to the results of the experiment described in Section 3.3. The identification procedure consists of two stages, Box–Jenkins identification to fit general polynomial transfer functions to the experimental

results, and parametric identification to find a set of parameter values for the new driver model. The procedure is run separately for each of the five drivers. In addition, the measured steering angles are averaged over the five drivers to give a set of 'averaged data', which is also used for identification. The averaged data should contain less random noise compared with the data for the individual drivers, allowing an average set of parameter values to be found more reliably. However, it relies on the assumption that the drivers were using similar control strategies. The first 15 s of each trial are excluded from the data used for identification, as the drivers may have taken some time to work out the conditions of the trial and settle on a control strategy. The final 30 s of each trial are also excluded, so that the fit of the last 30 s can be measured to validate the predictive power of the model and to check for over-fitting (see Section 3.5.4).

3.4.1 Box–Jenkins identification

The first identification stage involves fitting general transfer functions to the measured data to estimate the contribution of linear control behaviour to the measured steering actions. This gives an approximate upper bound on how well the parametric driver model could be expected to fit. The Box–Jenkins method is used to estimate polynomial transfer functions between each of the model inputs (f_t, f_v, f_ω) and the model output (δ) [211, 218]. The method also finds a model of the noise spectrum $H_n(s)$.

Odhams and Cole [214] investigated a similar identification method for a driver model, varying the orders of the polynomial transfer functions, and found that if the order is too low the fit will be poor but if it is too high bias may be introduced due to over-fitting. Using 5th order polynomials resulted in a good compromise, therefore this order is chosen for the Box–Jenkins identification. The Box–Jenkins method can also make allowances for time delays between each input channel and the output, however the method does not estimate these directly from the data so they have to be known in advance. To find optimal values of these time delays, Box–Jenkins identification is carried out with a range of different delays and a genetic algorithm is used to iterate towards values which give the best fit to the experimental results.

3.4.2 Parametric identification

The new parametric driver model depends on eleven variable parameters which are neither fixed in advance nor taken from the experimental conditions. Upper and lower bounds are chosen for these parameters based on physical considerations, as summarised in Table 3.3.

Ljung [211] presented two methods for identification of systems operating in closed-

Table 3.3: Upper and lower bounds for identified parameter values. The symbol * after a set of units indicates that the variable is filtered.

Parameter	q_δ	V_a	V_ω	V_p	W	τ_vi	τ_ve	T_t	T_p	ω_nm	ζ_nm
Units	–	m/s^{2*}	rad/s*	m	rad*	s	s	s	s	rad/s	–
Upper bound	2	1	1	5	1	0.5	0.5	1	2	50	2
Lower bound	10^{-3}	10^{-3}	10^{-3}	10^{-3}	10^{-3}	0.03	0.03	-1	0	0	0

loop, direct identification where the system is simulated in open-loop and indirect identification where the system is simulated in closed-loop. As the feedback transfer function (the vehicle) is known in this case the indirect method is the most appropriate, and should result in lower bias than the direct method. The simulated steering angle δ_sim can be compared with the measured steering angle δ_exp and the mean-square difference $(\delta_\mathrm{sim} - \delta_\mathrm{exp})^2$ minimised to find the optimum set of parameter values. This difference $(\delta_\mathrm{sim} - \delta_\mathrm{exp})$ is composed of modelling error, which can be reduced by improving the accuracy of the model, and random noise introduced by the driver, which cannot be reduced.

If the driver noise is not white, bias may be introduced into the identification of the driver model. Ljung [211] showed that this bias can be reduced by filtering the prediction error so that the noise term approximates white noise. This requires filtering by the inverse of the noise model $H_\mathrm{n}(s)$ (found in the Box–Jenkins identification procedure) to give a weighted prediction error ε. This increases the amplitude of high frequencies, however the bandwidth of a driver's steering control is physically limited. Therefore a low-pass filter is included, with a cutoff frequency of 30 rad/s, so that high-frequency errors are not penalised too heavily:

$$\varepsilon(s) = \frac{1}{H_\mathrm{n}(s)} \left(\frac{30}{s + 30} \right)^2 (\delta_\mathrm{sim}(s) - \delta_\mathrm{exp}(s)) \tag{3.13}$$

Previous studies have carried out simulations of similar identification procedures for driver models and shown that filtering by the inverse of the noise model is effective in reducing bias in the identified parameter values [213, 214].

Finding the optimum set of parameter values involves minimising the mean-square weighted prediction error ε. Due to the number of parameters involved and the complicated relationships between them this is a difficult minimisation task, which is likely to have many local minima. A stochastic method is required to explore the entire search space and find the global minimum solution. A genetic algorithm is therefore used, starting with a population of 100 random solutions between the upper and lower bounds and using principles of natural selection to 'mate' and 'mutate' the best solutions, allowing the

Table 3.4: Conditions for each step of the parametric identification procedure, to find a single set of parameter values for each driver. Parameters held constant in each step are shown by a bullet (•).

Step	Trials	Parameters held constant										
		q_δ	V_a	V_ω	V_p	W	τ_vi	τ_ve	T_t	T_p	ω_nm	ζ_nm
1	A1, A3–A6, A8, A10–A13								•	•		
2	A1, A3–A6, A8, A10–13					•			•	•		
3	A2, A7, A9, A14	•	•	•		•	•	•			•	•
4	A1–A14					•			•	•		

population to converge towards the global minimum over 100 iterations [212]. A second minimisation stage is then carried out to focus in on the minimum using a gradient search method, taking the genetic algorithm solution as the starting point. The Matlab function *fmincon* is used for this stage with the *SQP* algorithm.

Initially, single sets of parameter values are identified for each driver to fit the results of all trials. Minimisation over a multidimensional search space can be difficult, and as the number of parameters increases so does the difficulty of finding the global minimum. Therefore the identification procedure is carried out in several steps to reduce the number of parameters identified at any one time. The conditions for each step are given in Table 3.4. In step 1 parameter values are identified for the trials without preview. This allows the target shift T_t to be set to zero and the preview time T_p to be held constant at 0.1 s, since the driver is not able to obtain additional information by looking further ahead.

Parameters W, V_a, V_ω and V_p affect not only the linear component of the modelled control strategy, but also the predicted amplitude and distribution of the random noise introduced by the driver. It is desirable for the noise amplitude predicted by the model to match the noise amplitude found in the experiment. The modelling error is assumed to be small, so that the driver noise is given by the difference between the measured steering angle δ_exp and the modelled steering angle δ_sim. Simulations showed that the predicted noise amplitude is affected much more by the process noise than the measurement noise. Therefore, after step 1 the average ratio of the measured to the modelled noise amplitudes is found and used to scale W. In step 2, W is then held constant while the remaining parameter values are identified to fit the results of the non-preview trials once more.

In step 3 optimal values of T_t and T_p are found from the trials with preview. The value of V_p is also allowed to vary, because if the number of preview points increases the noise on each preview point must also increase to give the same overall level of uncertainty in the measurements. The target shift T_t was found to be unnecessary for trials with the fast vehicle, so T_t is set to zero for these trials. The other eight parameters are held constant at

the values found in step 2. In step 4 a further optimisation is carried out, holding T_t, T_p and W constant at the values found previously and identifying the remaining eight parameter values to minimise the average weighted prediction error across all fourteen trials.

Once a single set of parameter values is found to fit all of the trials as well as possible, separate parameter sets are identified for each trial individually. To reduce the computation time and the number of parameters needing to be optimised, the preview time T_p, the target shift parameter T_t and the process noise amplitude W are held constant, using the values found for the single parameter set. When running the parametric identification procedure for the averaged data, the value of W is held constant throughout at the average of the values identified for the separate drivers, to give a realistic predicted noise amplitude.

3.5 Results and analysis

In the following subsections, the results of the experiment and the model identification procedure are analysed in various ways. In Section 3.5.1 the agreement between the parametric driver model and the results of the experiments is investigated. The identified parameter values are compared between drivers and between trials in Section 3.5.2, and the noise levels predicted using these parameters are compared with those found in the experiment in Section 3.5.3. Additional measurements are used to check the model for over-fitting in Section 3.5.4, and the convergence of the identification procedure is tested using simulated results. In Section 3.5.5 the performance of each driver is compared by running simulations using the identified parameter values.

3.5.1 Agreement between model and measurements

It is possible to quantify the agreement between the measured and modelled steering angles by calculating the 'variance accounted for' (VAF). This value represents the percentage of the variance in the measured signals δ_{exp} which is matched by the model prediction δ_{sim}, and is given by:

$$\mathrm{VAF} = \left(1 - \frac{\sum_k \left\{\delta_{exp}(k) - \delta_{sim}(k)\right\}^2}{\sum_k \left\{\delta_{exp}(k)\right\}^2}\right) \times 100\% \tag{3.14}$$

VAF values are plotted in Figure 3.10 to quantify the agreement between the predicted and measured steering angles for each of the five drivers as well as the averaged data.

As expected, VAFs are largest for the Box–Jenkins model, giving an approximate upper bound on the percentage of the steering signal which is linear. VAFs are lowest

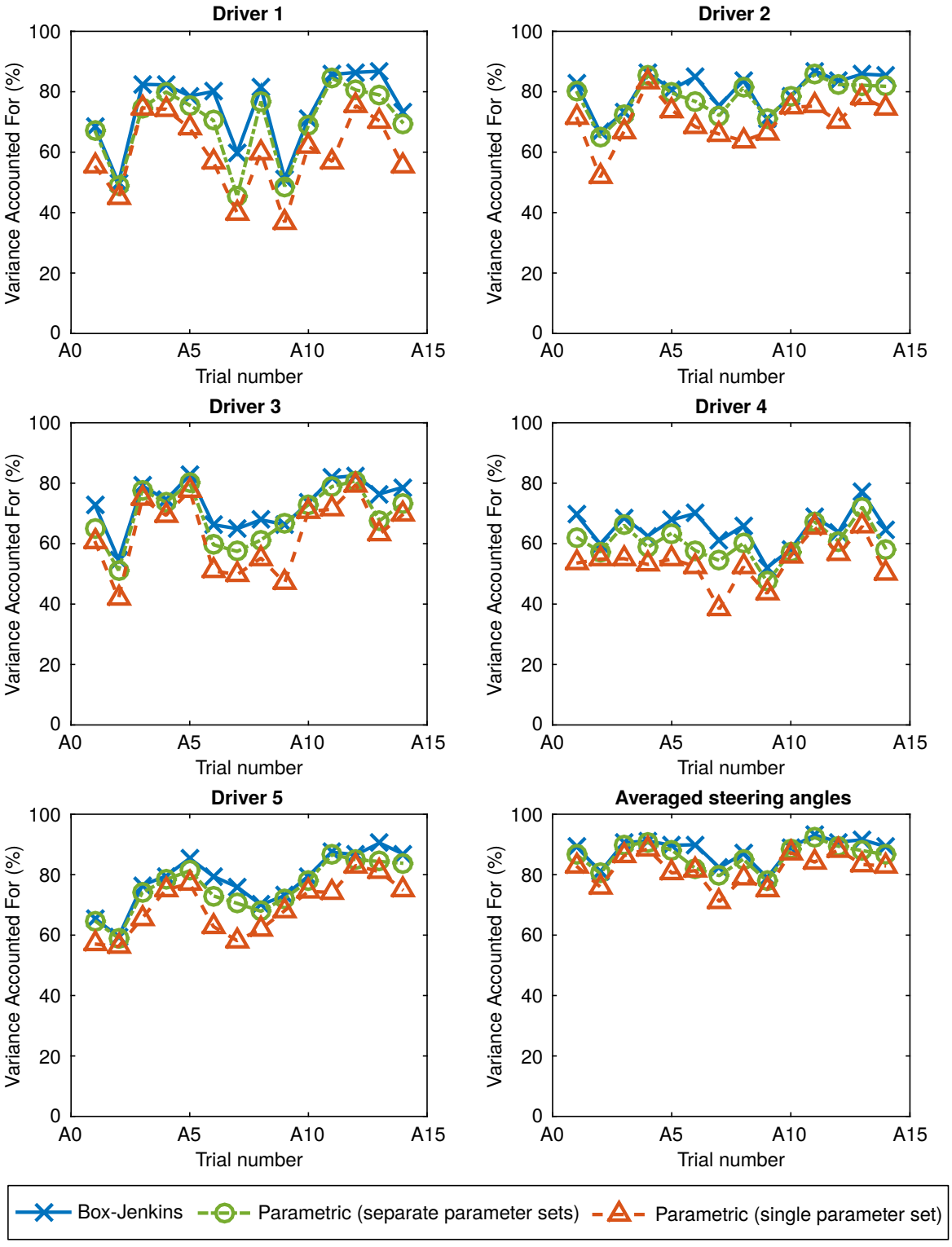

Figure 3.10: Agreement between driver model predictions and experimental data. VAF values are plotted for all five drivers and for the averaged data. The fit of the Box–Jenkins model is compared with the fit of the new parametric model, either using separate parameter sets fit to each trial or a single parameter set to fit the results of all trials.

for the single parameter sets, as the separate parameter sets are able to get closer to the optimum for each individual trial. In general the VAFs for the separate parameter sets are very close to the VAFs for the Box–Jenkins model, indicating that the parametric model structure can explain the observed linear driver steering behaviour very well. VAFs for the single parameter sets are reasonably close to the VAFs for the separate parameter sets. For the individual drivers there are some trials where the single parameter sets do not fit as well, showing that the drivers' individual control performance may change between trials, however the results using the single parameter set fit much better for the averaged data. The VAFs are higher for the averaged data than for the individual drivers, which is expected as averaging should reduce the amount of noise in the results. A single set of parameter values is found for the averaged data which gives VAFs greater than 71% for all trials, and 82% on average.

3.5.2 Identified parameter values

A comparison of the single parameter sets identified for each of the drivers is shown in Figure 3.11. In general the parameter values are similar between the different drivers, showing that the drivers were using similar control strategies. The parameter values found using the averaged data all fall within the range of the parameter values found for the individual drivers, so the averaged data appears to be a valid representation of a typical driver's steering control strategy.

The identified parameter values highlight various trade-offs between different parameters, which have similar effects on the modelled steering action. Comparison of the identified visual delay τ_{vi} and neuromuscular frequency ω_{nm} shows that drivers with lower values of one parameter also had lower values of the other. Decreasing the neuromuscular frequency increases the lag in the neuromuscular system, therefore this is compensated for by a reduction in the visual delay, although the vestibular delay is not affected. The neuromuscular damping ζ_{nm} decreases with ω_{nm}, possibly to compensate for some change in the characteristics of the neuromuscular system as ω_{nm} decreases.

One of the most significant differences between the drivers is in the steering cost q_δ. This parameter describes the trade-off between steering effort and path-following error, and is a choice made by each of the drivers rather than a physical limitation. The performance of the drivers is compared further in Section 3.5.5. Some difference between the drivers is also seen in the process noise W, and this is discussed in Section 3.5.3. Due to the complexity of the model and the number of parameters, as well as the amount of noise in the measurements for each driver, the fact that the parameter values are a similar order of magnitude and in most cases close in value for the different drivers is encouraging. Further

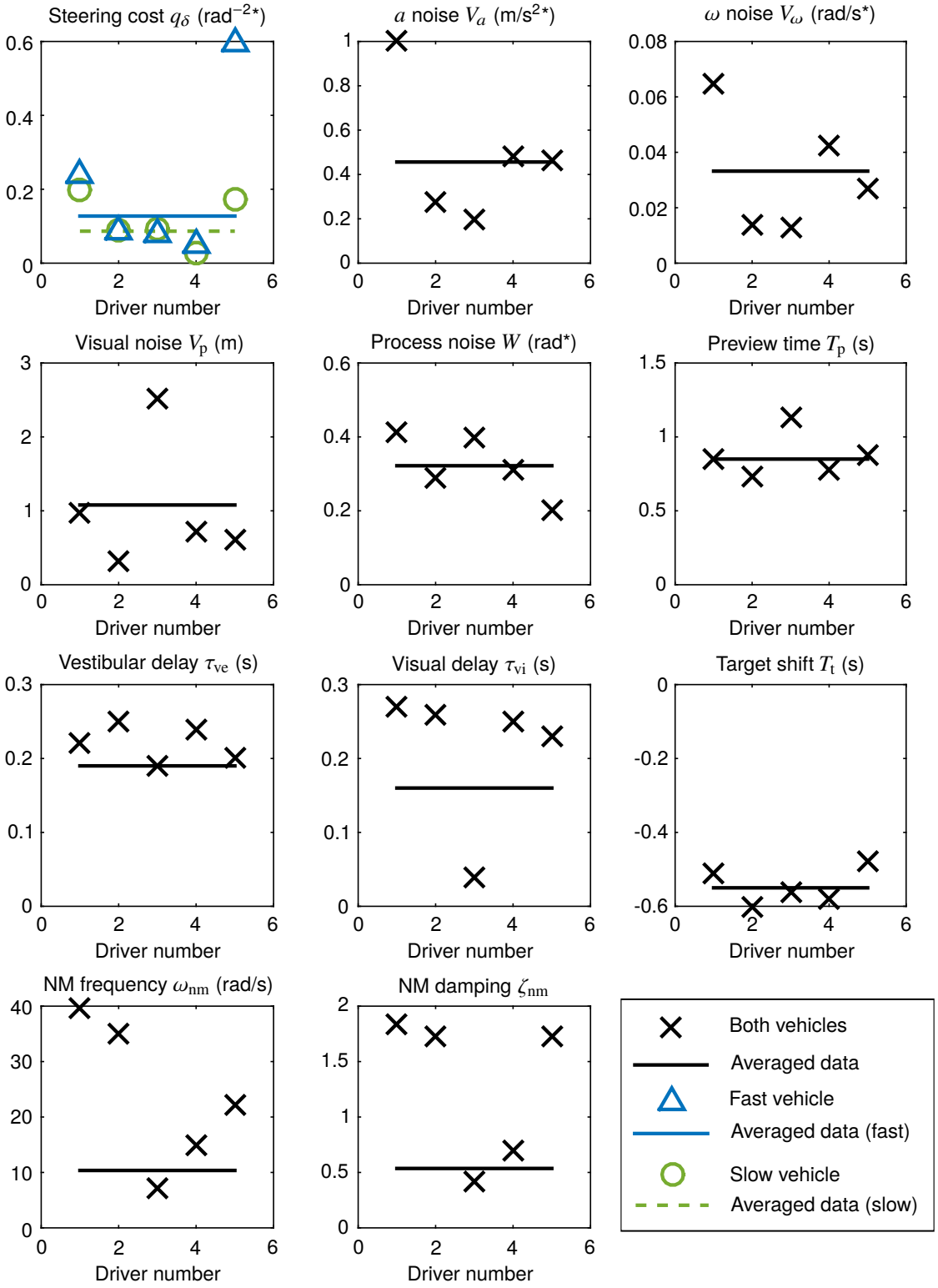

Figure 3.11: Single parameter sets found to fit all the trials. Values found for the individual drivers are shown by markers, and values found for the averaged data are shown by horizontal lines. Separate values of the steering cost q_δ are identified for the fast and slow vehicles.

discussion is given in Section 3.6 to determine whether the identified values are physically appropriate.

To investigate whether drivers' sensory parameters vary between trials, separate parameter sets identified for each trial using the averaged data are plotted in Figure 3.12. The process noise W, preview time T_p and target shift T_t are held constant during this identification procedure, however for the other parameters there is a wide spread of identified values. This highlights the difficulty of identifying such a large number of parameters for individual trials. Part of the reason for this large spread of results is that the effect of certain parameters is larger in some trials than others. For example, the visual noise amplitude V_p is not very important for trials with zero target (A3–A5, A10–A12) so a large range of identified values of V_p is seen for these trials. The noise amplitude V_ω is lowest for trials with both v and ω disturbances (A5–A7, A12–A14), indicating that for the other trials the driver did not place much weight on the angular velocity measurements. This shows that drivers use angular velocity measurements mainly to distinguish between translational and rotational disturbances. Comparison of the values of V_ω found for trials A5–A7 with those found for trials A12–A14 shows that V_ω is larger for the slower vehicle. This indicates that the measurement noise may be partly signal-dependent, as angular velocities were larger in the trials with the slow vehicle. Consistent visual delay values $\tau_{\mathrm{v}i}$ are identified for the trials with a target but without preview (A1, A6, A8, A13), which are close to the value identified for all the trials. When the driver can preview the target they can compensate for their visual delay, so it is more difficult to identify reliable values.

Further trends can be seen in the identified results which indicate how certain parameter values depend on the experimental conditions. For example, the neuromuscular damping ζ_nm is higher for trials with zero target (A3–A5, A10–A12) and lower for the remaining trials without preview (A1, A6, A8, A13) than for those with preview (A2, A7, A9, A14). Since the cost function weight q_δ is applied to the plant input $\hat{\delta}$ before the neuromuscular dynamics, the cost function is shaped by the neuromuscular transfer function. These variations in ζ_nm may therefore indicate changes in the driver's internal cost function. In addition, the visual noise V_p is higher for trials without preview, which could be because the drivers found it more difficult to take reliable measurements with this unnatural visual display.

The results shown in Figure 3.12 indicate that certain sensory parameters vary slightly under different conditions. It may be possible to develop a more accurate driver model by investigating and accounting for all of these variations. However, the agreement found between the measurements and the model predictions shown in Figure 3.10 demonstrates that a good approximation to the drivers' control strategies can be found using a constant set of parameter values.

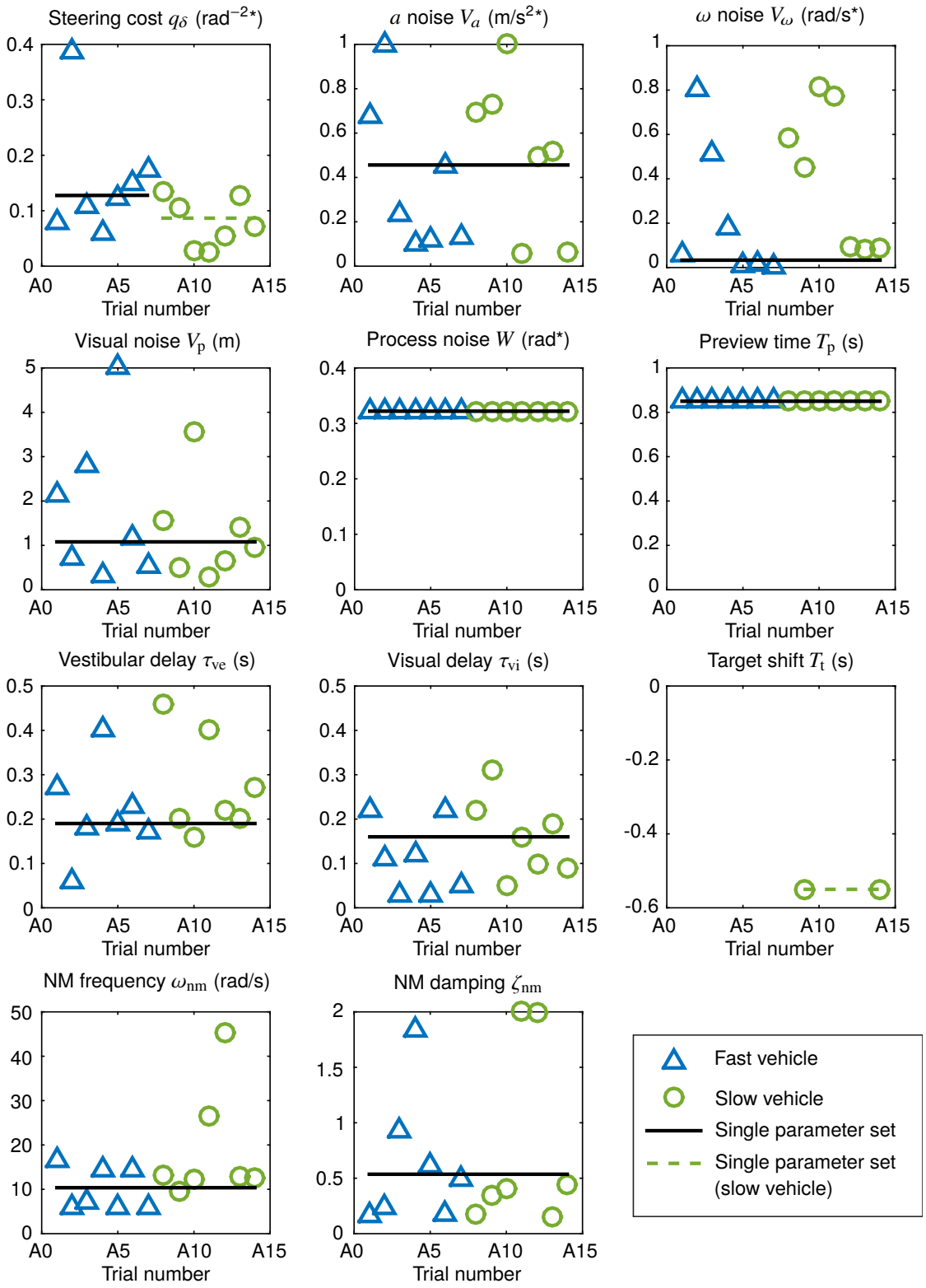

Figure 3.12: Parameter values identified for each trial separately using averaged data. The single parameter set identified to fit all of the trials for the averaged data is shown by horizontal lines.

3.5.3 Measured and modelled driver noise amplitudes

One of the objectives of the identification procedure described in Section 3.4.2 is to find a set of parameter values which predicts driver noise levels similar to those seen in the experiments. This is achieved by scaling the process noise amplitude W based on the ratio between the measured and modelled noise amplitudes. The measurement noise amplitudes V_a, V_ω and V_p are not scaled; while the Kalman filter is able to reduce the effects of measurement noise by using other measurements and an internal model of the system, the process noise is added immediately before the plant so cannot be reduced as effectively by the driver. Simulations confirmed that most of the noise in the modelled steering action originates from the process noise.

Assuming small modelling error, the driver noise is defined as $(\delta_\mathrm{sim} - \delta_\mathrm{exp})$. The ratio between the measured and modelled RMS noise amplitudes is shown in Figure 3.13a, using the single parameter sets identified for each driver. Overall the noise amplitudes match well between the model and the experiment. On average the ratio is close to 1, although the modelled noise is generally slightly larger than the measured noise, which could be because measurement noise amplitudes were not scaled. There is a reasonable amount of variation between trials, with the experimental noise generally larger for the trials with the slow vehicle (A8–A14).

To investigate the reasons behind the variation in noise amplitudes across the different trials, the values of W are scaled by the ratio of the experimental to the modelled RMS noise amplitudes (as shown in Figure 3.13a) for each trial, and the simulations are run

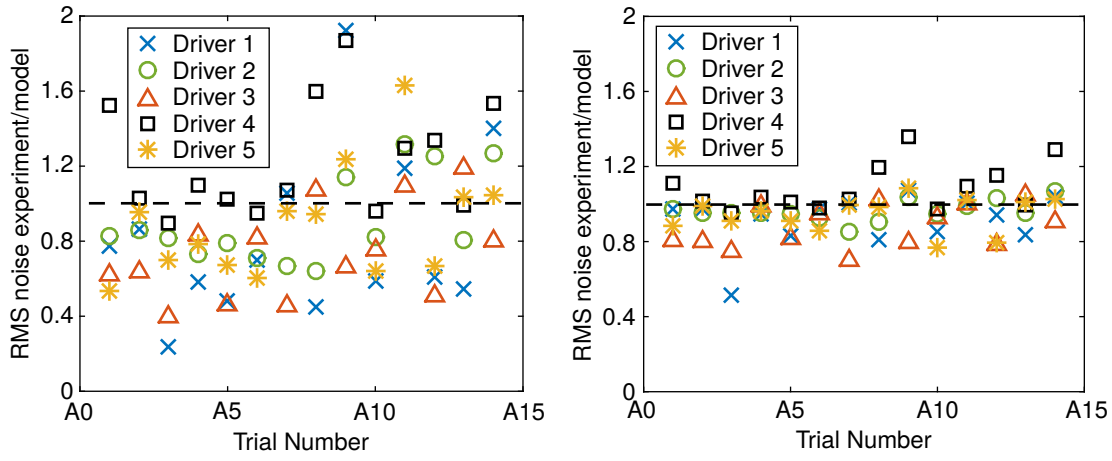

(a) Constant value of W **(b)** Adjusted values of W

Figure 3.13: Ratio of measured and modelled RMS driver noise amplitudes. In (a), a constant value of W is used for each driver, whereas in (b) the values of W have been adjusted for each trial to match the noise levels more closely.

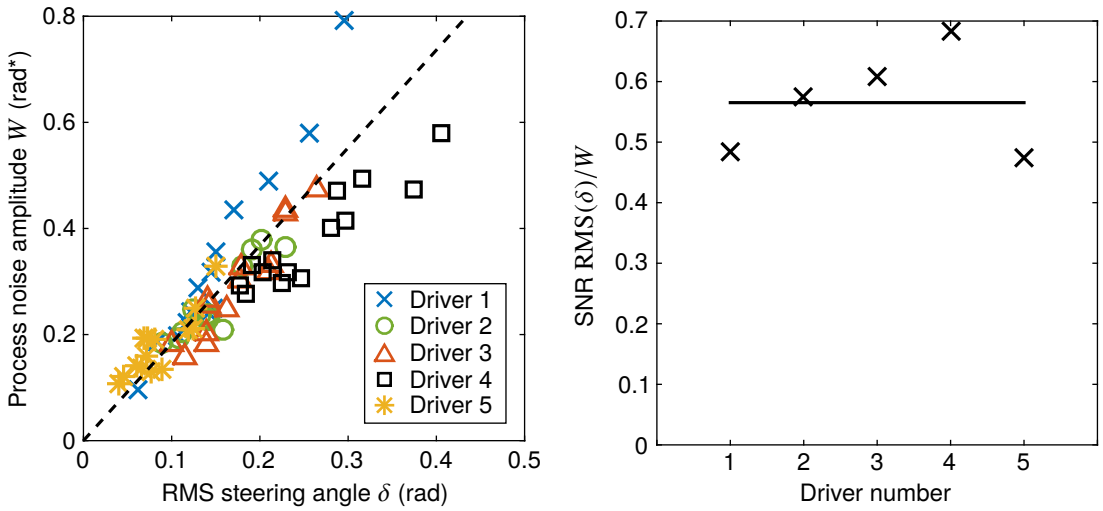

(a) W vs. RMS(δ) **(b)** Mean SNR (RMS(δ)/W)

Figure 3.14: Investigation into signal-dependent process noise. The identified process noise W is compared with the RMS steering angle δ in (a), and a strong linear correlation is seen. The mean SNR is compared between drivers in (b).

again. The agreement between the measured and simulated steering angles is not affected, with the VAFs using the adjusted values of W on average 0.4% higher than the VAFs using a constant value of W. The resulting ratios between measured and modelled noise amplitudes are shown in Figure 3.13b. These ratios are much closer to 1 than the ratios found using constant W values in Figure 3.13a. The predicted noise amplitude is still on average slightly larger than the measured noise amplitude, which could be a result of the measurement noise amplitudes not being adjusted.

The adjusted values of W are plotted against the RMS steering angle for each trial in Figure 3.14a. There is a clear linear relationship, showing that process noise is signal-dependent rather than additive. The amplitude RMS(δ) of steering actions applied by the driver varies between trials and depends on the task and the driver's internal cost function. Therefore it may be more appropriate to define a constant signal-to-noise ratio (SNR) RMS(δ)/W between the RMS steering angle and the RMS process noise, rather than a constant value of W. SNRs for each driver are compared in Figure 3.14b. There is some variation between the drivers, however comparison of Figure 3.14b with Figure 3.13b shows that the SNR correlates with the ratio of measured to predicted noise amplitudes. For example, driver 4 has a larger SNR in Figure 3.14b, but the model is shown to underestimate the noise level in Figure 3.13b, showing that the values of W should be slightly higher. The opposite is seen for drivers 1 and 5. Taking this into account, there is very little difference between the SNRs for the different drivers, with a value of 0.57 found on average. This value may seem very low (the noise level is almost twice that of that signal), however the

closed-loop dynamics of the driver allow some of the noise to be compensated for, so the effect of the noise is not as significant as the small SNR might suggest.

3.5.4 Model and procedure validation

Measurements from the last 30 s of each trial are not used in the identification procedure, but are kept to validate the predictive power of the different models and to check for over-fitting. If over-fitting had occurred, the model would fit the experimental results much better for the data that was used for identification. To check this, average VAF values are calculated over all the trials for each driver, either using the signals between 15 s–90 s (which are used for identification) or using the signals between 90 s–115 s (the last 5 s are neglected as the drivers may have steered differently as the end of the target line approached). The results are compared for all three models in Table 3.5.

Table 3.5 shows that some over-fitting may have occurred in the Box–Jenkins results and the results for the separate parameter sets, as the average VAF is lower in the final 30 s for all drivers except driver 4 using these models. This is not seen for the averaged data, showing that the reduction in driver noise due to the averaging of the measurements reduces the level of over-fitting. These results show that the VAFs given in Figure 3.10 for the Box–Jenkins model and single parameter sets may include a portion which is spuriously fitting to random variations in each trial. It also indicates that the separate parameter sets found for each trial may not always be reliable.

In contrast, the results for the single parameter sets do not show any evidence of over-fitting. VAFs are lower in the last 30 s for drivers 3 and 5, but higher for drivers 2 and 4 and very similar for driver 1. This shows that by optimising over all of the trials

Table 3.5: Validation of new driver model. Average VAF values over all the trials are compared, using the steering angles measured between 15–90 s (which are used in the identification procedure) and between 90–115 s (which are not used).

	Box–Jenkins average VAFs (%)		**Parametric (separate) average VAFs (%)**		**Parametric (single) average VAFs (%)**	
Driver	(15–90 s)	(90–115 s)	(15–90 s)	(90–115 s)	(15–90 s)	(90–115 s)
1	76.6	69.7	71.1	64.7	59.7	59.6
2	81.1	80.6	79.3	78.3	70.8	71.7
3	74.0	71.2	70.6	66.3	64.0	61.8
4	64.2	68.3	59.5	63.7	52.4	58.0
5	79.2	72.4	77.2	66.6	69.7	63.6
Averaged data	88.6	88.8	86.6	86.2	81.8	83.4

any random variations are evened out, allowing a single set of parameter values to be found without fitting to the random noise in the results. Therefore the single parameter sets identified to fit all the trials are more likely to be reliable than the separate parameter sets found for the individual trials.

Simulated measurements can be used to check that the identification procedure described in Section 3.4 reliably converges to the correct parameter values. Representative steering angles are created for each trial using the driver model with the parameter values identified for the averaged data over all trials, shown in Figure 3.11. Measurement and process noise are added with the identified amplitudes, to give results with similar noise levels to the real measurements. An ensemble of ten sets of simulated results for each trial is created with different random noise signals, and the identification procedure is run for each set. Since the agreement between measured and modelled noise amplitudes is investigated in more detail in Section 3.5.3, step 1 of the identification procedure given in Table 3.4 is omitted and the process noise amplitude W is set to the correct value.

The resulting identified parameter values are shown in Figure 3.15. These demonstrate that in general the procedure does reliably converge to the correct parameter values. There is some slight variation, as is expected when the measurements contain a significant amount of noise, however the identified parameters do not deviate substantially from their true values. Figure 3.15 highlights some small biases in the identified visual parameters, with both T_p and V_p underestimated slightly. This is likely to be because T_p is set to a small value of 0.1 s during step 2 of the procedure, resulting in a bias towards lower values during further steps. Although this bias should be considered when analysing the identified visual parameters, it only has a small bearing on the results and overall the identification procedure is shown to be reliable.

3.5.5 Driver performance comparison

The aim of the drivers during each trial was to follow the target f_t as closely as possible, which is modelled as a minimisation of the mean-square tracking error $e^2 = (f_\mathrm{t} - y)^2$. Therefore one way to quantify the performance of the drivers in each trial is to find the RMS value of e, and averaging this value over all the trials gives a performance metric for comparing the different drivers against each other. However, for a given driver, the accuracy with which they follow the target path also depends on their control effort, which can be quantified as the RMS value of the steering angle δ (or more accurately the plant input $\hat{\delta}$, however this cannot be measured directly from the experimental data). A driver who decides to use more steering effort may be able to achieve a lower path-following error than a driver who chooses to steer less. This trade-off is reflected in the cost function

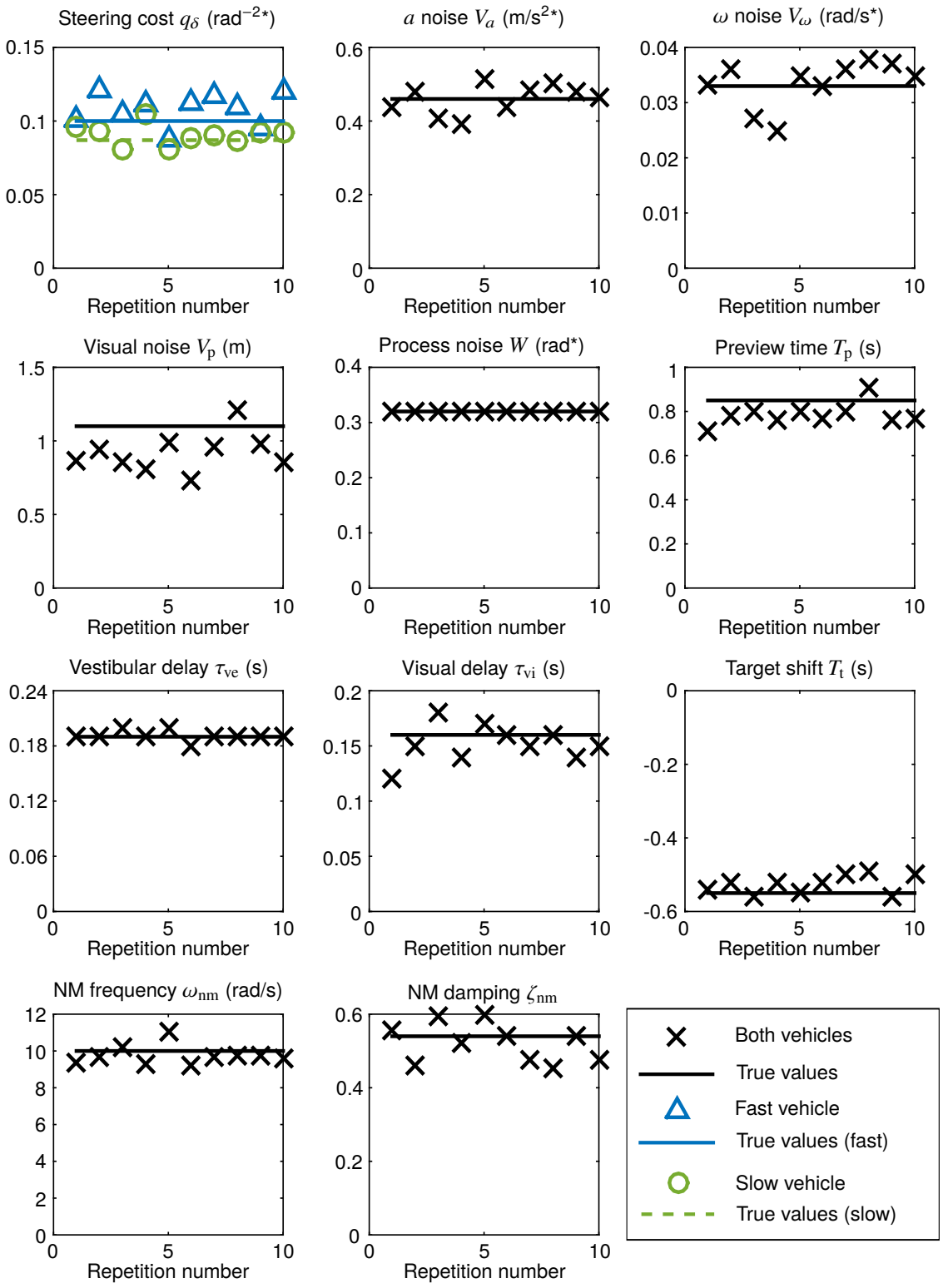

Figure 3.15: Validation of identification procedure. Identified parameter values are shown for ten repetitions of the procedure, using simulated measurements with added noise.

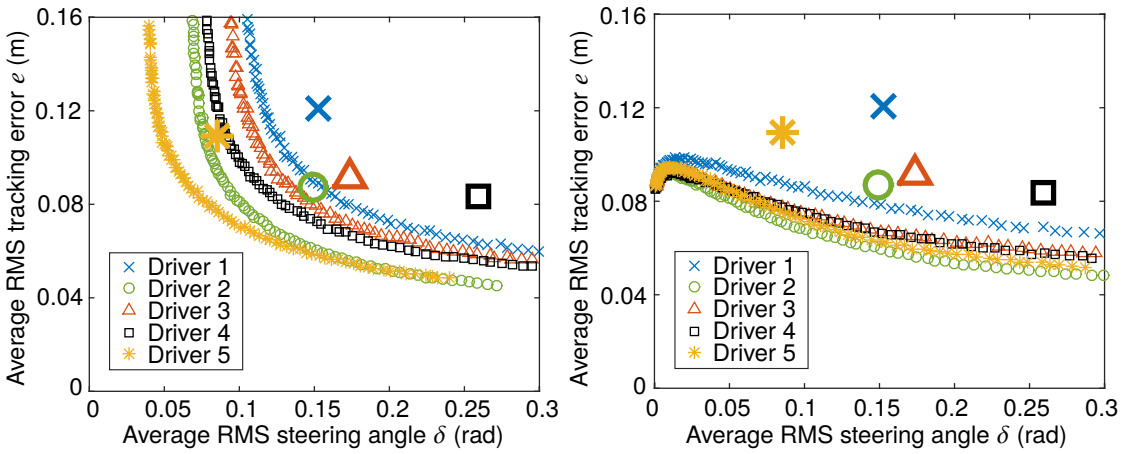

(a) Constant W **(b)** Constant SNR

Figure 3.16: Steering error against steering effort for each of the drivers. Experimental results averaged over all trials are shown by large markers. Simulated results with varying steering weight q_δ are shown by small markers.

of the parametric driver model (Equation 3.3), which includes costs on both e and $\hat{\delta}$.

The average RMS tracking errors and average RMS steering angles across all the trials for each driver are shown by the large markers in Figure 3.16. As expected, the general trend is that the path-following error decreases as the steering effort increases. Points towards the lower left of the graphs represent better drivers who achieved a lower tracking error with smaller steering actions. By this metric, driver 1 performed worse than drivers 2 and 5, and driver 2 also performed better than driver 3. However it is difficult to give a more general comparison of the drivers as it is not clear how tracking error varies with steering effort for a given driver.

To investigate the trade-off between tracking error and steering effort, simulations of all the trials are run using the parametric driver model with the parameter values identified for each driver. The steering cost q_δ is varied logarithmically between 10^{-2} and 10^2, and the average RMS tracking errors and steering angles are calculated for each driver. These results are shown by the small markers in Figure 3.16. In Figure 3.16a, the process noise amplitude W is kept constant as q_δ varied. In Figure 3.16b, for each value of q_δ the value of W is chosen based on the constant SNRs shown in Figure 3.14b for each driver.

The simulation results trace out performance curves for each of the drivers, showing the trade-off between steering effort and path-following error represented by the cost function weights. With constant values of W (Fig. 3.16a), the tracking error increases very steeply at low steering angle amplitudes, and significant differences are seen between the drivers. However, taking the more realistic approach of keeping the SNR constant (Figure 3.16b) gives much shallower curves. The differences between drivers are small, reflecting the

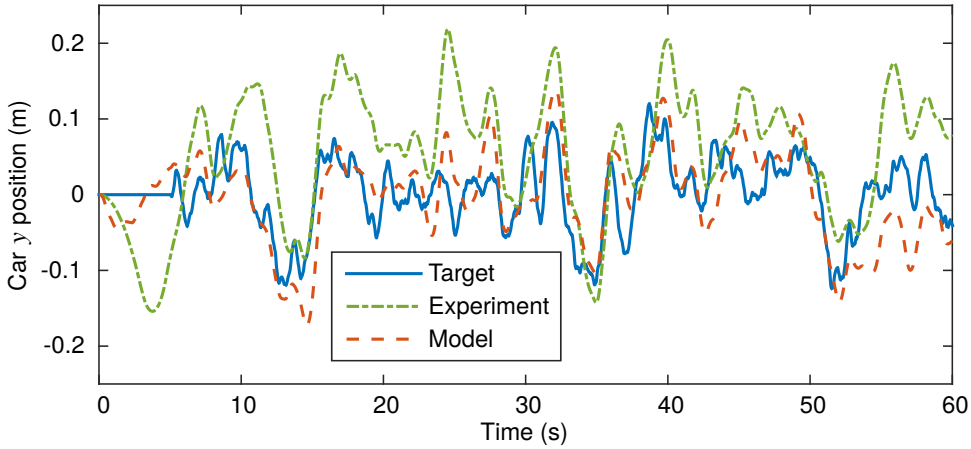

Figure 3.17: Measured and modelled vehicle lateral displacement y during the first 60 s of trial A7 with driver 2, using the adjusted process noise amplitude as described in Section 3.5.3.

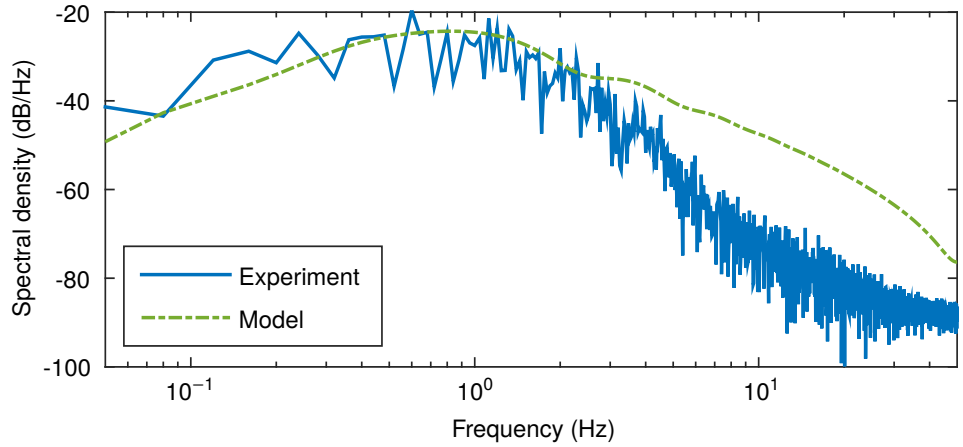

Figure 3.18: Spectral density of the driver noise referred to the steering angle δ, as found in the experiment and as predicted by the model for trial A7 with driver 2, using the adjusted process noise amplitude as described in Section 3.5.3.

similarity in the identified parameter values. It would be interesting to attempt to validate these results experimentally by asking drivers to steer with different amounts of effort, however drivers may find it difficult to consciously drive at a different operating point than they would naturally choose.

The performance curves would be expected to pass through the large markers representing the operating points found in the experiment, however the tracking errors from the simulations are much lower than the values found in the experiment. The reason for this can be seen by looking at the vehicle lateral displacements, as shown in Figure 3.17. Even though the RMS noise level on the steering angle is similar in the simulation and the experiment, the lateral displacement is much further from the target in the experiment. This is because the noise in the experimental results contains more low frequencies than

the modelled noise, leading to large low-frequency path-following errors. This can be seen in Figure 3.18, where the spectral density of the experimental noise ($\delta_{\text{sim}}(s) - \delta_{\text{exp}}(s)$) is compared with the spectral density predicted by the model.

These low-frequency discrepancies may result from the small lateral displacements of the target forcing function, which were difficult for the driver to see accurately. In the trial shown in Figure 3.17 the driver seems to have been consistently to the left of the target by about 10 cm, which may be because he wasn't able to see such a small misalignment. Figure 3.18 shows that the noise model spectral density does not match the results particularly well at low or high frequencies, so the assumption of white process and measurement noise may not be completely valid. However, at the mid-range frequencies which are more important for a driving task the fit is good.

3.6 Discussion

The results presented in Section 3.5 can be used to give an insight into driver steering control behaviour and sensory systems during a realistic driving task, allowing knowledge of the underlying mechanics of human perception to be combined with understanding of the higher-level control strategies used while driving.

3.6.1 General discussion of results

Experimental data has been used to identify parameter values for a new parametric driver model based on a physical understanding of human sensory dynamics. The VAF values presented in Section 3.5.1 show that the new model fits the experimental results almost as well as the upper bound given by the Box–Jenkins model. This result supports the hypothesis that driver steering control can be predicted using models of the underlying sensory mechanisms. The new model fits the results of all trials well with a single fixed set of parameter values. Simplifications have been made in the modelling of human sensory dynamics, such as neglecting visual perception of vehicle motion and assuming constant measurement noise on each previewed lateral displacement. The good agreement between the model and experimental results shows that these assumptions are reasonable.

Another assumption made in the model is that the measurement and process noise is Gaussian, white and additive. In Section 3.5.3 the process noise W is found to correlate linearly with RMS steering angle, indicating that process noise is signal-dependent rather than additive. The ω measurement noise V_ω is found in Section 3.5.2 to be larger for the slow vehicle than the fast vehicle. The angular velocities were also larger for the slow vehicle, so this result could indicate that the measurement noise is also signal-dependent.

Signal-dependent noise could be included explicitly in the driver model [41, 128], however this increases the complexity and computational requirements since the standard LQR and Kalman filter solutions are no longer optimal. As long as the conditions do not vary significantly over time a simpler solution may be to choose the additive noise amplitudes W, V_ω, V_a and V_p based on the expected average signal amplitudes. In Section 3.5.5 the model is shown to underestimate noise amplitudes at low frequencies and overestimate them at high frequencies. However the fit is better at the mid-range frequencies which are more important for driver steering control, so the assumption of Gaussian white noise may still be sufficiently accurate.

Parameter values identified for each of the five drivers are found in Section 3.5.2 to be similar in general. The trade-off between steering effort and path-following error is explored in Section 3.5.5, and simulations with signal-dependent process noise W show that performance curves for all drivers are similar. It is interesting that the professional driver (driver 5) did not perform any better than the other drivers during this experiment. This could be because the identified delays and noise amplitudes are linked to physical limitations which are similar in most healthy humans, so for simple tasks like those carried out in the experiment more experienced drivers do not necessarily have any advantage. The advantage of a professional driver is likely to be more apparent in the nonlinear handling regime near the limit of tyre adhesion, and in planning the optimum target trajectory.

3.6.2 Comparison of parameter values with results from literature

A review of relevant literature relating to sensory dynamics during driving is carried out in Chapter 2, therefore the identified parameter values can be compared with results from the literature to determine whether the new parametric driver model gives a realistic description of the function of sensory systems during driving. A comparison between the single set of parameter values identified to fit the averaged data and estimates from the literature is presented in Table 3.6.

There is some disagreement in the literature as to the values of delays in the visual and vestibular systems, and it can be difficult to distinguish between pure delays, lags and time taken to overcome threshold levels [111]. Transmission of vestibular reflex signals has been found to be very fast [117, 118], however other studies have suggested that neural processing of vestibular information may take longer than processing of visual information [119–121]. The identified vestibular delay of 0.19 s is slightly longer than the visual delay of 0.16 s, supporting the hypothesis that processing of vestibular information takes longer than visual information. Both of these values are within the (somewhat large) range suggested by results from the literature, and they can be used as a more specific

Table 3.6: Comparison of identified parameter values with estimates from literature. Identified values are found using the averaged data.

Parameter	q_δ (fast)	q_δ (slow)	V_a	V_ω	V_p	W
Units	$\mathrm{rad}^{-2\star}$	$\mathrm{rad}^{-2\star}$	$\mathrm{m/s}^{2\star}$	rad/s*	m	rad*
Identified	0.13	0.087	0.46	0.033	1.1	0.32
Literature	–	–	0.038	0.023	–	–

Parameter	τ_vi	τ_ve	T_t	T_p	ω_nm	ζ_nm
Units	s	s	s	s	rad/s	–
Identified	0.16	0.19	-0.55	0.85	10	0.54
Literature	0.10–0.56	0.05–0.44	–	1	5.65–23.2	0.24–0.43

estimate of sensory delays during a driving task.

Soyka et al. [68, 69] developed a signal-in-noise model of sensory thresholds, which can be used to infer noise amplitudes from measured threshold data. Estimated noise amplitudes using this approach are compared with identified values in Table 3.6. The identified value of V_ω is 1.4 times the value found from sensory threshold measurements, whereas the identified value of V_a is 12 times larger. Studies have found that vestibular thresholds may increase by factors between 1.5 and 6 during an active control task [137, 141–145, 147, 148], which can explain the larger value of V_ω but not of V_a. However, while the angular velocities in the experiment were very small and close to threshold levels, the accelerations were much larger than the perception threshold. The 'just noticeable difference' for accelerations increases with stimulus amplitude [139], so the identified noise amplitude V_a may include signal-dependent as well as additive noise. Taking this into account, the identified noise amplitudes are plausible.

Studies measuring drivers' gaze direction have found that drivers tend to look around 1 s ahead [6, 71, 79, 80]. They may also use their peripheral vision to gather additional information, however Land and Horwood [82] found that viewing the road path more than 1 s ahead is not necessary for good steering performance. The identified preview time T_p is 0.85 s, which is slightly shorter than the 1 s found in the literature. This may be a result of the small lateral target displacements and the assumption of constant visual noise V_p, when in reality the target would become more difficult to see as the preview distance increases. Previous studies have assumed that drivers look far enough ahead for the control gains on the previewed displacements to settle to zero, in order to achieve the best possible tracking performance [13, 14]. The LQR preview gains are plotted in Figure 3.19 for preview times of 0.85 s and 4 s. The gains take around 4 s to settle to zero, so this indicates that the drivers did not measure all the useful visual preview information in the experiment. The

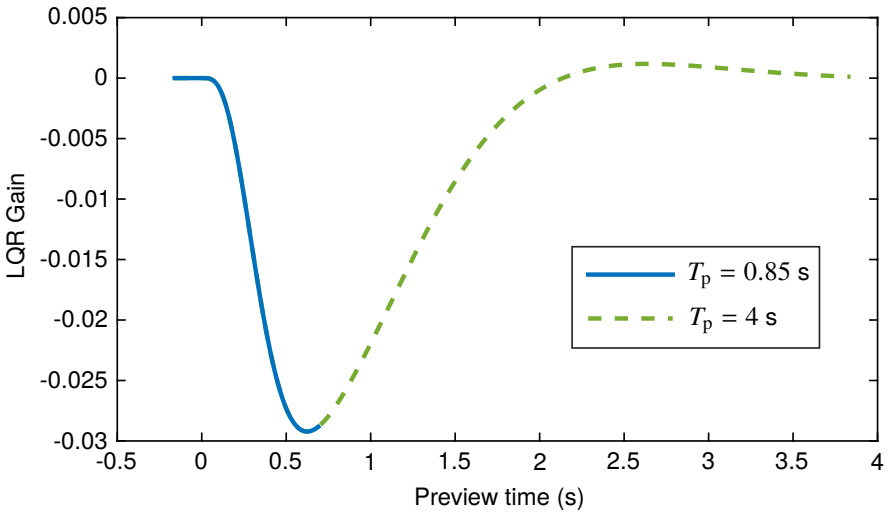

Figure 3.19: LQR gains on the previewed displacements for $T_p = 0.85$ s and $T_p = 4$ s. Due to the visual time delay, the first N_{vi} states correspond to target points which the car has already passed, hence why their gains are zero.

identified target shift T_t (which is only used for the slow vehicle) is 0.55 s, implying that the drivers steered 5.5 m ahead of the target on average. They may have aligned the front of the vehicle with the target rather than the centre of mass, although this cannot account for the full distance. Another explanation is that at low speeds the assumption of constant preview time could be invalid, and drivers actually look further ahead so that the preview distance isn't too short. This would cause them to steer earlier as observed.

The identified neuromuscular frequency ω_{nm} is between the values found for relaxed and tensed arms by Pick and Cole [15], however the identified damping ratio ζ_{nm} is higher than the values found in both cases. In reality the driver's neuromuscular system interacts in closed-loop with the spring-damper torque feedback of the steering wheel, however this interaction is not captured in the model. Therefore, the identified neuromuscular transfer function incorporates this complete closed-loop system, which acts as a low-pass filter between $\hat{\delta}$ and δ. While the transfer function for the neuromuscular dynamics in the model is intended to correspond to the dynamics of the driver's arm muscles, it also plays a role in shaping the cost function. The steering cost is applied to $\hat{\delta}$, based on the hypothesis that the driver aims to minimise control inputs to the neuromuscular dynamics. However, the driver may have other costs, for example derivatives or filtered versions of $\hat{\delta}$, and these may come across in the identified neuromuscular parameter values.

Overall, comparison of the identified sensory parameter values with values found in the literature shows the identified values to be physically plausible. Although the identified noise amplitudes are larger than values inferred from sensory threshold measurements, this aligns with expectations during an active control task with multimodal sensory stimuli. The

aim of the new driver model is to predict driver steering behaviour based on considerations of the physiological processes involved, so it is encouraging that the identified parameter values give a reasonable description of human sensory systems.

3.6.3 Implications and limitations

A novel model of driver steering control has been developed based on an optimal control strategy, incorporating models of the driver's sensory dynamics. The model fits experimental results well, and identified sensory parameters are physically plausible when compared with measurements from the literature. These results support the hypothesis that drivers achieve close to the best possible control performance within the limitations of their sensory and motor systems. Experienced drivers will have spent many hours driving, allowing them to learn how best to use sensory information to control a vehicle.

The new model gives a physical basis for the driver's control decisions which is lacking in many existing models. Furthermore, this work has more general implications for the understanding of neuronal information processing during active control tasks. The identified time delays and noise parameters give an insight into the limitations of human sensorimotor systems in such a task, and how they compare with previous studies which have generally taken measurements under controlled, passive conditions. It is also shown that the processing carried out in the brain during an active control task such as driving can be modelled reliably by an optimal controller and state estimator.

The driver model presented in this chapter has several limitations. The model is only derived for constant speed vehicles, and the yaw angle of the vehicle is assumed to be small. A linear vehicle model is used, which is a reasonable approximation for regular driving, however under more extreme conditions drivers may operate in the nonlinear region close to the limit of adhesion of the tyres. The current model is derived for random targets and disturbances, however further work is necessary to determine how drivers deal with more predictable or transient conditions. The derivation of the driver model assumes that there are no conflicts between the senses, and the experiment was carefully designed to allow the vehicle motion to be replicated at full scale. However, it is necessary to investigate how drivers behave when there are sensory conflicts, in particular when the motion is scaled or filtered. These limitations are addressed in Chapters 4 to 6.

3.7 Conclusion

A new parametric model of driver steering control has been developed, incorporating human sensory dynamics and hypothesising that the driver's control strategy is close to

optimal within the limitations of their sensory and motor systems. Model predictions match experimental results well, with identified parameter values able to fit averaged steering measurements with a 'variance accounted for' greater than 71% in all trials, and 82% on average. The identified parameter values are physically plausible compared with values from the literature. Identified vestibular delays are longer than visual delays, supporting previous studies which have suggested that processing of vestibular information takes longer than visual information.

The identified process noise amplitude W is linearly correlated with the RMS steering angle δ, showing that process noise is signal-dependent. The signal-to-noise ratio $\mathrm{RMS}(\delta)/W$ is consistent across the different trials and drivers, at around 0.57. Some evidence of signal-dependence is also seen in the identified measurement noise amplitudes. The model predicts smaller low-frequency and larger high-frequency driver noise amplitudes than were measured in the experiment, which indicates that the assumptions of the model do not characterise the noise profile completely. However, at mid-range frequencies which are more important for driver steering control the noise model fits well.

Differences between the test subjects mainly resulted from different cost function weightings, and if this is accounted for the performance of each driver was similar. A professional driver did not perform any better than less experienced drivers in this experiment. Further work is necessary to address the limitations of the current model, considering nonlinear vehicles, more realistic road profiles and the effects of sensory conflicts on a driver's control performance.

Chapter 4

Driver control with sensory conflicts

A new model of driver steering control incorporating sensory dynamics is proposed in Chapter 3, and an identification procedure is used to find parameter values to fit the results of an experiment carried out in a driving simulator with full-scale lateral and yaw motion. This chapter describes further experiments investigating how drivers steer with conflicts between their visual and vestibular measurements, caused by scaling or filtering the physical motion of the simulator relative to the virtual environment. The predictions of several variations of the new driver model are compared with the measurements to understand how drivers perceive sensory conflicts. Drivers are found to adapt well in general, unless the conflict is large in which case they ignore the physical motion and rely on visual measurements. Drivers make greater use of physical motion which they rate as being more helpful, achieving a better tracking performance. Sensory measurement noise is shown to be signal-dependent, allowing a single set of parameters to be found to fit the results of all the experiments. The model fits the measurements well, with an average 'variance accounted for' of 76%.

4.1 Introduction

In Chapter 3, a new model of driver steering control is developed incorporating models of the driver's sensory systems and assuming optimal integration of noisy sensory measurements. Values of the physical parameters of the model are found using an identification procedure to fit to results from an experiment carried out in a driving simulator, and are compared with estimates found from a review of the literature on sensory dynamics presented in Chapter 2. The model fits the experimental results well, and the parameter values are found to be physically plausible when compared with results from the literature.

The experiment carried out in Chapter 3 was carefully designed so that the lateral and yaw motion applied to the driver in the moving-base simulator matched the motion of the simulated vehicle at full scale. The information perceived by the driver's visual and vestibular systems was coherent, without any sensory conflicts. Studies summarised

in Chapter 2 indicate that humans generally integrate coherent sensory information in a statistically optimal fashion [164–169], and use an internal model of their surroundings to predict future system states [47, 48]. This is reflected in the driver model by a Kalman filter, which uses an internal model and sensory measurements to give an optimal state estimate. In Chapter 3 it is assumed that the driver's internal model closely matches the real driver-vehicle system, with any discrepancies represented as Gaussian process noise.

Carrying out experiments in a driving simulator allows the physical motion applied to the driver to be controlled independently from the displayed visual motion. By controlling the inputs to the driver's visual and vestibular systems separately, it is possible to identify the separate control actions resulting from the different sensory systems more effectively than in the full-scale motion experiment in Chapter 3. In particular, trials carried out with no physical motion allow the visual system to be explored in isolation, so that the distinct roles of the visual and vestibular systems in car driving can be studied. However, subjecting the driver to different visual and physical motion causes conflicts between the visual and vestibular measurements. The literature surveyed in Chapter 2 indicates that incoherent sensory information may not always be integrated in an optimal fashion, although exactly how sensory conflicts are resolved is not fully understood [195–210].

The driver model is adjusted in Section 4.2 to give a more realistic description of the driver's visual system, and to present various approaches to modelling perception of sensory conflicts. The procedures for three additional experiments carried out to measure drivers' control actions with scaled or filtered motion are described in Section 4.3, and the parameter identification procedure used to fit the driver model to the experimental results is discussed in Section 4.4. The results are presented in Section 4.5, and a single set of model parameter values is found to fit the results of all four experiments in Section 4.6. The implications of the results are discussed in Section 4.7, and the main conclusions are summarised in Section 4.8.

4.2 Driver model adjustments

The driver model developed in Chapter 3 assumes that the visual and physical motion presented to the driver are coherent. Various adjustments must be made to the driver model to represent steering behaviour in a simulator with scaled or filtered physical motion.

4.2.1 Modified visual system model

In Chapter 3, the driver's visual system is modelled as a straight-line preview of the upcoming road path, measuring the lateral displacements between the target path and a line

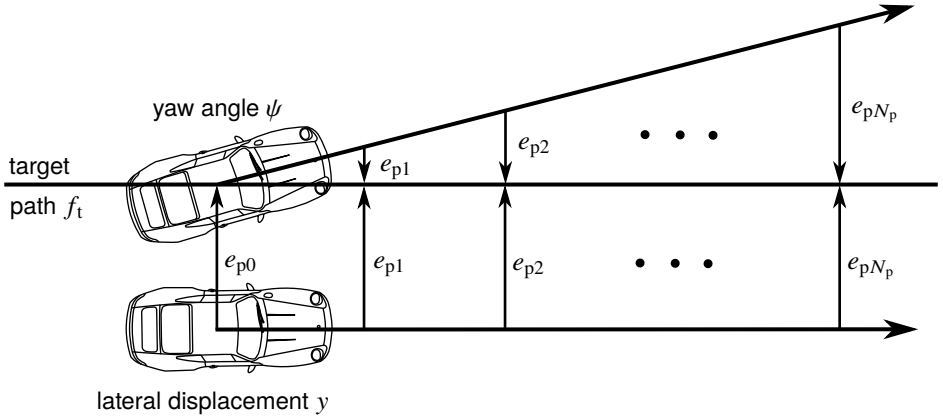

Figure 4.1: Effect of yaw and lateral motion on previewed displacements, with visual system model used in Chapter 3

projected ahead of the vehicle. This is a simple description which has been used in previous studies [13, 14]. However there are several disadvantages to this model which may become more apparent when the motion is scaled and the driver places a greater emphasis on the visual information. If the vehicle displaces laterally, the previewed displacements all change by the same amount. However if the vehicle yaws, the previewed displacements change in proportion to their distance from the vehicle, as shown in Figure 4.1. This means that as the preview time T_p increases, the influence of the yaw motion on the modelled steering control increases relative to the lateral motion. Therefore the relative weightings on lateral and yaw visual measurements are controlled by T_p, which could obscure other effects of varying the preview time. A further implication is that the driver's control action depends on T_p, even when there is zero target or no preview. This is unrealistic, as the driver cannot obtain additional information by looking further ahead in these conditions.

To address these issues, the model of the visual system is modified as shown in Figure 4.2, based on an intrinsic coordinate description derived by Timings and Cole [219]. The simulated driver measures the first lateral displacement e and the angles ϕ_0 to ϕ_{N_p} of each target segment, which are measured relative to the vehicle's yaw angle. Assuming small target and vehicle yaw angles, the previewed angles are given by:

$$\phi_n(k) = \frac{f_t(k+n+1) - f_t(k+n)}{UT_s} - \psi(k) \tag{4.1}$$

where f_t is the lateral displacement of the target path, ψ and U are the vehicle yaw angle and longitudinal speed and T_s is the sample time. The new model has one more plant output than before; instead of $(N_p + 1)$ previewed displacements with RMS measurement noise V_p there are $(N_p + 1)$ previewed angles with RMS noise V_ϕ plus a measurement of e with RMS noise V_e.

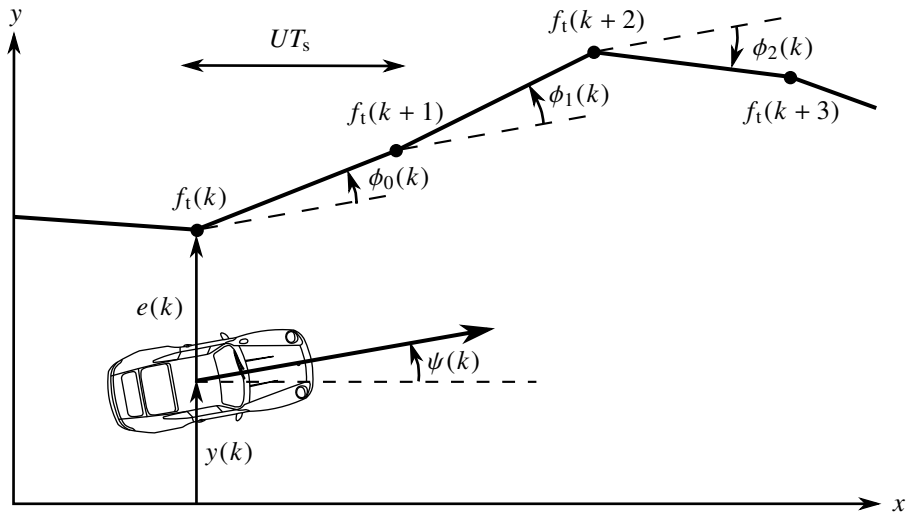

Figure 4.2: Modification made to model of the driver's visual system. Rather than previewing lateral displacements of the target path, the driver measures the current tracking error e and upcoming target angles $\boldsymbol{\phi}$.

The simulated driver's control action should not change with T_p if the target is a straight line or cannot be previewed, as the visual system will simply take more measurements of $(-\psi)$ as T_p increases. However, the Kalman filter will combine these additional measurements using a maximum likelihood estimation (MLE) method to give a more accurate estimate of ψ, so the previewed angle noise magnitude V_ϕ must be adjusted to compensate for this. The Kalman filter combines $(N_p + 1)$ measurements with variance V_ϕ^2 using MLE, giving a combined estimate with a variance of [173]:

$$\sigma_\phi^2 = \left(\sum_{i=1}^{N_p+1} \frac{1}{V_\phi^2} \right)^{-1} = \frac{V_\phi^2}{N_p + 1} \tag{4.2}$$

The combined variance σ_ϕ^2 should be independent of preview time, which can be achieved by choosing the noise V_ϕ on each previewed angle so that:

$$V_\phi = \sigma_\phi \sqrt{N_p + 1} \tag{4.3}$$

This method is found to achieve the desired result of a control action which is independent of the preview time when the target is zero or cannot be previewed. The new model also separates the visual perception of lateral displacements and yaw angles, allowing their relative weightings to be varied without changing the preview time. Drivers may also take measurements of lateral and yaw velocities using their visual system, however for simplicity these are neglected. Another advantage of this model is that it can easily be

adapted to investigate a more realistic driving manoeuvre with large target yaw angles, such as a corner or a circuit [219].

4.2.2 Perception of motion scaling or filtering

The driver model derived in Chapter 3 assumes that the motion of the simulator is at full scale. This assumption can be removed easily by inserting motion filters into the plant. The lateral acceleration is filtered by a lateral motion filter $H_{\mathrm{m}a}(s)$ before reaching the otoliths, and the yaw angular velocity is filtered by a yaw motion filter $H_{\mathrm{m}\omega}(s)$ before being perceived by the SCCs. A complete derivation of the plant including motion filters is given in Appendix A.

In Chapter 3 it is assumed that the driver has an accurate internal model of the driver-vehicle dynamics, with any discrepancies represented by Gaussian process noise. However, since humans in some circumstances exhibit suboptimal integration of conflicting sensory information (see Chapter 2), several variations of the model are developed to represent different assumptions about how the driver perceives the motion scaling or filtering. These variations are all based on internal model estimates $H'_{\mathrm{m}a}(s)$ and $H'_{\mathrm{m}\omega}(s)$ of the motion filters, which are not necessarily equal to the real motion filters $H_{\mathrm{m}a}(s)$ and $H_{\mathrm{m}\omega}(s)$.

The implemented driver model variations are summarised in Table 4.1. In model M0 the internal model motion filters are 0, so the simulated driver ignores any perceived physical motion. In model M1 the internal model motion filters are 1, so the simulated driver is not aware that the physical motion is scaled or filtered. In model M2 the correct scaling factors or filters are used in the internal model, representing a driver who can perceive and account for any scaling or filtering. In model M3 the internal model filters are defined as gains $K'_{\mathrm{m}a}$ and $K'_{\mathrm{m}\omega}$, which are optimised as part of the parameter identification

Table 4.1: Variations of the driver steering control model, represented by different internal models of the motion scaling factors

Model	Internal model lateral motion filter	Internal model yaw motion filter
M0	$H'_{\mathrm{m}a}(s) = 0$	$H'_{\mathrm{m}\omega}(s) = 0$
M1	$H'_{\mathrm{m}a}(s) = 1$	$H'_{\mathrm{m}\omega}(s) = 1$
M2	$H'_{\mathrm{m}a}(s) = H_{\mathrm{m}a}(s)$	$H'_{\mathrm{m}\omega}(s) = H_{\mathrm{m}\omega}(s)$
M3	$H'_{\mathrm{m}a}(s) = K'_{\mathrm{m}a}$ (optimised)	$H'_{\mathrm{m}\omega}(s) = K'_{\mathrm{m}\omega}$ (optimised)
M4	$H'_{\mathrm{m}a}(s) = \begin{cases} H_{\mathrm{HP1}}(s) & H_{\mathrm{m}a}(s) = H_{\mathrm{HP2}}(s) \\ H_{\mathrm{HP2}}(s) & H_{\mathrm{m}a}(s) = H_{\mathrm{HP1}}(s) \\ H_{\mathrm{m}a}(s) & \text{otherwise} \end{cases}$	$H'_{\mathrm{m}\omega}(s) = \begin{cases} H_{\mathrm{HP1}}(s) & H_{\mathrm{m}\omega}(s) = H_{\mathrm{HP2}}(s) \\ H_{\mathrm{HP2}}(s) & H_{\mathrm{m}\omega}(s) = H_{\mathrm{HP1}}(s) \\ H_{\mathrm{m}\omega}(s) & \text{otherwise} \end{cases}$

procedure to fit the measured steering angles. Finally, for the filtered motion trials an additional model M4 is defined, which assumes correct scaling factors but switches the two high-pass filters $H_{\mathrm{HP1}}(s)$ and $H_{\mathrm{HP2}}(s)$ (defined in Section 4.3.3), to investigate the extent to which drivers can perceive subtle differences in motion filters.

4.3 Sensory conflict experiments

To investigate how drivers steer when there are conflicts between the information perceived by their visual and vestibular systems, three experiments were carried out following a similar procedure to the full motion experiment described in Chapter 3. Each experiment consisted of trials lasting 120 s, in which the drivers followed a randomly deviating target line (close to a straight line) while random disturbances were added to the vehicle's lateral and yaw velocities. In the first two experiments the lateral and yaw motion were scaled by constant scaling factors; the first experiment focussed on trials where the driver could not preview the upcoming target path and the second involved only trials with preview. The third experiment investigated the effect of filtering the motion as well as scaling.

Except where specified otherwise experimental conditions were the same as in the full motion experiment described in Chapter 3. Forcing function filters $H_{ft}(s)$, $H_{fv}(s)$ and $H_{f\omega}(s)$ were given by Equations 3.9, 3.10 and 3.11. A linear single-track vehicle was used, with parameters summarised in Table 3.1. Two types of visual display were presented, one allowing the driver to preview the upcoming target and one without preview, as shown in Figure 3.9. Steering torque feedback was represented by a parallel spring and damper, as in Equation 3.12, with k_{STF} = 8 Nm/rad and c_{STF} = 1 Nms/rad. For ease of reference to the trials in the different experiments, each trial is labelled with a letter and a number, e.g. trial B8. The letter refers to the experiment, with A = full motion (experiment from Chapter 3), B = scaled motion without preview, C = scaled motion with preview and D = filtered motion. The number refers to the trial number within each experiment.

4.3.1 Scaled motion without preview

In the first experiment the physical motion was scaled relative to the virtual vehicle motion, and the drivers were not able to preview future target information, allowing visual delays to be identified more easily. In total 13 trials were carried out, with conditions summarised in Table 4.2. In addition, two of the trials from the full motion experiment (A6 and A13) are included in the analysis. Since the full motion trials and the scaled motion trials without preview were carried out on the same day by the same drivers, trials A6 and A13 were only carried out once per driver and the results are used in the analysis for both experiments.

Table 4.2: Experimental conditions for each scaled motion trial, without preview. Trials A6 and A13 from the full motion experiment are included in the analysis for comparison.

	Forcing function amplitudes			Motion filters			
Trial	W_t (m*)	W_v (m/s*)	W_ω (rad/s*)	$H_{\mathrm{m}a}(s)$	$H_{\mathrm{m}\omega}(s)$	**Vehicle**	**Preview**
A6	0.79	0.79	0.79	1	1	F	✗
B1	1.11	1.11	1.11	0.5	1	F	✗
B2	1.11	1.11	1.11	0.2	1	F	✗
B3	1.11	1.11	1.11	0	1	F	✗
B4	1.11	1.11	1.11	0	0	F	✗
A13	1.11	1.11	1.11	1	1	S	✗
B5	1.11	1.11	1.11	0.5	1	S	✗
B6	1.11	1.11	1.11	0.2	1	S	✗
B7	1.11	1.11	1.11	0	1	S	✗
B8	1.11	1.11	1.11	0	0	S	✗
B9	5.53	5.53	5.53	0.2	1	F*	✗
B10	5.53	5.53	5.53	0.2	0.5	F*	✗
B11	5.53	5.53	5.53	0.2	0.2	F*	✗
B12	5.53	5.53	5.53	0.2	0	F*	✗
B13	5.53	5.53	5.53	0	0	F*	✗

To limit the scope of the experiment the forcing function amplitudes W_t, W_v and W_ω were always equal to each other, although this equal amplitude varied across the trials to maximise use of the available simulator travel.

Three different vehicles were used in the experiment. The same fast (F) and slow (S) vehicles were used as in Chapter 3, with parameters summarised in Table 3.1. In trials A6 and B1–B4, the fast vehicle was used and various lateral motion scaling factors were tested, with trial B4 having no physical motion at all. Trials A13 and B5–B8 were the same but with the slow vehicle (and slightly different amplitudes). In trials B9–B13, the forcing functions were scaled up by a factor of five so that the lateral displacements of the vehicle were larger, giving vehicle motion of a more realistic amplitude. The lateral motion was scaled down by a factor of five to stay within the simulator limits, while different yaw scaling factors were tested. These trials were carried out with the fast vehicle, although to make it easier to follow this larger amplitude target the steering ratio G was scaled down by a factor of five, giving the F* vehicle which is also summarised in Table 3.1.

4.3.2 Scaled motion with preview

The second experiment consisted of twelve trials which also investigated scaled motion, but allowed the driver to preview the upcoming target to reflect a more realistic driving

Table 4.3: Experimental conditions for each scaled motion trial, with preview

	Forcing function amplitudes			Motion filters			
Trial	W_t (m*)	W_v (m/s*)	W_ω (rad/s*)	$H_{ma}(s)$	$H_{m\omega}(s)$	**Vehicle**	**Preview**
C1	5.53	5.53	5.53	0	0	F*	✓
C2	5.53	5.53	5.53	0	0.5	F*	✓
C3	5.53	5.53	5.53	0	1	F*	✓
C4	5.53	5.53	5.53	0.1	1	F*	✓
C5	5.53	5.53	5.53	0.2	1	F*	✓
C6	5.53	5.53	5.53	0.2	0.5	F*	✓
C7	5.53	5.53	5.53	0.2	0.2	F*	✓
C8	5.53	5.53	5.53	0.2	0	F*	✓
C9	5.53	5.53	5.53	−0.1	0	F*	✓
C10	5.53	5.53	5.53	−0.1	1	F*	✓
C11	5.53	5.53	5.53	−0.15	−0.15	F*	✓
C12	5.53	5.53	5.53	0.15	−0.15	F*	✓

scenario. Because the aim of this set of trials was to reflect more realistic driving conditions, the larger forcing function magnitudes used in trials B9–B13 were used throughout the experiment, and the fast (F*) vehicle was also used for all trials. The conditions for the scaled motion experiment with preview are given in Table 4.3. Before the experiment the drivers carried out a practice trial with the same conditions as trial A7, as a reminder of the procedure of the experiment. In trials C9–C12 negative scaling factors were applied to the motion, to investigate how drivers cope with conflicts in the direction of visual and physical motion. Because some of the motion conditions were rather unnatural, practice runs lasting 30 s were carried out before each trial to give the drivers additional time to settle into a control strategy.

4.3.3 Filtered motion

The final experiment was designed to investigate the extent to which drivers can perceive and compensate for filters of varying complexity applied to the vehicle motion. Two high-pass filters were used, the first $H_{HP1}(s)$ being a simple first-order high-pass filter with a cutoff frequency of 15 rad/s:

$$H_{HP1}(s) = \frac{s}{s + 15} \tag{4.4}$$

The second $H_{HP2}(s)$ includes a notch at 4 rad/s, which gives extra phase lead at high frequencies and allows the cutoff frequency for the high-pass filter to be reduced to 8 rad/s:

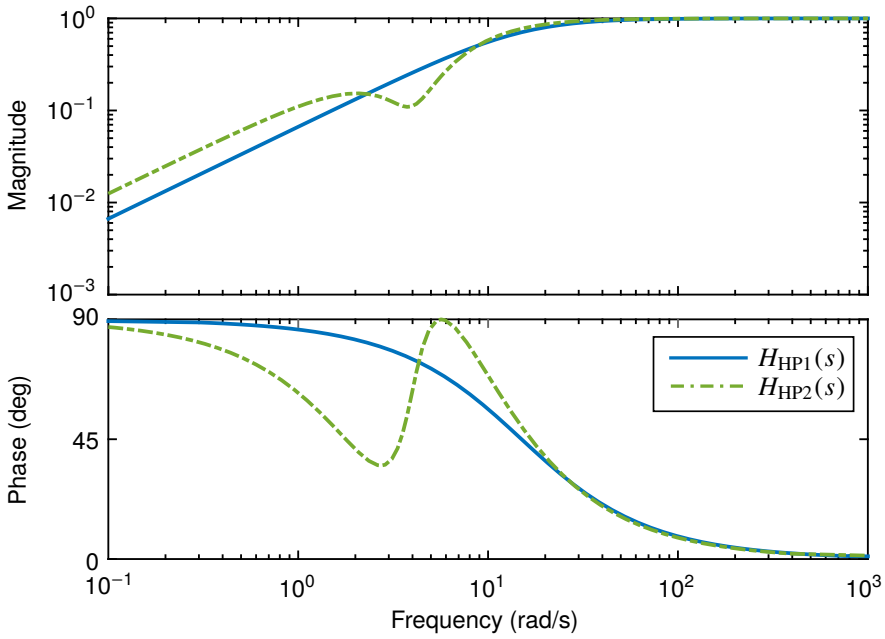

Figure 4.3: Bode diagram of motion filters $H_{HP1}(s)$ and $H_{HP2}(s)$

$$H_{HP2}(s) = \left(\frac{s^2 + 2s + 16}{s^2 + 8s + 16}\right)\left(\frac{s}{s + 8}\right) \tag{4.5}$$

These filters are much simpler than those normally used in driving simulators. They are designed to allow comparison between a simple filter and one with more complicated phase characteristics, to test the extent to which drivers are able to develop accurate internal models of filters with varying complexity. A Bode diagram of the two filters is shown in Figure 4.3. The conditions for each of the filtered motion trials are given in Table 4.4. There were twelve trials consisting of different combinations of motion gains and the two high-pass filters. Preview was included in all of the filtered motion trials, and drivers had 30 s of practice before the start of each trial. Trials D1 and D2 had the same conditions as trials C1 and C5, however they were repeated in the filtered motion experiment.

4.3.4 Full motion

The full motion experiment is described in detail in Chapter 3. However for reference the conditions of each trial are repeated in Table 4.5.

4.3.5 Test subjects and procedure

The experiments were each carried out by five drivers, one of whom was a professional test driver. The test subjects were the same across all the experiments, and were the same

Table 4.4: Experimental conditions for each trial with filtered motion

	Forcing function amplitudes			Motion filters			
Trial	W_t (m*)	W_v (m/s*)	W_ω (rad/s*)	$H_{\mathrm{m}a}(s)$	$H_{\mathrm{m}\omega}(s)$	**Vehicle**	**Preview**
D1	5.53	5.53	5.53	0	0	F*	✓
D2	5.53	5.53	5.53	0.2	1	F*	✓
D3	5.53	5.53	5.53	$H_{\mathrm{HP1}}(s)$	1	F*	✓
D4	5.53	5.53	5.53	$H_{\mathrm{HP2}}(s)$	1	F*	✓
D5	5.53	5.53	5.53	0.2	$H_{\mathrm{HP1}}(s)$	F*	✓
D6	5.53	5.53	5.53	0.2	$H_{\mathrm{HP2}}(s)$	F*	✓
D7	5.53	5.53	5.53	$H_{\mathrm{HP1}}(s)$	$H_{\mathrm{HP1}}(s)$	F*	✓
D8	5.53	5.53	5.53	$H_{\mathrm{HP2}}(s)$	$H_{\mathrm{HP2}}(s)$	F*	✓
D9	5.53	5.53	5.53	$H_{\mathrm{HP2}}(s)$	$H_{\mathrm{HP1}}(s)$	F*	✓
D10	5.53	5.53	5.53	$0.5H_{\mathrm{HP1}}(s)$	$H_{\mathrm{HP1}}(s)$	F*	✓
D11	5.53	5.53	5.53	$0.5H_{\mathrm{HP2}}(s)$	$H_{\mathrm{HP1}}(s)$	F*	✓
D12	5.53	5.53	5.53	$H_{\mathrm{HP1}}(s)$	-0.2	F*	✓

Table 4.5: Experimental conditions for each trial with full motion

	Forcing function amplitudes			Motion filters			
Trial	W_t (m*)	W_v (m/s*)	W_ω (rad/s*)	$H_{\mathrm{m}a}(s)$	$H_{\mathrm{m}\omega}(s)$	**Vehicle**	**Preview**
A1	1.58	0	0	1	1	F	✗
A2	1.58	0	0	1	1	F	✓
A3	0	1.58	0	1	1	F	**0**
A4	0	0	1.58	1	1	F	**0**
A5	0	1.11	1.11	1	1	F	**0**
A6	0.79	0.79	0.79	1	1	F	✗
A7	0.79	0.79	0.79	1	1	F	✓
A8	1.58	0	0	1	1	S	✗
A9	1.58	0	0	1	1	S	✓
A10	0	1.58	0	1	1	S	**0**
A11	0	0	1.58	1	1	S	**0**
A12	0	1.11	1.11	1	1	S	**0**
A13	1.11	1.11	1.11	1	1	S	✗
A14	1.11	1.11	1.11	1	1	S	✓

as those who completed the full motion experiment in Chapter 3. Within each experiment the order of the trials was randomised.

As well as collecting quantitative data such as the steering angle and vehicle motion, in the scaled motion experiment with preview and the filtered motion experiment the drivers were asked for subjective feedback about each trial. The drivers were asked to rate from -5 to 5 how useful the physical motion was in controlling the vehicle (i.e. 0 neutral, 5 very useful and -5 very distracting). They were also encouraged to give comments on what they perceived, their choice of control strategy and how well they felt able to adapt to the sensory conflict and control the vehicle.

In Chapter 3 the identification procedure was run for each of the drivers separately to investigate any differences between the steering control strategies of drivers with different levels of experience. In addition, the time domain steering signals were averaged over the five drivers to give a set of average responses for each trial, reducing the amount of noise in the measurements. Differences between the drivers were found to be small, and the parameters identified for the averaged data were all within the range of those identified for the individual drivers. Therefore in this chapter the analysis was carried out for the averaged results only.

4.4 Parameter identification

The identification procedure described in Section 3.4 is used to identify parameter values for the scaled and filtered motion trials. The fit of each of the model variations described in Section 4.2.2 is optimised to test which definition of the driver's internal model best represents the measured steering behaviour of real drivers.

Some of the parameter values are fixed during the identification procedure using the results from Chapter 3. The target shift T_t is set to zero for all trials without preview or using the fast vehicle, which covers all of the trials in the new experiments. The process noise W is found in Chapter 3 to depend linearly on the RMS steering angle δ. Therefore a constant signal-to-noise ratio SNR_W is defined, where:

$$\mathrm{SNR}_W = \frac{\mathrm{RMS}(\delta)}{W} \tag{4.6}$$

Based on the results from Chapter 3, SNR_W is set to 0.57.

The identification procedure is run for each trial to find the ten remaining parameter values: Steering cost q_δ, vestibular measurement noise V_a and V_ω, visual measurement noise σ_ϕ and V_e, time delays τ_vi and τ_ve, preview time T_p and neuromuscular parameters ω_nm and ζ_nm. For models M3 and M0, when the lateral or yaw scaling is zero the

corresponding noise values V_a and V_ω do not affect the simulated steering behaviour. Furthermore, when both scaling factors are zero the vestibular delay τ_{ve} does not affect the simulated steering behaviour, and for trials without preview T_{p} also does not affect the simulated steering behaviour, as explained in Section 4.2.1. This reduces the number of parameters that need to be identified for certain trials. For model M3 there are two additional parameters to identify: the internal model scaling factors $K'_{\text{m}a}$ and $K'_{\text{m}\omega}$.

When the driver is using both visual and vestibular information to work out the states of the vehicle it is difficult for the identification procedure to separate the responses to the two sets of sensory information. Therefore, parameter values are first identified for trials with no physical motion, and identified noise parameters for the visual system (V_e and σ_ϕ) are held constant while identifying the remaining parameter values for the other trials. As in Chapter 3, Box-Jenkins models are fitted to the results of each trial to give an upper bound on the agreement between a linear model and the experiment results, and to provide an estimate of the noise spectrum which is used to reduce bias in the identified parameter values.

4.5 Results

The results of the parameter identification procedure are presented and discussed in this section. Results are shown for each of the three new experiments in Sections 4.5.1 to 4.5.3. The identification procedure is also carried out once more for the full motion experiment, and these results are shown in Section 4.5.4.

4.5.1 Scaled motion without preview

The identification procedure is run first with the visual-only trials B4, B8 and B13. The visual noise amplitudes V_e and σ_ϕ are then held constant within each of the three sets of five trials (A6 & B1–B4, A13 & B5–B8, B9–B13) which used the same vehicle. The results rely on the assumption that the visual noise amplitudes are approximately constant within each set of five trials, which is reasonable as the trials within each set have the same vehicle parameters and forcing function amplitudes (except trial A6), so the characteristics of the visual motion perceived by the drivers should be similar within each set.

The agreement between the measured and predicted steering angles using the different variations of the driver model is quantified for each trial by calculating the variance accounted for (VAF) as defined in Equation 3.14. The results are shown in Figure 4.4. The highest VAF values are found for model M3, which is expected as all the other model variations are contained within the structure of model M3. Model M0 has the lowest VAF

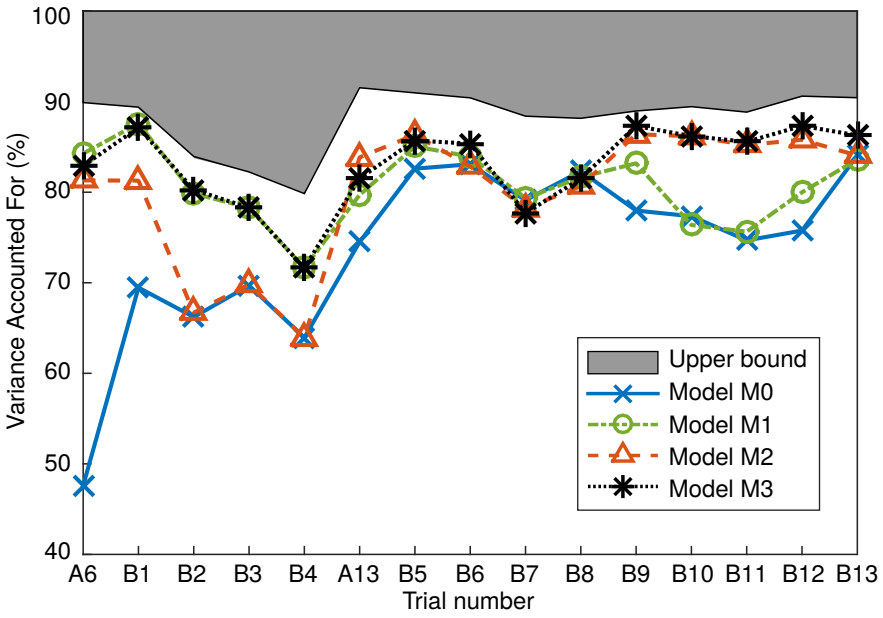

Figure 4.4: VAF values for trials with scaled motion, without preview. Results are presented for each model variation described in Section 4.2.2. The shaded area shows the upper bound given by the Box-Jenkins model.

values in all trials, showing that the drivers were making use of the physical motion to control the vehicle. For all trials one of models M1 and M2 fits the results almost as well as model M3, however the two models fit better for different trials. For trials A6 and B1–B4, which used the fast vehicle with small forcing functions, model M1 fits the best, indicating that the drivers were not aware of the scaling applied to the motion. For trials A13 and B5–B8, representing the slow vehicle with small forcing functions, models M1 and M2 both fit the results well. For trials B9-B13, which used the fast vehicle with large forcing functions, model M2 fits the results best, showing that with larger forcing functions the driver is able to estimate the correct motion scaling factors.

Identified measurement noise amplitudes for the trials carried out in this experiment are plotted against the corresponding RMS signal amplitudes in Figure 4.5. The noise amplitudes generally increase linearly with signal amplitude. This supports the hypothesis that measurement noise is signal-dependent, matching studies which found that sensory just-noticeable-difference (JND) values follow Weber's law [90, 130, 133, 139]. For the acceleration a and visual angles $\boldsymbol{\phi}$, very large noise amplitudes are identified for the lowest signal amplitudes. When the noise level is much larger than the signal, the driver places very little weight on that measurement. Therefore the results indicate that there are thresholds below which drivers are unable to perceive each sensory signal. This result is also found in previous studies of human sensory perception, as discussed in Section 2.4.

Two potential methods for modelling signal-dependent noise with thresholds are shown

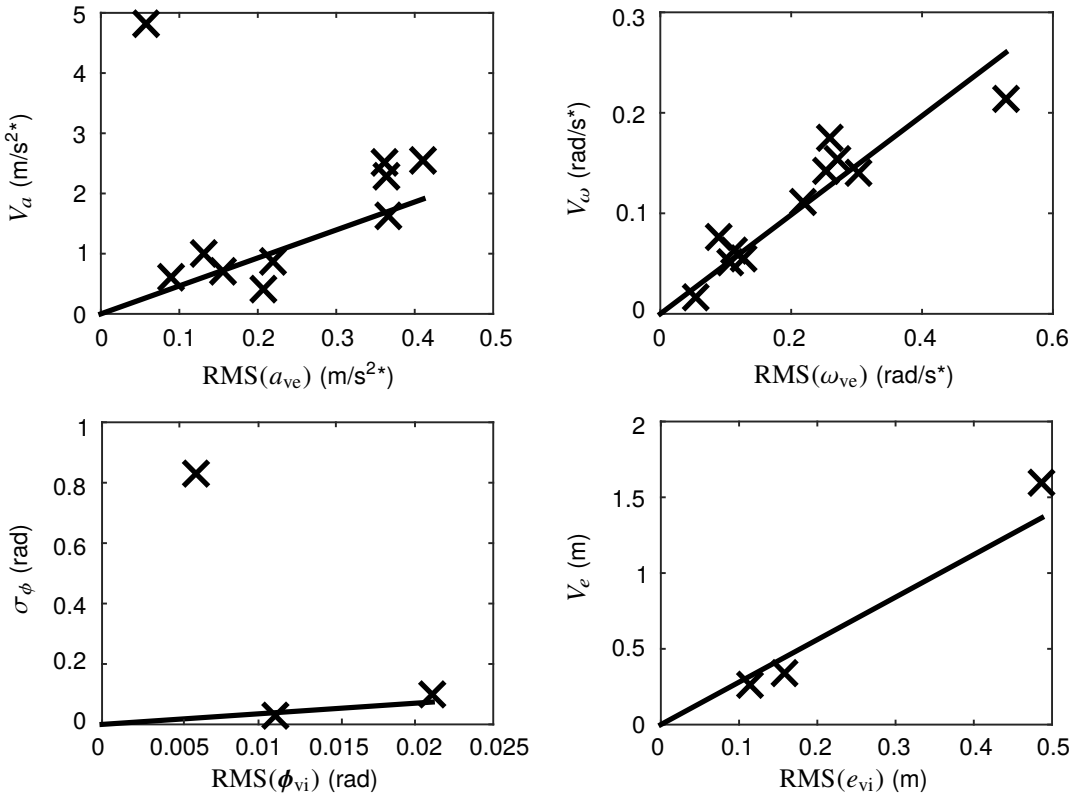

Figure 4.5: Identified measurement noise amplitudes vs. RMS signal amplitudes, using model M2. RMS values correspond to perceived signals, filtered by sensory transfer functions. Vestibular noise amplitudes V_a and V_ω are not plotted for trials with no translational or rotational motion. Visual noise amplitudes V_e and σ_ϕ are only plotted for the three no-motion trials. Trend lines ignore the high values at low amplitudes for V_a and V_e.

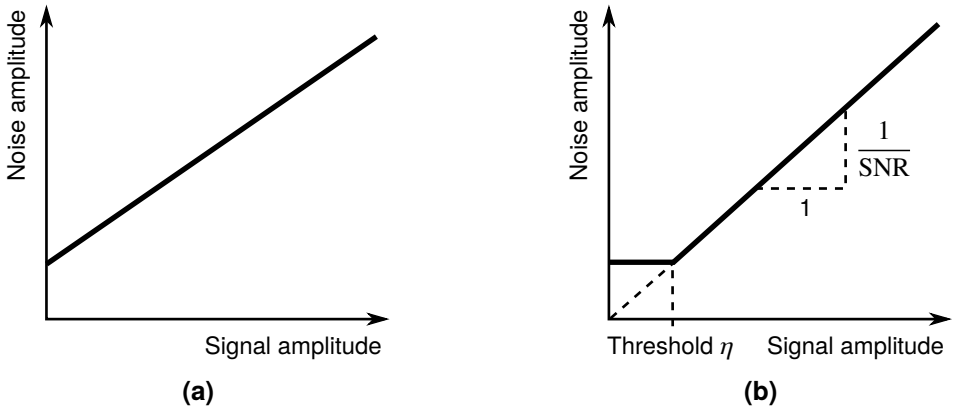

Figure 4.6: Two methods of modelling signal-dependent sensory noise. In (a) the threshold is represented by a non-zero y-intercept, in (b) the noise amplitude remains constant for low signal amplitudes.

in Figure 4.6. Previous studies have generally used the description shown in Figure 4.6a: a straight line with an intercept greater than zero on the noise axis to represent the sensory threshold [41]. An alternative description is shown in Figure 4.6b, where the noise amplitude is proportional to signal amplitude with zero intercept, but below the threshold level η the noise amplitude is constant. The results shown in Figure 4.5 support the description shown in Figure 4.6b, as the plotted points generally fit closely to straight lines passing through the origin. Although the identified noise magnitudes are much higher at low amplitudes in Figure 4.5, holding the noise amplitude constant as in Figure 4.6b will give similar results since the noise amplitude is still much larger than the signal amplitude. The noise characteristics of each sensory channel can therefore be described by a signal-to-noise ratio (SNR) and a threshold η, for example:

$$V_a = \begin{cases} \dfrac{\mathrm{RMS}(a_{\mathrm{ve}})}{\mathrm{SNR}_a} & \mathrm{RMS}(a_{\mathrm{ve}}) > \eta_a \\ \dfrac{\eta_a}{\mathrm{SNR}_a} & \mathrm{RMS}(a_{\mathrm{ve}}) < \eta_a \end{cases} \tag{4.7}$$

Similar relationships are defined for ω_{ve} and e_{vi}. Since the previewed target angles $\boldsymbol{\phi}_{\mathrm{vi}}$ are a vector of length N_{p} at each time step, the RMS value is taken over the whole vector:

$$\sigma_\phi = \begin{cases} \dfrac{\mathrm{RMS}(\boldsymbol{\phi}_{\mathrm{vi}})}{\mathrm{SNR}_\phi} & \mathrm{RMS}(\boldsymbol{\phi}_{\mathrm{vi}}) > \eta_\phi \\ \dfrac{\eta_\phi}{\mathrm{SNR}_\phi} & \mathrm{RMS}(\boldsymbol{\phi}_{\mathrm{vi}}) < \eta_\phi \end{cases} \tag{4.8}$$

Previous studies have modelled signal-dependent noise with an amplitude which varies over time depending on the instantaneous signal amplitude [41, 128]. However this approach makes the control and state estimation calculations significantly more complicated. It is reasonable to assume that the driver estimates constant noise amplitudes V based on the RMS signal amplitudes over a period of time, such as a single trial.

To investigate whether this signal-noise relationship can describe driver steering performance across a range of conditions, a single set of parameter values is identified to fit the results of all of the trials from this experiment. Model M2 is used as this gives the best fit to the results with the more realistic, larger forcing functions. SNRs are found from the reciprocals of the gradients of the trend lines shown in Figure 4.5. Thresholds are chosen to be the lowest RMS signal amplitude for which the identified noise magnitude isn't significantly above the trend line. For the angular velocity ω and path-following error e these values are simply the lowest signal amplitudes, as the trials did not have low enough signal amplitudes to fall below threshold levels. The remaining parameter values which are identified are: steering cost weight q_δ, visual and vestibular delays τ_{vi} and τ_{ve},

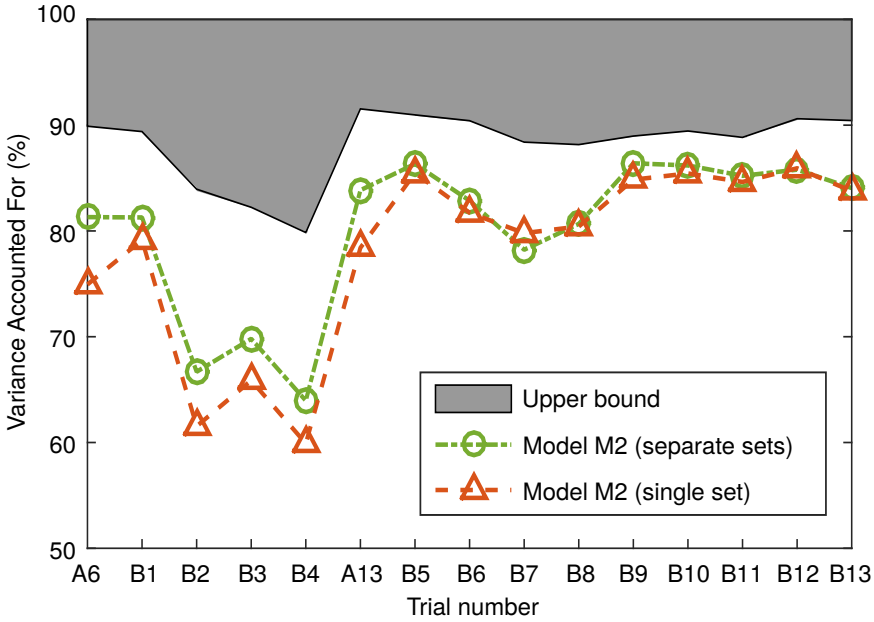

Figure 4.7: VAFs using a single parameter set identified to fit all trials, with scaled motion and without preview. VAFs are compared against values for separate parameter sets identified for each trial and an upper bound given by a Box-Jenkins model.

Table 4.6: Single set of parameter values for scaled motion trials without preview. Noise amplitudes are found from the signal-dependent relationship shown in Figure 4.5.

Parameter	q_δ (A6 and B1–B4)	q_δ (A13 and B5–B8)	q_δ (B9–B13)	τ_{vi}	τ_{ve}	ω_{nm}	ζ_{nm}
Units	$\text{rad}^{-2}\star$	$\text{rad}^{-2}\star$	$\text{rad}^{-2}\star$	s	s	rad/s	–
Value	0.0478	0.0356	0.210	0.20	0.22	16.6	0.224

and neuromuscular frequency ω_{nm} and damping ζ_{nm}. Three values of q_δ are identified, one for the fast vehicle with small forcing functions (trials A6 and B1–B4), one for the slow vehicle (trials A13 and B5–B8) and one for the fast vehicle with large forcing functions (trials B9-B13).

The resulting VAFs for each trial using the optimised single parameter set are compared against the Box-Jenkins upper bound and the separate parameter sets found for each trial in Figure 4.7. The single parameter set fits the results very well, almost as well as the separate parameter sets. This shows that the signal-dependent description of the driver's sensory noise levels allows the model to predict variations in control behaviour with different signal amplitudes. The results do not fit quite as well for the first five trials (the fast vehicle with small forcing functions), which may be related to the poor fit of model M2 under these conditions. The parameter values identified to fit all of the trials from this experiment are given in Table 4.6.

4.5.2 Scaled motion with preview

For the scaled motion experiment with preview, delays τ_{vi} and τ_{ve} are fixed at the values given in Table 4.6. Delays are more difficult to identify for the preview trials since the driver can use previewed information to plan steering actions in advance, as seen in Chapter 3. Parameter values are first identified for the trial with no physical motion (C1) and the visual noise amplitudes are fixed at the identified values when running the identification procedure across the remaining trials. For this experiment the preview time T_p is also allowed to vary between 0 and 2 s.

The resulting VAFs for each variation of the driver model are shown in Figure 4.8. In contrast to the results without preview, model M1 is the worst fit across all trials. Model M2 in general fits very well, with the VAFs almost the same as model M3. For some of the trials model M0 fits as well as model M2, in particular for the last four trials where there was negative scaling. This indicates that the drivers ignored the physical motion in these trials and controlled the vehicle mainly using visual measurements. This agrees with studies which have found that humans sometimes 'veto' sensory information which does not fit with other measurements [196, 200]. The VAFs are lower for the last four trials in general, which may be because the drivers were not able to make optimal use of such counter-intuitive physical motion.

The difference in VAFs between models M2 and M0 can be used as a measure of the

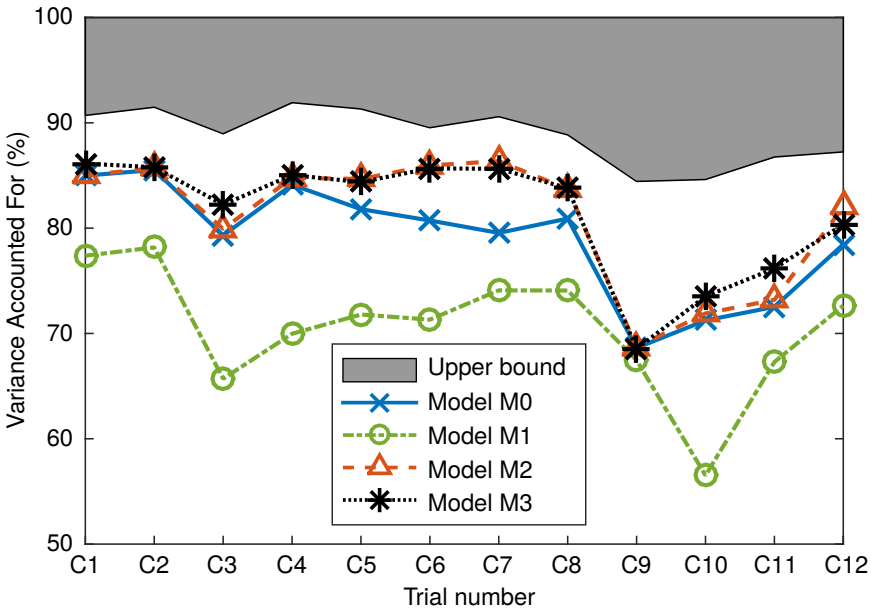

Figure 4.8: VAF values for trials with scaled motion, with preview. Results are presented for each model variation described in Section 4.2.2. The shaded area shows the upper bound given by the Box-Jenkins model.

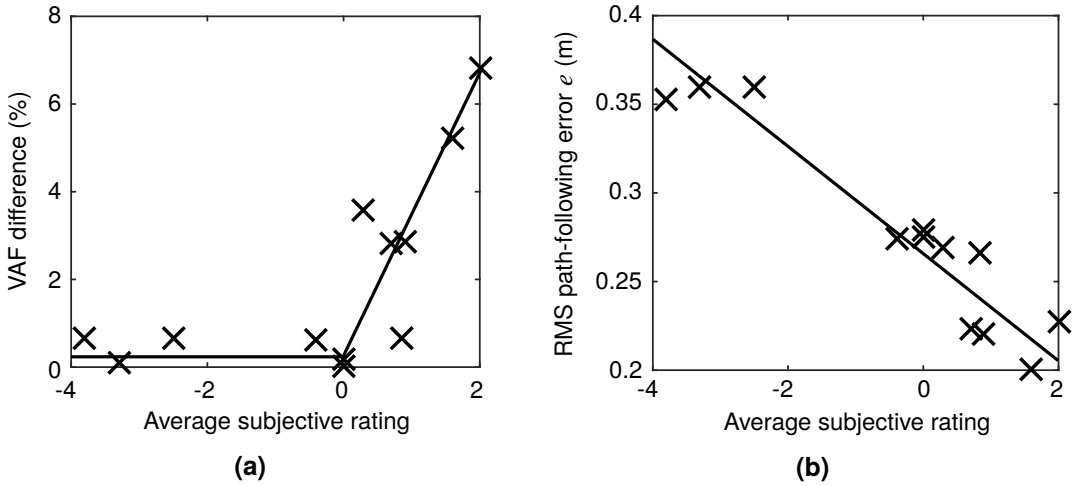

Figure 4.9: Correlation between metrics for scaled motion experiment with preview: RMS path-following error; difference in VAF values between models M2 and M0; and average driver subjective ratings.

extent to which drivers used the physical motion in a given trial. The difference should not be less than zero, as a similar control strategy to model M0 can always be achieved for model M2 by having large vestibular noise amplitudes. Another useful metric is the driver's success in tracking the line in each of the trials, which can be measured by finding the RMS path-following error $e = (f_t - y)$. The drivers were also asked to give subjective ratings of the extent to which the physical motion was helpful for the task. The ratings were given on a scale of -5 to 5, with positive values meaning the physical motion was helpful and negative values meaning the physical motion was unhelpful. The VAF difference, RMS path-following error and driver subjective ratings are compared in Figure 4.9. There is a clear correlation between the three metrics. Figure 4.9a shows that the higher the drivers rated the physical motion, the more they used their vestibular measurements to control the vehicle. For unhelpful physical motion (rated below zero) the drivers appear to have 'vetoed' the physical motion and focussed on visual measurements only. Figure 4.9b shows that the subjective ratings also correlate with path-following error, with drivers able to follow the target more closely for physical motion which was rated as more useful.

4.5.3 Filtered motion

For the third experiment the time delays are once again fixed at the values given in Table 4.6. Parameter values are first identified for the zero-motion trial (D1) and the visual noise amplitudes are then fixed when identifying parameter values for the remaining trials. The identification procedure is run for model variations M0, M2, M3 and M4. Model M1 is not used due to the poor performance seen in the scaled motion trials with preview.

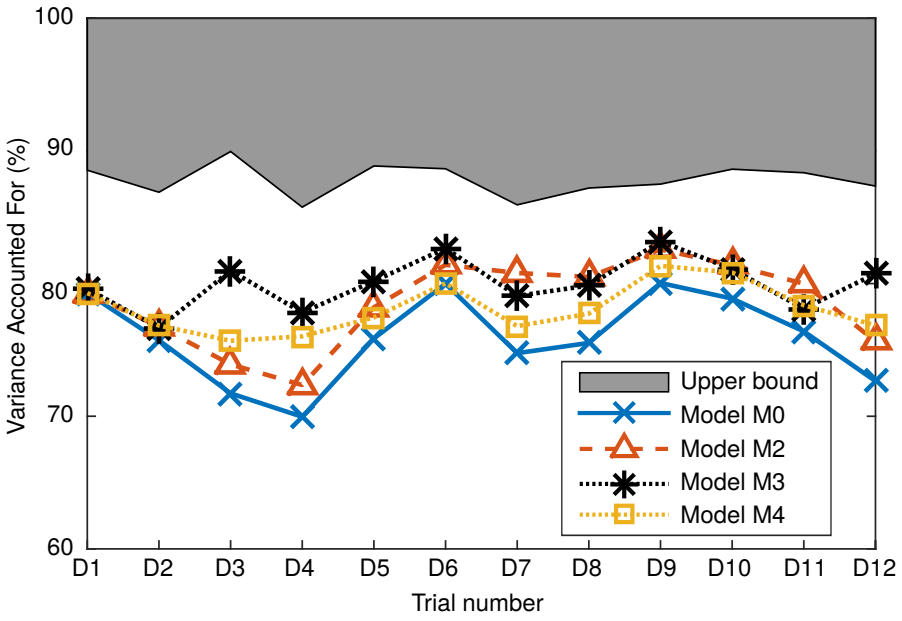

Figure 4.10: VAF values for trials with filtered motion. Results are presented for each model variation described in Section 4.2.2. The shaded area shows the upper bound given by the Box-Jenkins model.

The resulting VAFs are shown in Figure 4.10. Compared to the other experiments there is less variation in VAF values between the trials, and also less variation between models. Model M3 is always close to the best-fitting model. In contrast to the other experiments, model M3 does not contain all other model variations as it assumes the motion is scaled rather than filtered. The fact that model M3 still fits well could indicate that the driver cannot determine the complexities of a motion filter and instead assumes the motion is scaled. However, model M2 performs similarly in trials D1, D2 and D6–D12. There is not enough difference between the simulated control strategies in these trials to determine the extent to which the driver is aware of the filtering. It should be noted that model M3 has more scope to adapt to fit the measured results due to the two extra parameters $K'_{\mathrm{m}a}$ and $K'_{\mathrm{m}\omega}$, so the high VAF may be a result of over-fitting.

Model M3 does have a significantly larger VAF than model M2 in trials D3 and D4. These are trials where the yaw motion was at full scale, so would have been very large in comparison to the lateral motion. It is possible that the full-scale yaw motion dominated the drivers' perception, and they were not able to pay enough attention to the lateral motion to determine the motion filters, instead assuming the motion was scaled. Model M4 also has higher VAFs than model M2 in trials D3 and D4, however model M2 fits better than M4 for trials D6–D9. The results do not conclusively show the extent to which drivers can compensate for complicated filter dynamics, since there is no clear pattern to which of models M2 and M4 fits the results best.

Model M0 is always the worst-fitting of the models. This indicates that the driver is making use of the physical motion perceived through their vestibular organs. The only trials where the other models do not fit better than model M0 are trials D1, where there was no physical motion, and D2, where the motion was scaled rather than filtered. It is therefore evident that drivers are able to use filtered physical motion to inform their steering control strategy. General comparison of the VAF values shown in Figure 4.10 with the values found for the scaled motion trials in the previous experiments (shown in Figures 4.4 and 4.8) shows that the VAF values are around 5% lower on average for the filtered motion trials. This shows that the drivers did not match the modelled optimal controller as well in this experiment. This may be because the complexity of the motion filters made it more difficult for the drivers to build up an accurate internal model. It is interesting that trials D1 and D2 have lower VAF values than the equivalent trials C1 and C5 with the same conditions. Because the trial order was randomised in each experiment, exposure to trials with filtered motion could have affected the drivers' confidence in their internal models even for trials with scaled motion.

4.5.4 Full motion

The identification procedure is run once again for the trials from the full motion experiment described in Chapter 3, to check whether the results change with the updated model of the visual system and to compare the fit of the different model variations. Since there are no trials without physical motion and the forcing function amplitudes varied across the trials, the visual noise amplitudes are identified separately for each trial. The identification procedure is run for the trials without preview initially, then the time delays are fixed at the values given in Table 4.6) while parameter values are identified for the trials with preview.

The resulting VAF values are shown in Figure 4.11. Results for models M1 and M2 are identical, since the trials all had scaling factors of 1. The results for model M3 are no better than models M1 and M2, showing that the drivers were aware that the motion was not scaled. Model M0 fits as well as the other models for trials A1–A4 and A8–A11 which had one forcing function at a time, indicating that the drivers did not use the physical motion much for these trials. However for trials A5 and A12, where there were disturbances on both v and ω, model M0 fits slightly worse than the others. This shows that the physical motion is useful for determining the difference between v and ω disturbances, which is the same conclusion that was drawn in Chapter 3 when looking at identified sensory noise anplitudes. Model M0 fits much worse in trials A6–A7 and A12–A14, so with both target and disturbance forcing functions the physical motion is very useful to the drivers.

The VAFs for model M2 are very close to the upper bound given by the Box-Jenkins

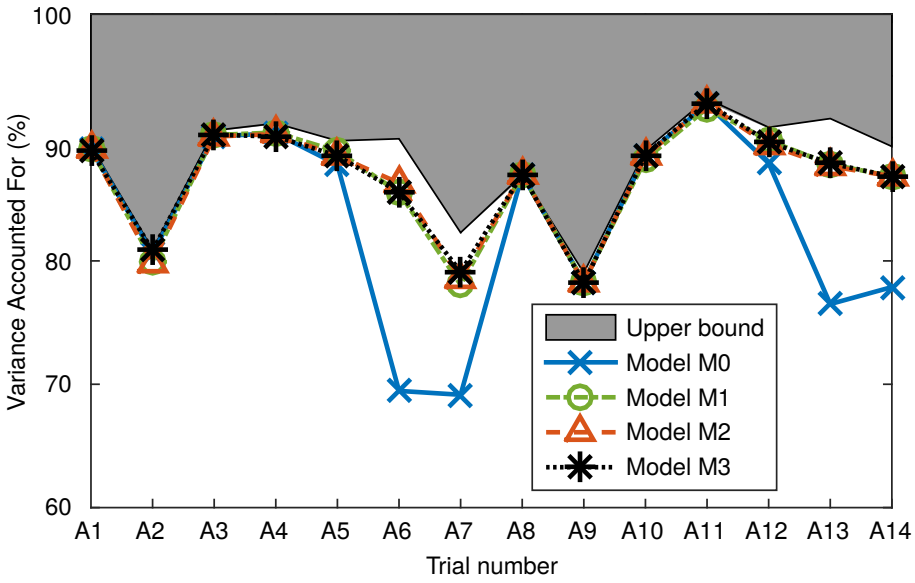

Figure 4.11: VAF values for trials with full motion. Results are presented for each model variation described in Section 4.2.2. The shaded area shows the upper bound given by the Box-Jenkins model.

model. They are slightly higher than the values found in Chapter 3 (shown in Figure 3.10), showing that the adjusted model of the visual system describes measured steering behaviour more effectively. The VAFs are closest to the Box-Jenkins upper bound for trials with only one forcing function (A1–A4 and A8–A11), but not quite as close for trials involving a combined target-following and disturbance-rejection task. This shows that increasing the complexity of the task reduces drivers' ability to perform it in an optimal manner.

4.5.5 Noise parameters and subjective ratings

In Section 4.5.1 identified sensory noise amplitudes are found to depend linearly on RMS stimulus amplitude for scaled motion trials without preview, as shown in Figure 4.5. Sensory noise amplitudes are plotted against RMS signal amplitudes for all of the trials in Figure 4.12. The results for the scaled motion trials with preview also fit the signal-dependent noise model, with SNRs generally similar to those seen for the trials without preview. However, SNR_ϕ is much larger for trials with preview, which may be because different information is measured in the two cases; without preview the driver only measures the vehicle yaw angle whereas with preview they also measure target path angles.

Identified noise amplitudes for the filtered motion trials also generally fit the signal-dependent relationship, although the identified values of V_a are sometimes much larger than expected, indicating that the drivers did not use acceleration measurements as much in certain trials. This could be a result of the yaw motion dominating the vestibular

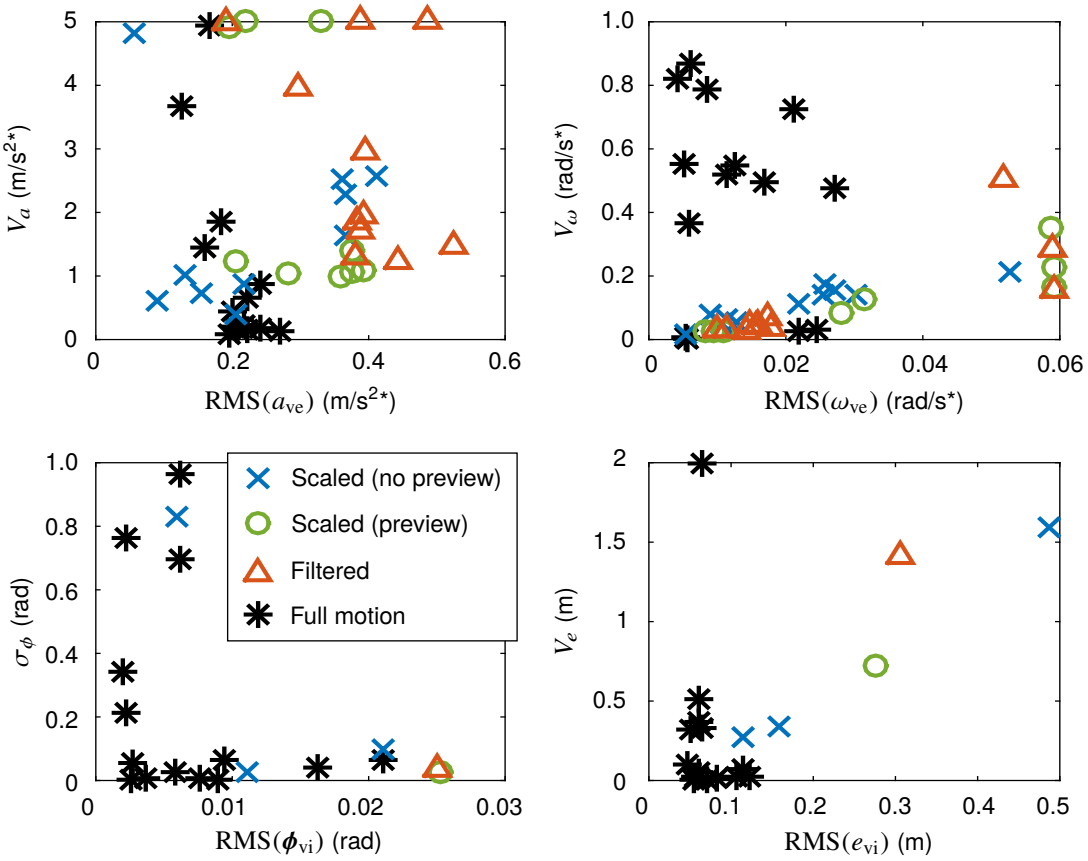

Figure 4.12: Noise vs. signal amplitudes for trials from all four experiments, using model variation M2.

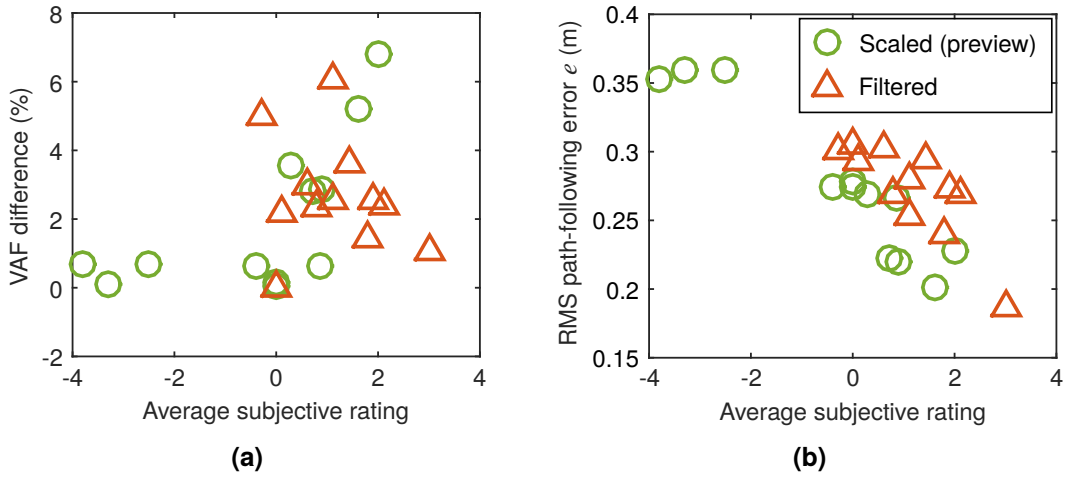

Figure 4.13: Correlation between three metrics for two experiments: scaled motion with preview and filtered motion. Metrics are RMS tracking error, difference in VAF values between models M2 and M0, and average driver subjective ratings.

measurements, as discussed in Section 4.5.3. There is no clear correlation between RMS signal amplitudes and sensory noise amplitudes for the full motion trials. For the other experiments trials without physical motion can be used to investigate the visual system in isolation, allowing the separate roles of the visual and vestibular systems to be studied. This is not possible for the full motion trials, resulting in unreliable estimates of the sensory noise amplitudes as shown in Figure 4.12.

In Section 4.5.2 a correlation is found between driver subjective ratings, path-following error and the VAF difference between models M2 and M0, shown in Figure 4.9. Subjective ratings were not collected for the full motion or scaled motion without preview experiments, however results for the scaled motion with preview and filtered motion experiments are plotted in Figure 4.13. Figure 4.13b shows that in both experiments the drivers' performance correlated with their subjective ratings, with drivers able to follow the target line more closely for more highly rated motion conditions. However the correlation between subjective ratings and VAF difference is not seen for the filtered motion trials in Figure 4.13b. This could be because the added complexity of the motion filters made it more difficult for the drivers to evaluate the motion conditions effectively compared to the scaled motion trials.

4.6 Single set of parameter values

In total, 51 trials were carried out across four experiments to investigate the role of sensory dynamics in a driver's control of a vehicle. The new driver model aims to replicate the processes carried out by the driver in order to predict steering control behaviour over a range of conditions. For the model to have predictive ability it is necessary to find a fixed set of parameters to fit the results from all the experiments as closely as possible. The four trials with negative scaling are excluded, since the drivers were found to veto the vestibular information under these unnatural conditions. Parameter values are identified for model M2, which is shown in Sections 4.5.1 to 4.5.4 to give the best overall fit to measured results, and model M0, to compare the agreement of a model which does not use vestibular measurements.

4.6.1 Identification procedure

In Section 4.5.1, sensory noise amplitudes are found to depend linearly on stimulus amplitudes, with thresholds below which the noise amplitudes remain constant. The noise characteristics for each sensory channel are therefore described by a signal-to-noise ratio (SNR) and a threshold η. The driver model depends on 16 variable parameters:

- Steering cost weight: q_δ
- Sensory SNRs: SNR_a, SNR_ω, SNR_ϕ, SNR_e
- Process noise SNR: SNR_W
- Sensory thresholds: η_a, η_ω, η_ϕ, η_e
- Visual and vestibular delays: τ_{vi}, τ_{ve}
- Neuromuscular frequency and damping: ω_{nm}, ζ_{nm}
- Preview time: T_{p}
- Target shift: T_{t} (see Chapter 3, only used for slow vehicle with preview)

In addition, separate values of SNR_ϕ are identified for the trials with preview ($\text{SNR}_{\phi\text{p}}$) and the trials without preview ($\text{SNR}_{\phi\text{NP}}$), as σ_ϕ is found in Section 4.5.2 to be much larger for trials with preview. The same threshold η_ϕ is used for both cases.

To reduce the risk of over-fitting and find more reliable parameter estimates, the procedure is carried out in several steps which minimise the number of parameters identified at any one time. The steering cost weight q_δ is a choice of the driver rather than a physical parameter, and is found to vary significantly between trials. Separate values of q_δ are therefore found for each trial using an initial estimate of the other parameter values, and these values of q_δ are then held constant throughout the remaining identification procedure. The initial estimate is formed from the parameters found to fit the scaled motion trials without preview in Section 4.5.1, plus values of $T_{\text{t}} = -0.55$ s (from Chapter 3), $T_{\text{p}} = 1$ s (from the values identified for previous trials) and $\text{SNR}_\phi = 0.841$ for the preview trials (the average of the scaled and filtered motion results). As explained in Chapter 3, the noise amplitudes in the model can be used to estimate the amount of driver noise measured in the steering angle, which can be compared to the modelling error to check the noise parameters are sensible. The process noise SNR (SNR_W) is therefore held constant during the parameter identification procedure, after which the predicted and measured noise amplitudes are compared. SNR_W is then adjusted and the identification procedure is repeated iteratively until the predicted and measured noise amplitudes are similar.

The number of parameters identified at one time can be reduced further by running the procedure for carefully chosen subsets of the trials before optimising across all trials. Firstly, parameter values are identified for trials with no physical motion, so that parameters V_a, V_ω, η_a, η_ω, τ_{ve} and T_{t} are not needed. The preview time T_{p} is fixed at a value of 1 s. Identifying parameters for the trials with no physical motion allows the visual system to be studied in isolation, giving more reliable estimates of the visual noise amplitudes. Therefore, values of SNR_e, SNR_ϕ, η_e and η_ϕ identified for the trials with no motion are held constant over the rest of the procedure. Next, parameter values are identified for all the trials without preview, so that T_{p} and T_{t} are not needed. These trials allow the delays τ_{vi} and

τ_{ve} to be estimated more reliably, as the driver cannot use preview to compensate for delays in their visual system. Therefore the values of τ_{vi} and τ_{ve} are fixed while the remaining eight parameters are optimised to fit all of the trials. Finally, all of the parameters except for SNR_W, T_p, T_t, τ_{vi} and τ_{ve} are optimised to fit the results of all the trials, using Matlab's *fmincon* function and starting from the values identified in the previous stage.

4.6.2 Results

The resulting VAF values using the identified parameter sets are plotted in Figure 4.14. The VAFs for model M0 are lower than for model M2 for all trials except those with negative motion scaling. This highlights the importance of considering vestibular measurements when modelling driver steering behaviour. For model M2, the fit is worse for the single parameter set than for the separate parameter sets, as expected. However, in general the model fits well, with an average VAF across all trials of 76%. The model does not fit as well for trials C9–C11 and C2–B4, which are also the worst-fitting trials using separate parameter sets. In general the model fits better for trials with scaled motion than with filtered or full motion. This could be because the full motion trials had unrealistically small forcing functions, and in the filtered motion trials the drivers were not able to build up accurate internal models of the motion filtering.

In addition to generating a noise-free steering angle prediction, the model can also estimate the amplitude of driver noise referred to the steering angle. This estimate can be

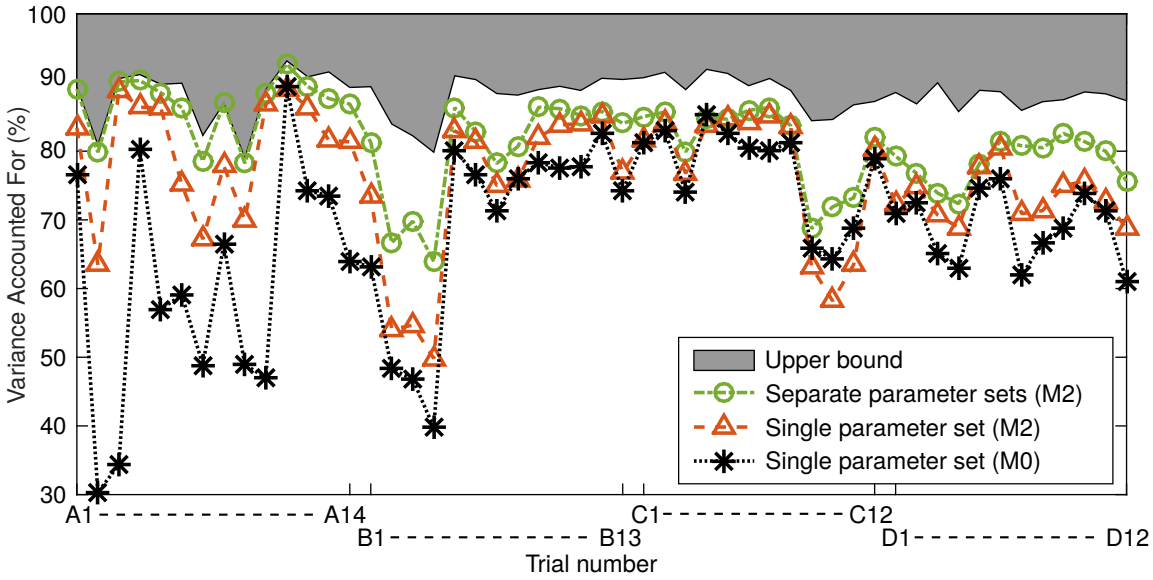

Figure 4.14: VAF values for all trials using a single set of parameter values, compared with VAFs for parameters found individually for each trial and the Box-Jenkins upper bound.

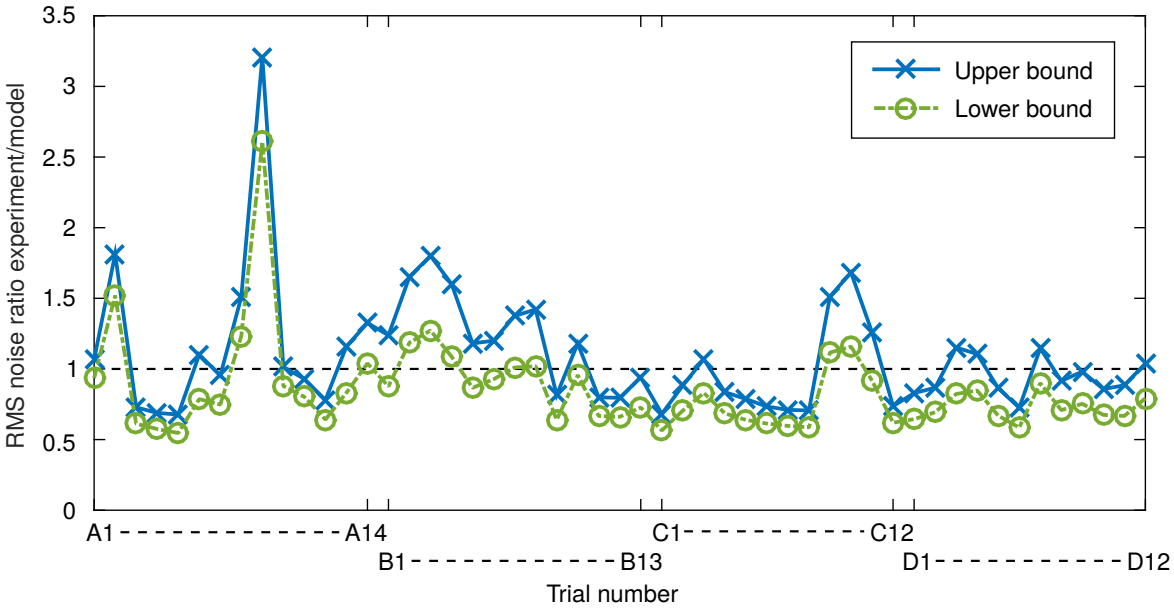

Figure 4.15: Bounds for ratio of measured to predicted noise amplitude. Predicted noise amplitude is defined by the identified single set of parameter values, measured noise amplitude is defined as $\mathrm{RMS}(\delta_{\mathrm{sim}} - \delta_{\mathrm{exp}})$ for the upper bound and $\mathrm{RMS}(\delta_{\mathrm{BJ}} - \delta_{\mathrm{exp}})$ for the lower bound.

compared with the measured noise level to check that the noise parameters give physically realistic values. The measured noise is estimated by finding the difference between the measured and modelled steering angle ($\delta_{\mathrm{sim}} - \delta_{\mathrm{exp}}$), however if the modelling error is significant this may give an overestimate. An alternative method is to find the difference between the measured steering behaviour and the Box-Jenkins prediction ($\delta_{\mathrm{BJ}} - \delta_{\mathrm{exp}}$), however this gives an underestimate since the Box-Jenkins model fits the results better than the parametric driver model. Nonlinear driver behaviour is assumed to be negligible. Using both methods to give upper and lower bounds, the ratios between the measured and predicted noise levels for model M2 are plotted in Figure 4.15. The upper and lower bounds are close together, giving an accurate estimate of the noise level in the experiments. On average the ratio is close to 1, showing that the noise parameters in the model are realistic, although the model underestimates the amount of noise in the target-only trials with preview (A2 and A9).

The values of the identified parameters are given in Table 4.7. The time delays and neuromuscular parameters are similar to the values found in Chapter 3, however SNR_W is larger and the magnitude of the target shift T_{t} is smaller. The noise parameters are compared with estimates from the literature in Section 4.7. These parameters can be used to simulate driver steering control under a variety of conditions and, supported by the VAF values shown in Figure 4.14, they should be able to give a good approximation to measured control behaviour.

Table 4.7: Single set of parameters identified to fit the results of all trials carried out across all four experiments. Model variation M2 is used for all trials.

Parameter	SNR_a	SNR_ω	$\mathrm{SNR}_{\phi\mathrm{p}}$	$\mathrm{SNR}_{\phi\mathrm{NP}}$	SNR_e	SNR_W	τ_{vi}	τ_{ve}
Units	–	–	–	–	–	–	s	s
Value	0.390	0.406	1.46	0.415	0.901	2.28	0.19	0.23
Parameter	T_{t}	T_{p}	ω_{nm}	ζ_{nm}	η_a	η_ω	η_ϕ	η_e
Units	s	s	rad/s	–	$\mathrm{m/s^2}$*	rad/s*	rad	m
Value	-0.26	0.87	14.3	0.537	0.221	0.0235	0.0129	0.0559

4.7 Discussion

A series of experiments was carried out to determine how drivers steer when the motion of the vehicle sensed through their vestibular organs doesn't directly match what they see with their visual system. The driver steering control model derived in Chapter 3, with an updated model of the visual system discussed in Section 4.2.1, can be used to predict the observed steering behaviour. Several variations of the model are defined in Section 4.2.2, based on different assumptions about the driver's internal model of motion scaling or filtering. Parameter values are identified for each model variation to give the best possible fit to measured results, as discussed in Section 4.4. In general model variation M2 fits the measurements best, showing that drivers are generally able to develop an internal model of the scaling or filtering applied to the motion, and adapt their control strategy to make optimal use of this knowledge. For trials carried out using the fast vehicle with scaled motion, no preview and small forcing functions, model M1 fits better, indicating that drivers may not be aware of any motion scaling when the forcing functions are small. In some trials model M0 fitted as well as the other models, showing that the drivers were not making significant use of the physical motion perceived through their vestibular organs.

The difference in VAF values between models M2 and M0 can be used to quantify the extent to which drivers use their vestibular measurements. In Section 4.5.2 a correlation is found between this measure, the average subjective ratings given by the drivers for how useful the physical motion was in controlling the vehicle, and the RMS path-following error which measures how closely the drivers followed the target. Drivers used higher rated physical motion more, ignoring or 'vetoing' physical motion which they considered to be unhelpful. They also achieved a better tracking performance for physical motion which they rated more highly. These results show that it is important for the driver to be subjected to realistic physical motion to achieve their best driving performance, and this has important implications for experiments carried out in driving simulators. The fact that

the results of the model correlate with both the opinions and performance of the drivers is encouraging, as it shows that the model is a reasonable description of how vehicle motion is perceived by drivers in reality. It also shows that the model may be used to give a quantitative estimate of how useful the physical motion is to the driver, without having to rely on subjective feedback.

In Chapter 3 the process noise amplitude W is found to be linearly dependent on RMS steering angle. In Section 4.5.1 this signal-dependence is also seen for the measurement noise, with a threshold below which the noise amplitude remains constant. This is similar to sensory threshold measurements from the literature, summarised in Chapter 2. Studies have measured thresholds below which motion cannot be perceived, and this has been linked to noise in the sensory systems by Soyka et al. [68, 69]. Just-noticeable difference (JND) values have also been found to increase linearly with stimulus amplitude, following Weber's law [90, 130, 133, 139]. Using this linear relationship between stimulus and noise amplitudes, a single set of parameter values is identified in Section 4.6 to fit the results of all 51 trials carried out over four experiments. The steering angles simulated using the single parameter set fit the measured results well, with VAFs of 76% on average. The driver model can therefore be used with these parameter values to predict driver steering behaviour under various conditions.

The values of the identified parameters can be compared with results from the literature to investigate whether they are compatible with studies of human sensory systems, summarised in Chapter 2. There is some disagreement in the literature as to whether vestibular or visual delays are longer, however the identified delay values of $\tau_{\text{vi}} = 0.19\ s$ and $\tau_{\text{ve}} = 0.23\ s$ indicate that the vestibular delay is slightly longer. This result supports studies which suggest that vestibular processing takes longer than visual processing [119–121]. The identified preview time T_{p} is 0.87 s, which is slightly shorter than the 1 s measured in eye-tracking studies [6, 71, 79, 80, 82]. It is similar to the value found in Chapter 3, where it was thought that the shorter preview time might be a result of the small forcing functions. However in this chapter it has also been found to fit well for trials with larger forcing functions. This shortened preview horizon may compensate for the fact that the noise on the previewed angles is constant, whereas in reality the uncertainty of visual measurements is likely to increase with distance ahead of the driver.

The identified sensory noise thresholds can be compared against values from the literature, discussed in Chapter 2. Sensory thresholds summarised in Table 2.3 can be converted to η values by multiplying by the identified SNRs, using Equation 4.7. Identified sensory noise parameters are compared with values found from the literature in Table 4.8. The identified thresholds are in general much larger than the values found from the literature. This could be for several reasons. Firstly, the values from the literature were

Table 4.8: Comparison of identified sensory thresholds with values from literature. Literature values are noise values summarised in Table 2.3 multiplied by SNRs given in Table 4.7. Visual noise values have been converted from velocities to displacements.

Parameter	η_a	η_ω	η_ϕ (no preview)	η_ϕ (preview)	η_e
Units	m/s^{2}*	rad/s*	rad	rad	m
Identified	0.221	0.0235	0.0129	0.0129	0.0559
Literature	0.015	0.0093	0.0005	–	0.0360

calculated from threshold measurements taken in passive conditions, focussing on one stimulus at a time. Studies have found that thresholds increase during an active control task and when multiple stimuli are presented together [137, 141–145, 147, 148]. Secondly, the identified noise parameters correspond to the noise added to each sensory signal, however by integrating the information perceived over time humans can develop more accurate sensory estimates. Taking account of these effects, the identified threshold values are reasonable in comparison with knowledge of sensory systems from the literature.

The new driver model is found to fit experimental data well over a range of conditions with a fixed set of parameter values. However, the model does not fit as well when sensory conflicts are large, for example trials C9–C12 with negative scaling. This indicates that distracting physical motion may lead to sub-optimal control strategies from the driver. The driver model also does not fit as well when the motion is filtered instead of scaled, which may be a result of discrepancies between the driver's internal model and the true motion filters. Further research is necessary to understand and quantify how errors in the driver's internal model affect their steering control actions.

4.8 Conclusion

The driver model presented in Chapter 3 has been extended to investigate the effects of conflicts between the motion perceived by a driver's visual and vestibular systems. This model is tested using experiments carried out by five drivers in a moving-base simulator. In general, drivers are found to develop an internal model of the motion scaling or filtering, and adjust their control actions accordingly. Drivers are able to do so more effectively with scaled motion than with filtered motion, indicating that their ability to compensate for motion filtering depends on the filter's complexity. With large discrepancies between the perceived physical and visual motion such as negative scaling, drivers 'veto' the physical motion and rely solely on visual measurements.

Drivers were found to make greater use of physical motion which they gave a higher

subjective rating, and this allowed them to achieve a better path-following performance. This highlights the importance of physical motion perception in allowing drivers to perform at their best, and must be considered carefully when designing experiments in a driving simulator. Sensory measurement noise is signal-dependent, with thresholds below which the noise magnitudes are constant. A single set of parameters has been found for the driver model which fits experimental results well overall across all 51 trials carried out over 4 experiments, with variance accounted for (VAF) values of 76% on average. These parameters also give estimated noise magnitudes which match the values measured in the experiments well. The driver model can be used with these parameter values to predict driver steering control behaviour over a wide range of conditions.

Chapter 5

Transient target and disturbance signals

A new model of driver steering control behaviour which incorporates the driver's sensory dynamics is developed in Chapters 3 and 4. The model is based around an optimal controller with filtered white noise target and disturbance forcing functions. However, during real driving targets often consist of combinations of regular shapes, and disturbances can include transient events such as impulses. The driver model is therefore updated to account for transient targets and disturbances, and the predictions of the model are compared with measurements of real drivers' responses to transient forcing functions. Simulator motion scaling and filtering is found to have a significant effect on drivers' responses, with more realistic physical motion resulting in faster reaction times and more successful disturbance rejection. The new model fits measured results well, although drivers are unable to develop an accurate internal model of motion filters, perceiving phase distortions introduced by filtering as disturbances.

5.1 Introduction

A review of the literature presented in Chapter 2 demonstrates that there is a significant opportunity for applying current knowledge of human sensory perception to models of driver-vehicle interaction. A new driver model incorporating sensory dynamics is therefore developed in Chapter 3, and extended in Chapter 4 to account for conflicts between visual and vestibular measurements when driving in a simulator. Experiments were carried out by real drivers for comparison with the predictions of the new model. To match the assumptions made in the derivation of a linear quadratic Gaussian (LQG) control strategy, the target and disturbance forcing functions in these experiments were formed from filtered white noise. This is a reasonable representation of certain disturbances which may be encountered during driving such as aerodynamic nonlinearities, road surface irregularities and driver noise. However, in some situations disturbances may consist of distinct, transient events such as hitting a kerb or pothole or a sudden gust of wind.

While the random target paths used in Chapters 3 and 4 allow the driver's visual system to be studied, in reality target manoeuvres often consist of smooth, regular shapes such as straight lines and corners. Obstacle avoidance manoeuvres in emergency scenarios can also be considered as a transient target event similar to a lane change [220, 221].

To investigate the separate roles of the driver's visual and vestibular systems, an experiment was carried out in Chapter 4 with the physical simulator motion scaled or filtered relative to the motion of the virtual vehicle. This resulted in conflicts between the driver's visual and vestibular measurements. In general, drivers were found to develop an internal model of the motion scaling and filtering to compensate for the sensory conflicts when combining measurements from their different senses. However, they did so less successfully when the motion was filtered rather than scaled. Filtering the motion results in phase distortions and complicated motion discrepancies, and it is unclear whether drivers can separate these from the effects of disturbances on the vehicle.

Previous studies investigating combined target-following and disturbance-rejection performance of drivers or pilots have generally considered random disturbances with stationary statistical properties [9, 36], although a limited amount of research has been carried out with transient disturbances. Drop et al. [35] showed that a predictable target signal allows pilots to employ some feedforward control behaviour, even if the future path isn't explicitly displayed. During experiments with simulated step wind gusts drivers have been found to achieve lower reaction times [114] and better control performance [222] when physical as well as visual motion information is available. Cole [17] measured and modelled the response of a driver's neuromuscular system to step steering torques, and Tagesson and Cole [223] used this model to explain driver responses to destabilising steering torques caused by split-friction braking. However, there is a lack of research into the sensory perception of transient vehicle disturbances during driving.

The driver model is adjusted to account for transient target and disturbance forcing functions in Section 5.2. The procedure for a new experiment investigating the response of real drivers to transient forcing functions is presented in Section 5.3. A parametric identification procedure used to fit the adjusted driver model to data from the experiment is described in Section 5.4, and the results of this are presented in Section 5.5 and discussed in Section 5.6. The main conclusions are summarised in Section 5.7.

5.2 Adjustments to driver model

The scope of the driver model developed in Chapters 3 and 4 is deliberately limited to study the effects of sensory dynamics on driver steering behaviour under controlled

conditions, and various simplifying assumptions are made to reduce the complexity of the model. However, under real-world driving conditions these assumptions may not be valid, therefore it is necessary to extend the model to represent a more realistic driving scenario. In Section 5.2.1 the model is extended to incorporate large-angle target paths. In Section 5.2.2 the implications of forcing functions which are transient rather than stochastic are discussed, and the model is adapted to account for these considerations.

5.2.1 Large-angle target

The model derived in Chapter 3 assumes that the driver follows a target line which is close to straight, with small lateral deviations of the target path given by the target forcing function f_t. The simulated driver takes measurements of the lateral displacements between the target and a straight line projected ahead of the vehicle, 'previewing' the upcoming road with their visual system. In Chapter 4 the model of the driver's visual system is revised to a more realistic description which consists of measurements of the current lateral displacement of the vehicle relative to the target, and the angles of each upcoming segment of the target path relative to the vehicle yaw angle. These models assume that both the target angles and the vehicle yaw angle are small in order to linearise the vehicle dynamics. However, to describe a range of realistic driving conditions it is necessary to extend the model to allow large-angle target paths such as circles and corners.

Timings and Cole [219] showed that vehicle motion can be linearised about a non-straight target path by describing the target and vehicle position in intrinsic coordinates. The updated description of the driver's visual system in Chapter 4 is a step towards this, however the definition of the target path also needs to be revised. The new intrinsic description of the target path is shown in Figure 5.1. As before, the target path coordinates are spaced a distance UT_s apart, however the target is defined by a curvature f_κ rather than a lateral displacement f_t. Rather than requiring the total target path angle and vehicle yaw angle ψ to be small, this method only assumes that the path curvature f_κ and the relative path-following angle ϕ_0 are small. The new model can be used to analyse the results of the experiments described in Chapters 3 and 4 by converting f_t to an equivalent f_κ:

$$f_\kappa(k) = \frac{f_t(k+1) - 2f_t(k) + f_t(k-1)}{(UT_s)^2} \tag{5.1}$$

The target white noise amplitude is the same for both descriptions of the target path ($W_\kappa = W_t$), however it is necessary to change the filter $H_{ft}(s)$ to $H_{f\kappa}(s)$:

$$H_{f\kappa}(s) = \left(\frac{s^2}{U^2}\right) H_{ft}(s) \tag{5.2}$$

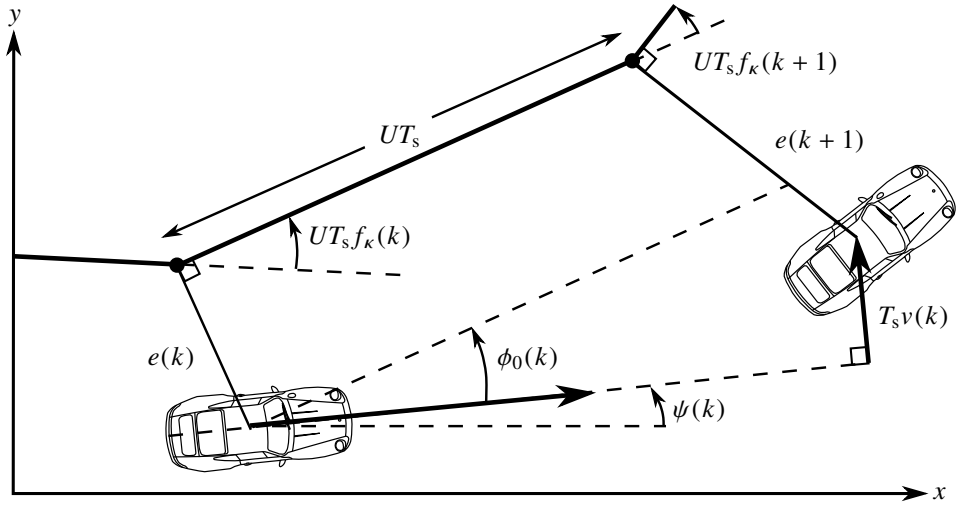

Figure 5.1: Intrinsic coordinate description of target, allowing large-angle target paths

The driver's visual system is modelled as in Chapter 4. The driver previews the upcoming road angles relative to the vehicle, given by $\boldsymbol{\phi} = \begin{Bmatrix} \phi_0 & \dots & \phi_{N_p} \end{Bmatrix}$, where:

$$\phi_n(k+1) = \phi_{(n+1)}(k) - T_s\omega(k) \tag{5.3}$$

and the most distant previewed angle ϕ_{N_p} is given by:

$$\phi_{N_p}(k+1) = \phi_{N_p}(k) - T_s\omega(k) + UT_s f_\kappa(k+N_p) \tag{5.4}$$

The driver also measures the path-following error e. Assuming small f_κ and ϕ_0, from the geometry in Figure 5.1 this can be found from:

$$e(k+1) = e(k) + UT_s\phi_0(k) - T_s v(k) \tag{5.5}$$

As in previous chapters, the target angles $\boldsymbol{\phi}_{vi}$ and tracking error e_{vi} measured by the driver's visual system are delayed by the visual delay τ_{vi}. The driver also measures the lateral acceleration a_{ve} and angular velocity ω_{ve}, which are delayed by the vestibular delay τ_{ve} and filtered by the vestibular dynamics.

The small angle assumptions made in this derivation allow a linear simulation to be run, even with large overall angles in the target path and the vehicle dynamics. However, to plot the path followed by the vehicle the Cartesian coordinates of the target path and vehicle must be calculated. For the target, the x and y components x_t and y_t are given by:

$$x_t(k+1) = x_t(k) + UT_s \cos\left(\sum_{i=0}^{k} UT_s f_\kappa(i)\right) \tag{5.6}$$

$$y_{\mathrm{t}}(k+1) = y_{\mathrm{t}}(k) + UT_{\mathrm{s}} \sin\left(\sum_{i=0}^{k} UT_{\mathrm{s}} f_{\kappa}(i)\right) \tag{5.7}$$

The position of the vehicle is linearised about the target path as shown in Figure 5.1 [219], and is given by finding the point located e away from the target coordinate in a perpendicular direction:

$$x(k) = x_{\mathrm{t}}(k) + e(k) \sin\left(\sum_{i=0}^{k} UT_{\mathrm{s}} f_{\kappa}(i)\right) \tag{5.8}$$

$$y(k) = y_{\mathrm{t}}(k) - e(k) \cos\left(\sum_{i=0}^{k} UT_{\mathrm{s}} f_{\kappa}(i)\right) \tag{5.9}$$

Because of the approximations made in the linearised derivation, the true longitudinal speed of the vehicle is not exactly U at all times, but accelerates and decelerates to keep in line with the target. However, assuming that the driver follows the target path reasonably closely these longitudinal accelerations are negligible.

5.2.2 Transient forcing functions

In Chapters 3 and 4 the forcing functions are defined as filtered white noise so that the LQR controller and Kalman filter implement a statistically optimal control strategy. The forcing functions used in the experiments were designed to match this description, with known spectra $H_{ft}(s)$ (or $H_{f\kappa}(s)$), $H_{fv}(s)$ and $H_{f\omega}(s)$, and magnitudes W_{t} (or W_{κ}), W_{v} and W_{ω}. It is assumed that the driver is aware of these spectra and magnitudes and includes them in an internal model of their surroundings.

While some sources of disturbances during driving can be described accurately by stationary random signals, others occur at distinct points in time and have particular transient characteristics. Transient disturbances could also represent a sudden departure from the linear regime of the tyre, such as an unexpected skid. More sustained manoeuvres involving the nonlinear region of the tyre are investigated in Chapter 6. Target paths in real driving generally do not follow a random distribution, although it may be possible to model them as such with a much lower frequency spectrum than the targets used in Chapters 3 and 4. Often target paths consist of discrete, transient manoeuvres such as lane changes, corners and circuits that follow predictable curvature profiles.

In Chapter 4 several driver model variations are suggested, where the driver's internal model representations $H'_{\mathrm{m}a}(s)$ and $H'_{\mathrm{m}\omega}(s)$ of the motion filters do not match the true filters $H_{\mathrm{m}a}(s)$ and $H_{\mathrm{m}\omega}(s)$. A similar approach can be taken for transient forcing functions,

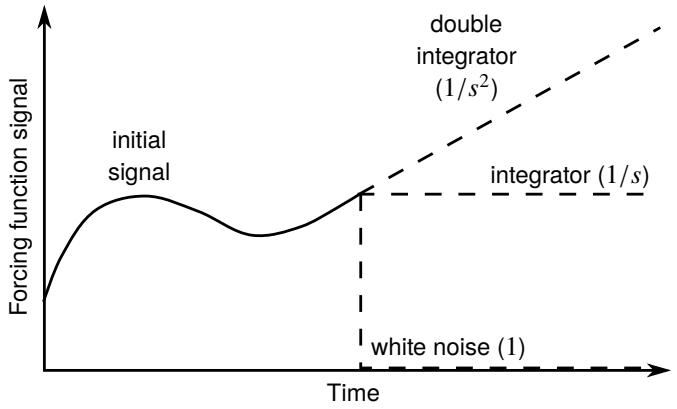

Figure 5.2: Predicted forcing function signals based on three internal model filters: white noise; an integrator; and a double integrator.

by defining internal model representations $H'_{fv}(s)$, $H'_{f\omega}(s)$ and $H'_{f\kappa}(s)$ of the target and disturbance spectra. For simplicity three basic filters are considered: White noise (unity transfer function), an integrator (transfer function $1/s$) and a double integrator (transfer function $1/s^2$). These filters define the expected relative amplitudes of frequencies in the forcing function signal, however they also predict the future trajectory of the signal in the time domain, as shown in Figure 5.2. If the driver has measured the initial forcing function signal given by the solid line, the three filters give different predictions about what is most likely to come next. If white noise is assumed, the predicted future values are all zero, independent of what has come before. For an integrator, the future values are assumed to be equal to the previous measured value, and for a double integrator the signal continues at a constant gradient.

The three types of target used in the experiment described in Section 5.3 were a straight line (for which all filters would give the same results since f_κ is always zero), lane changes and corners. The target curvature profile f_κ is shown for the lane change and corner tracks in Figure 5.3. The lane change consists of two short impulses, so the prediction shown in Figure 5.2 for a white noise spectrum would be the most accurate. The corner consists of a triangular curvature profile. The prediction of the double integrator would be consistent with this, although it would be inaccurate close to the middle and end of the corner. Using an integrator as the equivalent target filter should give a reasonable prediction for both of these cases. In normal driving the path followed by a driver will have a smoothly varying curvature, since large changes would cause a sudden jump in acceleration, therefore the choice of an integrator $H'_{f\kappa}(s) = 1/s$ is appropriate. The disturbances used in the experiment were based on impulses, therefore it is most appropriate to choose white noise equivalent filters $H'_{fv}(s) = H'_{f\omega}(s) = 1$.

In addition to the spectra of the forcing functions, the simulated driver has an internal

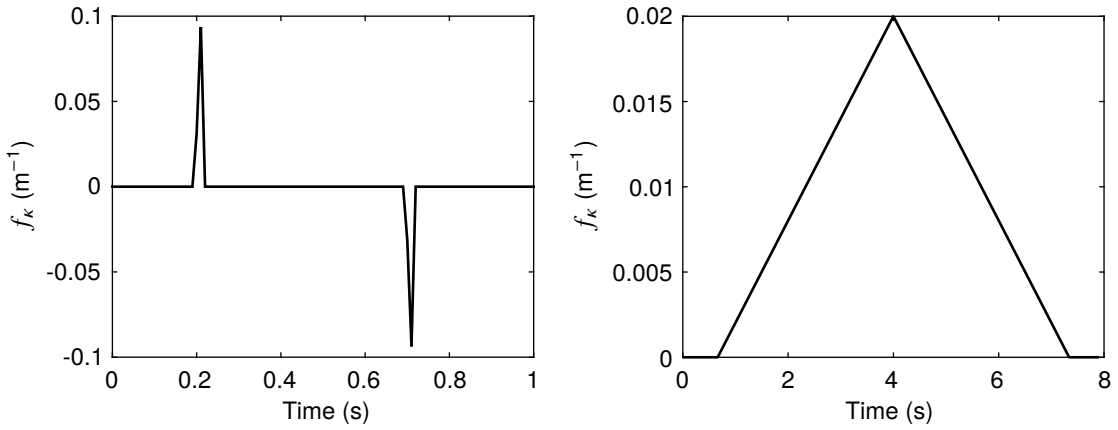

(a) Lane change **(b)** Corner

Figure 5.3: Target curvature profiles f_κ for a lane change and a corner

model of the RMS amplitudes W'_κ, W'_v and W'_ω of their white noise representations. In Chapters 3 and 4 these are assumed to equal the true RMS amplitudes of the white noise signals from which the forcing functions are calculated, bandwidth-limited by the Nyquist frequency $1/(2T_s)$. For transient forcing functions it is necessary to find equivalent white noise amplitudes for the forcing functions, but it is not obvious how they should link to the signal itself. Similarly, the driver's internal model includes estimates of the RMS measurement noise amplitudes V_a, V_ω, V_e and V_ϕ, and the process noise amplitude W. In Chapter 3 the process noise is found to vary linearly with the RMS steering angle, and similar relationships are found for the measurement noise in Chapter 4. Noise amplitudes V are linearly dependent on stimulus magnitude M, with a constant signal-to-noise ratio (SNR) and a threshold η, for example:

$$V_a = \begin{cases} \dfrac{M_a}{\mathrm{SNR}_a} & M_a > \eta_a \\ \dfrac{\eta_a}{\mathrm{SNR}_a} & M_a < \eta_a \end{cases} \tag{5.10}$$

In Chapter 4, stimulus magnitudes are defined as the RMS signal value, for example $M_a = \mathrm{RMS}(a_{\mathrm{ve}})$. However, the RMS value may not always be an appropriate measure of the magnitude of transient signals. For example, in a straight line trial with impulse disturbances there are large periods of zero signal between impulses, resulting in a very small RMS value. Alternatively, in a corner the driver is subjected to large steady-state centripetal accelerations, resulting in a large RMS acceleration. To investigate how drivers perceive transient signals, equivalent signal magnitudes M are identified to fit experimental data using a procedure described in Section 5.4. The results are discussed in Section 5.5.

The driver model assumes that the forcing functions have stationary statistical properties

during each trial, hence the need to define equivalent filters and magnitudes for each signal. However, in reality transient forcing functions have time-varying characteristics. A time-varying Kalman filter was implemented with time-varying signal magnitudes $M(k)$ which were proportional to the current value of the corresponding signal, however the results were found to fit measured steering behaviour poorly. It is reasonable to assume that for a short trial the driver bases their control strategy on constant equivalent magnitudes. However, over longer, more variable driving scenarios (for example if one trial were to transition directly into another) the driver may use learning or adaptive methods to adjust their control strategy. A limited amount of research has been carried out to identify pilots' responses to time-varying motion gains and vehicle dynamics [224–226], however further research is necessary to understand how drivers adapt to changing conditions.

5.3 Experiment procedure

Experiments were carried out in Chapters 3 and 4 to measure the steering behaviour of real drivers so that parameter values for the new driver model could be identified. Drivers carried out a combined target-following and disturbance-rejection task in a moving-base simulator, with the target and disturbance signals formed from filtered white noise. A new experiment was designed to investigate how drivers respond to target and disturbance signals formed from distinct, transient events, with a procedure similar to the previous experiments. A linear single-track vehicle model was used, with parameters summarised in Table 3.1. The longitudinal speed U was always 40 m/s, however the steering ratio G varied depending on the conditions of the trial to make it easier for the drivers to carry out small or large manoeuvres as necessary. The target line was always fixed to the road so the drivers could preview the upcoming target.

To allow the drivers to follow large-angle target paths without exceeding the simulator limits, and to investigate how drivers' responses to transient disturbances are affected by sensory conflicts, the physical motion of the simulator was scaled or filtered relative to the motion of the virtual vehicle in a similar way to the experiments described in Chapter 4. Four motion conditions were tested: no motion, full motion, scaled motion and filtered motion. The scaled motion trials used scaling factors of 0.2 on the lateral motion and 0.5 on the yaw motion. The filtered motion trials had scaling factors in the same ratio, adjusted for each trial to fit within the simulator limits, with both lateral and yaw motion also filtered by a high-pass filter given by:

$$H_{\mathrm{HP3}}(s) = \left(\frac{s}{s+5}\right)^2 \tag{5.11}$$

5.3.1 Disturbances

Three types of disturbance were used in the experiment: white noise disturbances for comparison with previous results; transient impulse disturbances; and 'shaped' disturbances which were designed to mimic discrepancies caused by filtering the vehicle motion. The impulse disturbances were formed of lateral and/or translational impulse accelerations, designed to act for a short amount of time to push the vehicle in one direction. This is not possible if the disturbances are added directly to v and ω as in Chapters 3 and 4, since velocity step disturbances would require a constant steering angle from the driver after the impulse. The vehicle model was modified to add f_v and f_ω to the lateral and yaw accelerations rather than velocities, as shown in Figure 5.4. There are nine possible combinations of the signs of v and ω impulse disturbances (including zero meaning that no disturbance is added), as shown in Table 5.1. Some or all of these impulse combinations were included in each transient disturbance trial.

One of the objectives of the experiment was to determine the extent to which drivers can tell the difference between disturbances and phase distortions introduced by filtering

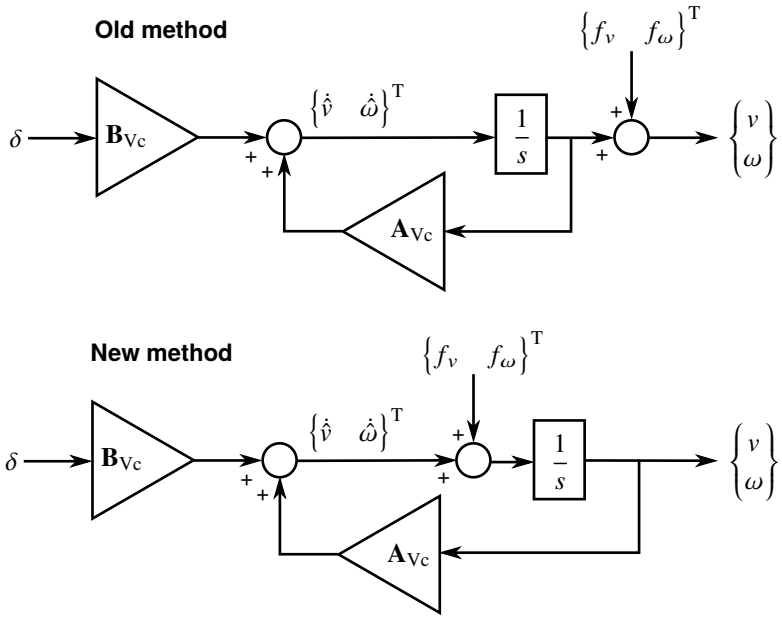

Figure 5.4: Comparison of old and new methods for adding disturbances to vehicle

Table 5.1: Possible combinations of signs of f_v and f_ω impulse disturbances

Impulse disturbance number	I1	I2	I3	I4	I5	I6	I7	I8	I9
Sign of f_v	0	0	0	1	1	1	−1	−1	−1
Sign of f_ω	0	−1	1	0	−1	1	0	−1	1

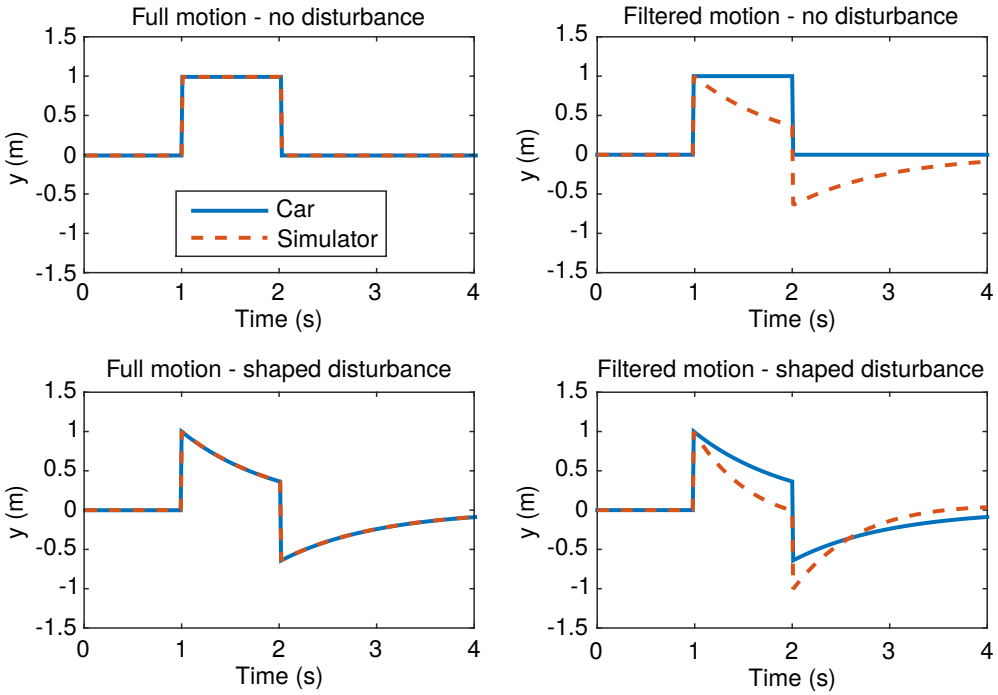

Figure 5.5: Design of shaped transient disturbances. Vehicle and simulator motion is compared using motion filters and/or shaped disturbances

the vehicle motion. To investigate this, 'shaped' disturbances were created. They were designed corresponding to each impulse disturbance to give resulting vehicle motion equal to the filtered motion of the simulator. The design of the shaped disturbances is illustrated in Figure 5.5. In the top left is a trial with full motion and no added shaped disturbance. The car undergoes some motion, which may result from an impulse disturbance or the driver steering to follow a target. In the top right is the same trial, with filtered motion. In the bottom left, a shaped disturbance is added to the full motion trial so that both the simulator and vehicle motion match the simulator motion from the trial shown in the top right. In the bottom right is a filtered motion trial with an added shaped disturbance.

The shaped disturbances were calculated so that, if the driver were to steer identically in both cases, the vehicle motion with an added shaped disturbance would match the simulator motion with filtered motion and no additional disturbance. The latter was found by simulating each impulse disturbance using the driver model, including any target-following components such as lane changes. If the lateral and angular velocities of the car are v and ω, and the corresponding simulator velocities are v_{smr} and ω_{smr}, the shaped disturbances f_v and f_ω can be found from:

$$\begin{Bmatrix} (v_{\mathrm{smr}} - v)(k+1) \\ (\omega_{\mathrm{smr}} - \omega)(k+1) \end{Bmatrix} = \mathbf{A}_{\mathrm{V}} \begin{Bmatrix} (v_{\mathrm{smr}} - v)(k) \\ (\omega_{\mathrm{smr}} - \omega)(k) \end{Bmatrix} + \begin{Bmatrix} f_v(k) \\ f_\omega(k) \end{Bmatrix} \tag{5.12}$$

$$\begin{Bmatrix} f_v(k) \\ f_\omega(k) \end{Bmatrix} = \begin{Bmatrix} (v_{\text{smr}} - v)(k+1) \\ (\omega_{\text{smr}} - \omega)(k+1) \end{Bmatrix} - \mathbf{A}_{\text{V}} \begin{Bmatrix} (v_{\text{smr}} - v)(k) \\ (\omega_{\text{smr}} - \omega)(k) \end{Bmatrix} \tag{5.13}$$

Shaped disturbances S1 to S9 were calculated for the nine impulse disturbance variations I1 to I9 outlined in Table 5.1, combined with any transient manoeuvres introduced by the target in each trial.

Due to the adjustments made to the method of adding disturbances shown in Figure 5.4, new filters were defined for the white noise disturbances:

$$H_{fv}(s) = \left(\frac{s}{s+0.2}\right)^2 \left(\frac{3}{s+3}\right)^2 \tag{5.14}$$

$$H_{f\omega}(s) = \left(\frac{s}{s+0.2}\right)^2 \left(\frac{6}{s+6}\right)^2 \tag{5.15}$$

The white noise disturbance amplitudes were $W_v = 31.6$ m/s^2* and $W_\omega = 15.8$ rad/s^2*.

5.3.2 Targets

Three types of target were used in the experiment: a straight line to investigate the effects of transient disturbances in isolation; lane changes to measure responses to small-displacement transient target events; and a track consisting of a series of corners to investigate how drivers steer for a more realistic large-angle target profile. The nature of the three target profiles required different sets of disturbances to be included in each case.

5.3.2.1 Straight line

Trials were carried out with a straight line target to measure the feedback component of driver steering control in isolation. Since drivers' responses are expected to be symmetrical in the lateral direction, identical impulse disturbances were not tested in both directions. In addition, no useful measurements would be obtained with no target or disturbances. Therefore only four out of the nine impulse disturbances given in Table 5.1 were tested: I3, I4, I5 and I6. The equivalent shaped disturbances were also tested, and the direction of each disturbance was randomised. Each trial was split into blocks lasting 8 s, with one disturbance at the start of each block, and the order of the blocks was randomised. Blocks began at multiples of 10 s, plus up to two seconds added randomly so the driver could not guess when the disturbance would occur. Four trials were carried out with the straight line target, testing each motion condition. An example of the disturbances from one of the straight line trials is given in Figure 5.6.

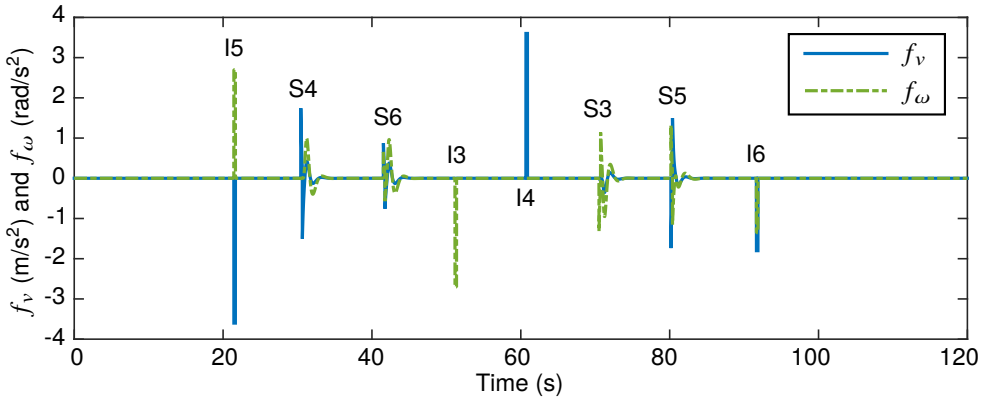

Figure 5.6: Disturbance signals for trial T2, with a straight line target and full motion

5.3.2.2 Lane changes

To investigate how drivers respond to transient target events in addition to disturbances, trials were carried out with a target consisting of continuous lane changes as shown in Figure 5.7a. The direction of the lane change alternated, and the disturbances were added at the onset of the lane change. The nature of the control task depends on the direction of the disturbances relative to the lane change, therefore all nine impulse disturbances given in Table 5.1 were tested, plus the shaped versions of each of them. The order of the disturbances was randomised, and as there were eighteen disturbances in total they were split over two trials. It was not possible to carry out the lane changes with full motion without exceeding the simulator limits, and due to time constraints lane change trials with no motion were not carried out. Since each condition required two trials to test all the disturbances, four trials were carried out in total to investigate lane changes with scaled and filtered motion.

5.3.2.3 Corners

The intrinsic target description given in Section 5.2.1 allows the vehicle motion to be linearised about a large-angle target path. Therefore a target profile was designed to investigate how drivers follow a more realistic target with large angles, consisting of corners connected by straights. The layout of this target is shown in Figure 5.7b. It consists of clothoid corners, with a triangular curvature profile as shown in Figure 5.3b. The shape of each corner is identical, although the direction varies to avoid the drivers developing motion sickness from constantly turning in the same direction.

It was not possible for the motion to be full-scale or scaled for the cornering trials, due to the large low-frequency components in the vehicle yaw angle and lateral acceleration. Therefore trials were carried out with filtered motion and no motion. In addition, it is

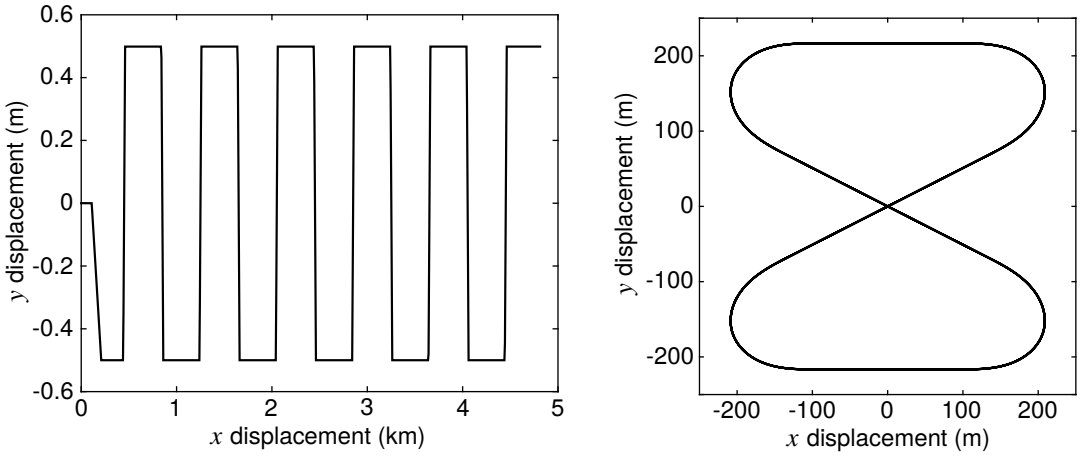

(a) Lane Change **(b)** Corners

Figure 5.7: Lane change and corner targets for transient disturbance experiment. Corresponding curvature profiles f_v are shown in Figure 5.3.

difficult to define a shaped disturbance in the same way as the straight line and lane change trials because the discrepancy between full and filtered motion is very large, so only the impulse disturbances were used. The disturbances were placed at one of two points of the corner, the onset of the change in curvature (corner entry) and the point of maximum curvature (mid-corner). As with the lane change trials, the disturbances for the corner trials were split over two trials for each condition to reduce the length of each trial and allow the drivers to take breaks if necessary.

5.3.3 Trials and procedure

The conditions of each of the trials carried out in the experiment are given in Table 5.2. In addition to trials containing a mixture of impulse and shaped transient disturbances, three additional trials were carried out with white noise disturbances, to compare with previous results and investigate how drivers react to a transient target profile with random disturbances. Each trial began with around 20 s of practice time for the drivers to adapt to the conditions of the trial. Trial T1 was carried out first, followed by trials T2 to T9 in a random order and then trials T10 to T15 in a random order.

As in previous experiments five drivers were tested, four normal drivers (drivers 1 to 4) and one professional test driver (driver 5). Drivers 1, 4 and 5 were the same as those who carried out the experiments in Chapters 3 and 4, however drivers 2 and 3 were new test subjects. The results of all five drivers were also averaged to give a set of averaged data, which should contain less noise than the data from the individual drivers. Except where otherwise indicated, parameter values were identified to fit the averaged data.

Table 5.2: Conditions of each trial for the transient disturbance experiment. Motion filter $H_{\mathrm{HP3}}(s)$ is given in Equation 5.11.

Trial	Target	Disturbances	Motion filters		Steering ratio
			$H_{\mathrm{m}a}(s)$	$H_{\mathrm{m}\omega}(s)$	G
T1	Straight line	White noise	0.2	0.5	3.3
T2	Straight line	Transient	1	1	0.6
T3	Straight line	Transient	0.2	0.5	3.3
T4	Straight line	Transient	$0.4H_{\mathrm{HP3}}(s)$	$H_{\mathrm{HP3}}(s)$	3.3
T5	Straight line	Transient	0	0	3.3
T6	Lane change	Transient	0.2	0.5	3.3
T7	Lane change	Transient	0.2	0.5	3.3
T8	Lane change	Transient	$0.3H_{\mathrm{HP3}}(s)$	$0.75H_{\mathrm{HP3}}(s)$	3.3
T9	Lane change	Transient	$0.3H_{\mathrm{HP3}}(s)$	$0.75H_{\mathrm{HP3}}(s)$	3.3
T10	Corners	White noise	0	0	10
T11	Corners	White noise	$0.1H_{\mathrm{HP3}}(s)$	$0.25H_{\mathrm{HP3}}(s)$	10
T12	Corners	Transient	0	0	10
T13	Corners	Transient	0	0	10
T14	Corners	Transient	$0.1H_{\mathrm{HP3}}(s)$	$0.25H_{\mathrm{HP3}}(s)$	10
T15	Corners	Transient	$0.1H_{\mathrm{HP3}}(s)$	$0.25H_{\mathrm{HP3}}(s)$	10

5.4 Parameter identification

Parameter values for the driver model are identified in Chapter 4 to fit the results of 51 trials carried out under a range of conditions. When using the model to simulate the transient disturbance trials many of the parameters are fixed at these values, given in Table 4.7. However various additional parameters are introduced for trials with transient target or disturbance profiles. These are:

- Target and disturbance equivalent magnitudes W'_κ, W'_v and W'_ω. In previous chapters the target and disturbance forcing functions were generated from filtered white noise, in which case the internal model representations W'_κ, W'_v and W'_ω were equal to the true RMS values W_κ, W_v and W_ω of these white noise signals. However if the forcing functions consist of transient events it is necessary to find equivalent magnitudes for the transient signals.
- Sensory signal equivalent magnitudes M_a, M_ω, M_ϕ and M_e. In Chapter 4, sensory noise is found to be proportional to the magnitudes of the corresponding sensory signal. With white noise disturbances these magnitudes can be characterised as the RMS values of the signals, however this may not be appropriate when the sensory signals contain transient events (see Section 5.2.2).

- Cost function weight q_δ. The value of this weight must be identified as it may vary from trial to trial.

The values of these additional parameters are identified using a similar procedure to Chapters 3 and 4 to fit the predictions of the driver model to the steering angles measured in the experiment.

In Chapter 4 several variations of the driver model are presented based on possible differences between the driver's internal model of the motion scaling or filtering and the real system. These variations are summarised in Table 4.1. Model variations M0 to M3 are also used for analysing the results of the transient experiment. In model M0 the driver assumes there is no motion, and in model M1 the driver assumes the motion is at full scale. In model M2 the driver's internal model matches the true motion scaling factors or filters, and in model M3 optimal internal model yaw and lateral motion scaling factors are identified to fit the measured results as closely as possible.

In addition to predicting steering angle signals, the driver model can also estimate the amplitude of random driver noise referred to the steering angle. In Chapters 3 and 4 the process noise amplitude is adjusted to give predicted noise amplitudes similar to those measured in the experiment. Preliminary simulations showed that it was not possible to do this accurately with the transient disturbance experiment results, possibly due to the time-varying nature of the driver noise in these trials. Therefore the steering angle equivalent magnitude M_δ is set to the RMS steering angle RMS(δ) in each trial, and the noise amplitude is not considered in the parameter identification procedure.

5.5 Results

The results of the transient disturbance experiment can be analysed in various different ways. In Section 5.5.1 the performance of the five drivers in the experiment is compared. Results of the parameter identification procedure are presented in Section 5.5.2 for the trials with white noise disturbances, and Section 5.5.3 for the trials with transient disturbances. Particular consideration is given to the shaped disturbances in Section 5.5.4, and attempts to fit a single fixed set of parameter values to the results of multiple trials are described in Section 5.5.5.

5.5.1 Driver performance comparison

Data measured in the transient disturbance experiment can be used to compare the performance of the five drivers. A representative example of the steering angles measured

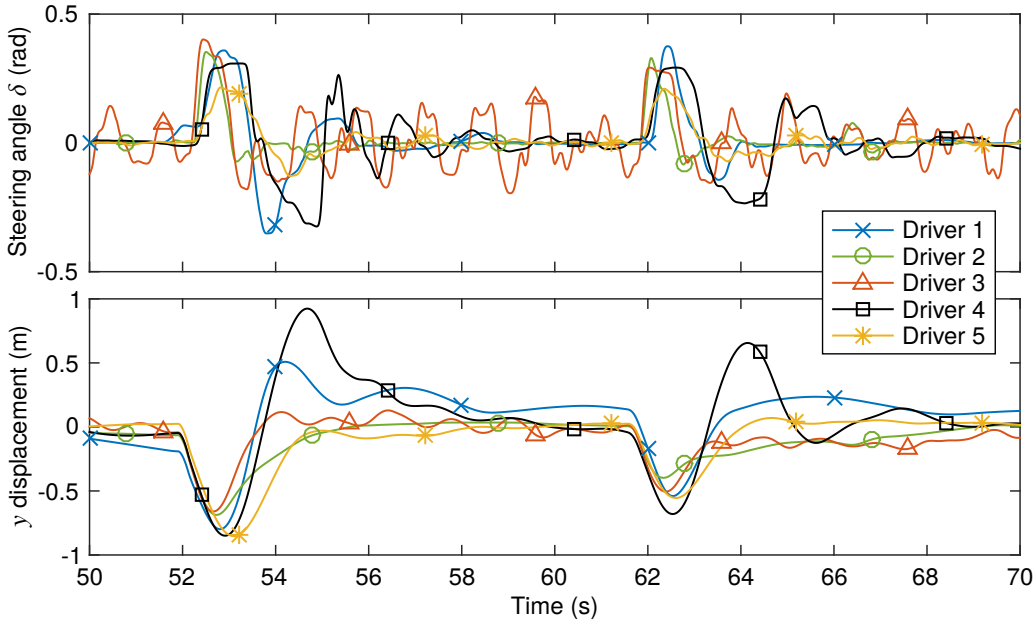

Figure 5.8: Examples of each driver's measured steering behaviour. Steering angles and vehicle lateral displacements measured for each driver are compared for a section of trial T5.

for each driver is shown in Figure 5.8. The results are taken from a section of trial T5, which had a straight-line target and no motion feedback. There is evidence of a variation in steering strategies between the drivers, with different levels of oscillation in the measured steering angles. However each driver seems to be consistent in their choice of strategy, as the responses of each driver to the two disturbances shown in Figure 5.8 are generally consistent with each other. This indicates that a fixed-parameter driver model is appropriate, with drivers adopting a consistent control strategy throughout a given trial.

An interesting observation from Figure 5.8 is that the steering action of driver 3 contains an oscillation at a frequency just under 1 Hz. The oscillation is consistent and periodic, and doesn't diminish after each disturbance. It is therefore unlikely to result from driver noise or instability in the driver-vehicle control loop, so it appears so be deliberate. One possible interpretation is that the driver is attempting to perform a 'dual control' task [227]. This is a control task which has the additional objective of learning the system dynamics. The driver may be adding in a known disturbance and measuring the resulting car movements so that the vehicle dynamics can be better understood. As seen in Figure 5.8, the effect of this oscillation on the path-following error is minimal.

An alternative method of comparing the performance of the different drivers is to plot the RMS path-following error e against the RMS steering angle δ for each driver and trial, as in Figure 5.9. The values for each trial are given by the small markers, with the average values for each driver given by large markers. The results for each trial appear in

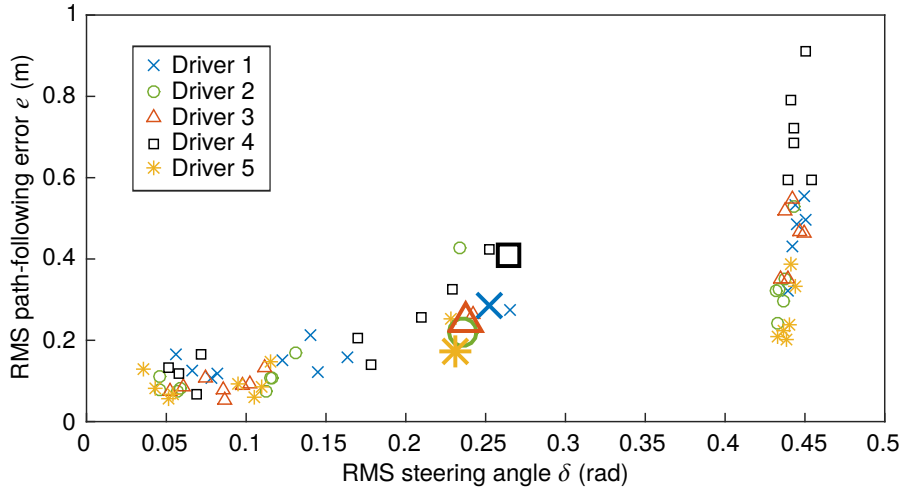

Figure 5.9: Performance of each driver in each trial of the transient experiment. Average values across all trials are shown by large markers.

three distinct groups, the first for the straight line trials which are grouped between RMS steering angles of around 0.05 and 0.1 rad, the second for the lane change trials with RMS steering angles between around 0.1 and 0.3 rad. The third group is for the cornering trials, which required a large amount of low-frequency steering, resulting in much larger RMS steering angles.

A surprising result seen in Figure 5.9 is that, when averaged across all trials, the drivers who steered the least also achieved the lowest path-following errors. This is the opposite to what would be expected, as it is assumed that the driver's cost function represents a trade-off between steering effort and target-following performance. This discrepancy may be a result of differences in the experience of the different drivers, with more experienced drivers able to achieve a lower path-following error while also minimising steering effort. Indeed the best driver from the results in Figure 5.9 is driver 5, who is a professional test driver. Since the shaped disturbances mimicked a high-pass filter and pushed the vehicle back towards the line after the initial impulse, drivers with more aggressive steering strategies may have overreacted in their response to the initial disturbance. The vehicle lateral displacements plotted in Figure 5.9 indicate that variations in path-following performance between the drivers were often caused by overshooting the target when responding to the initial disturbance.

5.5.2 White noise disturbances

Three of the trials (T1, T10 and T11) had filtered white noise rather than transient disturbances, providing a link between previous results and the new experiment. For these

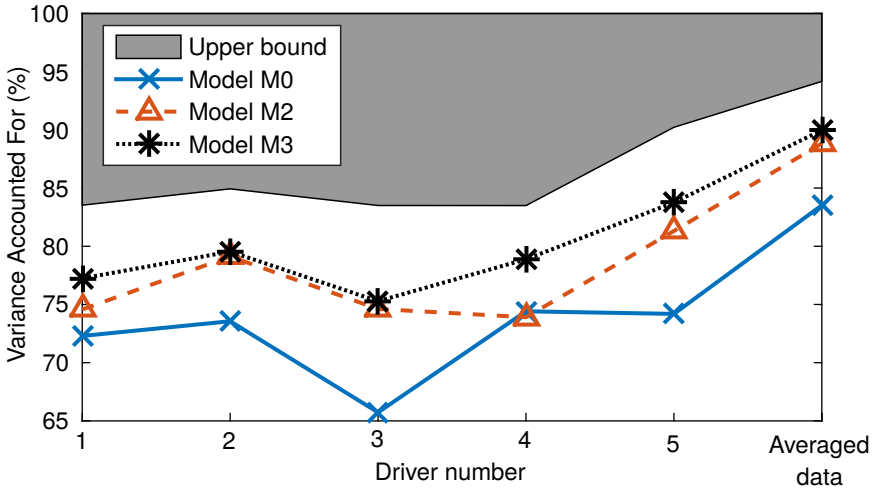

Figure 5.10: VAF values for trial T1, for each driver and averaged data, using model variations M0, M2 and M3. The shaded area shows the upper bound given by a Box–Jenkins model.

trials it is not necessary to identify values for all of the parameters listed in Section 5.4, as many can be fixed using knowledge of the conditions of the trials. Trial T1 had white noise disturbances with a straight-line target, so is fully within the scope of the model used in Chapter 4. The only parameter value that must be identified is the steering cost q_δ. Signal magnitudes M_a, M_ω, M_ϕ and M_e are all set to the RMS values of the corresponding signals, as in Chapter 4. The correct forcing function magnitudes W_κ, W_v and W_v and filters $H_{fv}(s)$ and $H_{f\omega}(s)$ are used in the simulated driver's internal model.

Optimal values of q_δ are identified to give the best fit to the results of trial T1 for each of the drivers separately, plus the averaged data. The resulting VAF values are shown in Figure 5.10, comparing model variations M0, M2 and M3 with the upper bound given by a Box–Jenkins model. Model M1 is not shown as it was found to become unstable with the chosen parameter values. In general the VAF values are high, particularly considering that only one parameter value is identified (except for model M3 where the two internal model scaling factors are also identified). This shows that the parameters found from previous experiments are still applicable to a similar trial carried out on a different day, with some different drivers. Except for driver 4, model M2 fits better than model M0, showing that the physical motion information was used by the drivers.

Trials T10 and T11 combined filtered white noise disturbances with a large-angle cornering target. This is an important situation to consider, as it is arguably the closest match to real target and disturbance signals during normal driving. Since the disturbances are filtered white noise, internal model representations W'_v, W'_ω, $H'_{fv}(s)$ and $H'_{f\omega}(s)$ can be set equal to their true values. However, the target has a transient profile, therefore $H'_{f\kappa}(s)$ is set to an integrator as explained in Section 5.2.2, and the equivalent magnitude

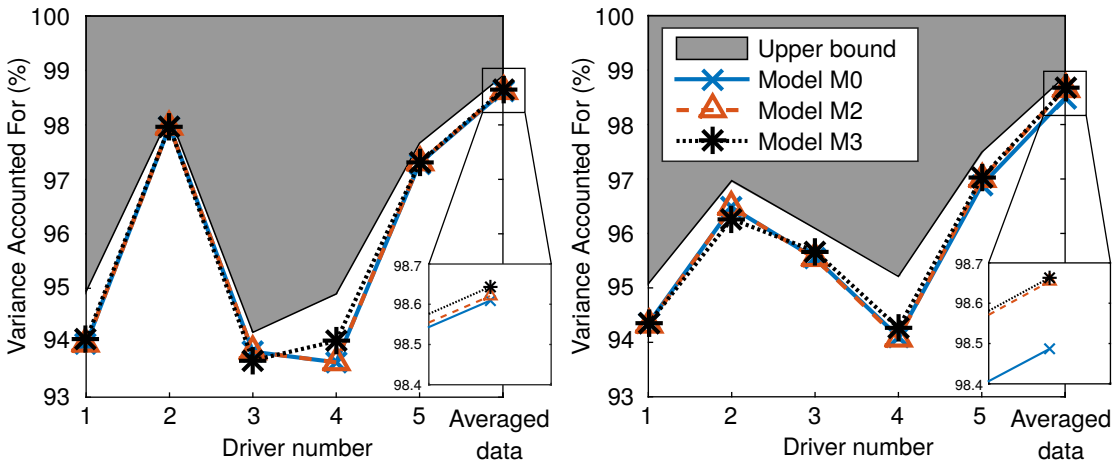

(a) Trial T10 **(b)** Trial T11

Figure 5.11: VAF values for trials T10 and T11, for each driver and averaged data, using model variations M0, M2 and M3. The shaded area shows the upper bound given by a Box–Jenkins model.

W'_κ is identified to fit experimental measurements. The measured target angles are clearly dominated by the transient target profile, therefore an equivalent magnitude M_ϕ is also identified. However, the other measured signals do not contain significant transient components, therefore their RMS values are an appropriate quantification of the signal magnitudes. The values of M_a, M_ω and M_e are set to the corresponding RMS signal values.

Parameter values are identified for trials T10 and T11 for each driver and the averaged data, and the resulting VAF values are plotted in Figure 5.11. The VAFs are much higher for these trials than for trial T1, since the steering angle signal contains large low-frequency target-following components which must be similar for any controller that is able to follow the target line successfully. Since trial T10 had no motion, models M0 and M2 are equivalent in this trial. Model M3 fits slightly better for driver 4, however otherwise all model variations give similar results. The VAFs are also close to the upper bound given by the Box–Jenkins model, showing that the parametric driver model estimates the true driver steering behaviour well and that it was reasonable to use the RMS values for M_a, M_ω and M_e. The VAF values for each of the model variations are also close to the Box–Jenkins upper bound for trial T11, as shown in Figure 5.11b. For drivers 2 and 3 model M3 fits better than M0, which in turn fits slightly better than M2. However for the other drivers, and the more reliable averaged data, all model variations fit the results similarly. Closer inspection of the averaged data results reveals than model M3 fits best as expected, and model M2 fits better than M0. This indicates that the drivers were using the motion, however it didn't make a significant difference to their control actions.

The values of the parameters identified for trials T1, T10 and T11 are given in Table 5.3.

Table 5.3: Parameter values and noise ratio identified for trials T1, T10 and T11, using the averaged data and driver model variation M2. Values given in brackets are fixed based on the conditions of the trials.

Trial	Identified parameter values				Noise ratio (experiment/model)
	q_δ (rad^{-2*})	M_ϕ/RMS($\boldsymbol{\phi}$)	M_ϕ/RMS(ϕ_0)	W'_κ/RMS($\dot{f}_\kappa$)	
T1	2.52	(1)	(1)	(1)	0.941
T10	2.19	0.181	1.47	7.13	0.681
T11	0.32	0.482	3.85	6.68	0.350

The order of magnitude of the identified values is similar for trials T10 and T11, although the steering cost q_δ is higher for trial T10, showing that drivers put in less steering effort when there was no physical motion feedback. For both trials M_ϕ is lower than the RMS value of $\boldsymbol{\phi}$. In Chapter 4 the RMS value of $\boldsymbol{\phi}$ is calculated over the entire vector of previewed angles, however for large-angle targets which curve away from the vehicle this value is large. It may instead be more appropriate to link σ_ϕ to the RMS value of the yaw tracking error ϕ_0. This removes the large low-frequency components in the RMS value, since ϕ_0 mostly consists of small variations around the target path. For trial T10, which is likely to give a more accurate estimate of visual system parameters, the identified value of M_ϕ is 1.47 times the RMS value of ϕ_0. For the trials carried out in Chapter 4, in which M_ϕ is chosen to equal RMS($\boldsymbol{\phi}$), the value of RMS($\boldsymbol{\phi}$) is generally between 1.3 and 1.5 times the value of RMS(ϕ_0). This means that if M_ϕ was instead defined as RMS(ϕ_0), SNR$_\phi$ should be decreased by a factor of around 1.4 from the value given in Table 4.7 to give equivalent results. Doing so would result in a ratio M_ϕ/RMS(ϕ_0) close to unity for trial T10 in Table 5.3, showing that it is appropriate to let M_ϕ = RMS(ϕ_0) even for large-angle target paths.

For both of trials T10 and T11, the identified equivalent target forcing function magnitude W'_κ is around 7 times larger than the RMS value of the equivalent white noise input, which is the derivative of f_κ since the equivalent target filter $H'_{f_\kappa}(s)$ is chosen in Section 5.2.2 to be an integrator. This could be partly due to the straight sections of the cornering track, which add periods of zero curvature and reduce the overall RMS value. However the maximum value of the derivative of f_κ is only around 1.5 times larger than the RMS value, so the identified value of W_κ is too large for any measure of the magnitude of the target signal. This result indicates that the drivers put more weight on target following than would be expected for a white-noise target of similar magnitude.

Table 5.3 also includes the ratio between the RMS noise level measured in the experiment (defined as the RMS difference between the measured steering angle and the

Box-Jenkins prediction) and the noise level predicted by the model. For trial T1 this value is close to 1, showing that the parameter values found in Chapter 4 give a realistic estimate of the driver noise amplitude. However, the model overestimates the noise level in trials T10 and T11, showing that the equivalent noise amplitudes in the driver's internal model may not adequately represent noise levels for signals containing transient components.

5.5.3 Transient disturbances

The remaining trials combined transient disturbances with straight line, lane change and cornering targets. The transient disturbances consisted of impulse accelerations and shaped disturbances, which are discussed in further detail in Section 5.5.4. Each trial was carried out with either no motion, full motion, scaled motion or filtered motion, allowing the effects of different motion conditions on the drivers' steering responses to be studied. The averaged steering responses to each of the impulse disturbances in the straight line trials are plotted in Figure 5.12, and the corresponding path-following errors are shown in Figure 5.13. These allow driver steering behaviour under different motion conditions to be interpreted more easily than responses to random white noise disturbances. It should be noted that the disturbance magnitudes were smaller in trial T2, however they were exactly the same in trials T3 to T5, allowing the responses to be directly compared for all conditions except full motion.

Figures 5.12 and 5.13 show that the drivers steered similarly for disturbances I3, I4 and I5, which indicates that drivers respond to v and ω disturbances in similar ways. The steering response was smaller for disturbance I5, in which f_v and f_ω acted in opposite directions. It is clear that the motion conditions had a significant and consistent effect on the steering responses. Figure 5.12 shows that the response time was similar for the three conditions with motion, however the drivers steered later and at a lower initial steering rate without motion. This shows that physical motion information reduces drivers' reaction times to disturbances, even if the motion is scaled or filtered. In some cases the drivers overshot the target in their initial response, requiring a second smaller steering action in the opposite direction to the disturbance. This happened less in the full motion trial, although this may be a result of lower amplitude disturbances. Comparison of the scaled motion and filtered motion results shows that drivers steered more in their initial response and returned to zero steering angle earlier with scaled motion, with a similar amount of overshoot in both conditions.

The effects of the motion conditions on the path-following error e can be seen in Figure 5.13. The error was smallest for the full motion trial, where the disturbance amplitudes were smaller. The vehicle returned to the line slightly earlier with scaled rather

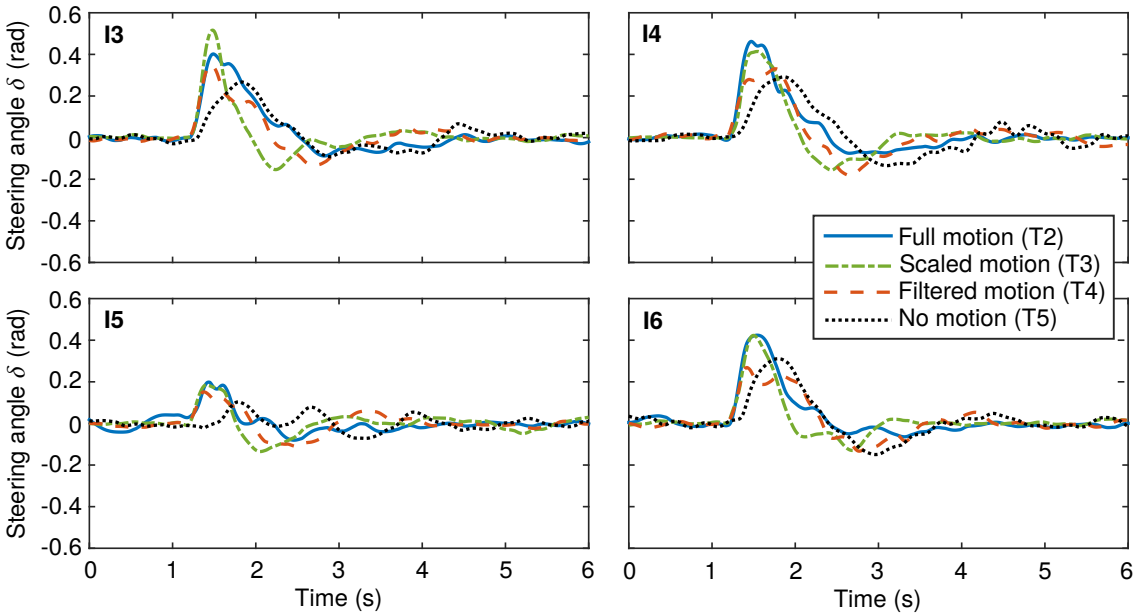

Figure 5.12: Steering angle responses to impulse disturbances in straight line trials, for four impulse types with various motion conditions. The same disturbances were used with scaled, filtered and no motion. Smaller amplitude disturbances were used with full motion.

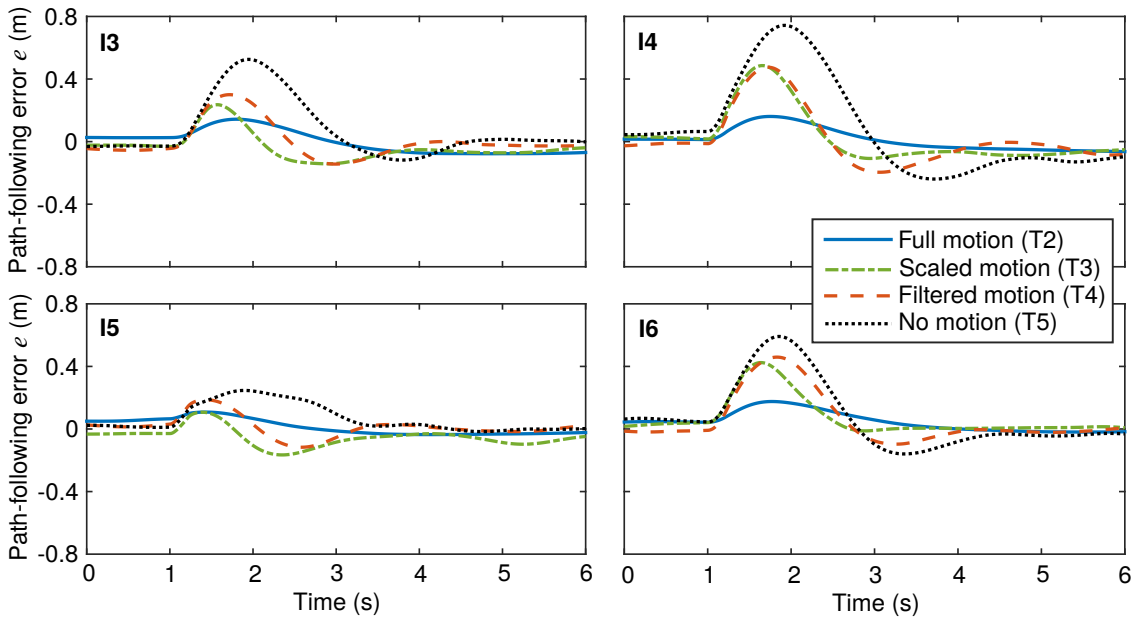

Figure 5.13: Path-following error from impulse disturbances in straight line trials, for four impulse types with various motion conditions. The same disturbances were used with scaled, filtered and no motion. Smaller amplitude disturbances were used with full motion.

than filtered motion, although the maximum deviations from the path were similar in both cases. The path-following error was much larger with no motion, showing that physical motion information allows drivers to respond to impulse disturbances more effectively. The differences between motion and no motion are shown in Figure 5.13 to be greater than the differences between scaled and filtered motion.

Similar plots for the lane change trials are shown in Figures 5.14 and 5.15. Only scaled motion and filtered motion were tested, and there were nine types of impulse disturbance to account for all possible combinations given in Table 5.1. The lane change manoeuvre required one steering action in the direction of the lane change, followed by a counter-steer of similar magnitude to straighten the car. Differences between the scaled and filtered motion results are largest for disturbances I3–I6 and I9. These are the combinations where at least one of the impulse disturbances acted in the direction of the lane change. For the other combinations all disturbances were acting opposite to the lane change direction, reducing the need for a counter-steering action to straighten the vehicle.

The steering angles plotted in Figure 5.14 show that differences between the two motion conditions are small for the initial steering action. However the return phase was carried out significantly later with filtered motion and often required an additional small correction. The path-following errors plotted in Figure 5.15 show that this delayed counter-steer caused the vehicle to overshoot the target with filtered motion when there was a disturbance acting in the direction of the lane change. These results show that drivers are able to carry out lane changes with disturbances much better when the motion is scaled rather than filtered.

Comparison of the steering angles and path-following errors for the cornering trials with transient disturbances (T12–T15) did not reveal clear differences between the trials with filtered motion and no motion. This could be because the task (and therefore the motion) was dominated by the feedforward cornering component, which meant that the filtered motion did not provide the drivers with much additional useful information about the disturbances. If it were possible to carry out these trials with scaled or full motion more clear differences may have been seen.

The identification procedure described in Section 5.4 can be used to fit the driver model to measurements from the trials with transient disturbances. The resulting VAFs using models M0, M1, M2 and M3 are plotted in Figure 5.16. In general the VAF values are high, with model M3 fitting best as expected. VAF values are higher for the lane-change trials than the straight-line trials, and much higher for the cornering trials. As discussed in Section 5.5.2, this is because the low-frequency components associated with following the targets dominate the measured steering angles in these trials. Model M2 fits the results well for many of the trials, however model M1 fits better for trials T8 and T9 which had filtered motion. Model M2 fits worse than model M3 for trial T4, which also had filtered

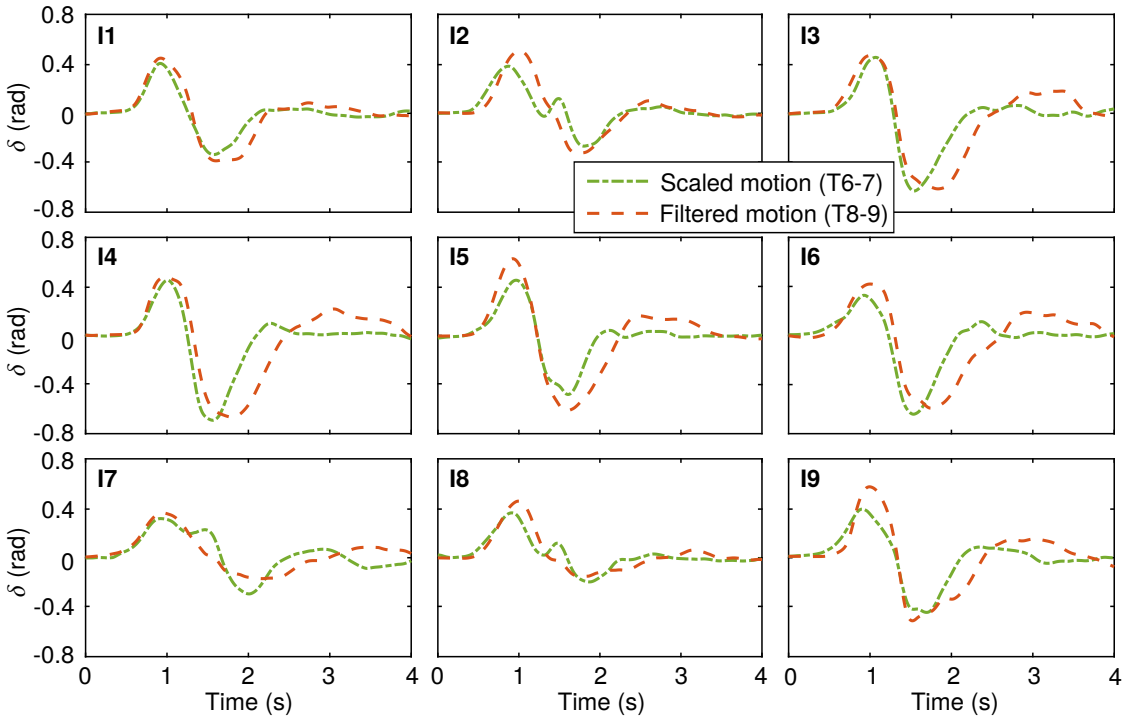

Figure 5.14: Steering angle responses to impulse disturbances in lane change trials, for nine impulse types with scaled or filtered motion.

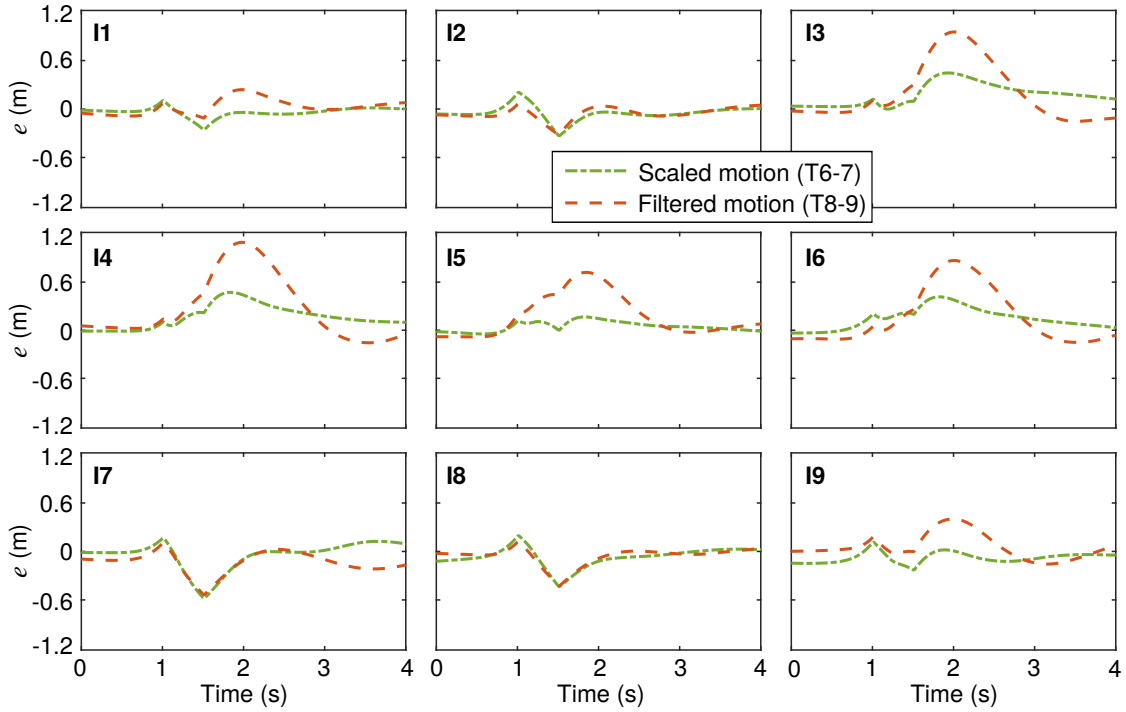

Figure 5.15: Path-following error from impulse disturbances in lane change trials, for nine impulse types with scaled or filtered motion.

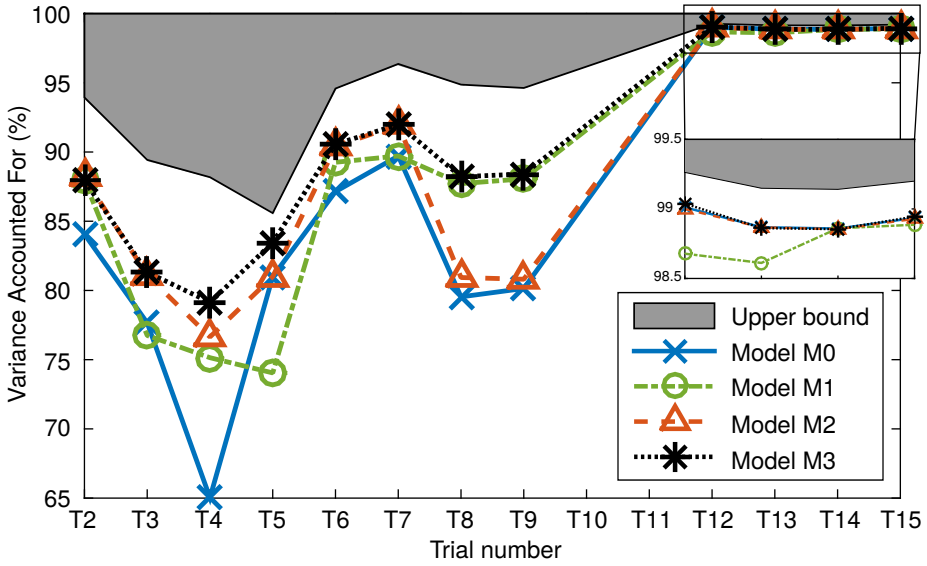

Figure 5.16: VAF values for trials with transient disturbances, comparing different model variations using the averaged data. The shaded area shows the upper bound given by a Box–Jenkins model.

motion. This indicates that the drivers had difficulty learning accurate internal models of the motion filters, which is similar to the result found in Chapter 4. Some insight into the consequences of this can be found by looking at the time histories of the steering response measured in the lane change trials compared with the predictions of models M1 and M2, plotted in Figure 5.17.

Comparison of Figure 5.17a with Figure 5.17b shows that with filtered motion the steering response was larger, more oscillatory and spread over a longer time period. The prediction of model M2 does not exhibit such a significant oscillation, in contrast to model M1 which is able to fit the measured behaviour well. This indicates that the drivers exhibited some sub-optimal control behaviour, which can be accounted for by model M1 due to the discrepancy between the true motion filters and the driver's internal model. The fact that this sub-optimal control behaviour is seen with filtered motion but not with scaled motion supports the hypothesis that it arises from errors in the driver's internal model of the motion filters. Introducing errors into the internal model degrades the optimality of the control behaviour, causing oscillations or instability. By choosing the noise values in the identification procedure model M1 can be tuned to give a similar amount of oscillation to the steering signal measured in the experiments. However model M1 is not a good candidate for an overall model of driver steering control, since it is not possible to find a fixed set of parameter values which fits the experimental results well over a range of trials. Further work is necessary to quantify discrepancies in the driver's internal model, and investigate how they affect the control performance of the driver.

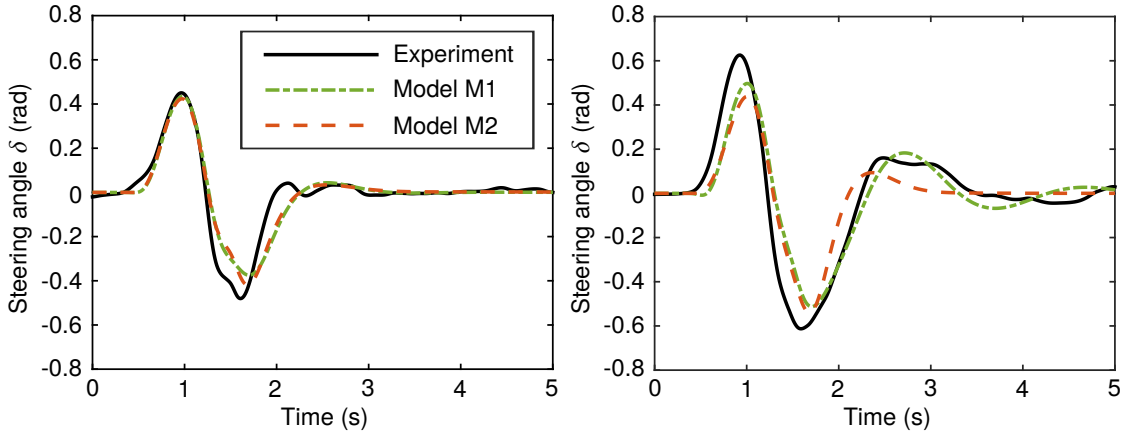

(a) Scaled motion (T6 and T7) **(b)** Filtered motion (T8 and T9)

Figure 5.17: Measured and predicted steering responses using models M1 and M2. Steering angles are compared for impulse disturbance I5 in lane change trials with (a) scaled or (b) filtered motion.

5.5.4 Shaped disturbances

In addition to impulse acceleration disturbances, trials T2 to T9 contained shaped disturbances which were designed to imitate distortions resulting from filtering the vehicle motion, as explained in Section 5.3.1. The aim was to investigate the extent to which drivers can distinguish between disturbances and motion filtering distortions. This question can be approached from two directions: Firstly, will a driver react to a shaped disturbance as if it were a filtering distortion? Secondly, will a driver react to a filtering distortion as if it were a disturbance? These questions are addressed by comparing simulations using the driver model with results measured in the experiment. A new variation of the driver model M5 is defined, in which the driver's internal model of the motion filters $H'_{\mathrm{m}a}(s)$ and $H'_{\mathrm{m}\omega}(s)$ is equal to $H_{\mathrm{HP3}}(s)$ (see Equation 5.11), multiplied by additional scaling factors $K'_{\mathrm{m}a}$ and $K'_{\mathrm{m}\omega}$, which are optimised during the identification procedure in a similar way to model M3:

$$H'_{\mathrm{m}a}(s) = K'_{\mathrm{m}a} H_{\mathrm{HP3}}(s) \tag{5.16}$$

$$H'_{\mathrm{m}\omega}(s) = K'_{\mathrm{m}\omega} H_{\mathrm{HP3}}(s) \tag{5.17}$$

This model variation represents a driver who believes that the motion is filtered, which may be an erroneous assumption caused by shaped disturbances. The identification procedure is run using this model for all trials with transient disturbances. The resulting VAFs are compared with models M2 and M3 in Figure 5.18. The important trials for the first question are trials T3, T6 and T7, which had scaled motion and included shaped disturbances. Model

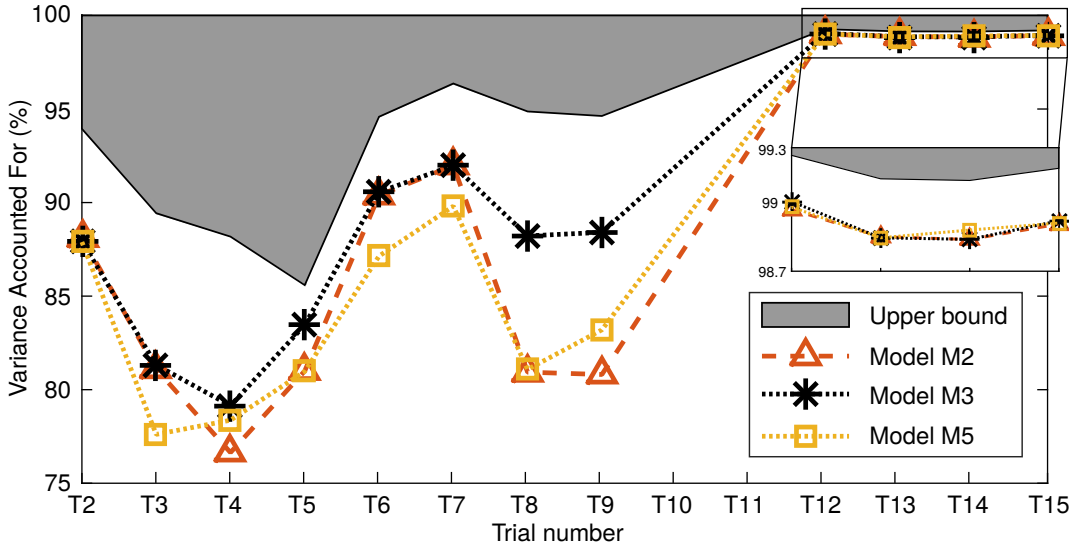

Figure 5.18: VAF values using model M5 for trials with transient disturbances, compared with models M2 and M3 and the Box–Jenkins upper bound.

M5 fits the measurements worse than models M3 and M2 for these trials, showing that the shaped disturbances did not make the drivers believe the motion was filtered.

The second question can also be answered by looking at the results shown in Figure 5.18. Model M3 represents a driver who believes that the motion is scaled, which implies that any distortions caused by filtering of the motion are perceived as disturbances. This can be compared with model M2, in which the driver is aware of the correct filtering, and model M5, which allows for the driver misidentifying the motion gains while still being aware of the filtered motion. The important trials for this question are T4, T8 and T9, which had filtered motion. In trial T4 differences between the models are small, however model M3 fits the results best. In trials T8 and T9 model M3 fits much better than models M2 and M5. This indicates that in trials with filtered motion the drivers steered as if the motion was scaled, implying that any phase distortions caused by the filtering were perceived as disturbances. M5 fits slightly better for the cornering trials, which could indicate that drivers are able to perceive the filtering better when there is a larger discrepancy between the scaled and filtered motion. However model M2 still fits worse than M3, so they are not necessarily able to learn the motion filters accurately. Drivers may simply be able to discount the lowest frequencies involved in the feedforward target-following task.

5.5.5 Single parameter set

For the driver model to provide useful predictions of driver steering behaviour it is necessary to find a single fixed set of parameters which can match experimental results over a range

of conditions. Therefore a single parameter set is identified to fit the results of trials T1 to T15. Model M2 is used to represent a driver who is aware of the motion scaling conditions, although results from Sections 5.5.3 and 5.5.4 show that this model may not be as accurate for filtered motion trials. Section 5.2.2 explains how driver responses to transient disturbances can be modelled by including equivalent magnitudes for each signal in the simulated driver's internal model. Results presented in Section 5.5.3 show that this method can give a close fit to each individual trial. However it is not obvious how to link these equivalent magnitudes to the properties of the signals to describe results across different trials. Two hypotheses are tested: the first that the perceived magnitude of each signal is proportional to its RMS value, for example:

$$M_a = K_a \text{RMS}(a_{\text{ve}}) \tag{5.18}$$

The second hypothesis is that the perceived magnitude of each signal is proportional to the maximum signal value:

$$M_a = K_a \max(|a_{\text{ve}}|) \tag{5.19}$$

Using results discussed in Section 5.5.2, the RMS value of the previewed target angles is defined as $\text{RMS}(\phi_0)$ rather than $\text{RMS}(\boldsymbol{\phi})$, and similarly for the maximum value.

A similar identification procedure is used to that described in Section 4.6. Gains K are identified corresponding to each signal magnitude M and forcing function amplitude W' to scale either the RMS or maximum signal values as described in Equations 5.18 and 5.19. RMS and maximum values are calculated from the data averaged over the five drivers. The steering angle gain K_δ is fixed at a value of 1 in both cases. Initially a parameter set is identified with a single steering cost q_δ fixed across all trials. Separate values of q_δ are then identified to fit each trial separately in a similar way to the procedure in Section 4.6, and these are held constant while identifying optimal signal gains once more.

The resulting VAF values are plotted in Figure 5.19. As expected, VAFs are lower with a single fixed set of parameters than with separate parameter values for each trial. The lowest VAFs are for trial T4, which had filtered motion. The model is expected to fit less well for filtered motion trials, as it assumes the drivers have an accurate internal model of the motion filtering, which is found in Sections 5.5.3 and 5.5.4 to be untrue. In general the VAFs for the single parameter sets are reasonably close to the separate parameter sets. However the 'max' model fits best for the straight line trials, whereas the 'RMS' model fits best for the lane change trials. Both models fit similarly for the cornering trials. These results indicate that neither the RMS value nor the maximum value are appropriate descriptions of the signal magnitudes under all conditions, so the equivalent signal magnitudes may depend on more complicated signal properties or a combination of

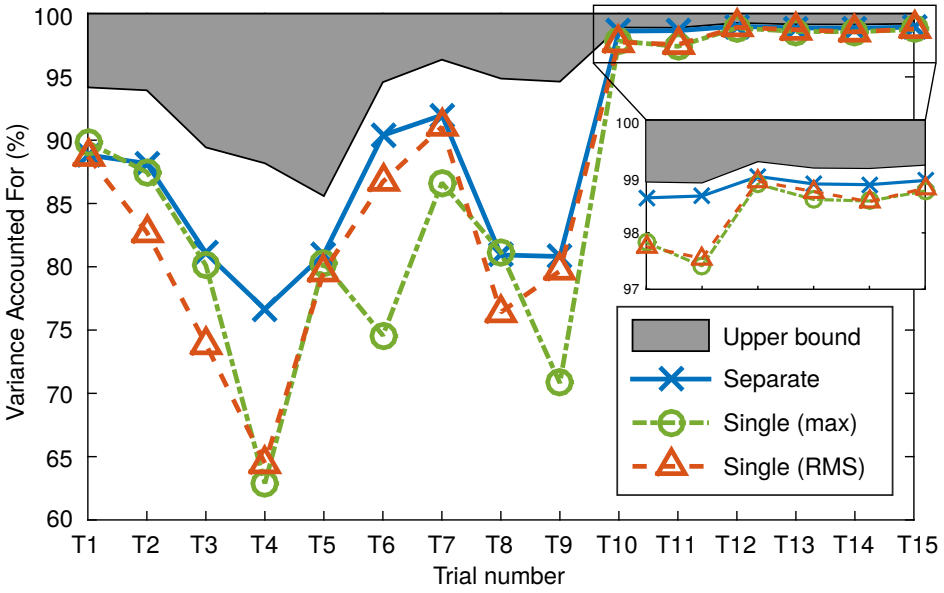

Figure 5.19: VAFs for single parameter set fit to all trials of transient experiment, with signal magnitudes proportional to either RMS value or maximum signal value

Table 5.4: Single set of parameter values identified to fit all trials in transient disturbance experiment, for the 'RMS' model and the 'max' model. Values given in brackets were fixed.

	Identified equivalent magnitude gains							
Model	K_a	K_ω	K_ϕ	K_e	K_δ	$K_{f\kappa}$	K_{fv}	$K_{f\omega}$
RMS	0.32	0.046	9.6	10	(1)	0.10	0.33	8.9
max	0.24	0.35	8.7	10	(1)	0.0095	3.7	8.3

factors. Overall the 'RMS' model is a slightly better fit to experimental results.

The identified parameter values are given in Table 5.4. There are clear similarities between many of the values found using the two models. This is interesting as the RMS value is a lower estimate of signal amplitude than the maximum value, so lower gains would be expected for the 'max' model. However the driver's control strategy depends on the relative rather than absolute noise values, so these similarities may be a result of setting K_δ to 1 for both models. Small gains K_a and K_ω are found for the vestibular measurements, whereas large gains K_ϕ and K_e are found for the visual measurements. Similarly, a small gain $K_{f\kappa}$ is found for the target and larger gains K_{fv} and $K_{f\omega}$ are found for the disturbances. These results show that the drivers placed more emphasis on disturbance-rejection than target-following compared with previous trials. This is the opposite result to that found in Section 5.5.2 for trials T10 and T11, although Figure 5.19 shows that the single parameter set models do not fit as well for these trials.

In Section 5.5.3 various effects of the simulator motion conditions on the drivers'

control responses are observed. Simulations can be carried out using the single parameter set given in Table 5.4 to investigate whether these effects are predicted by the model. The 'RMS' model is used, since this gives the best overall fit to experimental results, and the steering cost q_δ is fixed at a value of 1. The results of the simulations are shown in Figures 5.20, 5.21, 5.22 and 5.23. They can be compared with the experimental results shown in Figures 5.12, 5.13, 5.14 and 5.15.

In general the predictions of the model demonstrate similar effects to those seen in the experimental results. The steering angles plotted in Figure 5.20 show that the simulated driver steers later and at a lower initial rate with no motion, similarly to Figure 5.12. However with filtered motion the steering response is closer to the zero motion case than the scaled motion case, which is different to the experimental results. Figure 5.21 shows that the predicted path-following error is larger for less realistic motion conditions, similarly to Figure 5.13. However the predicted differences are smaller than those seen in the experiments.

Figures 5.22 and 5.23 also show similar effects to the experimental results presented in Figures 5.14 and 5.15 for the lane change trials. The simulated driver initiates the return phase of the lane change manoeuvre later with filtered rather than scaled motion, resulting in a larger path-following error. However, once again the differences are not as large in the simulations as in the experimental results. This is for two reasons. Firstly, the value of q_δ was kept constant in the simulations whereas in reality the driver's cost function may depend on the motion conditions. Secondly, results given in Sections 5.5.3 and 5.5.4 show that in reality drivers developed an inaccurate, possibly lower-order model of the motion filtering. This would have degraded the driver's steering performance, resulting in larger path-following errors as seen in Figure 5.15. However the fact that the effects of different motion conditions predicted by the model are qualitatively similar to those seen in the experiments is encouraging.

5.6 Discussion

The new driver model incorporating sensory dynamics is updated in Section 5.2 to account for target and disturbance signals consisting of transient events rather than filtered white noise. The model is based on the hypothesis that on average drivers carry out a statistically optimal control strategy within the limitations of their sensory dynamics. With white noise forcing functions this optimal control strategy can be calculated accurately and efficiently. However, when the forcing functions are transient some of the assumptions made in the model break down. It is necessary to approximate the transient signals as random processes

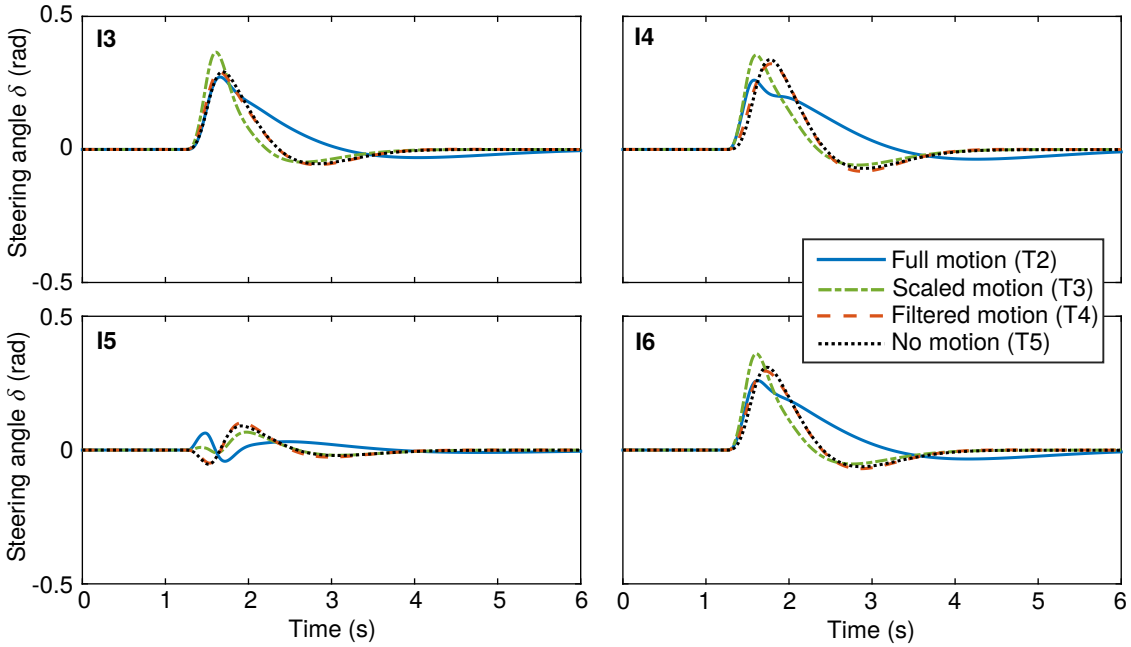

Figure 5.20: Model steering responses to impulse disturbances in straight line trials, for four impulse types with various motion conditions. The same disturbances were used with scaled, filtered and no motion. Smaller amplitude disturbances were used with full motion.

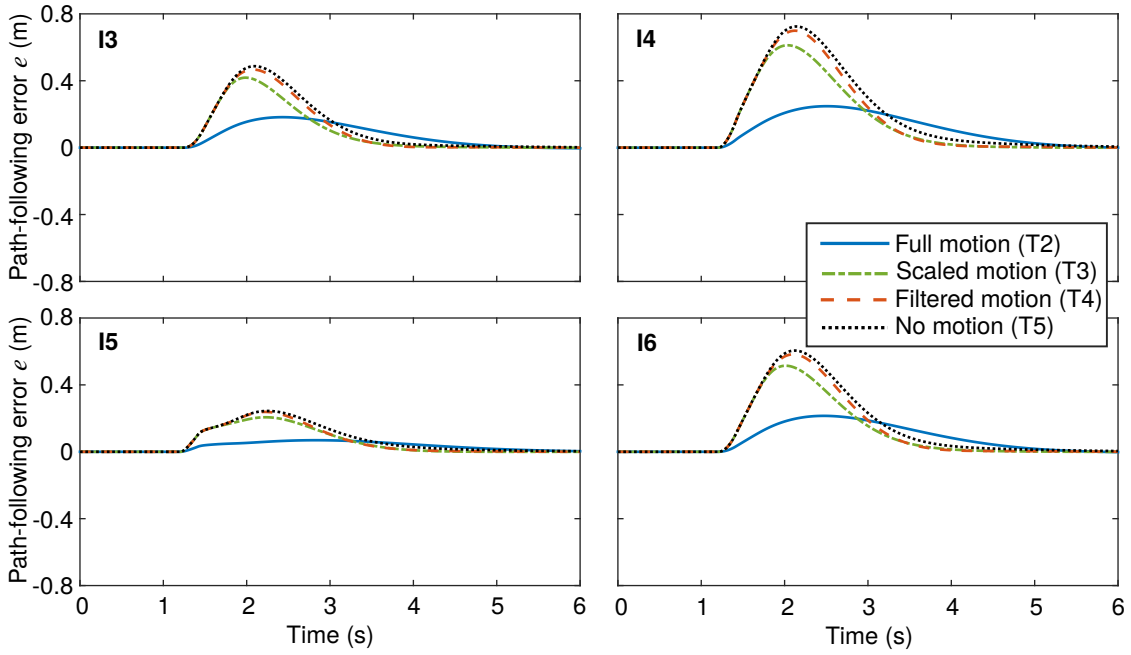

Figure 5.21: Model path-following error from impulse disturbances, for four impulse types with various motion conditions. The same disturbances were used with scaled, filtered and no motion. Smaller amplitude disturbances were used with full motion.

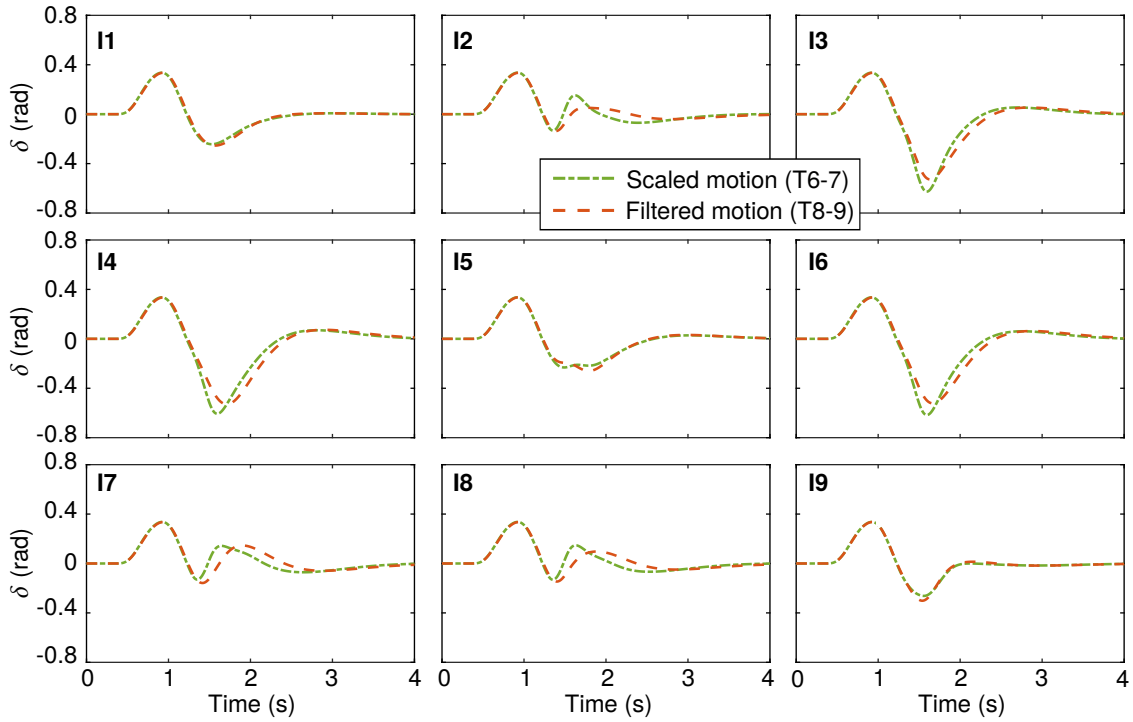

Figure 5.22: Model steering responses to impulse disturbances in straight line trials, for nine impulse types with scaled or filtered motion.

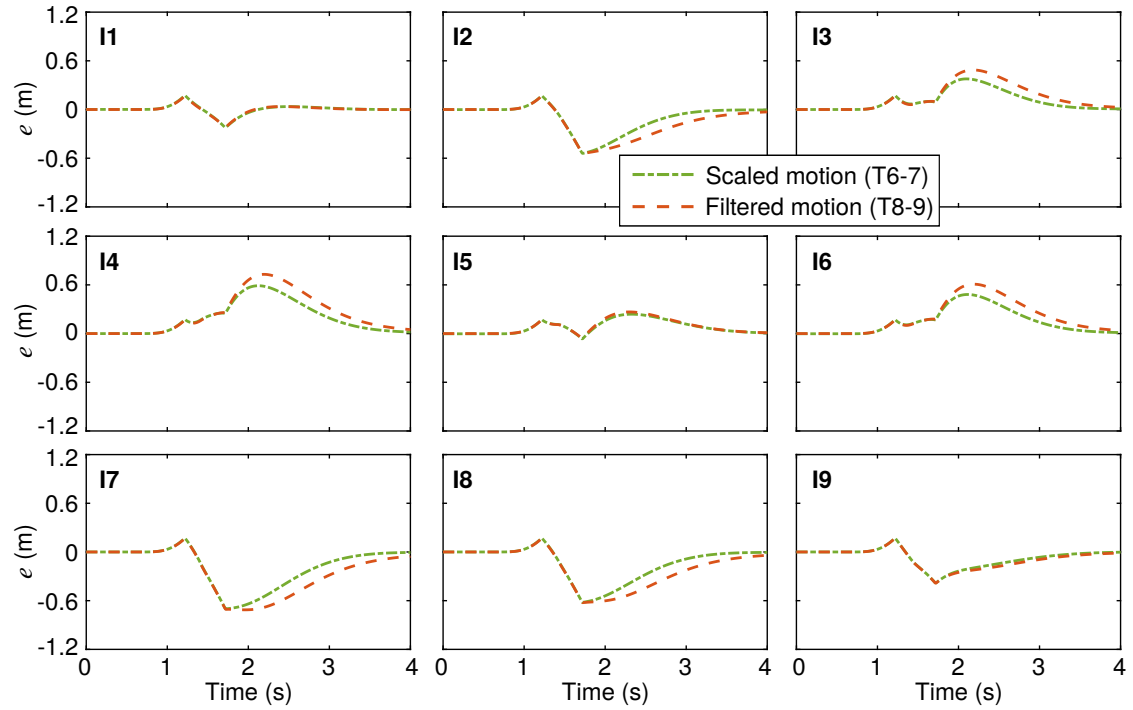

Figure 5.23: Model path-following error with impulse disturbances in straight line trials, for nine impulse types with scaled or filtered motion.

with equivalent filters and amplitudes. However this approximation does not result in a statistically optimal control strategy, as it ignores the time-varying nature of the statistical properties of the signals. It is assumed that drivers' learning and adaptation processes are slow, so that within each trial the driver can be considered as a non-adaptive controller. Results shown in Section 5.5 indicate that this assumption is reasonable.

An experiment was carried out as described in Section 5.3 to investigate the behaviour of real drivers subjected to transient disturbances. One of the challenges of analysing the results of an experiment with transient forcing functions is the lack of useful information in the measured steering signals compared with the experiments carried out in Chapters 3 and 4. With white noise forcing functions the driver must constantly respond to varying target and disturbance signals, resulting in a continuous measurement of driver control responses over the length of the trial. In contrast, transient forcing functions only 'force' the driver for a small fraction of the trial. This makes it difficult to identify reliable estimates of parameter values, since there is insufficient information to separate the effects of different parameters. On the other hand, measurements with transient disturbances give a new perspective on important features of driver steering control, and they also allow differences in a driver's control strategy to be more easily interpreted.

The results of the experiment are analysed in Section 5.5. The five drivers were found to steer in different ways, including one driver who appeared to add an intentional oscillatory disturbance in order to measure the state of the vehicle, following a 'dual control' strategy [227]. This is investigated further in Chapter 7. Parameter values identified in Chapter 4 are used to compare the driver model with the results of trials containing white noise disturbances. The model fits the results well, showing that reliable estimates can be obtained for trials carried out at a different time to the experiments used to identify parameter values, and with some new drivers. The model is also able to fit results from trials with white noise disturbances but a more realistic cornering target.

In general the new driver model is able to fit experimental results well, even when the assumptions of the model no longer strictly match the experimental conditions. For trials with full motion, no motion or scaled motion drivers are able to build an accurate internal model of the motion conditions and react to the perceived motion appropriately. However, when the motion is filtered drivers are found to develop an inaccurate internal model of the filtering, causing their steering behaviour to be somewhat oscillatory. In Section 5.5.4, evidence is presented to show that drivers may perceive filtered motion as scaled in some conditions, replacing the motion filters in their internal model with equivalent scaling factors. This implies that any phase distortions introduced by the motion filters are interpreted by the drivers as disturbances. Motion filters should therefore be carefully designed to minimise these distortions. It should be noted that in these experiments the

drivers had a limited amount of practice time, and with more experience drivers may be able to develop more accurate internal models of the motion filters. However the results indicate that in the absence of sufficient learning time, drivers may rely on a lower-order approximation to the motion filters in their internal model.

In previous chapters, model M2 is found to give a reasonable fit to experimental results under a range of conditions. This model variation assumes that any discrepancies between the real system and the driver's internal model can be included as part of the Gaussian process noise. However the results found in Sections 5.5.3 and 5.5.4 highlight one of the problems with this approach. Gaussian noise should on average have no impact on the predicted control strategy. However more systematic errors in the driver's internal model can reduce the stability of the driver-vehicle system, resulting in oscillatory control responses. Further work is necessary to quantify differences between the true system and the driver's internal model, and to investigate how they affect the steering control performance of the driver.

Measurements from trials with transient impulse disturbances allow differences in driver steering control under various motion conditions to be observed more clearly than with random disturbances. Drivers are found to respond to disturbances earlier and more effectively with physical motion, which agrees with the result found by Wierwille et al. [114] that driver reaction times decrease when physical motion information is available. The simplicity of the motion conditions is also found to affect driver control performance, with drivers following a lane change much better with scaled motion than with filtered motion. This has implications for experiments carried out in driving simulators, either with a fixed base or with limited travel, as drivers may not perform as well as they would in a real vehicle. These results agree with previous studies which have found that physical motion information improves driver performance in a simulator [26, 114, 228]. These effects are replicated using a fixed-parameter model in Section 5.5.5, although differences between motion conditions are not as large as those observed in the experiment. This could be due to drivers' cost functions varying between trials, or drivers developing inaccurate internal models of the motion filtering.

The single parameter set found in Section 5.5.5 fits experimental results reasonably successfully, although neither the RMS nor the maximum signal values give a reliable measure of perceived signal magnitudes under all conditions. Perceived signal magnitudes are likely to depend on a combination of various properties of the signals. The transient disturbance experiment tested drivers under a range of different conditions. However, not all of the conditions are particularly representative of real driving scenarios. Whereas the trials subjected drivers to a series of transient disturbances, in reality such disturbances occur rather infrequently, and are generally superposed onto background random disturbances.

This means that transient disturbances in reality are likely to be unexpected, unlike in the experiments where the drivers were prepared for them. Drivers are therefore likely to judge the signal magnitudes based on the underlying random disturbance signals and then respond to the occasional transient disturbance based on these expectations.

5.7 Conclusion

The new driver model has been updated to account for target and disturbance signals with transient rather than random characteristics, and an experiment was carried out to test real drivers under these conditions. Driver performance was found to depend on the motion conditions, with smaller reaction times and more accurate disturbance rejection when physical motion feedback was present. Furthermore, drivers were found to respond to disturbances more accurately when the physical motion was scaled rather than filtered. These measured effects can be matched by predictions made by the updated driver model, however it is difficult to find a fixed-parameter model to describe transient steering behaviour under all conditions. Perceived magnitudes of transient signals cannot be described fully by either the RMS or maximum values.

Drivers are generally able to develop an accurate internal model of scaled physical motion, however when the motion is filtered drivers are found to rely on a simplified internal model such as equivalent scaling factors, with any phase distortions caused by motion filtering perceived as disturbances. This causes oscillatory steering behaviour and a reduced control performance. Further work is necessary to quantify discrepancies in the driver's internal model and understand how they affect steering control behaviour.

Chapter 6

Control of nonlinear vehicle dynamics

While a linear model can represent the behaviour of a vehicle under normal driving conditions, for more aggressive manoeuvres it is necessary to consider the nonlinear behaviour of the tyres. The driver model developed in previous chapters is therefore extended to account for nonlinear vehicle behaviour, and various nonlinear controllers and state estimators are implemented based on different linearisations of the true nonlinear dynamics. To compare the model predictions with the behaviour of real drivers, an experiment was carried out in a driving simulator with a nonlinear vehicle. Drivers were found to perform better when motion feedback was available, steering less and following the target more closely. Comparing the experimental results with predictions from the driver model shows that drivers are able to account for the time-varying operating point of a nonlinear vehicle. The model is also able to match the behaviour of experienced drivers near the friction limit of the tyres, however further work is necessary to understand how an inaccurate internal model impedes the performance of less experienced drivers.

6.1 Introduction

In previous chapters a new model of driver-vehicle steering control is developed incorporating human sensory dynamics. The new driver model is derived for a linear vehicle, however in more extreme manoeuvres the vehicle may operate near the friction limit of the tyres and the operating point of the vehicle may vary rapidly. It is therefore necessary to develop a model which can describe a driver's control of nonlinear vehicle dynamics.

Control of nonlinear vehicles has previously been motivated by finding the minimum lap time for a racing car [7, 219, 229]. Nonlinear control algorithms are also increasingly being developed for autonomous or semi-autonomous active steering systems [230–232]. However, these applications involve finding an optimal control performance rather than matching the behaviour of a human driver. Various studies have attempted to model the nonlinear control behaviour of a human driver, however they have neglected the effects of

sensory dynamics [19–21, 233]. The aim of this work is to extend the results of previous chapters to develop a more realistic nonlinear driver model that takes account of the limitations of a human driver. For simplicity only constant-speed vehicles are considered, although the same principles could be extended to model a driver's combined lateral and longitudinal control strategy.

An overview of the development of the nonlinear driver model is presented in Section 6.2; for a more detailed mathematical derivation see Appendix A. Simulations were carried out in [234] to compare different approaches to nonlinear control and state estimation, and these results are used to guide the choices made in this chapter. To compare the predictions of the model with the nonlinear steering behaviour of real drivers an experiment was carried out in a driving simulator, as described in Section 6.3. Similarly to previous chapters, a parameter identification procedure is used to fit the model to the results of the experiment. The procedure is adjusted to account for the challenges of finding parameter values for a nonlinear driver model, as discussed in Section 6.4. The results of the experiment and parameter identification are presented in Section 6.5 and discussed in Section 6.6. The main conclusions are summarised in Section 6.7.

6.2 Nonlinear driver model

The new driver model presented in Chapters 3 to 5 is derived for a constant-speed vehicle with linear tyres. To represent a more realistic range of driving conditions the model must be extended to account for a driver's control of nonlinear vehicle dynamics. This requires changes to the plant, state estimator and controller. A more detailed mathematical derivation of the nonlinear driver model is outlined in Appendix A, and preliminary simulations carried out using this model are presented in [234].

6.2.1 Plant

The plant for the nonlinear driver model is very similar to the plant derived for the linear vehicle in Chapter 3, including modifications made to the visual system and target description in Chapters 4 and 5. The only difference between the linear and nonlinear plant is a nonlinear vehicle, in which the states describing the lateral velocity v and angular velocity ω are found from the general equation:

$$\begin{Bmatrix} v(k+1) \\ \omega(k+1) \end{Bmatrix} = A_{\mathrm{V}} \left(\begin{Bmatrix} v(k) \\ \omega(k) \end{Bmatrix}, \delta(k) \right) + \mathbf{B}_{\mathrm{V}(:,2)} f_v + \mathbf{B}_{\mathrm{V}(:,3)} f_\omega \tag{6.1}$$

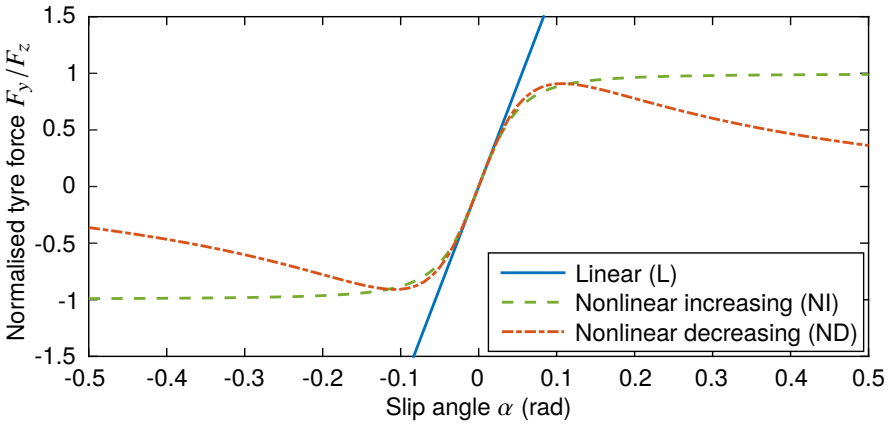

Figure 6.1: Nonlinear tyre force-slip characteristics

where A_V is a nonlinear function. The disturbances are added linearly to the lateral and angular accelerations as explained in Chapter 5. The remaining plant states are linear, so they can be calculated using the linear state-space matrices derived in previous chapters.

In the experiment described in Section 6.3 the nonlinear vehicle was based on the single-track model used in previous chapters, travelling at a constant speed of $U = 40$ m/s. The linear vehicle included tyres with constant cornering stiffnesses C_f and C_r. For the nonlinear vehicle these were replaced with nonlinear tyres, with lateral characteristics described by the 'magic formula' [235]:

$$F_y = F_z D \sin(C \tan^{-1}(B(1-E)\alpha + E \tan^{-1}(B\alpha))) \tag{6.2}$$

For small slip angles this function is approximately linear, so an equivalent linear vehicle can be found by letting $C_f = \mathrm{d}F_{yf}/\mathrm{d}\alpha_f = BCDF_{zf}$ and $C_r = \mathrm{d}F_{yr}/\mathrm{d}\alpha_r = BCDF_{zr}$. Three different tyres were simulated: a linear tyre (L), a nonlinear tyre with force monotonically increasing as a function of slip angle (NI), and a nonlinear tyre with force decreasing past the friction limit (ND). The force-slip characteristics of these three tyres are shown in Figure 6.1, and the nonlinear tyre parameters are given in Table 6.1. All three tyres have the same cornering stiffness at zero slip angle ($C_f/F_{zf} = C_r/F_{zr} = 18$ rad^{-1}). Two different vehicles were simulated, one with understeering characteristics and one with oversteering characteristics. This was achieved by varying the balance of the vertical loads F_{zf} and F_{zr} between the front and rear tyres. For simplicity the remaining parameters were kept the same, including the position of the centre of mass, therefore the difference in lateral loads could be accounted for by changes in the distribution of aerodynamic forces. The parameter values for the two vehicles are given in Table 6.2. In trials NL5–NL8 (see Section 6.3.4) the steering ratio G was lowered to 7 to reduce the steering torque feedback in order to make these trials more comfortable for the drivers.

Table 6.1: Nonlinear tyre parameter values

	Tyre parameters			
Tyre	B	C	D	E
Nonlinear increasing (NI)	12	1.5	1	1
Nonlinear decreasing (ND)	9	2.2	0.909	0.5

Table 6.2: Nonlinear vehicle parameter values

Parameter	Mass m	Length l_f	Length l_r	Force $F_{z\mathrm{f}}$	Force $F_{z\mathrm{r}}$	Moment of inertia I	Steering ratio G	Speed U
Units	kg	m	m	N	N	kgm^2	–	m/s
Understeering vehicle	650	1.85	1.65	9500	15000	450	10	40
Oversteering vehicle	650	1.85	1.65	12000	13000	450	10	40

6.2.2 State estimator

State estimation for a nonlinear plant can be achieved using an extended Kalman filter, which operates on the same principles as the linear Kalman filter used in previous chapters. Extended Kalman filters approximate the nonlinear plant dynamics by linearisation or similar transformations. There are several variations of the extended Kalman filter which can be implemented using code provided by the EKF/UKF Matlab toolbox [236]. These include:

- LKF: Linear Kalman filter. A linear Kalman filter, found by linearising the plant states about zero slip angle.
- EKF1: First-order extended Kalman filter. A linearised approximation to the plant states is found at each time step.
- EKF2: Second-order extended Kalman filter. A quadratic approximation to the plant states is found at each time step.
- UKF: Unscented Kalman filter. The nonlinear state covariance functions are approximated at each time step using an unscented transform.
- FSF: Full state feedback. The state estimate is equal to the real states, removing the effects of sensory dynamics.

Detailed derivations of each of the extended Kalman filters are given in [236]. These state estimators were compared in [234], and the three extended Kalman filters (EKF1, EKF2 and UKF) were found to given identical results under most conditions. Therefore, EKF1 is used for the simulations carried out in this chapter, since it is the fastest to simulate.

FSF was found to result in a better control performance as expected, however it does not account for the sensory limitations of a human driver.

6.2.3 Controller

The aim of the nonlinear controller is to calculate an optimal plant input which minimises the cost function:

$$J = \sum_{k=0}^{\infty} \left\{ q_e e_{\mathrm{vi}}(k)^2 + q_\delta \hat{\delta}(k)^2 \right\} \tag{6.3}$$

similarly to the LQR controller used in previous chapters. Various methods have been implemented in the literature to control a nonlinear vehicle. Early approaches were based on adaptive versions of classical control methods [19, 233], however advances in computing power have increased the feasibility of optimisation-based methods. Full nonlinear optimisation can be achieved using nonlinear programming algorithms [229, 231], however faster performance can be found by linearising the system dynamics [7, 20, 21, 219, 230, 232], and solving based on linear model predictive control (MPC) [237].

Various nonlinear controllers are implemented based on MPC, calculating an optimal control sequence $\hat{\boldsymbol{\delta}}$ over the prediction horizon, then taking the first of these as the next control input $\hat{\delta}$. Whereas the LQR controller used in previous chapters has an infinite control horizon, for the MPC controllers the control horizon is chosen to equal the prediction horizon T_p.

The nonlinear plant equations can be written in discrete-time state-space form:

$$\begin{aligned} \boldsymbol{x}(k+1) &= A(\boldsymbol{x}(k)) + \mathbf{B}\hat{\delta}(k) + \mathbf{G}\boldsymbol{w}(k) \\ \boldsymbol{y}(k) &= \mathbf{C}\boldsymbol{x}(k) + \boldsymbol{v}(k) \end{aligned} \tag{6.4}$$

where $\boldsymbol{x}$ is the plant states, $\boldsymbol{y}$ is the plant outputs, $\hat{\delta}$ is the plant input, $\boldsymbol{w}$ is the process noise (including white noise representations of the target and disturbances) and $\boldsymbol{v}$ is the measurement noise. To reduce the computational load of the controller a reduced plant is defined which includes only the states required by the controller, as explained in Appendix A. The nonlinear state feedback function A can be linearised about states $\boldsymbol{x}_\mathrm{L}(k+n)$, predicted n time steps ahead of the current time step k, with the approximation:

$$A(\boldsymbol{x}(k+n)) \approx A(\boldsymbol{x}_\mathrm{L}(k+n)) + \hat{\mathbf{A}}_n(\boldsymbol{x}(k+n) - \boldsymbol{x}_\mathrm{L}(k+n)) \tag{6.5}$$

where $\hat{\mathbf{A}}_n$ is the Jacobian $\mathrm{d}A/\mathrm{d}\boldsymbol{x}$ evaluated at $\boldsymbol{x}_\mathrm{L}(k+n)$. Five different model predictive controllers are implemented, with varying levels of approximation to the nonlinear plant dynamics as illustrated in Figure 6.2:

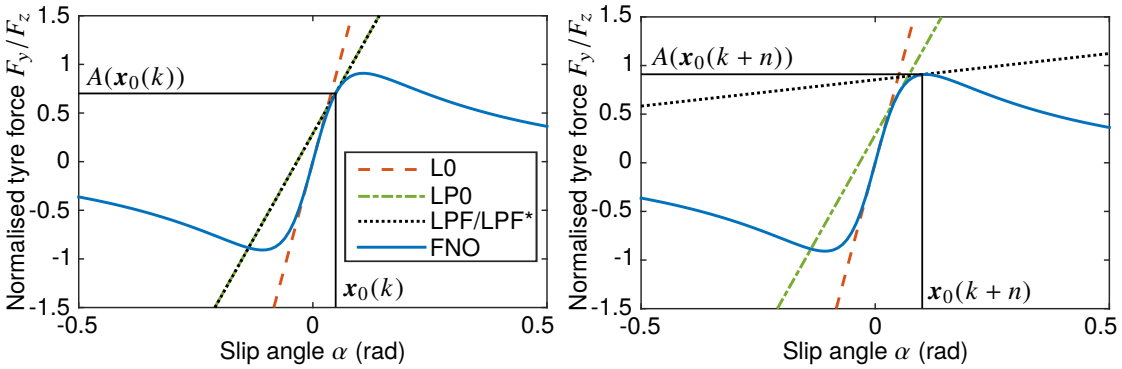

(a) Current time **(b)** Future prediction

Figure 6.2: Illustration of linearisation carried out by different nonlinear controllers

- L0: Linearisation about zero slip angle, $\boldsymbol{x}_{\mathrm{L}}(k+n) = \mathbf{0}$. This gives the same result as the LQR controller derived in previous chapters (assuming the control horizon is sufficiently long).
- LP0: Linearisation about the initial prediction state $\boldsymbol{x}(k)$ [20, 230, 232]. $\hat{\mathbf{A}}$ is constant over the prediction horizon, linearised about $\boldsymbol{x}_{\mathrm{L}}(k+n) = \boldsymbol{x}(k)$.
- LPF: Linearisation about the full prediction horizon [21, 219]. The solution starts from a nominal control sequence $\hat{\boldsymbol{\delta}}_0$, which is the previous optimal sequence shifted by one time step, with a corresponding state trajectory $\mathbf{X}_0 = \begin{bmatrix}\boldsymbol{x}_0(k) & \dots & \boldsymbol{x}_0(k+N_{\mathrm{p}}-N_{\mathrm{vi}}+1)\end{bmatrix}$. The linearised matrix $\hat{\mathbf{A}}_n$ is calculated about each nominal state $\boldsymbol{x}_{\mathrm{L}}(k+n) = \boldsymbol{x}_0(k+n)$.
- LPF*: LPF constrained to stop the slip angles exceeding the force peak, plus a constraint on the maximum change in $\hat{\boldsymbol{\delta}}$ from the nominal control sequence [7].
- FNO: Full nonlinear optimisation [229, 231]. The full nonlinear equations are used to predict the plant trajectory up to the prediction horizon.

A detailed derivation of each controller is given in Appendix A. Simulations were run to compare the five controllers in [234]. In general a trade-off was found between simulation speed and control performance. FNO performed best overall, however in many cases LPF* performed equally well, and it was much faster to simulate. The only scenario in which FNO performed significantly better than LPF* was with an oversteering vehicle and ND tyres, which was particularly difficult to control for all controllers and state estimators.

6.3 Nonlinear experiment procedure

Simulations were carried out in [234] to compare the performance of the various nonlinear state estimators and controllers presented in Section 6.2. However, the best-performing

model does not necessarily correspond to the best model of a human driver, since drivers may exhibit sub-optimal control behaviour or use a simplified internal model of the nonlinear plant. A new experiment was designed and carried out in a simulator to test how human drivers control a constant-speed vehicle with nonlinear tyres. The objectives of the experiment were to:

- measure driver control performance for small perturbations about different operating points on the tyre curve.
- measure driver control performance as the operating point varies through a manoeuvre.
- investigate limitations of driver control near the friction limit of the tyres.

The overall procedure was similar to the experiments described in previous chapters, with drivers following a target line while disturbances were added to the vehicle's lateral and angular velocities. The target line was always fixed to the road so the drivers could preview the upcoming target. The vehicle travelled at a constant longitudinal speed of 40 m/s throughout each of the trials, and the remaining tyre and vehicle parameters are given in Tables 6.1 and 6.2.

6.3.1 Targets

Two different types of target were used in the experiment: a circle to measure driver behaviour for small variations about a non-zero operating point; and a set of corners to measure driver behaviour with a constantly varying operating point. The layout of both targets is shown in Figure 6.3. The circle target consists of a straight line segment which leads into a circle of constant radius R_{circ}. Two different radii were tested, a larger radius $R_{\text{circ1}} = 140$ m and a smaller radius $R_{\text{circ2}} = 70$ m. The cornering target consists of four corners, each following a clothoid profile. The minimum radius varies between the corners, with $R_1 = 78$ m, $R_2 = 65$ m, $R_3 = 71.5$ m and $R_4 = 58.5$ m.

6.3.2 Disturbances

For the trials with the circle target the disturbances were formed from filtered white noise as in Chapters 3 and 4, to investigate responses to stochastic fluctuations about a steady operating point. The disturbance filters $H_{fv}(s)$ and $H_{f\omega}(s)$ were the same as those used in Chapter 5, given in Equations 5.14 and 5.15. For the cornering trials, both filtered white noise disturbances (with spectra given by Equations 5.14 and 5.15) and transient disturbances were tested. The transient disturbances were formed of acceleration impulses as defined in Chapter 5, however the 'shaped' disturbances tested in the experiment in

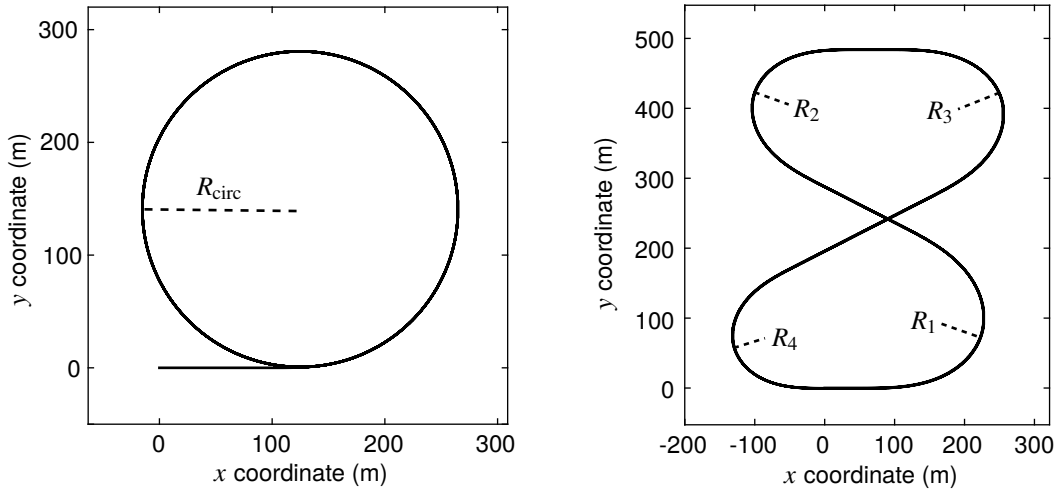

(a) Circle **(b)** Corners

Figure 6.3: Target lines used in the nonlinear vehicle experiment

Chapter 5 were not used, due to the difficulty of implementing these for a large-angle target path. In Chapter 5, various combinations of transient v and ω disturbances were applied to the vehicle at the beginning and middle of each corner. In the nonlinear experiment, the transient v and ω disturbances always had the same sign and acted in the middle of the corner, but their direction relative to the corner was varied. Each of the four corners with different radii was tested with transient disturbances in each direction, plus with no disturbance, giving twelve corner/disturbance combinations per trial.

6.3.3 Motion scaling and filtering

Since the targets all had large steady-state lateral accelerations and steadily increasing yaw angles, trials with scaled or full motion could not be run without exceeding the simulator limits. Therefore each trial had either filtered motion or no motion. For the filtered motion trials, both sway and yaw motion were filtered by high-pass filters given by:

$$H_{\text{HP}}(s) = \left(\frac{s}{s + \omega_{\text{HP}}}\right)^2 \tag{6.6}$$

For the cornering trials, the cutoff frequency ω_{HP} was 4 rad/s. In the circular trials it was possible to have a much lower cutoff frequency of 0.2 rad/s, as the motion was small apart from a large steady-state angular velocity and corresponding centripetal acceleration. However, the transient caused by the entry into the circle would have resulted in a large change in acceleration, therefore physical motion was switched off until 10 s into the trial. The filters were also multiplied by scaling factors of 0.2 for the sway motion and 0.5 for

the yaw motion. Each trial was repeated with and without physical motion using exactly the same disturbance signals, to allow a direct comparison of how the physical motion feedback was used by the drivers.

6.3.4 Trials and procedure

The conditions of each of the trials carried out in the experiment are shown in Table 6.3. There were sixteen trials in total, half using a circular target and half using the cornering target. Each condition was repeated with and without physical motion feedback, using exactly the same disturbances so that the performance of the drivers with and without motion could be compared directly.

Each trial began without disturbances to allow the drivers to get used to controlling the vehicle. Disturbances began after 15 s for the circle trials, and after 2 corners for the cornering trials. The circle trials with radius R_{circ1} (NL1–NL4) were carried out first, with the order of these trials randomised. They were followed by the circle trials with radius R_{circ2} (NL5–NL8) in a random order. Each of the trials with a circle target lasted 120 s. The cornering trials with the understeering vehicle (NL9–NL12) were then carried out in a random order, followed by the cornering trials with the oversteering vehicle (NL13–NL16)

Table 6.3: Conditions of each trial for the nonlinear vehicle experiment

		Disturbances					
Trial	**Target**	**Type**	W_v (m/s^{2*})	W_ω (rad/s^{2*})	**Motion**	**Vehicle**	**Tyre**
NL1	Circle R_{circ1}	White noise	31.6	15.8	Filtered	Understeering	L
NL2	Circle R_{circ1}	White noise	31.6	15.8	None	Understeering	L
NL3	Circle R_{circ1}	White noise	31.6	15.8	Filtered	Understeering	NI
NL4	Circle R_{circ1}	White noise	31.6	15.8	None	Understeering	NI
NL5	Circle R_{circ2}	White noise	23.7	11.9	Filtered	Understeering	NI
NL6	Circle R_{circ2}	White noise	23.7	11.9	None	Understeering	NI
NL7	Circle R_{circ2}	White noise	23.7	11.9	Filtered	Understeering	ND
NL8	Circle R_{circ2}	White noise	23.7	11.9	None	Understeering	ND
NL9	Corners	White noise	23.7	11.9	Filtered	Understeering	NI
NL10	Corners	White noise	23.7	11.9	None	Understeering	NI
NL11	Corners	Transient	–	–	Filtered	Understeering	NI
NL12	Corners	Transient	–	–	None	Understeering	NI
NL13	Corners	White noise	15.8	7.9	Filtered	Oversteering	NI
NL14	Corners	White noise	15.8	7.9	None	Oversteering	NI
NL15	Corners	Transient	–	–	Filtered	Oversteering	NI
NL16	Corners	Transient	–	–	None	Oversteering	NI

in a random order. Each of the cornering trials lasted 170 s. The experiment was carried out by the same five drivers as the transient disturbance experiment described in Chapter 5. Drivers 1 to 4 are normal drivers and driver 5 is a professional test driver.

6.4 Parameter identification

In previous chapters, parameter values are identified to optimise the fit of the driver model to experimental results using a procedure which combines a genetic algorithm with a gradient search optimisation. This procedure is effective in finding optimal values of several parameters simultaneously, however to find reliable parameter values each optimisation requires many thousands of simulations of the driver model. The nonlinear model takes much longer to simulate than the linear model, so it is not feasible to identify a large number of parameter values in the same way. Therefore, where possible parameter values for the nonlinear driver model are taken from previous work, and only the necessary parameters are identified.

It is assumed that the addition of nonlinear vehicle dynamics should not significantly affect the parameter values for the model, since the parameters describe the physical systems of the driver rather than the vehicle. Most of the parameters are therefore set to the values identified in Chapter 4, given in Table 4.7. Signal-dependent relationships have been found for the driver noise amplitudes, for the process noise in Chapter 3 and measurement noise in Chapter 4, allowing noise amplitudes to be estimated based on the corresponding RMS signal amplitudes. In Chapter 4 the RMS value for the previewed road angles is calculated over the entire vector $\boldsymbol{\phi}$, however in Chapter 5 it is found to be more appropriate to link the previewed angle noise amplitude to the RMS value of the first previewed angle ϕ_0. To give equivalent results using this method the signal-to-noise ratio SNR_ϕ should be reduced to a value of 1.04, therefore this value is used for simulations using the nonlinear driver model.

Experiments carried out in Chapter 5 showed that for signals containing significant transient components it is not always appropriate to calculate noise amplitudes based on the RMS signal amplitude. Therefore, several equivalent signal magnitudes M are defined for the steering angle and each sensory measurement, and equivalent forcing function amplitudes W'_κ, W'_v and W'_ω are used in the driver's internal model. For a trial with a large-angle transient target and white noise disturbances, results from Chapter 5 show that equivalent magnitudes for most signals can be set equal to their RMS values, although a suitable equivalent target amplitude W'_κ must be identified. Trials with transient disturbances require equivalent magnitudes to be identified for the plant input and outputs,

Table 6.4: Equivalent signal magnitudes identified for nonlinear driver model. Identified parameter values are given by a bullet (•).

Disturbances	M_a	M_ω	M_ϕ	M_e	M_δ	W'_v	W'_ω	W'_κ
White noise	RMS(a_{ve})	RMS(ω_{ve})	RMS(ϕ_0)	RMS(e_{vi})	RMS(δ)	W_v	W_ω	•
Transient	•	•	•	•	•	•	•	•

and the forcing functions. The equivalent magnitudes identified for different trials from the nonlinear experiment are summarised in Table 6.4. In addition, the steering cost weight q_δ is identified for each trial since it can vary depending on the choice of the driver.

The preview time T_p is identified in Chapter 4 to be 0.87 s. However, the LQR controller has an infinite control horizon, and uses an internal model of the target spectrum to predict future values of the target ahead of the prediction horizon. In the nonlinear model the control horizon is equal to the prediction horizon, therefore it may be necessary to use a larger value of T_p. One possible value is 1 s, since eye-tracking studies have measured that drivers focus on a point on the road around 1 s ahead of them [6, 71, 79, 80]. Alternatively, a preview time of 2 s allows the simulated driver to account for vehicle behaviour twice as far into the future. The identification procedure is run with values of T_p = 0.87 s, 1 s and 2 s to investigate which value best describes the behaviour of real drivers.

Simulations carried out in [234] showed that all nonlinear state estimators perform similarly, therefore the fastest (EKF1) is used in the identification procedure. FNO is the best performing controller, however it is matched closely by LPF* under all conditions except an oversteering vehicle with ND tyres. This condition was not tested in the experiment, therefore controller LPF* is expected to give an optimal performance for all trials. Since LPF* is much faster than FNO, LPF* is used in the identification procedure and FNO is run once at the end to check it gives identical results. While these controllers minimise the cost function most successfully, real drivers may be unaware of the full nonlinear dynamics or may use simplifications to reduce their mental load, resulting in a sub-optimal control performance. To test this hypothesis, parameter values are also identified for controller LP0, and for a combination of controller L0 and state estimator LKF. As in previous chapters, Box–Jenkins models are identified to fit the results of each trial, however since the plant is nonlinear this no longer gives an upper bound on the fit of the parametric driver model.

Due to numerical issues the RMS difference between the measured and modelled steering angle does not vary smoothly with the parameter values. This means that gradients of the optimisation function cannot be calculated reliably, so the gradient search method cannot be used. Parameter values are therefore identified using a genetic algorithm only,

with 10 iterations and a population of 12. This should be sufficient to give a reasonable estimate of the two optimal parameters in the trials with white noise disturbances, however it may lack the accuracy of previous estimates. In previous chapters, measurements from all five drivers are averaged to give results for an average driver, with lower noise levels than the separate measurements. However this is not possible for nonlinear trials, since the principle of superposition does not apply with nonlinear dynamics. Therefore parameter values are identified separately for each trial and driver.

6.5 Results

The results of the nonlinear vehicle experiment and the parameter identification procedure can be analysed in various ways. In Section 6.5.1 the experimental results are used to compare the performance of the five drivers and investigate the effects of physical motion feedback. The agreement between the predictions of the driver model and the measured results is quantified in Section 6.5.2. Simulations are run in Section 6.5.3 to investigate the extent to which the driver model can match steering behaviour observed in the experiment, and in Section 6.5.4 the performance of drivers and the model near the friction limits of the tyres is investigated.

6.5.1 Driver steering performance

Steering angles and path-following errors measured during two corners of trial NL15 are plotted for each driver in Figure 6.4. This trial had a cornering target and transient disturbances were added in the middle of the corners. The steering signals of the different drivers all contain a significant oscillatory component, with a frequency and an amplitude which are consistent over time and between the drivers, although the phase varies between drivers. Since the oscillation is consistent and does not change in mid-corner it does not appear to be caused by the disturbances. A similar oscillation is seen for one of the drivers in Chapter 5. As discussed, this oscillation may be evidence of a dual-control strategy, where drivers add a deliberate oscillation and measure the response of the vehicle in order to estimate the vehicle operating point. Some of the drivers indicated in their comments that this was a strategy they were deliberately carrying out. Dual control strategies for determining the vehicle operating point are discussed further in Chapter 7. In the section of trial NL15 plotted in Figure 6.4, drivers 1 and 4 had larger overall path-following errors than the other drivers, both being consistently around 0.5 m away from the target line. This could be because some drivers do not factor small steady-state path-following errors into their cost function as significantly as others.

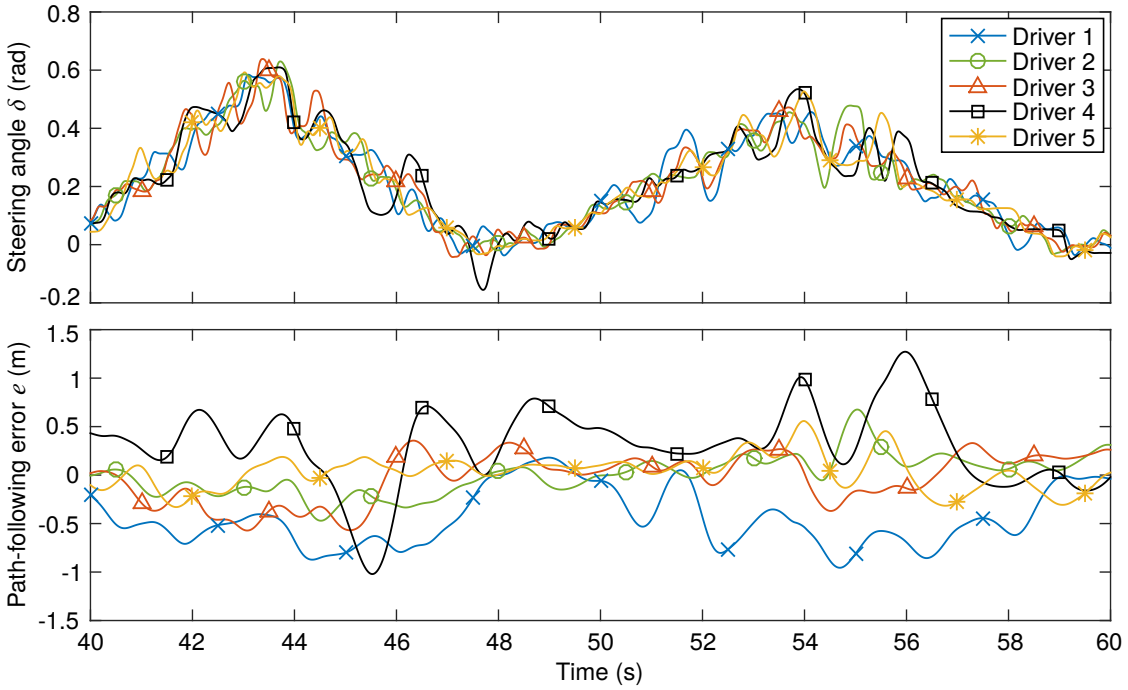

Figure 6.4: Measured steering angles and path-following errors for all drivers during two corners of trial NL15, with radii R_4 and R_1 and transient disturbances added in mid-corner

Eight pairs of identical trials were carried out with and without physical motion feedback. This allows the influence of physical motion on the drivers' control performance to be determined by comparing these pairs of trials directly. The percentage change in RMS steering angle and path-following error when motion feedback was added is shown in Figure 6.5. The percentages are found with respect to the largest RMS value within each pair, giving a symmetric percentage difference between -100% and 100%. The median value over the five drivers for each pair of trials is also shown in Figure 6.5, chosen instead of the mean due to outliers caused by accidental spins or skids in some of the trials.

Figure 6.5 shows that the addition of physical motion allowed the drivers to control the vehicle better. With physical motion drivers were able to steer less while also following the target line more closely. These results agree with findings from previous chapters indicating that physical motion information is useful to drivers, and show that this can be true even when the motion is filtered. It is possible that physical motion is even more important for a nonlinear vehicle, as it is necessary for the driver to estimate the nonlinear operating point to be able to control the vehicle effectively. Physical motion feedback gives the drivers extra information which they can use to calculate the operating point of the vehicle more accurately.

The performance of each driver in each trial from the nonlinear vehicle experiment is compared in Figure 6.6. There is considerable variation between trials, which may

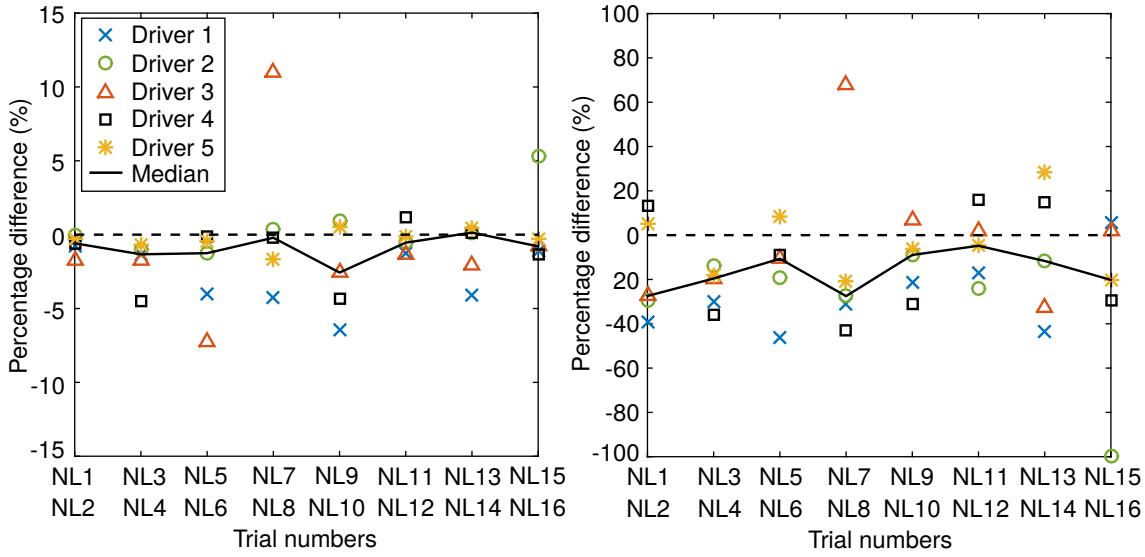

(a) Steering angle δ **(b)** Path-following error e

Figure 6.5: Change in RMS steering angle and path-following error with physical motion. Percentage differences are plotted for each driver and the median over the five drivers.

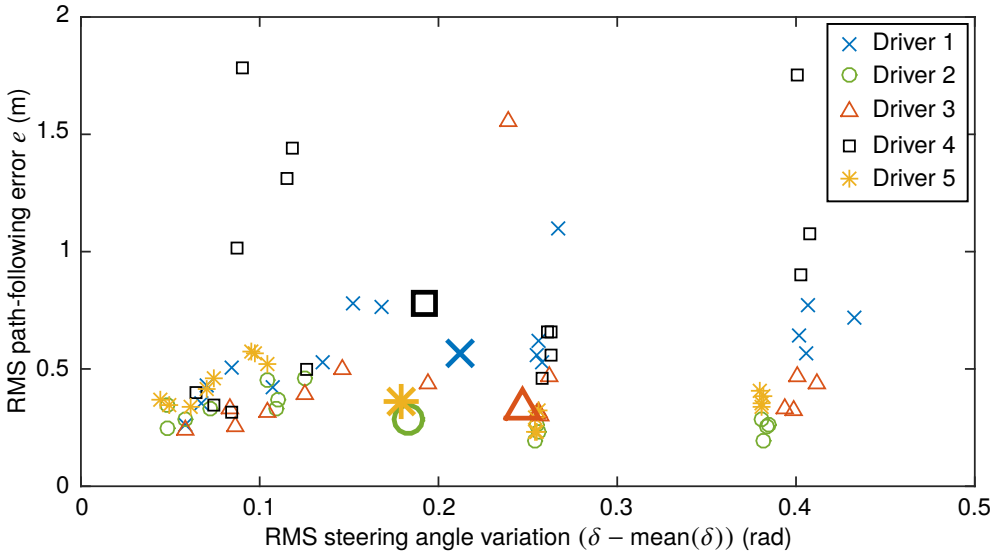

Figure 6.6: Comparison of performance of each driver in nonlinear experiment. Individual trials are shown by small markers, the median over all trials is shown by large markers.

be partly a result of varying conditions; in particular the cornering trials required larger steering variations than the circular trials. Differences are also partly due to the control performance of the drivers in each trial. In a few trials the driver-vehicle system became unstable, resulting in path-following errors which were too large to fit within the axis limits in Figure 6.6. The median values for each driver are shown in Figure 6.6 by the large markers. Clear differences can be seen between the drivers. In general, the path-following

error would be expected to decrease as the steering angle variation increases, with drivers who put in more effort able to follow the path more closely. This is the case for drivers 1, 3 and 4, however drivers 2 and 5 performed better than the others on both counts. This may indicate differences in experience between the drivers, and since driver 5 is a professional test driver these results are consistent with expectations.

6.5.2 Driver model fit

Various possible approaches to nonlinear state estimation and control are proposed in Section 6.2. These methods were implemented and simulations were used to compare the performance of each combination of controller and state estimator in [234]. In general, the more complicated implementations were found to take longer to simulate but result in a better control performance. It is not known whether human drivers can carry out true optimal control of a nonlinear vehicle, or whether they use simplifications similar to the controllers and state estimators presented in Section 6.2. Therefore the predictions of various combinations of controller and state estimator are compared with the experimental results to investigate which combination best describes the control behaviour of a human driver. Similarly to previous chapters, the fit of the driver model to the experimental results is quantified by calculating the variance accounted for (VAF). VAF values for different combinations of controller and state estimator are plotted in Figure 6.7.

In general the VAF values are high. This is partly due to the large low-frequency target-following components which dominate the steering response, however it also shows that all the controller/state estimator combinations can predict measured driver steering behaviour. There is a large variation in VAFs between drivers, showing that the control of some drivers is more predictable than others, which could result from different levels of experience. VAFs are largest for drivers 2 and 5, who are also shown to be the better-performing drivers in Figure 6.6. Low VAFs are seen for trial NL16 with driver 2, due to the car undergoing a large skid in a particular section of this trial, however apart from this the model fits the results of driver 2 well.

Differences between models are difficult to see in Figure 6.7 due to the large VAF values, therefore the difference between the VAF found for each combination and the value found for LPF*/EKF1 is plotted in Figure 6.8. For trials NL1 to NL4 (with the large radius circular target) all models fit the results similarly, showing that for low-slip manoeuvres it is not necessary to consider the varying operating point of the nonlinear tyres. However for the other trials significant differences are seen between models. The largest VAFs are for LPF*/EKF1, showing that drivers are able to consider the nonlinear operating point of the vehicle, including how it might vary over the prediction horizon. In many cases this

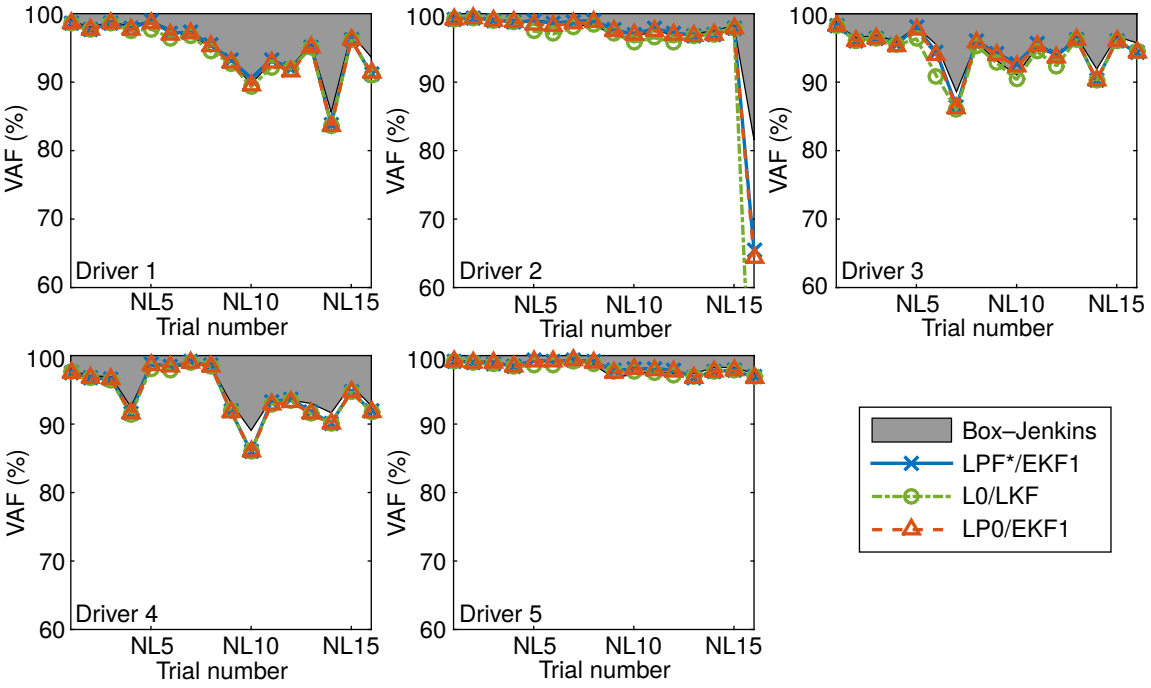

Figure 6.7: VAF values for various nonlinear driver models, with $T_\mathrm{p} = 1$ s. Trials NL1 to NL8 had a circle target and trials NL9 to NL16 had a cornering target.

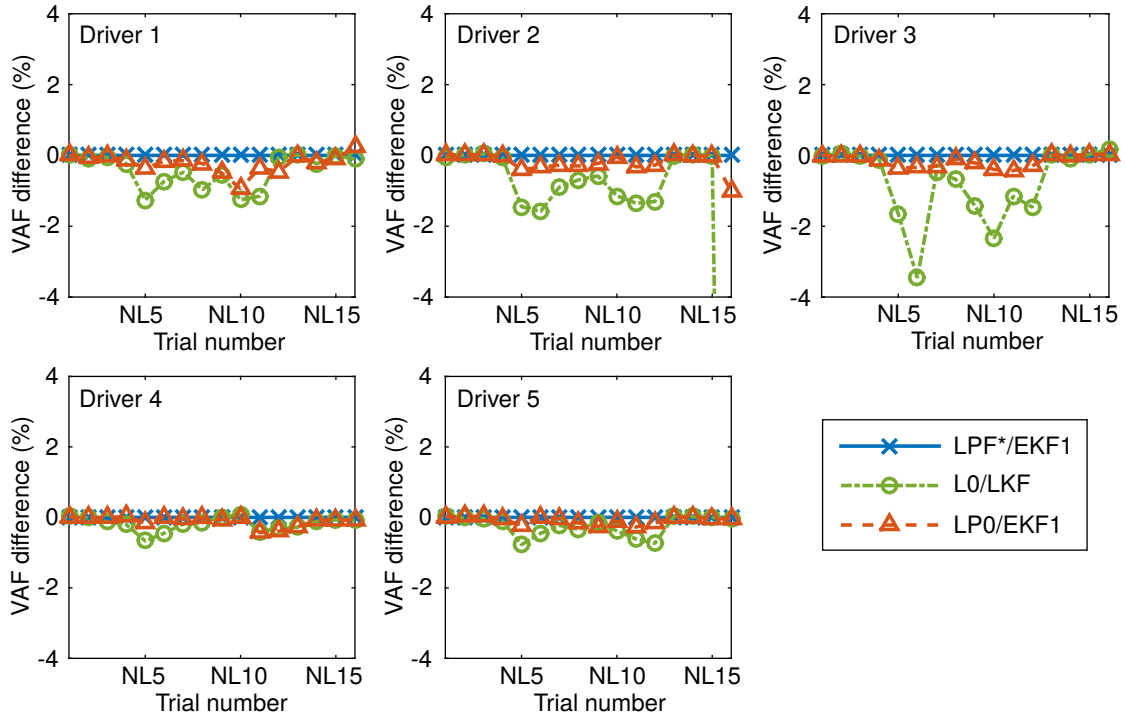

Figure 6.8: Difference between VAF values with various nonlinear driver models, and with controller LPF* and state estimator EKF1. Preview time is $T_\mathrm{p} = 1$ s.

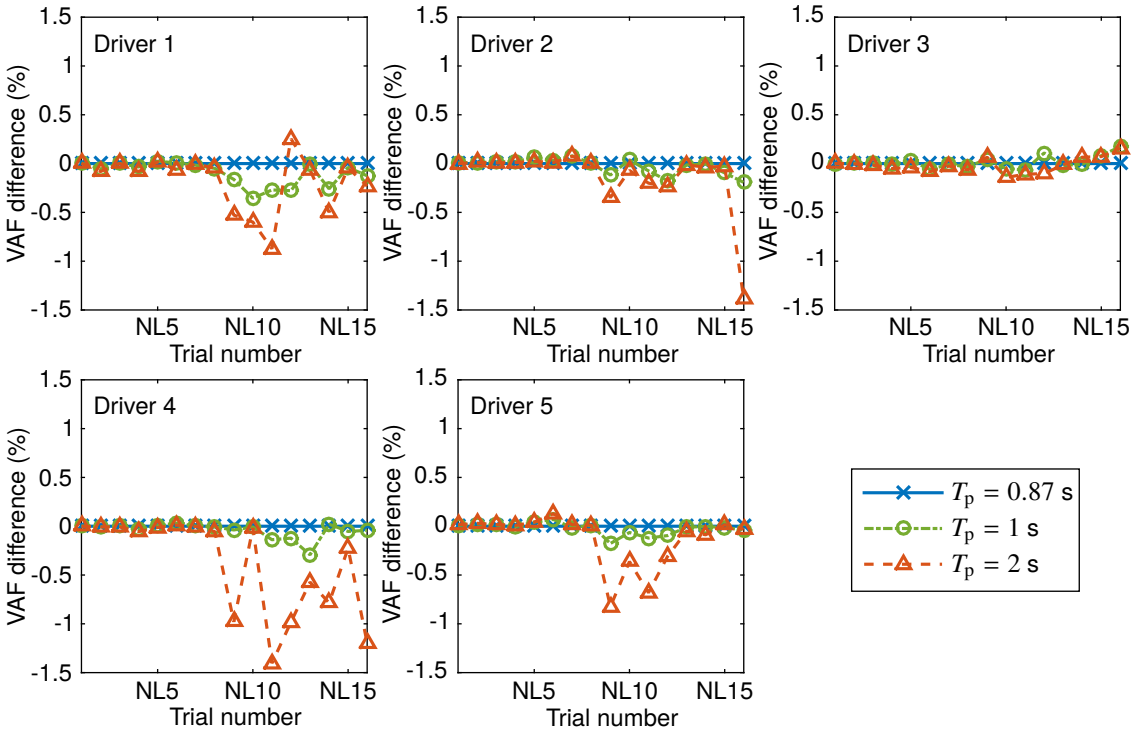

Figure 6.9: Difference between VAF values with various preview times and with $T_p = 0.87$ s, using EKF1 and LPF*

model is seen in Figure 6.7 to fit better than the Box–Jenkins model, showing that no linear model can fully capture the control behaviour of the drivers.

Parameter values are identified for model LPF*/EKF1 with three different preview times, $T_p = 0.87$, 1 and 2 s. The differences between the VAFs found for each preview time and the results found for $T_p = 0.87$ s are plotted in Figure 6.9. Some variation can be seen between the drivers. For drivers 1, 3 and 4 the shorter preview times generally fit the results better. For drivers 2 and 5, who had larger overall VAF values in Figure 6.7, the longer preview times fit better for the circular trials and the shortest preview time fits best for the cornering trials. There is little difference between preview times of 0.87 s and 1 s (which is expected as the values are similar) however the VAFs are significantly lower in many trials for a preview time of 2 s. Therefore a preview time of around 1 s is an appropriate choice to match observed steering behaviour. This is consistent with results from eye-tracking studies [6, 71, 79, 80], indicating that drivers do not predict the motion of the vehicle past the point at which they direct their gaze.

Parameter values identified for each of the trials are shown in Figure 6.10, averaged over the five drivers. Trials with transient disturbances (NL11, N12, NL15 and N16) are excluded as the number of identified parameters is too large for these trials to give reliable values with the limited number of iterations of the identification procedure. For

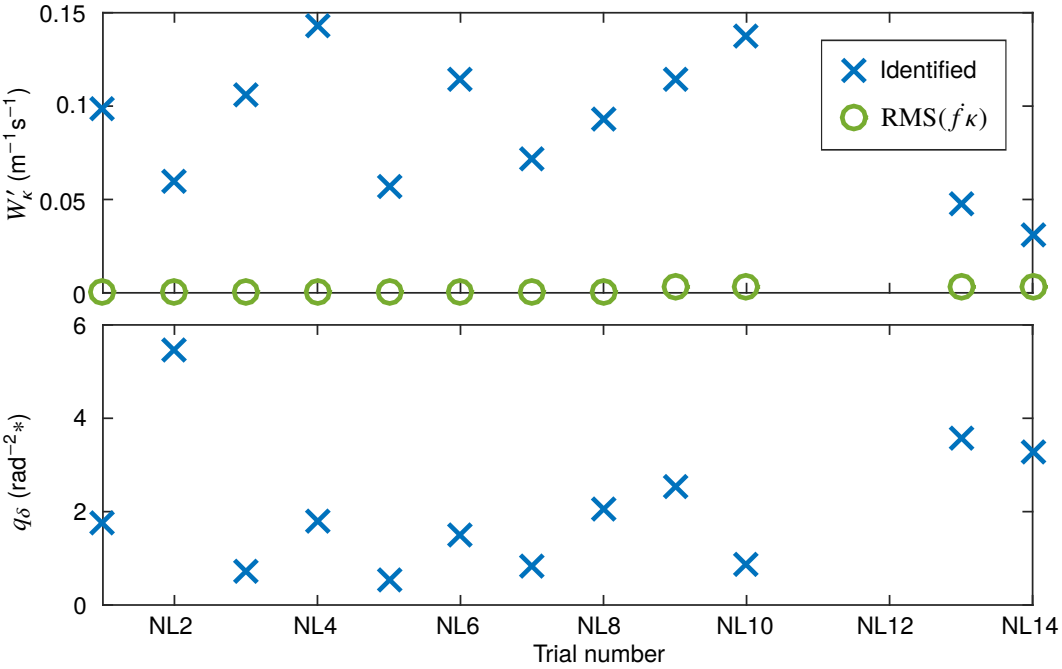

Figure 6.10: Mean parameter values identified for trials with white noise disturbances, using controller LKF* with $T_\mathrm{p} = 1$ s. Identified parameters are the steering cost weight q_δ and the equivalent target magnitude W'_κ.

the remaining trials with white noise disturbances two parameter values are identified, the equivalent target magnitude W'_κ and the steering cost weight q_δ. Figure 6.10 shows that there is some variation in the values of q_δ and W'_κ identified for different trials, however the values remain within a similar order of magnitude. The identified value of q_δ is around 2 rad^{-2}* on average, and the identified value of W'_κ is generally around 0.1 m^{-1}s^{-1}. This is much larger than the corresponding RMS signal amplitudes (which are zero for the circular trials). As in Chapter 5, it is difficult to find a consistent link between the properties of the target and the identified equivalent magnitudes.

Simulations are also run with controller FNO, using the parameter values identified for LPF*. The resulting steering angles are almost identical, showing that in the conditions tested LPF* is able to find the optimal nonlinear steering signal. This is expected, as LPF* and FNO have been found to give identical values under almost all conditions [234].

6.5.3 Predicted effects of physical motion

Simulations can be carried out to determine the extent to which the driver model can predict effects seen in the measurements taken from real drivers. The main aim of these simulations is to find whether the model predicts the effects of adding physical motion feedback seen in Section 6.5.1. The experimental results show that the addition of physical

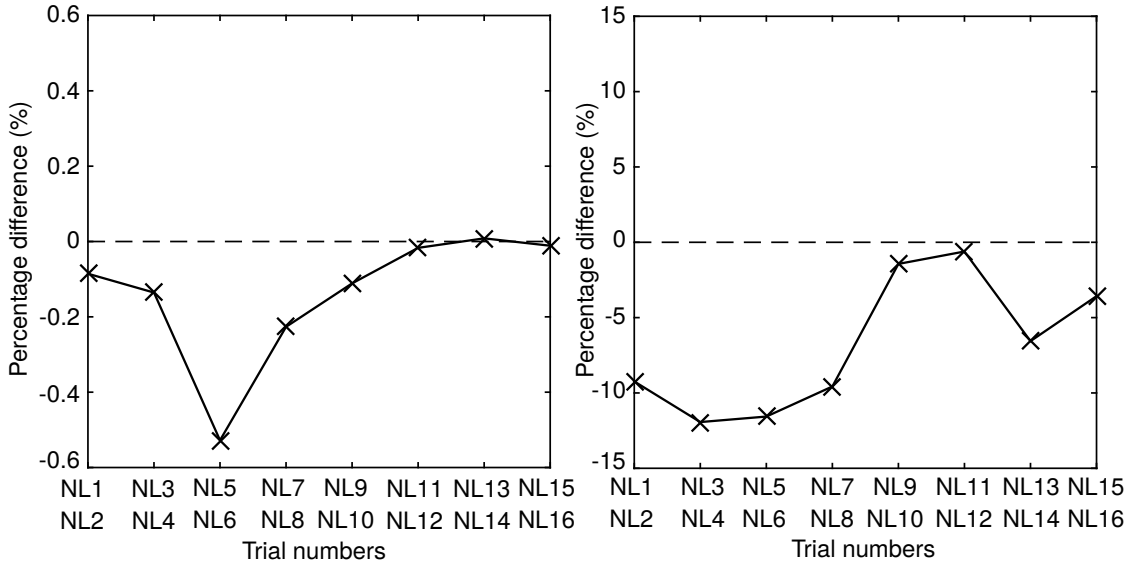

(a) Steering angle δ **(b)** Path-following error e

Figure 6.11: Predicted change in RMS steering angle and path-following error with physical motion, calculated using simulations of the nonlinear driver model with LKF* and EKF1.

motion allowed drivers to steer less and follow the target path more accurately on average.

Based on the results shown in Section 6.5.2, controller LPF* and state estimator EKF1 are used for the simulations. Parameter values for the model are fixed using values found in previous experiments, as discussed in Section 6.4. Approximate average values of $q_\delta = 2$ rad^{-2}* and $W'_\kappa = 0.1$ m^{-1}s^{-1} are taken from Figure 6.10. RMS signal magnitudes in each trial are the median of the RMS values measured for the five drivers. The predicted percentage differences in RMS steering angle and path-following error with the addition of physical motion are plotted in Figure 6.11. These can be compared with the experimental results shown in Figure 6.5. In general the percentage differences are smaller in magnitude for the simulations in Figure 6.11 than the experimental results in Figure 6.5. This may be a result of driver noise or internal model discrepancies in the measured results. However the overall trends are the same, with the addition of physical motion predicted to allow the driver to steer less and follow the target path more closely.

6.5.4 Performance near friction limits

One of the objectives of the experiment, defined in Section 6.3, was to investigate the performance of drivers near the friction limits of the tyres. The experiment was carefully designed to push the drivers near the limit on occasion without being so difficult that they were not able to control the vehicle. On a few occasions drivers did lose control of the vehicle, in which case the trials were repeated to get a complete set of data. However this

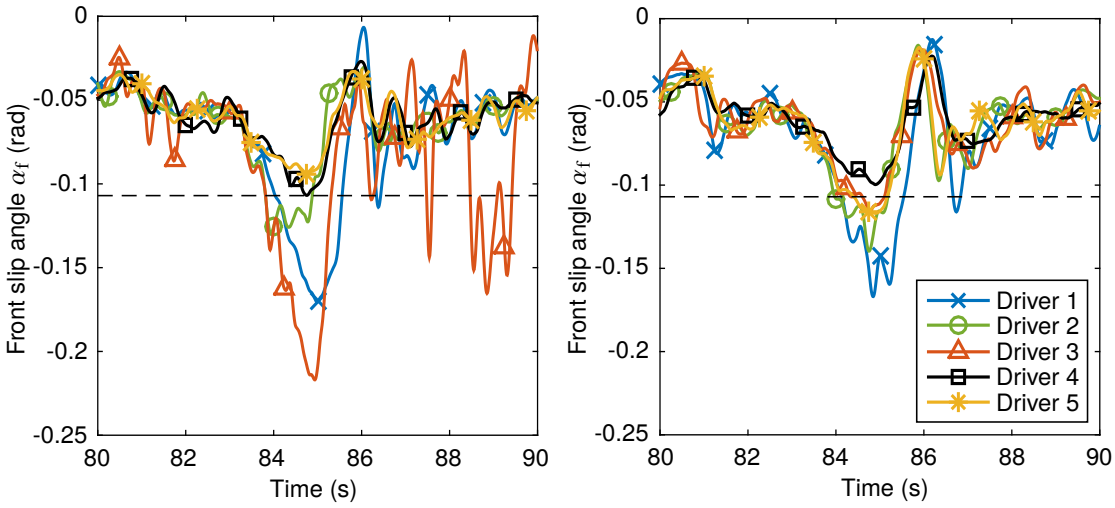

(a) Trial NL7 (motion) **(b)** Trial NL8 (no motion)

Figure 6.12: Front slip angle for each driver during a period of trials NL7 and NL8. These trials are identical except for the inclusion of physical motion feedback in trial NL7. The friction limit of the tyre is given by the horizontal dashed line.

shows that real drivers sometimes have trouble controlling a vehicle near the friction limit.

Figure 6.12 shows a particular period of trial NL7, and the identical trial NL8 with no physical motion feedback, where the random disturbances pushed the vehicle near the friction limit of the tyres. The effects of this depend on the driver's control actions, and it is clear that there is some variation between drivers and over the two trials. In trial NL7 drivers 4 and 5 both managed to keep the vehicle within the friction limit, which is likely to result in a better control performance. Driver 2 exceeded the friction limit briefly but was able to reduce the slip angle again quickly. Driver 1 went further into the negative-slip region of the tyre, and exhibited a degree of oscillatory control before the vehicle was stabilised again. Driver 3 started in a very similar position to driver 2, however driver 3 was unable to control the vehicle effectively, going far into the negative slip region and losing stability for several seconds afterwards.

In trial NL8 driver 4 once again stayed within the friction limit, however driver 5 exceeded it briefly. Drivers 1 and 2 both exceeded the friction limits by similar amounts to trial NL7. Driver 3 controlled the vehicle similarly to driver 5, indicating that the instability seen in Figure 6.13a may have been a random occurrence. Drivers are modelled as having stochastic measurement and process noise perturbations, and the performance plotted in Figure 6.12 depends in part on how these random signals happened to affect the steering control at that crucial point of the trial. However, differences between drivers may also be caused by systematic differences in control strategy, which could depend on experience or internal model accuracy. For example, in trial NL7 drivers 2 and 3 started off in similar

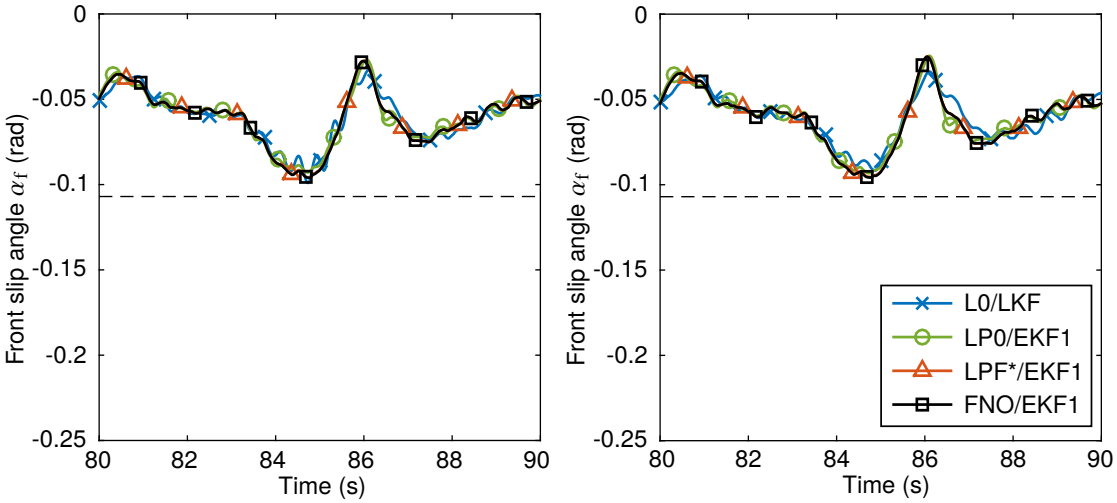

(a) Trial NL7 (motion) **(b)** Trial NL8 (no motion)

Figure 6.13: Simulated front slip angle for a period of trials NL7 and NL8. These trials are identical except for the inclusion of physical motion feedback in trial NL7. The friction limit of the tyre is given by the horizontal dashed line.

positions due to the combination of the disturbances and the driver noise, however driver 2 was able to recover control of the vehicle quickly whereas driver 3 underwent a significant period of instability. Over the course of the experiment these differences led to observable differences in performance, as seen in Figure 6.6.

It is difficult to determine the effects of adding physical motion feedback on control performance near the limit by comparing Figures 6.12a and 6.12b. Since each line only shows one run of a small section of each trial, most differences are likely to result from random driver noise. However, some general patterns can be observed. At around 86 s the average slip angles are closer to zero for trial NL8 than trial NL7. This could be a result of drivers overreacting to reduce the slip angle as quickly as possible. With physical motion feedback drivers were generally able to bring the slip angle within the limits without losing as much lateral slip, which allowed them to follow the circular target line more closely. Over the course of the experiment this could have led to the improved path-following performance found with the addition of physical motion feedback in Section 6.5.1.

The corresponding slip angles predicted by the various combinations of controller and state estimator tested in Section 6.5.2 are plotted in Figure 6.13. These are found by simulating the driver models with the conditions described in Section 6.5.3. In general all combinations perform similarly, although small differences are seen and there is an oscillatory component for the linear model. All combinations avoid going past the friction peak of the tyre, which is likely to be because no driver noise is added during the simulations. There is also very little difference between the slip angles with and without physical

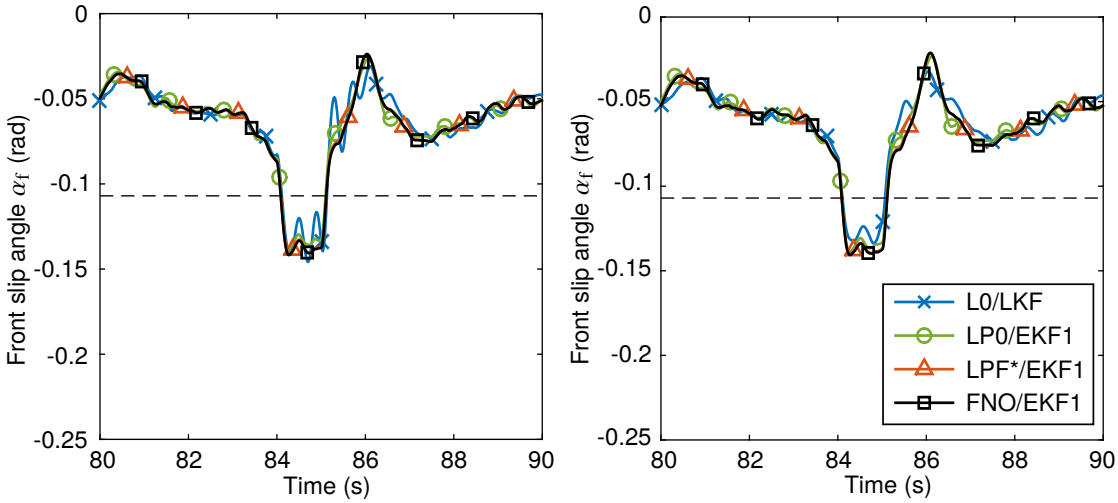

(a) Trial NL7 (motion) **(b)** Trial NL8 (no motion)

Figure 6.14: Simulated front slip angle for trials NL7 and NL8, with driver noise added to push the vehicle past the friction limit. These trials are identical except for the inclusion of physical motion feedback in trial NL7. The friction limit of the tyre is given by the horizontal dashed line.

motion feedback. The slip angles look very similar to the signals plotted for drivers 4 and 5 in Figure 6.12a, showing that the models give a good description of the behaviour of more successful drivers near the friction limit. However they may not be able to represent a driver who is less able to control the nonlinear vehicle near the limit of friction.

The slip angles plotted in Figure 6.13 avoid exceeding the peak force of the tyre since there is no driver noise in the simulated signals. To test how the controllers behave past the peak, a short transient impulse is added to the process noise w at 84 s. The resulting slip angles are plotted in Figure 6.14. All combinations are able to control the vehicle, although the prediction of the linear model has a significant oscillatory component. This indicates that the drivers who are shown to have more difficulty stabilising the vehicle in Figure 6.12 may have an incomplete or simplified internal model of the system dynamics. The slip angle peak at 86 s is slightly closer to zero for trial NL8 than for trial NL7, which is similar to the measured results shown in Figure 6.12.

6.6 Discussion

The driver model developed in previous chapters is extended to account for a driver's control of nonlinear vehicle dynamics. Various candidate controllers and state estimators are proposed, as outlined in Section 6.2. A preliminary study was carried out to compare the control performance and computational efficiency of these methods [234]. An experiment

was designed to investigate the extent to which these models represent the control behaviour of human drivers, as described in Section 6.3, and a parameter identification procedure described in Section 6.4 is used to fit the driver model to experimental results.

Analysis of the measured steering signals in Section 6.5.1 shows that the drivers' steering actions contained significant oscillatory components. This is similar to a result found for one driver in Chapter 5. It is thought that this could indicate a 'dual control' strategy, where the driver adds a known oscillation and measuring the response of the vehicle to try to determine the vehicle operating point. This is investigated further in Chapter 7. The addition of motion feedback helped drivers steer with less effort and follow the target path more closely. This agrees with results found in previous studies [222, 228, 238], and shows that fixed-base simulators may result in worse driver performance than moving-base simulators or a real vehicle. Simulations described in Section 6.5.3 demonstrate a similar reduction in steering angle and path-following error with the addition of physical motion, showing that the driver model is able to predict effects seen in the experiment. The reduction is smaller in the simulations than the measured results, which could be a result of driver noise causing larger differences between the two scenarios. Alternatively, the absence of physical motion may result in the driver building up a less accurate internal model, resulting in a further reduction of the driver's control performance.

In general the nonlinear driver model is able to match experimental results well, although the fit is better for better-performing drivers, including an experienced professional driver. The model is a better representation of more experienced drivers than the sub-optimal behaviour of inexperienced drivers. For trials involving low-slip manoeuvres a linear driver model can fit as well as a nonlinear model, showing that the linear driver model developed in previous chapters is a reasonable approximation for normal driving conditions. However, for more extreme manoeuvres the best fit to measured driver behaviour is found using a model which considers the full time-varying nonlinear dynamics of the vehicle. This shows that drivers are able to take account of a changing nonlinear operating point. A slightly longer preview time of 1 s fits measured results slightly better than the 0.87 s identified in previous chapters, which be may a result of the finite control time for the MPC controllers. The value of 1 s is similar to preview times measured in eye-tracking studies [6, 71, 79, 80], indicating that drivers generally direct their gaze towards the furthest road information that they consider in their control calculation. It is possible, however, that drivers use more distant previewed information when planning a target trajectory [7, 219].

Various combinations of controller and state estimator are shown in Section 6.5.4 to be able to control the vehicle beyond the tyre friction limit. Previous models used constraints to keep the tyres below the friction peak [7], however the results shown in Section 6.5.4

indicate that this is not always necessary. Simulations presented in [234] indicate that linearised controllers have difficulty controlling an oversteering vehicle past the friction peak, so the performance of the controllers past this peak may depend on the dynamics of the vehicle. The measured performance of the various drivers near the friction limits of the tyres is compared in Section 6.5.4. Some drivers performed better than others, which could be due to a combination of stochastic driver noise and differences in experience and ability. The performance of the best drivers was similar to the driver model prediction, showing that the model is able to predict experienced drivers' behaviour well. Less experienced drivers found it harder to control the vehicle, resulting in some large unstable oscillations in steering angle. Similar oscillations are found when simulating the driver model using a linear controller and Kalman filter, so the measured behaviour of inexperienced drivers may result from inaccuracies in the drivers' internal models. Previous studies have used multiple linearised internal models to represent differences in drivers' awareness of the nonlinear vehicle behaviour [21]. Further investigation is required to understand the learning processes used by drivers to develop an internal model of a nonlinear vehicle, and how an inaccurate internal model can affect a driver's control performance.

6.7 Conclusion

The linear driver model developed in previous chapters has been modified to represent a driver's control of a nonlinear vehicle. This is an improvement on previous nonlinear driver models which have not considered the sensory dynamics of the driver. An experiment was carried out in a simulator to measure how real drivers control a vehicle with nonlinear tyres. The addition of motion feedback was found to help drivers to steer less aggressively, and follow the target path more closely. For manoeuvres involving large slip angles a nonlinear driver model accounting for the time-varying nonlinear operating point fits the measured results best, particularly for more experienced drivers. The model is also able to provide accurate predictions of the effects of adding motion feedback and the performance of more experienced drivers near the limit of friction. Further work is necessary to understand the learning processes used to build up an accurate internal model, and how poorly developed internal models affect the control strategy of less experienced drivers.

Chapter 7

Driver model applications and limitations

The role of human sensory dynamics in car driving is investigated in previous chapters using a new driver model identified to fit experimental results. In this chapter the predictions, applications and limitations of the new model are explored through a series of simulations. New techniques are developed to allow reliable simulations without reference to experimental data, and these are used to explore how sensory dynamics affect a driver's perception and performance. A simple optimisation of a vehicle parameter is carried out, and the new driver model is shown to predict difficulties real drivers have controlling unstable vehicles, unlike an ideal driver model with full state feedback. This result allows vehicle systems to be designed to fit a real driver, considering performance and stability simultaneously. The simulations presented in this chapter highlight the advantages of using driver models incorporating sensory dynamics to design vehicle systems which interact more naturally with the human driver.

7.1 Introduction

A new model of driver steering control is developed in Chapters 3 to 6 which incorporates the sensory dynamics of a human driver. The complete model is summarised in Appendix A, and is a significant extension of previous models which represent an 'ideal' driver with no sensory dynamics, delays or noise [12–14]. The driver controls a plant combining the open-loop dynamics of the vehicle with the driver's neuromuscular and sensory systems. The 'ideal driver' model assumes that the driver has full state feedback, whereas in reality the driver must estimate the plant states based on noisy, filtered, delayed sensory measurements. A series of experiments was carried out in a driving simulator in Chapters 3 to 6, to compare the predictions of the model with measured steering behaviour. The new model is able to fit the results of the experiments well, showing that it is representative of the steering control strategy used by human drivers.

The work described in previous chapters focuses on the development, identification and validation of the new driver model. In this chapter the applications of the new model are explored through simulations implemented to answer several important questions which may be of interest to automotive engineers. The new model can give an insight into how human drivers perceive and use sensory measurements, as shown through simulations presented in Section 7.4.1. It can also be used to investigate the performance of human drivers in various circumstances, as summarised in Section 7.4.2. Furthermore, a realistic driver model can allow vehicle designers to evaluate the driver-vehicle system in closed loop in order to optimise the design and set-up of the vehicle, as shown in Section 7.4.3. In some cases the new model incorporating sensory dynamics is compared with an ideal driver model with full state feedback, to highlight the advantages of including sensory dynamics in a driver model.

In previous chapters, predictions from simulations using the driver model are compared with results from experiments carried out by human drivers. However, often it is desirable to obtain simulated results without going through a time-consuming and expensive testing process. To carry out reliable simulations without measured data for reference some adjustments must be made to the simulation procedure. Several new techniques to allow reliable simulations without corresponding experimental data are presented in Section 7.2. There is a large range of situations which could be simulated using the new driver model, therefore a set of default conditions is chosen to limit the scope of the investigations and allow each simulation to focus only on the important variables. These conditions are defined in Section 7.3.

The simulations presented in this chapter are not intended to represent an exhaustive list of all the potential uses of the new driver model, nor are they always a perfect match to realistic driving conditions. They aim to illustrate the potential applications and limitations of the new model and motivate further research. It is also hoped that some of the simulation results are interesting to automotive engineers, and highlight the importance of considering drivers' sensory dynamics. There is considerable potential for applying these techniques to real-world problems, and extending them to investigate further implications of sensory dynamics for driver steering control.

7.2 Simulation techniques

In Section 7.4 various simulations are presented to explore the predictions of a driver model incorporating sensory dynamics. This model is developed in previous chapters using measurements from experiments undertaken by human drivers. However, to extract reliable

predictions from the new model it is necessary to be able to run repeatable simulations without relying on any measured results. Various techniques are developed to achieve this, as described in Sections 7.2.1 to 7.2.3.

7.2.1 Calculating expected values

The new driver model is derived based on statistical principles, and includes various signals which are approximated as Gaussian white noise. It is possible to generate approximate white noise signals and include these as inputs to the driver model, however since these are random signals they will change each time the simulation is repeated. It is often necessary to find a reliable, consistent estimate of the expected value of a signal based on the statistics of the random inputs. This can be achieved using spectral analysis theory [239].

For a linear time-invariant system $y(j\omega) = H(j\omega)u(j\omega)$, with one input u, one output y and transfer function $H(j\omega)$, the power spectral density (PSD) $S_y(\omega)$ of the output is given by:

$$S_y(\omega) = |H(j\omega)|^2 \, S_u(\omega) \tag{7.1}$$

where $S_u(\omega)$ is the PSD of the input. The expected RMS value of y for a single-sided spectrum is given by:

$$\mathrm{E}\left[\mathrm{RMS}(y)\right] = \sqrt{\int_0^\infty S_y(\omega)\,\mathrm{d}\omega} \tag{7.2}$$

Simulated Gaussian white noise can be generated by choosing a random sequence of numbers from a normal distribution. This gives noise with a constant spectral density at all frequencies up to the Nyquist frequency $\omega = \pi/T_\mathrm{s}$. If the input u is zero-mean Gaussian white noise with variance σ_u^2, the input PSD is given by:

$$S_u(\omega) = \begin{cases} T_\mathrm{s}\sigma_u^2/\pi & 0 \le \omega \le \pi/T_\mathrm{s} \\ 0 & \text{otherwise} \end{cases} \tag{7.3}$$

If the system $y(j\omega) = \mathbf{H}(j\omega)\boldsymbol{u}(j\omega)$ has several uncorrelated white noise inputs $\boldsymbol{u}$, the output PSD is equal to the sum of the output PSD values resulting from each input separately, calculated using Equation 7.1. The expected RMS value can then be calculated as usual from Equation 7.2. This method can be implemented to find expected values of signals calculated using the linear driver model. The transfer function $\mathbf{H}(j\omega)$ which gives the desired output based on the stochastic forcing function and driver noise inputs must be derived, taking account of the closed-loop driver-vehicle system. Equations 7.1 and 7.2 can then be used to calculate the expected RMS value of the signal based on the RMS

forcing function and driver noise amplitudes. The resulting expected value is repeatable and does not depend on the specific values of any random signals. This procedure is only valid for a linear model; for the nonlinear model the expected signal values can only be found approximately through simulation with randomly generated noise signals.

7.2.2 Finding consistent signal and noise magnitudes

Experimental results from Chapter 3 indicate that the process noise magnitude W depends linearly on the magnitude of the steering angle RMS(δ), with a constant signal-to-noise ratio SNR_W. Similarly, in Chapter 4 measurement noise is found to be signal-dependent, with constant SNRs for each sensory channel plus thresholds η below which the noise amplitude remains constant. When fitting the driver model to experimental results in previous chapters, the RMS signal magnitudes can be taken directly from the measurements. However, when running simulations without corresponding measurements from human drivers these RMS values are not known until after the simulation. Since these values vary with the driver model parameters there is a circular dependence between RMS signal magnitudes and driver noise magnitudes. To produce a reliable simulation of driver behaviour it is necessary to find a consistent set of RMS signal and noise magnitudes, based on the identified SNRs and thresholds.

An iterative procedure can be used to achieve a consistent set of RMS signal and noise magnitudes, as illustrated in Figure 7.1. Initially the driver model is simulated based on an arbitrary estimate of the RMS signal amplitudes. These values are then updated with the expected RMS signal amplitudes from the simulation, calculated using the procedure described in Section 7.2.1, and the process is repeated iteratively. This procedure is able to converge on a consistent set of RMS values, except in cases where the driver-vehicle system becomes unstable (see Section 7.4.2.2).

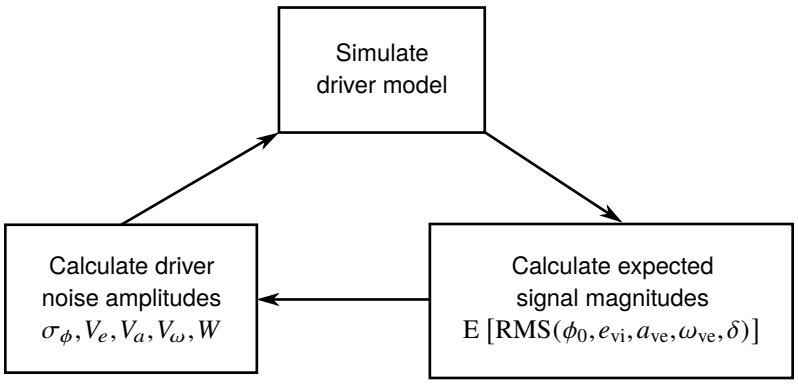

Figure 7.1: Iterative procedure used to find consistent signal and noise magnitudes

7.2.3 Equivalent scaling factors

Experiments were carried out in Chapter 4 to investigate the extent to which drivers in a simulator are able to adapt to scaling or filtering of the physical motion feedback. In general drivers were found to be able to build an accurate internal model of motion scaling, however they found it more difficult to do so for filtered motion. Evidence was found in Chapter 5 to indicate that drivers may assume that motion is scaled rather than filtered, perceiving any filtering distortions as disturbances. Modelling this requires substituting the real motion filters $H_{\mathrm{m}a}(s)$ and $H_{\mathrm{m}\omega}(s)$ with 'equivalent scaling factors' (ESFs) in the driver's internal model estimates $H'_{\mathrm{m}a}(s)$ and $H'_{\mathrm{m}\omega}(s)$. To investigate how such a misunderstanding of the motion filtering may affect a driver's control performance, a procedure is defined to find ESFs for a given set of filtering conditions.

The results found in Chapters 4 and 5 do not give a clear indication of how ESFs depend on the properties of the motion filters. It is plausible that the driver might judge the scaling of the motion based on differences between the amplitudes of motion perceived through their visual and vestibular systems. One way to model this is to define the ESFs as the ratio between the expected RMS values of the signals perceived by the vestibular system with motion filters and the expected values with full motion. This can be written mathematically as:

$$H'_{\mathrm{m}a}(s) = \frac{\mathrm{E}\left[\mathrm{RMS}(a_{\mathrm{ve}})\right]}{\mathrm{E}\left[\mathrm{RMS}(a_{\mathrm{ve}}) \mid H_{\mathrm{m}a}(s) = 1\right]} \tag{7.4}$$

$$H'_{\mathrm{m}\omega}(s) = \frac{\mathrm{E}\left[\mathrm{RMS}(\omega_{\mathrm{ve}})\right]}{\mathrm{E}\left[\mathrm{RMS}(\omega_{\mathrm{ve}}) \mid H_{\mathrm{m}\omega}(s) = 1\right]} \tag{7.5}$$

The expected values are calculated using the method described in Section 7.2.1. The driver model is then simulated iteratively as described in Section 7.2.2 to give a consistent set of ESFs in addition to signal and noise magnitudes. This procedure has some limitations, as the vestibular transfer functions shape the expected values in a different way to the visual system, however it is a simple way of calculating reasonable ESFs.

The new driver model assumes that drivers have a near-perfect internal model of the system dynamics, with any discrepancies modelled as white Gaussian process noise. However, this neglects the potential effects of more systematic internal model discrepancies, which may affect the performance and stability of the driver-vehicle system. There are a number of ways in which such discrepancies could occur, of which replacing motion filters with ESFs is one possibility. The results of simulations with this substitution can be used to gain a general insight into how internal model discrepancies might affect the performance of a driver.

7.3 Default simulation conditions

The new driver model can be used to simulate a wide range of scenarios by changing the characteristics of the modelled driver, vehicle or target and disturbance signals. Simulations are presented in Section 7.4 which give a general introduction to some of the potential applications of the new model. To allow each simulation to focus only on the important variables a default set of conditions is defined, which is used for all simulations except where otherwise indicated. For a real application the simulation conditions can be adjusted to match the particular scenario being studied.

To allow the simulations to be compared with results from previous chapters, many of the conditions are chosen to match those used for the experiments carried out by human drivers. In general a linear vehicle is used, since this allows simulations to be run much more quickly and expected signal values to be calculated reliably using the procedure described in Section 7.2.1. The vehicle parameters are those given for the base vehicle in Table 3.1, with a constant longitudinal speed $U = 40$ m/s. Disturbances are added directly to the lateral and yaw accelerations as described in Chapter 5. In simulations of the nonlinear driver model, the understeering vehicle parameters given in Table 6.2 are used with the nonlinear increasing tyre parameters from Table 6.1.

In Chapter 5 it is found to be difficult to define a fixed set of parameter values to model a driver's response to transient disturbances, since the noise magnitudes are dependent on the characteristics of the transient signals. Furthermore, the procedure described in Section 7.2.1 for finding expected signal magnitudes relies on the forcing functions being formed from filtered white noise. Therefore all simulations presented in Section 7.4 use filtered white noise target and disturbance signals. This is a reasonable approach for vehicle design and evaluation, since the results are dependent on the general statistical properties of the target and disturbances rather than one specific realisation of the signals.

The disturbance filters $H_{fv}(s)$ and $H_{f\omega}(s)$ are given by Equations 5.14 and 5.15, with RMS magnitudes $W_v = 30$ m/s^2* and $W_\omega = 25$ rad/s^2*. This matches the spectra of the disturbances used in Chapter 5, and each disturbance requires a similar level of steering response from the driver. The target filter is chosen to give a curvature profile similar to real driving, with larger low-frequency components than the targets used in previous chapters, given by:

$$H_{f\kappa}(s) = \left(\frac{1}{s+1}\right)^2 \tag{7.6}$$

with $W_\kappa = 0.15$ m^{-1}*. To represent driving a real car, motion filters $H_{\mathrm{m}a}(s)$ and $H_{\mathrm{m}\omega}(s)$ are set to unity.

Most of the driver parameters are set to the identified values given in Table 4.7. Following the results of Chapter 5, SNR_ϕ is adjusted to a value of 1.04, with the signal magnitude M_ϕ defined as $\text{RMS}(\phi_0)$. All other signal magnitudes are defined by the RMS values, found using the iterative procedure described in Section 7.2.2. A value of 1 is used for the cost function weight q_δ, which is a reasonable average of values found in previous chapters. In general it is assumed that the driver has a perfect internal model of the plant, although a few simulations explore the implications of internal model discrepancies by replacing the motion filters with ESFs as described in Section 7.2.3. Simulations are also run for an 'ideal' driver model, which has full state feedback and no process or measurement noise. This removes the effects of sensory dynamics and delays, and is in line with previous models of driver steering control [12–14].

7.4 Simulations and results

Simulations are run using the new driver model to test the predictions of the model, understand the model's limitations and motivate further research. The simulations are designed to answer various questions which may be of interest to automotive engineers. These questions are split into three categories: those relating to the driver's perception are presented in Section 7.4.1; results concerning the performance of the driver are shown in Section 7.4.2; the implications of using the new model for the design of vehicles are investigated in Section 7.4.3.

7.4.1 Perception

The new driver model includes representations of the physical systems used by drivers to perceive vehicle motion. It is possible to use the model to explore how these sensory systems operate during driving, what they perceive and how the measurements are used.

7.4.1.1 How does each sensory measurement affect the driver's control action?

A Kalman filter is used in the new model to represent the driver's integration of sensory measurements from their visual and vestibular systems. The measurements are combined to give an optimal state estimate based on an internal model of the system and estimates of the process and measurement noise magnitudes. Using the linear relationship between signal and noise magnitudes identified in previous chapters, it is possible to use the driver model to explore how each sensory measurement is used under different conditions.

Transfer functions can be found between each of the sensory measurements and the simulated steering angle, using the principle of linear superposition to split the steering

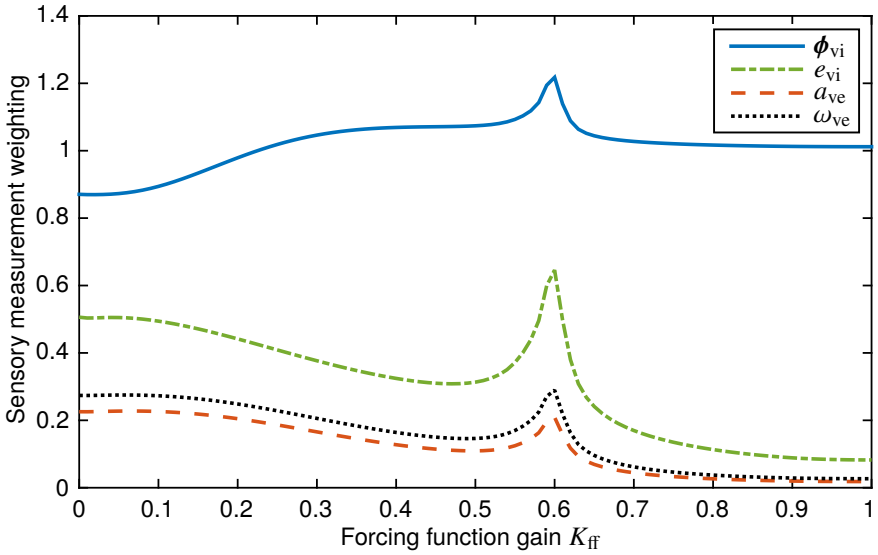

Figure 7.2: Sensory weightings with various forcing function amplitudes. Weightings show the proportion of steering angle RMS resulting from each sensory measurement with the task varying between disturbance-rejection and target-following.

signal into contributions from each measurement. The procedure described in Section 7.2.1 is used to calculate the expected RMS values of the steering angle contribution from each sensory measurement. These values are then divided by the total expected steering angle RMS in order to give a measure of the relative weighting of each of the sensory measurements.

To investigate how a driver's use of sensory measurements depends on the control task, relative weightings are found for various target and disturbance forcing function amplitudes. A forcing function gain K_{ff} is varied from 0 to 1, such that $W_\kappa = 0.15K_{\mathrm{ff}}$ m^{-1}*, $W_v = 30(1 - K_{\mathrm{ff}})$ m/s^2* and $W_\omega = 25(1 - K_{\mathrm{ff}})$ rad/s^2*. This gives a task which transitions from disturbance-rejection only (following a straight target path) at $K_{\mathrm{ff}} = 0$ to target-following only at $K_{\mathrm{ff}} = 1$.

The relative weightings of the sensory measurements for different levels of target and disturbance signals are shown in Figure 7.2. The weightings add up to more than 1 since the contributions of the different measurements are sometimes out of phase with each other, so combine destructively. In all cases the visual measurements, particularly the previewed target angles $\boldsymbol{\phi}_{\mathrm{vi}}$, are weighted much more highly than the vestibular measurements. For the disturbance-only task ($K_{\mathrm{ff}} = 0$) each vestibular measurement is weighted around a quarter as strongly as the previewed target. However as the task becomes increasingly target-following the influence of the vestibular measurements generally decreases while the previewed target weighting increases. For pure target-following there is a small non-zero weighting on the vestibular measurements, which is likely to be a result of the feedback

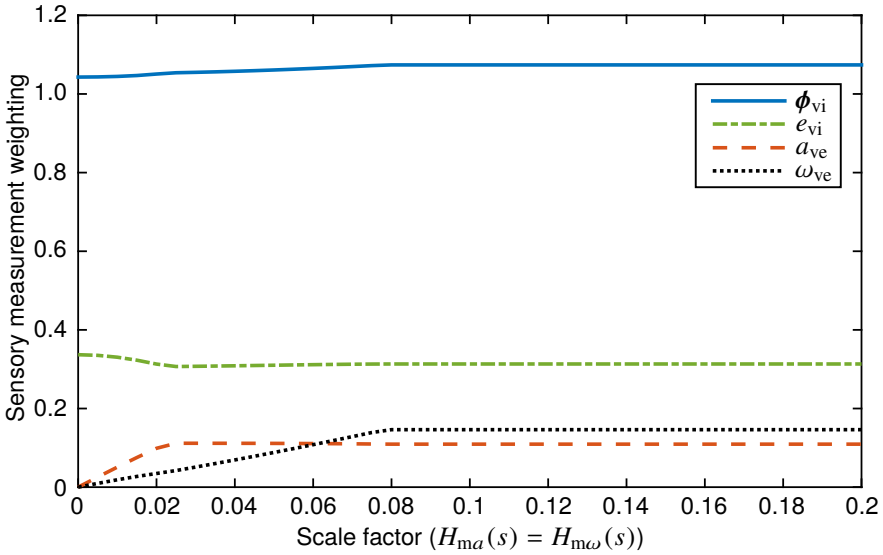

Figure 7.3: Sensory weightings with various scaling factors on the physical motion feedback.

component introduced by driver noise. There is a peak in all responses for K_{ff} around 0.6, where the different sensory measurements interact particularly destructively.

To investigate how a driver's use of sensory measurements depends on signal amplitude, relative sensory weightings are also found with the lateral and yaw physical motion scaled by various factors from 0 to 1. The results are shown in Figure 7.3. For signals which are above threshold levels, the sensory weightings are independent of signal amplitude. This is a result of the signal-dependent measurement noise; when the signal amplitude increases the noise level increases in proportion, therefore the overall reliability of the signal is unchanged. Below threshold levels sensory weightings decrease approximately linearly to zero, and the weightings of other sensory measurements vary slightly to compensate.

7.4.1.2 How accurately can a driver estimate the vehicle states?

The new driver model can be used to investigate how accurately a driver is able to estimate the states of the vehicle, depending on the simulated driving task and the driver noise amplitudes. This can be quantified by finding the perception error, defined as the difference between the true and estimated states. The procedure described in Section 7.2.1 is used to calculate the expected RMS perception error for the two vehicle states, v and ω. Target and disturbance amplitudes are varied by changing K_{ff} in a similar way to the results presented in Figure 7.2. The expected perception errors are plotted as a percentage of the total expected RMS value of each state in Figure 7.4. The perception errors are largest for disturbance-rejection only, and decrease as the target-following component increases. This is expected, as the driver can use previewed target information to predict the future motion

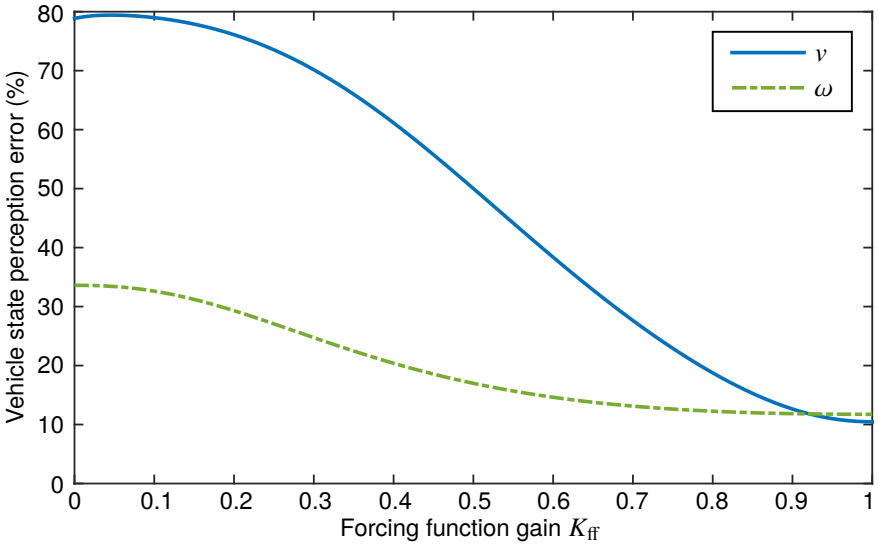

Figure 7.4: Vehicle state perception error with various forcing function amplitudes, defining a task which varies between disturbance-rejection and target-following.

of the vehicle, whereas disturbances affect the vehicle states but are only perceived after the sensory delays.

For pure target-following ($K_{\mathrm{ff}} = 1$), perception errors for both v and ω are around 10% of the total signal. These errors arise primarily from the driver noise, which has a similar effect to disturbances. When disturbances are added the perception error in v is much larger than in ω, however this may depend on the conditions of the simulation such as the vehicle dynamics and disturbance distributions. Simulations are also carried out with varying motion scaling factors, and the perception errors are found to remain constant for motion above threshold levels, similarly to the results seen in Figure 7.3.

7.4.1.3 How do sensory dynamics affect a driver's estimate of the operating point of a nonlinear vehicle?

When controlling a nonlinear vehicle it is even more important for the driver to be able to estimate the vehicle states correctly. This is because the nonlinear vehicle responds differently to steering inputs as the operating point changes. For the constant-speed vehicle with nonlinear tyres tested in Chapter 6, the operating point of the vehicle can be defined by the front and rear slip angles α_{r} and α_{f}. Results from an experiment carried out in a simulator in Chapter 6 showed that real drivers can account for the time-varying operating point of a nonlinear vehicle.

Simulations of the nonlinear driver model are run to determine how sensory dynamics affect a driver's ability to estimate the operating point of a nonlinear vehicle. Similarly to

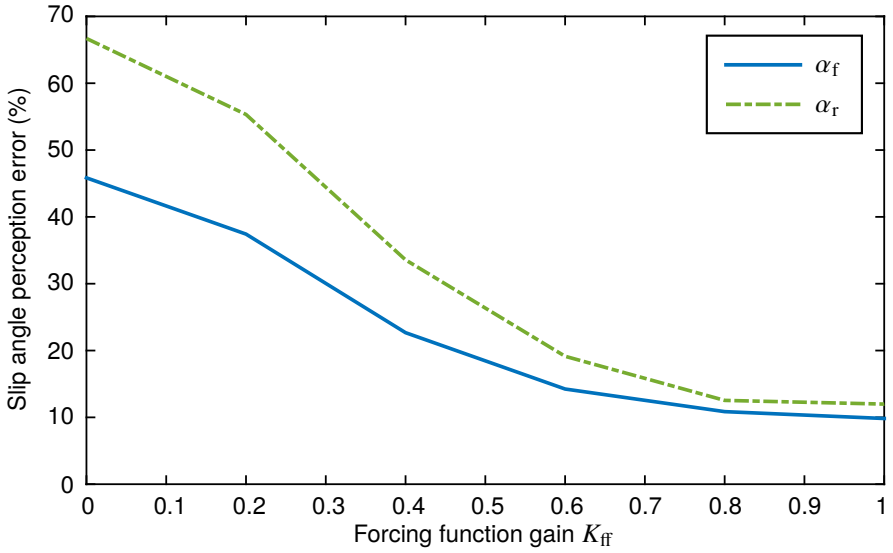

Figure 7.5: Slip angle perception error with various forcing function amplitudes, defining a task which varies between disturbance-rejection and target-following.

the results presented in Figure 7.4, the forcing function gain K_{ff} is varied from 0 to 1 to change the task from disturbance-rejection to target-following. The RMS perception error for the front and rear slip angles is found in each case as a percentage of the total RMS value of each slip angle. The procedure described in Section 7.2.1 to calculate expected values cannot be used for a nonlinear model, therefore simulated white noise signals are used as inputs to the driver model. Due to the uncertainty introduced by using simulated random noise signals, each condition is repeated 100 times and the mean results are found.

The resulting slip angle perception errors are shown in Figure 7.5. Similarly to the state perception errors shown in 7.4, the operating point perception errors increase with disturbance amplitude. For pure target-following ($K_{\mathrm{ff}} = 1$) the slip angles are estimated with an inaccuracy of around 10%. With the conditions tested the front slip angle is estimated more accurately than the rear slip angle, however this is likely to depend on the vehicle dynamics.

7.4.1.4 Can a dual-control strategy be used to enhance the driver's understanding of the system dynamics?

In the transient disturbances experiment carried out in Chapter 5, one driver was found to add a deliberate oscillation into their steering action. It was hypothesised that this could be evidence of a dual-control strategy, where the response to a deliberate disturbance is measured to understand the system dynamics better [227]. A similar result was found for all five drivers in the nonlinear vehicle experiment in Chapter 6. Simulations are therefore

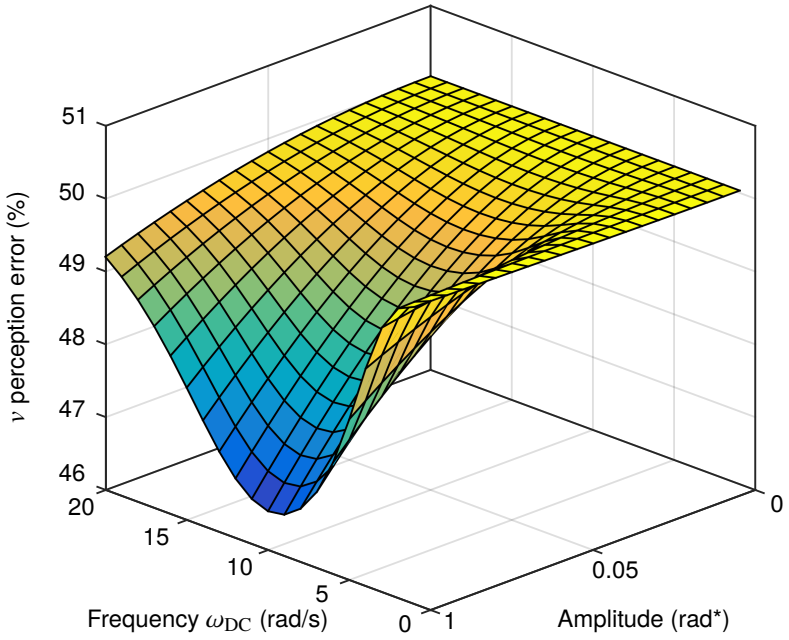

Figure 7.6: Effect of dual-control disturbances on v perception error. RMS v perception error is plotted as a percentage of RMS v magnitude, for dual-control disturbances with various amplitudes and frequencies.

carried out to investigate how such a dual-control strategy could be used during driving.

The driver model is modified by adding an additional dual-control disturbance to the control signal $\hat{\delta}$. This disturbance is also included as an input to the state estimator, to represent a deliberate disturbance which is controlled by the driver. To give an oscillation with a consistent frequency as observed in the experiments, the dual-control disturbance distribution $H_{\mathrm{DC}}(s)$ is described by a notch filter:

$$H_{\mathrm{DC}}(s) = \frac{s^2 + Q_{\mathrm{DC}} s + \omega_{\mathrm{DC}}^2}{s^2 + (1/Q_{\mathrm{DC}})s + \omega_{\mathrm{DC}}^2} \tag{7.7}$$

with $Q_{\mathrm{DC}} = 10$. The frequency ω_{DC} and amplitude of the dual-control disturbance are varied, and the expected RMS v perception error is calculated as a percentage of RMS(v).

The results are shown in Figure 7.6. As the amplitude of the dual-control disturbance increases, the perception error decreases as a proportion of the overall signal magnitude. This indicates that the driver is able to predict a larger proportion of the variation in v, and this could help them learn a more accurate internal model of the vehicle dynamics. The largest reduction in perception error is found for a frequency around 10 rad/s, which is similar to the frequency of the oscillations measured in Chapter 6. This shows that a dual-control strategy could explain the oscillations seen in the experiments.

Similar simulations are carried out with the nonlinear driver model, since the dual-

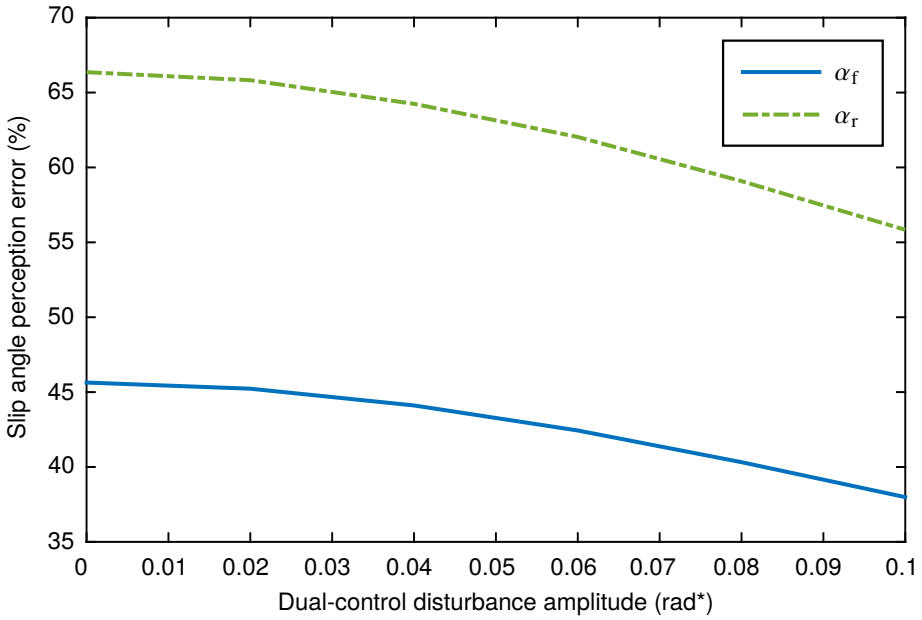

Figure 7.7: Effect of dual-control disturbances on slip angle perception error. RMS α perception error is plotted as a percentage of RMS α magnitude, for a sinusoidal dual-control disturbance added with a frequency $\omega_{DC} = 10$ rad/s.

control oscillation was mainly seen in Chapter 6 during experiments with nonlinear tyres. The dual-control disturbance is formed from a pure sinusoid with a fixed frequency $\omega_{DC} = 10$ rad/s, and the amplitude is varied. Each simulation is repeated 100 times and the mean front and rear slip angle perception errors are calculated. The low-frequency target signal defined in Section 7.3 was found to cause a large amount of variability in the RMS perception errors, making it difficult to find reliable results. Therefore the target magnitude W_κ is set to zero.

The results are shown in Figure 7.7. Similarly to the results for the linear vehicle presented in Figure 7.6, increasing the amplitude of the dual-control disturbance results in a lower percentage perception error for the front and rear slip angles. This shows that the addition of a known disturbance can allow the driver to understand the operating point of a nonlinear vehicle better.

7.4.2 Performance

It is important to be able to understand how the closed-loop driver-vehicle system will perform under different conditions, in order to predict how drivers will react in certain situations and design vehicles to achieve a desired performance level. It is hoped that the inclusion of sensory dynamics in a driver model will result in a more realistic representation of the performance of a real driver.

7.4.2.1 Over what bandwidth can a driver react to target and disturbance signals?

It has been observed that drivers are limited in the bandwidth of control actions they can apply to a vehicle. This is partly due to their neuromuscular dynamics filtering the steering control input [15, 16], however sensory dynamics may also play a role. The noise and delays in a driver's sensory systems limit the speed with which the driver is able to respond to disturbances, which has a bandwidth-limiting effect.

The linear driver model is simulated to investigate how well drivers are able to respond to different frequencies contained within white noise target and disturbance signals. The forcing function filters are all set to unity, with $W_\kappa = 0.01$ m^{-1}*, $W_v = 10$ m/s^2* and $W_\omega = 10$ rad/s^2*. The PSD of the path-following error $S_e(\omega)$ is found both with and without driver steering control. The ratio between these PSDs is then calculated to demonstrate the proportion of the forcing function signals which cannot be controlled by the driver. The simulation is repeated for three steering weights of $q_\delta = 0.1$, 1 and 10.

The results are shown in Figure 7.8. For the target forcing function f_κ the driver is able to follow all low-frequency components, however they are unable to follow components above 15 rad/s at all. The proportion of target components followed at frequencies between 0 and 15 rad/s depends on the steering cost weight, with a lower cost resulting in better target-following as expected. This result follows the intuitive expectation for a bandwidth-limited system.

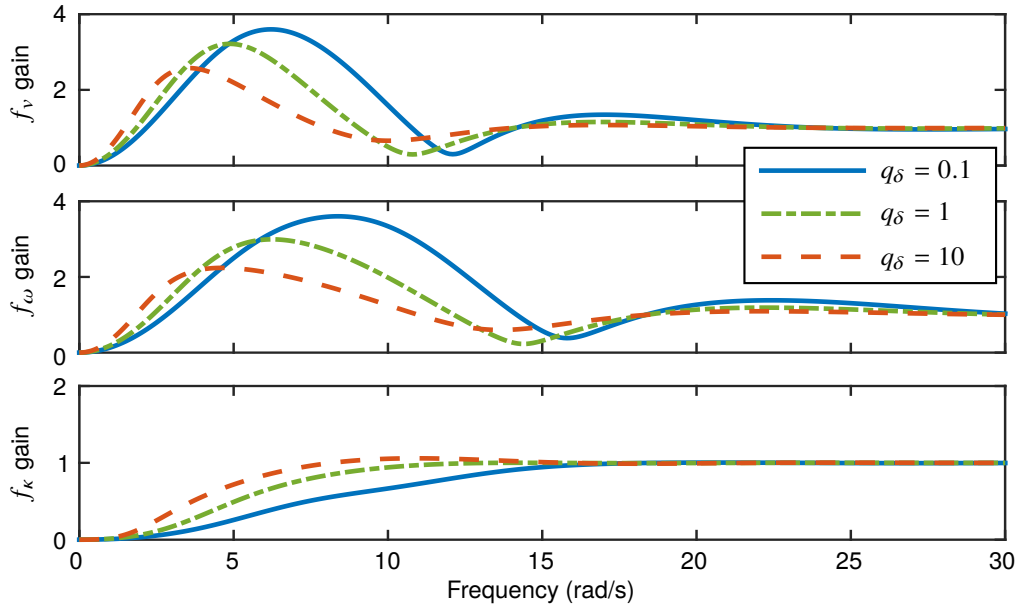

Figure 7.8: Bandwidth of driver responses to target and disturbance signals. Results are presented as a gain which represents the ratio between the path-following error e with and without driver control at each frequency.

For the disturbance forcing functions f_v and f_ω the results are more surprising. The driver is similarly able to remove the effects of the lowest-frequency disturbances, and is unable to respond to high-frequency disturbances. However, some of the effects of disturbances in the mid-frequency range are amplified by the driver, which seems like a poor control choice. This occurs because, unlike the target, the disturbances cannot be previewed. The driver is unaware of what disturbances are coming next, so cannot tailor their control response to reduce the disturbances at all frequencies. Since low-frequency disturbances affect the path-following error the most, the driver aims to minimise these as much as possible, even if it results in a poor performance at mid-range frequencies.

It should be noted that the results presented in Figure 7.8 show what happens when the driver responds to white noise forcing functions. Since the driver has an internal model of the forcing function distributions, if the forcing functions contain a greater proportion of high frequencies the driver will adapt their control strategy to place more emphasis on reducing the high-frequency disturbances.

7.4.2.2 Under what conditions is the driver-vehicle system stable?

Stability is an important consideration during the design and evaluation of vehicle systems. A stable system responds to a bounded input with a bounded output, whereas the output of an unstable system grows indefinitely. Open-loop stability of the plant depends on the characteristics of the vehicle dynamics. Analysis of the single-track vehicle model shows that the open-loop vehicle stability criterion is given by [240]:

$$(l_\mathrm{f} + l_\mathrm{r})^2 C_\mathrm{f} C_\mathrm{r} + mU^2(l_\mathrm{r} C_\mathrm{r} - l_\mathrm{f} C_\mathrm{f}) > 0 \tag{7.8}$$

The driver operates as a closed-loop control system with the vehicle, potentially allowing the plant to be stabilised even for an unstable vehicle. The ideal driver model is derived as an LQR controller with full state feedback. If the plant is stabilisable the LQR controller is guaranteed to give a stable closed-loop system [241]. The driver model with sensory dynamics combines the LQR controller with a Kalman filter, giving an LQG control strategy. If the plant is detectable and the internal model is a perfect representation of the real plant, this is also guaranteed to give a stable closed-loop system [241]. This means that for any sensible linear vehicle model (which may be open-loop unstable), for a fixed set of noise amplitudes the simulated driver-vehicle system is stable.

Although the simulated driver-vehicle system is stable for a fixed set of noise amplitudes, under some circumstances the iterative procedure described in Section 7.2.2 fails to converge on a set of signal and noise amplitudes which are consistent with the signal-dependent noise characteristics. This lack of convergence can be considered as an

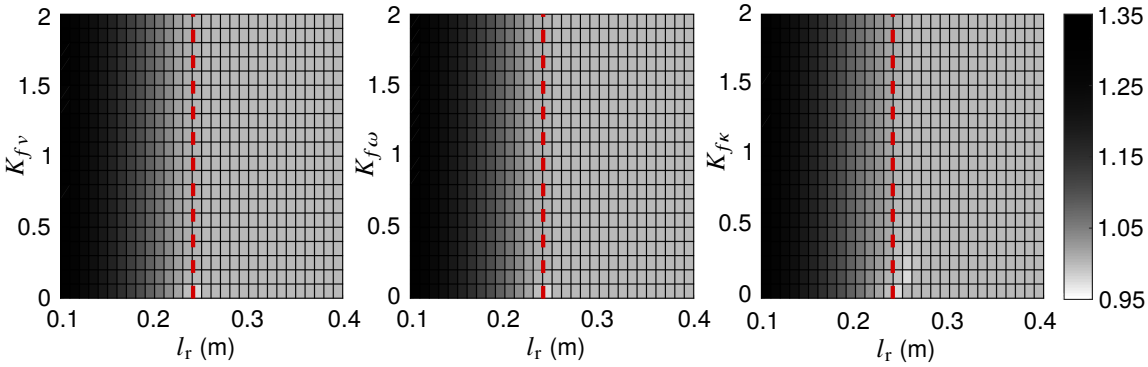

Figure 7.9: Stability of driver-vehicle system. Signal-noise iteration gain K_{SNI} is plotted for various forcing function amplitudes and vehicle centre of mass positions. The limit of stability ($K_{\mathrm{SNI}} = 1$) is shown by the dashed red lines.

indication of the instability of the driver-vehicle system, as the increase in expected signal amplitudes resulting from the driver's control of the vehicle causes the noise amplitudes to keep growing without converging on an equilibrium point. The change in the expected steering angle RMS between each iteration of the procedure given in Section 7.2.2 can be quantified as a signal-noise iteration gain K_{SNI}, given by:

$$K_{\mathrm{SNI}} = \frac{\mathrm{E}\left[\mathrm{RMS}(\delta)\right](i+1)}{\mathrm{E}\left[\mathrm{RMS}(\delta)\right](i)} \tag{7.9}$$

where i is the iteration number. This value is found to converge towards a constant factor after a sufficient number of iterations. A stable system converges to a gain $K_{\mathrm{SNI}} = 1$, with values greater than 1 indicating that the driver-vehicle system is unstable.

The signal-noise iteration gain K_{SNI} is plotted in Figure 7.9 to investigate the stability of the driver-vehicle system under various conditions. The open-loop stability of the vehicle is varied by changing the centre of mass position l_{r}, with the total wheelbase kept constant by choosing l_{f} such that $l_{\mathrm{f}} + l_{\mathrm{r}} = 3.5$ m. Each forcing function is investigated independently, with the other forcing function amplitudes set to zero. The forcing function amplitudes are varied by changing gains K_{fv}, $K_{f\omega}$, and $K_{f\kappa}$, such that $W_v = 30K_{fv}$ m/s^2*, $W_\omega = 25K_{f\omega}$ rad/s^2* and $W_\kappa = 0.15K_{f\kappa}$ m^{-1}*.

Figure 7.9 shows that the stability of the driver-vehicle system is independent of forcing function amplitude. The open-loop vehicle stability criterion is given by Equation 7.8, which is plotted for varying centre of mass position in Figure 7.10. The vehicle is unstable when the centre of mass is near the rear of the car, for $l_r < 0.24$ m. This is the same as the point at which the closed-loop driver-vehicle system is seen to become unstable in Figure 7.9. Therefore, with the vehicle and forcing functions tested, the stability criterion for the closed-loop driver-vehicle system is the same as for the open-loop vehicle.

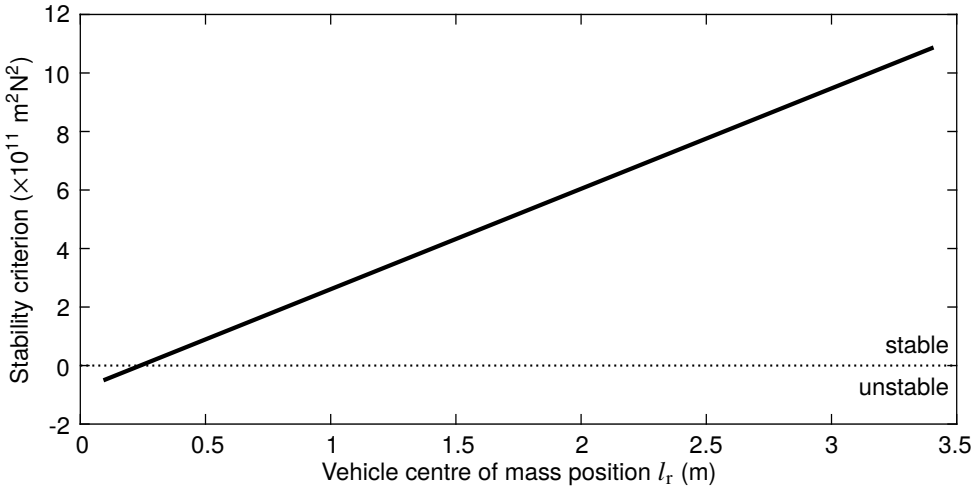

Figure 7.10: Stability criterion for single-track vehicle with varying centre of mass position

7.4.2.3 Do drivers perform differently in a simulator compared to a real vehicle?

The increasing availability of high-performance driving simulators has resulted in a large amount of vehicle validation taking place in a simulated environment. This allows new concepts and designs to be tested quickly and cheaply. However, since simulators are limited in their ability to reproduce physical motion feedback, with some having a fixed base, the sensory signals perceived by the driver's vestibular system in a simulator will be different to those perceived in a real car. The new driver model can be used to investigate whether this affects the steering performance of the driver, and the extent to which measurements taken in a simulator are applicable to a real vehicle.

The expected RMS path-following error and steering angle are calculated with various scaling factors applied to the physical motion feedback, to represent a simulator with scaled (or no) motion. All other conditions are set to the values defined in Section 7.3, and it is assumed that the driver has a perfect internal model of the plant. The results are shown in Figure 7.11. The driver's performance is independent of the scaling factor if the motion is above threshold levels, similarly to the driver's weighting of the sensory measurements shown in Figure 7.3. For simulators with no or sub-threshold motion, the RMS path-following error and steering angle increase slightly as expected. However the difference is small, showing that drivers are able to achieve a good level of steering performance with visual feedback only.

To investigate how drivers perform in simulators with filtered motion, further simulations are carried out with high-pass motion filters given by:

$$H_{\mathrm{m}a}(s) = K_{\mathrm{m}a}\left(\frac{s}{s+\omega_{\mathrm{m}a}}\right)^2 \tag{7.10}$$

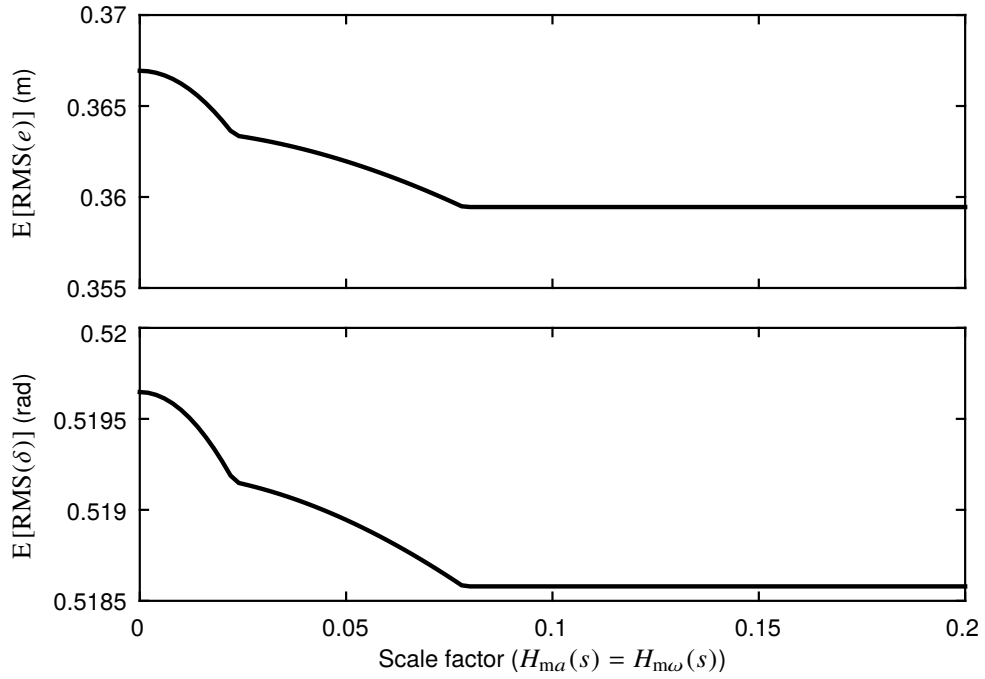

Figure 7.11: Expected RMS path-following error e and steering angle δ with different motion scaling factors

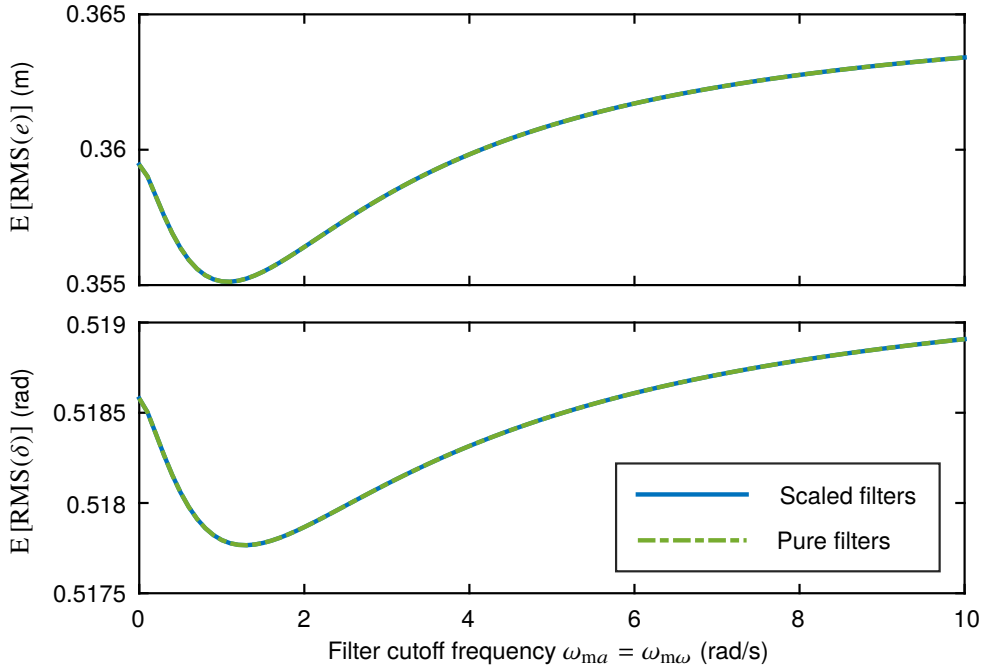

Figure 7.12: Expected RMS path-following error e and steering angle δ with different cutoff frequencies

$$H_{m\omega}(s) = K_{m\omega}\left(\frac{s}{s+\omega_{m\omega}}\right)^2 \tag{7.11}$$

with the cutoff frequency $\omega_{ma} = \omega_{m\omega}$ varied between 0 and 10 rad/s. For each cutoff frequency two conditions are tested: 'pure' filters with $K_{ma} = K_{m\omega} = 1$ and 'scaled' filters, where K_{ma} and $K_{m\omega}$ are chosen to give expected signal amplitudes $\mathrm{E}\,[\mathrm{RMS}(a_{ve})] = 0.3$ m/s^2* and $\mathrm{E}\,[\mathrm{RMS}(\omega_{ve})] = 0.03$ rad/s*. The resulting expected RMS path-following error and steering angle are plotted in Figure 7.12, showing that the performance of the driver varies with the frequency content of the physical motion feedback. The best driver performance is not achieved with full motion ($\omega_{ma} = \omega_{m\omega} = 0$), since the lowest frequencies contribute significantly to the RMS signal amplitude, increasing the noise amplitude due to the signal-dependent relationship without giving the driver much useful information about the vehicle dynamics. Figure 7.12 shows that scaling the filtered motion does not affect the performance of the driver. This is due to the linear signal-noise relationship, similarly to the results shown in Figure 7.11. Further discussion into whether this is a realistic result is presented in Section 7.5.

7.4.2.4 How does an incorrect internal model affect the performance of the driver?

Results from Chapters 4 and 5 show that under some circumstances drivers can have difficulty building up an accurate internal model of the plant. In particular, it is found that drivers may not correctly account for filtered motion, and instead drive as though the motion is scaled. This can be represented by replacing motion filters with equivalent scaling factors (ESFs) in the internal model. A procedure for finding ESFs for a given motion filter is defined in Section 7.2.3. This can be used to run simulations which give a general insight into how a driver's performance might be affected by inaccuracies in the internal model.

The effects of varying the motion filter cutoff frequency on the performance of a driver with an incorrect internal model are analysed using simulations similar to the results presented in Figure 7.12, replacing the motion filters in the internal model with ESFs. The results of the simulations are shown in Figure 7.13. Comparison of Figure 7.13 with Figure 7.12 shows that the performance of the driver is significantly affected by the internal model discrepancies. The same results are found for full motion ($\omega_{ma} = \omega_{m\omega} = 0$) in both cases, since the ESFs are 1 therefore the internal model is correct. However, as the filter cutoff frequency increases the performance of the driver degrades significantly. For larger cutoff frequencies the plots are slightly jagged due to small numerical inconsistencies when calculating the ESFs. Scaling the filtered motion does not affect the performance of the driver, as seen in Figure 7.12 for a correct internal model.

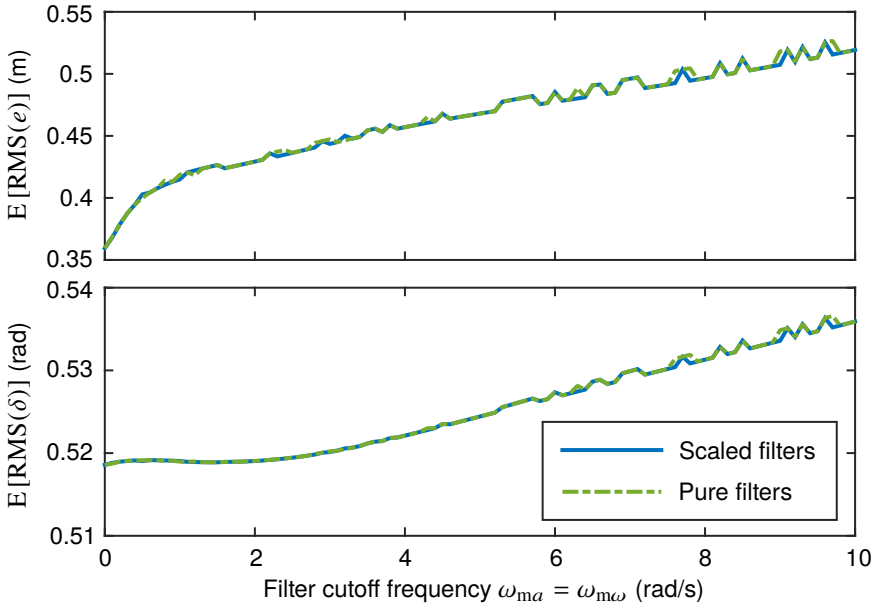

Figure 7.13: Expected RMS path-following error e and steering angle δ with different cutoff frequencies, using ESFs in place of motion filters in the driver's internal model

7.4.2.5 How does a driver's vestibular system influence their performance?

In previous chapters, a model of driver steering control which includes the driver's vestibular system (model M2) is shown to predict measured steering behaviour more accurately than a model which includes only the visual system (model M0). Simulations in Section 7.4.1.1 show that vestibular measurements are used primarily for disturbance-rejection during driving. To understand further how vestibular measurements affect the steering control performance of drivers, simulated steering angles and path-following errors are plotted in Figure 7.14 for models with and without vestibular dynamics, compared against a model with full state feedback. These signals are created for a trial with a target only ($W_v = 0$ m/s^2*, $W_\omega = 0$ rad/s^2*) and a trial with disturbances only ($W_\kappa = 0$ m^{-1}*).

Figure 7.14 shows that there are significant differences between steering angles and path-following errors predicted using models which include sensory dynamics and those predicted by a model with full state feedback. Smaller differences are also seen between models with and without vestibular dynamics. These differences are more significant for disturbance-rejection than for target-following, supporting the finding in Section 7.4.1.1. Expected RMS values of δ and e for each model are given in Table 7.1. The model with full state feedback steers less and follows the target much more closely than a more realistic model which incorporates sensory dynamics. Using vestibular measurements also allows the driver to steer less with lower path-following error, although once again this effect is more significant when there are disturbances. This shows that drivers use their vestibular

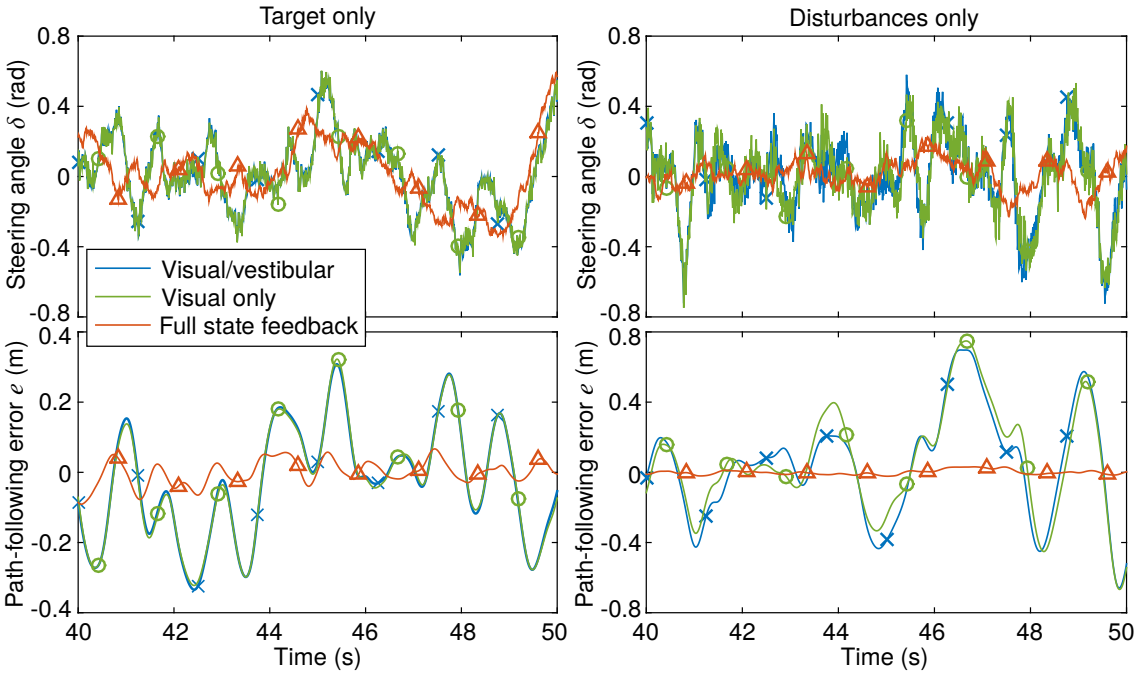

Figure 7.14: Effect of vestibular system on steering angle δ and path-following error e. Simulated signals predicted by the driver model are compared for trials with a target only (no disturbances) and disturbances only (straight line target).

Table 7.1: Change in expected RMS δ and e due to vestibular system

	Target only		**Disturbances only**	
	$\mathrm{E}\,[\mathrm{RMS}(\delta)]$ (rad)	$\mathrm{E}\,[\mathrm{RMS}(e)]$ (m)	$\mathrm{E}\,[\mathrm{RMS}(\delta)]$ (rad)	$\mathrm{E}\,[\mathrm{RMS}(e)]$ (m)
Visual/vestibular	0.47688	0.16324	0.19347	0.28134
Visual only	0.47692	0.16405	0.20228	0.30188
Full state feedback	0.46245	0.02738	0.07008	0.01225

system to improve the disturbance-rejection component of their steering performance.

7.4.3 Vehicle design

Vehicle design is increasingly being guided by optimisation algorithms, using detailed mathematical models of the vehicle dynamics and systems. The open-loop response of the vehicle can be predicted reliably, however in reality the vehicle and driver operate as a closed-loop system. This section explores how the new driver model can be used to optimise the design and set-up of a vehicle, considering the full closed-loop driver-vehicle system. The results are compared with predictions from an ideal driver model which does not consider sensory dynamics.

7.4.3.1 Does including sensory dynamics affect the optimal car set-up compared to an ideal driver model?

A simple optimisation of a vehicle parameter can be used to illustrate the differences observed when sensory dynamics are considered in a driver model. Results using the new driver model are compared with results from an ideal driver model with full state feedback. The aim of the optimisation is to minimise the expected RMS path-following error $\mathrm{E}\,[\mathrm{RMS}(e)]$. The linear vehicle described in Section 7.4.3 is used, and for simplicity only one parameter is varied. The variable parameter is the position of the centre of mass of the vehicle, defined by varying l_r and choosing l_f such that $l_\mathrm{f} + l_\mathrm{r} = 3.5$ m. The remaining vehicle parameters and the target and disturbance signals are set to the default conditions described in Section 7.3. This is a simplified example of the sort of optimisation which might be carried out in reality, and it can be used as an indication of how sensory dynamics affect optimisation results.

The results of the simulations are shown in Figure 7.15. It is clear that including sensory dynamics results in a significantly different prediction to the ideal driver model. The expected path-following error is much lower overall for the ideal driver, which is expected as this model is unaffected by driver noise and is able to respond to disturbances instantly. The optimal centre of mass position predicted using the model with sensory dynamics is 0.9 m in front of the optimal position predicted by the ideal driver model. The ideal driver model predicts that the optimal centre of mass position is close to the rear

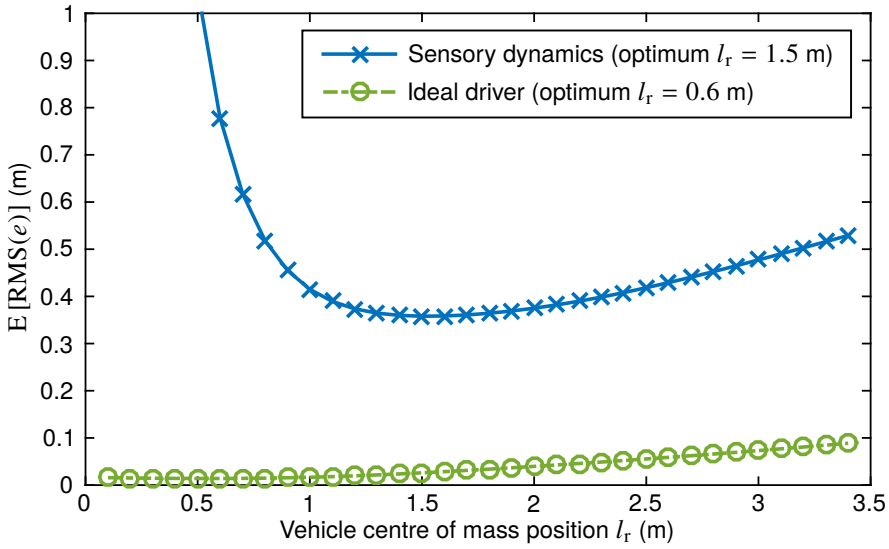

Figure 7.15: Optimal centre of mass position with or without sensory dynamics. The expected RMS path-following error e is calculated with varying centre of mass position l_r, using an ideal driver model or a model incorporating sensory dynamics.

of the vehicle, however the performance of the model with sensory dynamics becomes rapidly worse as l_r decreases below 1 m.

The differences between the predictions of the model with sensory dynamics and the ideal driver model can be explained by considering how moving the centre of mass affects the response of the vehicle. Figure 7.10 shows that the vehicle becomes less stable as l_r decreases, and is open-loop unstable for $l_r < 0.24$ m. Figure 7.15 shows that the ideal driver is able to stabilise the vehicle effectively, and benefits from the increased vehicle response for a given steering input at low values of l_r. However, the model with sensory dynamics predicts that the driver will have difficulty controlling the vehicle when it gets close to instability, resulting in a poor control performance. This is more representative of real drivers, whose physical limitations restrict their ability to control a less stable vehicle. Although the results presented in Section 7.4.2.2 indicate that the driver-vehicle system is stable as long as the vehicle is open-loop stable, Figure 7.15 shows that for a vehicle close to the limit of stability the driver's control performance can be very poor.

7.4.3.2 Will a vehicle optimised in a driving simulator give the same results as in a real car?

Validation and optimisation of vehicle systems is increasingly being aided by test drivers in driving simulators. The new driver model can be used to determine whether the optimal set-up in a simulator differs from the optimal set-up of a real vehicle. The optimisation procedure described in 7.4.3.1 is repeated with different scaling or filtering applied to the vehicle motion, and compared with the full motion results shown in Figure 7.15. The motion conditions tested are full motion, no motion (to represent a fixed-base simulator), scaled motion (with $H_{ma}(s) = 0.2$ and $H_{m\omega}(s) = 0.2$) and filtered motion (with $H_{ma}(s) = 0.2H_{HP3}(s)$ and $H_{m\omega}(s) = 0.2H_{HP3}(s)$, where $H_{HP3}(s)$ is defined in Equation 5.11). In addition, simulations are carried out with filtered motion where the internal model motion filters are replaced with ESFs, as described in Section 7.2.3. The results using the ideal driver model do not depend on the motion scaling or filtering, therefore only the model with sensory dynamics is used.

The results of the simulations with different motion conditions are compared in Figure 7.16. In general the differences between the motion conditions are very small, and far less significant than the effect of excluding sensory dynamics seen in Figure 7.15. The expected path-following error is slightly higher with no motion, indicating that results found in a fixed-base simulator may not be exactly the same as a real car. The driver's performance with scaled motion is exactly the same as with full motion as long as the motion is above threshold levels, as seen in Figure 7.11. If the driver is able to develop an

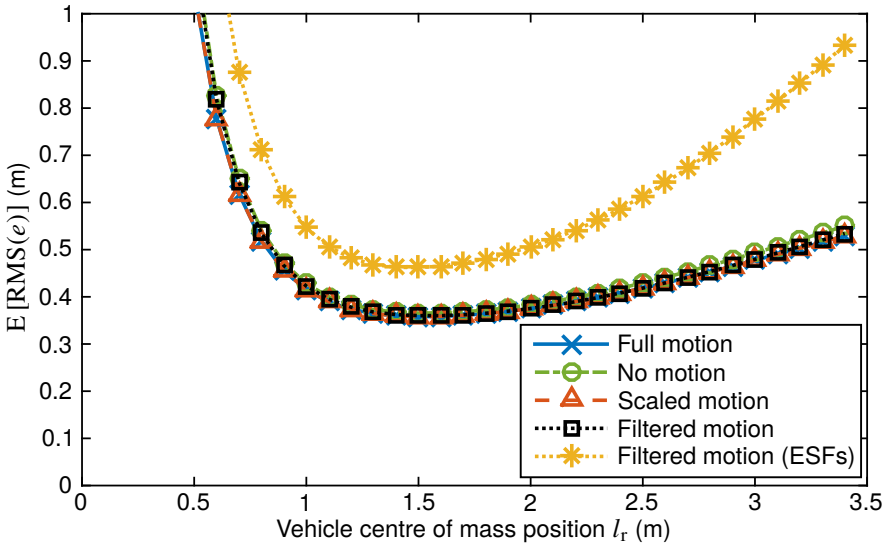

Figure 7.16: Optimal centre of mass position with various motion conditions

accurate internal model of the motion filters, the results for filtered motion lie between the full motion and no motion results. However, if the driver's internal model is inaccurate the results found in the simulator may be significantly different to the real car, as shown by the model with ESFs in Figure 7.16. For the conditions tested the optimal value of l_r is similar, but for a more complicated scenario the differences in performance with an inaccurate internal model could lead to a different optimal vehicle set-up.

7.5 Discussion

The results of various simulations are presented in Section 7.4, carried out using procedures described in Section 7.2 and conditions defined in Section 7.3. In this section the implications of the results are discussed, along with the observed limitations of the new driver model and recommendations for further work.

7.5.1 Key results from simulations

The work carried out in this chapter provides some key insights into how sensory information is used by drivers, and how sensory dynamics affect a driver's control of a vehicle. The relative weightings the driver puts on different sensory measurements are investigated in Section 7.4.1.1, and the visual system is shown to be the most important sensory system for driver steering control. This is an expected result, as it is clearly much easier to drive with no physical motion feedback than with no visual measurements. Vestibular measurements are used a small amount in a pure target-following task to counter the effects of driver

noise, however they are much more highly weighted when disturbances are added to the vehicle. This is shown in Section 7.4.2.5 to improve the disturbance-rejection component of driver steering performance compared with using visual measurements alone. For the simulated conditions the vehicle states are estimated with an inaccuracy of around 10% for a pure target-following task, but the perception errors increase significantly with added disturbances. A similar result is found for a nonlinear vehicle, with the driver's knowledge of the operating point decreasing with increased disturbance amplitudes. The driver's sensory weightings are found in Section 7.4.1.1 to be independent of signal amplitude for signals above threshold levels. This is due to the signal-dependent noise relationship, which also causes the simulated driver's control performance to be independent of motion scaling, as discussed further in Section 7.5.2.

Results from experiments described in Chapters 5 and 6 showed that drivers sometimes add a deliberate oscillation to their steering control, with a consistent frequency and amplitude. It was hypothesised that this might be a result of drivers carrying out a dual-control strategy, adding a known disturbance and measuring the response in order to increase their understanding of the states of the vehicle [227]. Simulations carried out in Section 7.4.1.4 show that adding a known disturbance can decrease the state estimation error as a percentage of the total signal amplitude. Similarly, the addition of a known disturbance can help the driver understand the operating point of a nonlinear vehicle more accurately. This allows the driver to develop a better understanding of the vehicle response, which may assist with the learning of an accurate internal model. Under the conditions tested, the optimal frequency for the additional known disturbance is around 10 rad/s, similar to the frequency of oscillations measured in Chapters 5 and 6. This provides some evidence to support the hypothesis that the measured oscillations could have been the result of a dual-control strategy.

It is known that driver steering control is limited in its bandwidth due to the influence of neuromuscular dynamics [15, 16], however sensory dynamics also play a role in limiting the bandwidth of a driver's response to target and disturbance signals. In Section 7.4.2.1 the frequency content of the vehicle path-following error resulting from white noise target and disturbance signals is compared with and without driver steering control. The simulated driver is able to follow all of the lowest frequency target components, however for the conditions tested they are unable to follow target components above 15 rad/s. The response at medium frequencies depends on the driver's steering effort represented by the cost function weighting. The effects of disturbances are amplified at some frequencies. This is because the disturbance signals are not previewed, so the driver has to estimate what may be coming next based on an internal model of their statistical characteristics. This results in the driver prioritising the lowest frequencies which have the greatest effect on

path-following error, at the expense of some higher and mid-range frequencies. If the disturbances are known to have more high frequency components, the driver will adapt their control strategy accordingly to give more weighting to these higher frequencies.

The stability of the driver-vehicle system is investigated in Section 7.4.2.2. Although for a fixed set of noise amplitudes the closed-loop driver-vehicle system is stable, in some conditions the procedure described in Section 7.2.2 does not converge on a consistent set of signal and noise amplitudes. This can be taken as a measure of the stability of the driver-vehicle system, since it indicates that the noise magnitudes cause a destabilising increase in signal amplitude. Under the conditions tested the overall stability of the closed-loop driver-vehicle system depends only on the open-loop stability of the vehicle itself. However, results presented in Section 7.4.3 show that for vehicles near the limit of stability the control performance of the driver can be very poor.

One of the most important outcomes of the new driver model is found in Section 7.4.3, resulting from a simple optimisation of the centre-of-mass position of a vehicle using the new driver model. Similar procedures are frequently carried out in industry to guide the vehicle design and evaluation process. The results are compared with the predictions of an ideal driver model with full state feedback, which is representative of many driver models used previously [12–14]. Including sensory dynamics results in a significantly different optimal point, as the new model is able to predict difficulties real drivers have in controlling vehicles which are close to instability. Currently, stability is generally considered separately from optimal performance, however the new driver model allows the performance of the vehicle to be optimised without relying on arbitrary stability constraints.

7.5.2 Driver model limitations

Predictions from the new driver model in Section 7.4.2.3 indicate that scaling the physical motion in a simulator does not affect the driver's control performance, as long as the RMS signal amplitudes are above threshold levels. This implies that a driver in a simulator with scaled motion of sufficient amplitude should drive exactly as they would in a real vehicle. In reality, simulator motion is usually high-pass filtered, allowing the driver to feel more high-frequency motion while removing the low frequencies that quickly use up simulator travel. Figure 7.12 shows that the driver's performance can be improved by removing some of the lowest frequencies, however it also implies that scaling this filtered motion would have no effect on the driver. The reason for this is that the measurement noise amplitude increases in proportion to the overall signal RMS, resulting in a measurement with the same level of reliability independent of the scaling.

This signal-dependent noise characteristic was measured from experimental data in

Chapter 4, and it is consistent with perception tests carried out in the literature [90, 126, 130, 133, 139]. However, these studies generally focussed on sinusoidal stimuli with a single frequency. Driving a real vehicle involves a large amount of low-frequency motion, due to the large steady-state accelerations involved in cornering, however this is superposed with higher-frequency motion caused by disturbances and the driver's steering responses. Since the driver model relates the noise amplitude to the RMS signal amplitude, the large steady-state components result in a large noise level, which causes the simulated driver to have difficulty perceiving small variations around the steady state. However in reality drivers are observed to be sensitive to these small high-frequency changes.

There are various possible reasons for this mismatch between the predictions of the model and what is observed in reality. Firstly, the model assumes that the measurement noise PSD is constant at all frequencies, however Figure 3.18 shows that this results in an underestimation of low-frequency driver noise and an overestimation of high-frequency driver noise. Noise amplitudes are calculated based on the RMS value of the overall signal, however it may be more appropriate to relate the noise amplitude at each frequency to the corresponding signal amplitude at that frequency. Alternatively, the discrepancy could result from sensory adaptation effects. Humans have been found to adapt to low frequency motion under some conditions [98], and various studies have identified the effects of 'sensory cancellation', whereby humans are less sensitive to self-generated stimuli [242, 243]. This could explain why large-amplitude signals from the target-following feedforward control, which are self-generated by the driver's control actions, do not disproportionately affect high-frequency disturbance perception.

A simple method for modelling these sensory cancellation effects is to ignore the target-following component in the calculation of the driver noise amplitudes. This method is used to run simulations similar to those presented in Section 7.4.2.3, accounting for sensory cancellation. The results are shown in Figure 7.17, and they are closer to what would be expected than the previous results shown in Figure 7.12. For pure filters the best performance is achieved with full motion, since the large low-frequency target-following motion no longer dominates the RMS signal amplitude. The scaled filters perform worse at low cutoff frequencies due to the scaling of the perceived motion signals. Similar results can be found by high-pass filtering the sensory signals before calculating the signal and noise amplitudes. Further work is necessary to understand how drivers are affected by sensory cancellation, and how this effect can be modelled reliably.

Another limitation of the new driver model is the assumption that the driver has a perfect internal model of the plant, with any discrepancies modelled as driver noise. Experimental results from Chapters 4 and 5 showed that in some conditions drivers build up incorrect internal models, and this can cause more systematic instabilities in the driver-vehicle

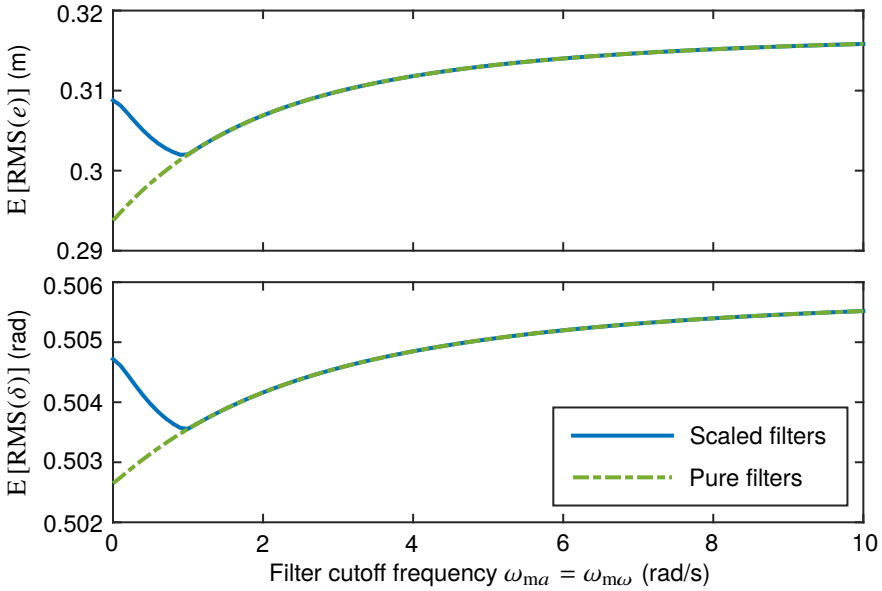

Figure 7.17: Expected RMS path-following error e and steering angle δ, with sensory cancellation of responses to target-following control actions, for various cutoff frequencies

system. The procedure described in Section 7.2.3 models one possible type of internal model discrepancy, where motion filters are replaced with equivalent scaling factors in the driver's internal model. Simulations carried out in Section 7.4.2.4 show that this error can cause significantly worse control performance, and in Section 7.4.3.2 it is shown that optimisations carried out in a simulator can give different results to a real car if the driver is unable to develop an accurate internal model of the motion filtering.

7.5.3 Further work

The results presented in this chapter highlight some important results which are found using a new model of driver steering behaviour incorporating sensory dynamics. In many cases these results are found to match behaviours observed in real drivers, however further experimental work is needed to validate the findings. In Section 7.2 some general techniques are developed to allow simulations to be carried out for a range of conditions, without reference to measured data. These allow the model to be applied to a variety of conditions for different uses, including but not limited to those presented in Section 7.4. The results presented in Section 7.4 indicate that there is significant further potential for using the new driver model to assist with the design of vehicle systems and to increase understanding of the control behaviour of human drivers.

Some of the limitations of the driver model which are demonstrated by the simulations in Section 7.4 are discussed in Section 7.5.2. In particular there is a discrepancy between

the predictions of the model and the behaviour of real drivers when small-amplitude high-frequency motion is superposed on large-amplitude low-frequency motion. Although some potential explanations for this behaviour and methods to overcome this are discussed in Section 7.5.2, further work is necessary to understand how drivers behave in these conditions. Another limitation discussed in Section 7.5.2 is the assumption that the driver has a perfect internal model of the plant. Simulations are carried out in Section 7.4 with a simple internal model discrepancy, resulting from the replacement of motion filters with equivalent scaling factors as discussed in Section 7.2.3. In reality there may be discrepancies in other aspects of the internal model such as vehicle parameters and forcing function distributions, and these discrepancies may change over time as the driver learns more about the system. Further research is necessary to understand how drivers learn an internal model over time, and to understand in more detail the impact of internal model discrepancies on the driver's control performance.

7.6 Conclusion

The new driver model can give various insights into how drivers perceive and use sensory measurements. The visual system is found to be the dominant sensory system, with the influence of vestibular measurements increasing with the level of disturbances. Disturbances also reduce the driver's ability to accurately estimate the vehicle states compared to a pure target-following task, where perception errors are around 10% of the total state RMS. Drivers can add a known oscillation to increase their understanding of the system dynamics, following a 'dual-control' strategy as measured in previous experimental work.

Due to the signal-dependent driver noise, the driver's control performance is unchanged with signal amplitude for amplitudes above threshold levels, although it is affected by frequency content. This disagrees with observed behaviour, although the discrepancy could be explained by sensory cancellation reducing the driver's sensitivity to self-generated motion. Drivers are able to follow some proportion of target signals up to around 15 rad/s, however the response to mid-frequency disturbances is sacrificed to focus on low-frequency signals which affect the vehicle lateral displacement most significantly.

The stability of the driver-vehicle system is predicted to be equivalent to the open-loop stability of the vehicle. However the driver's control performance can be poor for vehicles near the limit of stability. The new driver model is able to predict the difficulties real drivers have in controlling unstable vehicles, resulting in a different optimal vehicle parameter compared with an ideal driver with full state feedback. This result allows the vehicle to be optimised considering performance and stability simultaneously. The simulations

presented in this chapter show that there is significant potential for the use of sensory dynamics in driver modelling, allowing a greater understanding of the human driver and aiding the development of more reliable vehicle systems.

Chapter 8

Conclusions and future work

The work described in this thesis provides novel insights into the role of sensory dynamics in the steering control of a human driver. In this chapter the main findings are summarised, and the implications of the results are discussed. In addition, recommendations are made for future work to build on the results discovered in this thesis and develop further understanding of how drivers interact with vehicles.

8.1 Summary of findings

Chapters 1 to 7 describe a body of research carried out to develop understanding of how drivers interact with vehicles. The aim of this work, defined in Chapter 1, was:

> *to understand the impact of sensory dynamics on the control performance of a human driver in real and virtual environments.*

The findings summarised in this section show how understanding of the influence of drivers' sensory dynamics has been significantly increased through measurement and modelling of driver steering control. The findings are split into sections which illustrate how each of the objectives defined in Chapter 1 has been fulfilled. The implications of these findings are discussed in Section 8.2. While there is still more to be understood, this work has provided a platform onto which future research can be built, as discussed in Section 8.3. A general conclusion to the thesis is presented in Section 8.4.

8.1.1 Relevance of sensory dynamics results from the literature

- Key results from published literature on human sensory dynamics are summarised in Chapter 2.
- Sensory transfer functions are well-researched, and can be applied directly to models of human control behaviour.

- Humans generally integrate coherent sensory information in a statistically optimal fashion, but there is no consensus on how sensory conflicts are resolved.
- Sensory noise amplitudes and delays often increase under active, multimodal conditions. Therefore results from passive measurements cannot be applied directly to an active control task such as driving.
- Identified parameter values for the new driver model are reasonable when compared with results from the literature (Chapters 3 and 4).

8.1.2 Development of new driver model

- A new model of driver steering control has been developed incorporating sensory dynamics, noise and delays.
- Process noise added to the driver's control action is signal-dependent, increasing linearly with RMS steering angle (Chapter 3).
- Sensory measurement noise is also signal-dependent, increasing linearly with the corresponding RMS signal amplitude, with thresholds below which the noise amplitude remains constant (Chapter 4). This is consistent with sensory threshold characteristics observed in the literature (Chapter 2).
- A single fixed set of parameter values can be used to predict driver steering behaviour over a range of conditions. The model fits the results of 51 trials with a variance accounted for value of 76% on average (Chapter 4).
- For transient target and disturbance signals driver noise amplitudes cannot be linked to RMS signal amplitudes. They depend on the nature of the transient signals, which is difficult to describe with a fixed-parameter model (Chapter 5).
- The driver model is extended to the control of nonlinear vehicles in Chapter 6. Drivers are able to predict the time-varying operating point of a nonlinear vehicle over the prediction horizon.
- The nonlinear driver model is able to predict the performance of experienced drivers near the limit of tyre friction (Chapter 6).

8.1.3 Effects of limited physical motion feedback

- In general, drivers build up an internal model of scaling factors applied to the physical motion feedback. They are also able to do so to some extent for filtered motion, although less successfully (Chapter 4).
- With large discrepancies between the visual and physical motion, such as negative scaling factors, drivers 'veto' the physical motion and rely on visual

measurements (Chapter 4).

- Drivers reacted more quickly to disturbances and followed the target more accurately when physical motion was present. Drivers also followed the target more accurately when the motion was scaled rather than filtered. These effects can be predicted by the model (Chapter 5). Adding filtered motion feedback allows drivers to steer less aggressively and more accurately than with no motion, which is also predicted by the model (Chapter 6).
- When the physical motion is filtered drivers may have a lower-order internal model, such as equivalent scaling factors which cause phase distortions to be perceived as disturbances (Chapter 5).

8.1.4 Differences between drivers

- For a simple steering task differences between drivers are mainly a result of their chosen control effort. All drivers have similar sensory delays and noise amplitudes independent of experience (Chapter 3).
- More experienced drivers responded to transient disturbances with smaller steering actions while following the target more closely. Less experienced drivers overreacted to the initial disturbance (Chapter 5).
- More experienced drivers were able to control a nonlinear vehicle with less steering effort and better tracking performance (Chapter 6).
- Less experienced drivers were worse at controlling a nonlinear vehicle near the limit of tyre friction, which may be a result of having less accurate internal models of the vehicle (Chapter 6).

8.1.5 Impact of sensory dynamics on driver steering control

- Chapter 7 shows how simulations using the new driver model can be used to understand the role of sensory dynamics in driver steering control.
- The visual system is the dominant sense during driving, with the influence of vestibular measurements increasing with the level of disturbances.
- Disturbances reduce the driver's ability to estimate the vehicle states accurately.
- Drivers sometimes add a deliberate oscillation to their steering action (measured in Chapters 5 and 6). This allows them to understand a larger proportion of the system dynamics or operating point, and develop more accurate internal models.
- The driver model predicts that a driver's control performance is unchanged with motion scaling for motion above threshold levels. This is in contrast

with observed behaviour, which may be a result of sensory cancellation of self-generated motion.

- Drivers can follow some proportion of target signals up to 15 rad/s, however the effects of mid-frequency disturbances are sometimes amplified by the driver to prioritise low frequencies which have a greater effect on path-following error.
- The stability of the closed-loop driver-vehicle system is predicted to be equivalent to the open-loop stability of the vehicle.
- The new driver model predicts difficulties real drivers have controlling vehicles near the limit of stability, unlike an ideal driver model. This allows stability to be considered while optimising the performance of a vehicle.

8.2 Implications and discussion

A novel model of driver steering control has been developed incorporating human sensory dynamics. The model describes the physiological processes involved in driving in order to predict the driver's control responses under various conditions. A review of relevant literature on sensory dynamics in Chapter 2 highlights key results which are used in the new driver model. However it also shows that some sensory parameters may vary during active, multimodal control tasks, therefore not all parameter values can be taken directly from published results. Parameter values are therefore identified to fit experimental results, motivated by studies from the aerospace industry [32–40]. This is thought to be the first time these techniques have been applied to identify sensory parameters during driving.

A series of experiments was designed to measure the control behaviour of human drivers for identification and validation of the new model. Several novel methods were developed, such as designing trials to fit within simulator motion limits at full scale and preventing the driver from previewing the upcoming target so that visual delays could be measured more reliably. Identified parameter values are found to be reasonable when compared with results from the literature, indicating that the model is a good description of the physical processes carried out by the driver. The model is able to fit experimental results well under a range of conditions, giving a reliable quantitative prediction of driver steering behaviour. With transient disturbances it is not clear how driver noise amplitudes link to the properties of the signals, however in reality drivers may choose noise amplitudes based on the long-term statistical characteristics of target and disturbance signals.

Results show that drivers in a simulator are able to incorporate scaling of the physical motion feedback into an internal model of the controlled dynamics so that sensory measurements can be used effectively. However, they are less able to account for more

complicated or unnatural physical motion feedback. If the motion is filtered they may only learn simplified models of the filters, erroneously perceiving filtering distortions as vehicle disturbances. If the motion feedback is very unnatural, such as negative scaling factors tested in Chapter 4, drivers may veto the motion altogether and rely on visual measurements only. These results highlight the importance of ensuring that any filtering of the physical motion feedback in a simulator is simple enough for the driver to be able to learn an accurate internal model.

One of the objectives of the thesis was to determine whether sensory dynamics can characterise differences between drivers with different levels of experience. For the simple control task carried out in Chapter 3 little difference was found between drivers, except in the cost function weighting which is a choice of the driver. Identified sensory parameters are similar between drivers, indicating that the parameters reliably describe the fundamental physical characteristics of human sensory systems. A greater difference in driver performance was seen during experiments with transient disturbances in Chapter 5 and nonlinear tyres in Chapter 6. More experienced drivers were found to perform better during more complicated driving scenarios, which may be a result of more accurate internal models and a better understanding of the operating point of a nonlinear vehicle. Previous studies have hypothesised that differences in driver experience can be represented by different numbers of linearised internal models of the full nonlinear dynamics [21].

The influence of sensory dynamics in driver steering control is explored through simulations in Chapter 7, using the new driver model. Several interesting results are found which illustrate the importance of considering drivers' sensory dynamics. These results have not been experimentally verified, however many of them match anecdotal observations from drivers and automotive engineers. One particularly important finding is that the new model predicts difficulties real drivers have controlling a vehicle near the limit of stability. Currently, stability is generally considered separately from performance during vehicle design, based on empirical stability metrics. The new driver model allows the performance and stability of the driver-vehicle system to be optimised simultaneously.

8.3 Recommendations for future work

The work described in this thesis has contributed significantly to understanding of the role of sensory dynamics during driving. Nevertheless, there is still a great deal more to learn about how drivers control a vehicle. In this section potential areas for further study are recommended, discussing how future work could build upon the outcomes of this thesis to discover more about driver-vehicle interaction and the influence of sensory dynamics.

8.3.1 Application of new driver model

A new driver model has been developed based on the physiological processes carried out by a human driver. Simulations carried out in Chapter 7 illustrate some of the potential applications of the new model. The model can be used to understand how drivers perceive and use sensory information. It can also predict how the performance of a human driver will change in different conditions, and this information can be used in the design and optimisation of vehicle systems. The simulations described in Chapter 7 demonstrate some of the possibilities, however there are undoubtedly many more situations in which the new driver model can be applied.

Results presented in Chapter 7 highlight a range of interesting predictions of the model using simple simulations. Several of these results match anecdotal observations of the behaviour of real drivers, however further work is needed to explore and validate these results thoroughly. The simulations should be compared with experimental measurements to demonstrate the extent to which they agree with the control performance of real drivers, and to investigate any areas where the model may not give accurate predictions.

The new driver model is shown in Chapter 7 to predict the performance limitations of real drivers more reliably than driver models currently in use. This result requires further experimental validation, although it does match observations that drivers sometimes have difficulty controlling a vehicle which is near the limit of stability. The new model could therefore have important industrial applications, since optimisation techniques are increasingly used in the design of vehicle dynamics and systems. Using the new driver model, in future it may be possible to carry out more accurate virtual evaluations of vehicle systems, reducing dependence on subjective testing with real drivers.

8.3.2 Removing limitations of new driver model

To allow the identification of reliable parameter values, the driver model was initially derived with various simplifying assumptions. Many of these assumptions are gradually relaxed throughout the thesis, for example by considering transient target and disturbance signals in Chapter 5 and nonlinear dynamics in Chapter 6. However there are still some limitations to the model which should be addressed in future work.

8.3.2.1 Variable speed

Perhaps the most significant limitation of the new driver model is the restriction to constant-speed vehicles, neglecting longitudinal vehicle dynamics and control. As noted in Chapter 1, the objective for speed control is less clearly defined than for lateral steering control,

and depends on the aims of the driver. Various models of driver speed control for different situations have been developed in previous studies [7, 8, 22–31], and these could be used as a basis for extending the new driver model to include variable-speed vehicles.

Allowing the speed of the vehicle to vary adds a number of complications. Firstly, it results in additional nonlinearity since several of the plant states are multiplied by the longitudinal speed. For a realistic vehicle model several additional effects must be considered such as aerodynamics, load transfer and combined tyre slip. Furthermore, it is necessary to consider the driver's perception of the longitudinal motion of the vehicle, which may require several additional sensory inputs to be modelled. These could be considered separately from the lateral measurements, however in reality the same sensors are often used to detect both lateral and longitudinal motion as a combined vector. Variable-speed vehicles also require one additional control input from the driver (if acceleration and braking are considered together), resulting in a complicated interaction between steering and speed control.

It is suggested that research into sensory perception for variable-speed vehicles should begin with simple cases, using a similar approach to the work in this thesis to gradually increase the complexity of the model. Firstly, speed control can be considered in isolation to understand how longitudinal motion is perceived and controlled without any lateral dynamics. Steering control experiments could be carried out with randomly-varying speed, treated similarly to the disturbances used in the constant-speed driver model. This could provide useful information about drivers' speed perception and the resulting effects on steering control behaviour. In many situations drivers are able to plan speed changes in advance, so further experiments could use predictable speed profiles to determine whether drivers use knowledge of future vehicle speed in their lateral control calculations. Finally the full combined steering and speed control task could be tested.

8.3.2.2 Additional sensory systems

The new driver model focuses on the driver's use of sensory measurements from the visual and vestibular systems, which are considered to be the two most important senses under normal driving conditions. However, there are various other sensory systems which have been neglected, and these could be added to the model in future work. Additional sensory measurements can be added in a similar way to the visual and vestibular measurements, with transfer functions representing the perceptual dynamics and corresponding sensory delays and measurement noise.

One important source of sensory information is the driver's perception of torque feedback through the steering wheel. In the experiments carried out in this thesis the steering

wheel acted as a passive spring and damper. However, in reality torque is transmitted from the tyres to the steering wheel, giving drivers information about the states of the vehicle. Drivers can sense arm muscle lengths and forces using muscle spindles and Golgi tendon organs, as discussed in Chapter 2 [46, 103–108]. Previous research has investigated the passive and reflex responses of drivers' neuromuscular systems [15–18], however sensory perception aspects have not been considered.

There are various other body sensors used during driving, collectively known as somatosensors. These include pressure sensors which detect the push of the seat against the driver's body [102] and graviceptors which respond to the motion of fluid within the body [101]. Many of these are difficult to quantify, and can't easily be studied in isolation from the vestibular system. However one case which could be modelled is the perception of forces in the driver's neck. Previous research has measured the movement of a driver's head relative to the vehicle, and modelled the activation of neck muscles to stabilise the head [244]. These activation forces could be used as an additional sensory input by the driver, giving useful information about the acceleration of the vehicle.

8.3.2.3 Internal model discrepancies and learning

The importance of the driver's internal model has been demonstrated through the work presented in this thesis. The driver uses an internal model of the controlled dynamics to plan future control actions and to integrate measurements from different senses. In general drivers have been found to have reasonably accurate internal models, and to update these models as the driving conditions change. However, in some circumstances drivers were found to develop inaccuracies in their internal model, particularly when physical motion feedback was filtered. When developing the new driver model it was assumed that discrepancies in the internal model could be represented as Gaussian process noise. However, simulation results show that discrepancies in the internal model can cause more fundamental instabilities in the driver-vehicle control system. A real driver will always have some discrepancy between the internal model and the real plant, so further work is necessary to quantify these discrepancies and investigate their effects. Studies have considered the robustness of drivers to random disturbances [8, 9], and this work could be extended to investigate robustness to more systematic internal model errors.

In the experiments described in this thesis the drivers had a limited amount of time to practise before each trial and adapt to the conditions. With more practice time the drivers may have developed more accurate internal models of the motion filters. The statistical characteristics of the target and disturbance signals were constant throughout each trial, and it was assumed that the drivers based their control strategy on estimates of these statistical

properties. However, in reality driving conditions can vary over time, and drivers must update their internal model to account for any changes. The learning processes carried out by the driver have largely been ignored in previous research, so they are an important future area of study. Recent advances in machine learning techniques can provide a good theoretical basis for investigation into drivers' learning abilities.

8.4 General conclusion

A new model of driver steering behaviour has been developed to understand how sensory dynamics influence the interaction between a driver and a vehicle. Optimal control and state estimation theory is used to model the control calculations of a human driver who is affected by sensory filtering, delays and noise. Carefully designed experiments were carried out with real drivers in a simulator under a variety of conditions, and the results were compared with the predictions of the model. The new model is found to give a realistic description of the physical processes carried out by human drivers, matching experimental results well.

The new driver model has allowed drivers' use of sensory dynamics to be explored through simulation, resulting in several novel insights. The suitability of the model for the design of vehicle systems has been demonstrated, allowing limitations in the performance of the driver-vehicle system to be predicted more reliably than with drivers models used currently. This work has highlighted the importance of considering sensory dynamics when predicting the control behaviour of human drivers. The results demonstrated in this thesis can be used as a basis for further study and development of more accurate models of driver-vehicle interaction.

References

[1] D. Sperling and D. Gordon. "Two billion cars: driving toward sustainability". New York, NY, USA: Oxford University Press, 2009.

[2] The Society of Motor Manufacturers and Traders. "SMMT motor industry facts 2016". Tech. rep. London, UK, 2016.

[3] International Organization of Motor Vehicle Manufacturers (OICA). "Climate change and CO2 brochure". Tech. rep. Paris, France, 2014, p. 6.

[4] T. Gordon and M. Lidberg. "Automated driving and autonomous functions on road vehicles". In: *Vehicle system dynamics* 53.7 (2015), pp. 958–994.

[5] SAE International. "Taxonomy and definitions for terms related to driving automation systems for on-road motor vehicles (j3016)". Tech. rep. 2016.

[6] E. Donges. "A two-level model of driver steering behavior". In: *Human factors* 20.6 (1978), pp. 691–707.

[7] J. P. Timings and D. J. Cole. "Minimum maneuver time calculation using convex optimization". In: *Journal of dynamic systems, measurement, and control* 135.3 (2013), p. 031015.

[8] J. P. Timings and D. J. Cole. "Robust lap-time simulation". In: *Proceedings of the institution of mechanical engineers, part D: journal of automobile engineering* 228.10 (2014), pp. 1200–1216.

[9] G. Braghieri et al. "Quantification of road vehicle handling quality using a compensatory steering controller". In: *Journal of dynamic systems, measurement, and control* 139.3 (2017), p. 031010.

[10] C. C. MacAdam. "Understanding and modeling the human driver". In: *Vehicle system dynamics* 40.1-3 (2003), pp. 101–134.

[11] M. Plöchl and J. Edelmann. "Driver models in automobile dynamics application". In: *Vehicle system dynamics* 45.7-8 (2007), pp. 699–741.

[12] C. C. MacAdam. "Application of an optimal preview control for simulation of closed-loop automobile driving". In: *IEEE transactions on systems, man, and cybernetics* SMC-11.6 (1981), pp. 393–399.

[13] R. S. Sharp and V. Valtetsiotis. "Optimal preview car steering control". In: *Vehicle system dynamics* 35.Suppl.1 (2001), pp. 101–117.

[14] D. J. Cole, A. J. Pick, and A. M. C. Odhams. "Predictive and linear quadratic methods for potential application to modelling driver steering control". In: *Vehicle system dynamics* 44.3 (2006), pp. 259–284.

[15] A. J. Pick and D. J. Cole. "Dynamic properties of a driver's arms holding a steering wheel". In: *Proceedings of the institution of mechanical engineers, part D: journal of automobile engineering* 221.12 (2007), pp. 1475–1486.

[16] A. J. Pick and D. J. Cole. "A mathematical model of driver steering control including neuromuscular dynamics". In: *Journal of dynamic systems, measurement, and control* 130.3 (2008), p. 031004.

[17] D. J. Cole. "A path-following driver–vehicle model with neuromuscular dynamics, including measured and simulated responses to a step in steering angle overlay". In: *Vehicle system dynamics* 50.4 (2012), pp. 573–596.

[18] D. A. Abbink et al. "Measuring neuromuscular control dynamics during car following with continuous haptic feedback". In: *IEEE transactions on systems, man, and cybernetics, part B: cybernetics* 41.5 (2011), pp. 1239–1249.

[19] A. Ungoren and H. Peng. "An adaptive lateral preview driver model". In: *Vehicle system dynamics* 43.4 (2005), pp. 245–259.

[20] M. Thommyppillai, S. Evangelou, and R. S. Sharp. "Car driving at the limit by adaptive linear optimal preview control". In: *Vehicle system dynamics* 47.12 (2009), pp. 1535–1550.

[21] S. D. Keen and D. J. Cole. "Application of time-variant predictive control to modelling driver steering skill". In: *Vehicle system dynamics* 49.4 (2011), pp. 527–559.

[22] G. Prokop. "Modeling human vehicle driving by model predictive online optimization". In: *Vehicle system dynamics* 35.1 (2001), pp. 19–53.

[23] A. M. C. Odhams and D. J. Cole. "Models of driver speed choice in curves". In: *Proceedings of 7th international symposium on advanced vehicle control (AVEC 04)*. 2004, pp. 1–6.

[24] M. L. Ritchie, W. K. McCoy, and W. L. Welde. "A study of the relation between forward velocity and lateral acceleration in curves during normal driving". In: *Human factors* 10.3 (1968), pp. 255–258.

[25] G. D. Herrin and J. B. Neuhardt. "An empirical model for automobile driver horizontal curve negotiation". In: *Human factors* 16.2 (1974), pp. 129–133.

[26] G. Reymond et al. "Role of lateral acceleration in curve driving: driver model and experiments on a real vehicle and a driving simulator". In: *Human factors* 43.3 (2001), pp. 483–495.

[27] D. J. Bottoms. "The interaction of driving speed, steering difficulty and lateral tolerance with particular reference to agriculture". In: *Ergonomics* 26.2 (1983), pp. 123–139.

[28] K. DeFazio, D. Wittman, and C. Drury. "Effective vehicle width in self-paced tracking". In: *Applied ergonomics* 23.6 (1992), pp. 382–386.

[29] R. Lot and N. Dal Bianco. "Lap time optimisation of a racing go-kart". In: *Vehicle system dynamics* 54.2 (2016), pp. 210–230.

[30] E. R. Boer. "Car following from the driver's perspective". In: *Transportation research part F: traffic psychology and behaviour* 2.4 (1999), pp. 201–206.

[31] T. Kondoh et al. "Identification of visual cues and quantification of drivers' perception of proximity risk to the lead vehicle in car-following situations". In: *Journal of mechanical systems for transportation and logistics* 1.2 (2008), pp. 170–180.

[32] D. M. Pool et al. "Effects of peripheral visual and physical motion cues in roll-axis tracking tasks". In: *Journal of guidance, control, and dynamics* 31.6 (2008), pp. 1608–1622.

[33] J. Ellerbroek et al. "Role identification of yaw and sway motion in helicopter yaw control tasks". In: *Journal of aircraft* 45.4 (2008), pp. 1275–1289.

[34] F. M. Nieuwenhuizen et al. "Influences of simulator motion system characteristics on pilot control behavior". In: *Journal of guidance, control, and dynamics* 36.3 (2013), pp. 667–676.

[35] F. M. Drop et al. "Identification of the feedforward component in manual control with predictable target signals." In: *IEEE transactions on cybernetics* 43.6 (2013), pp. 1936–1949.

[36] P. M. T. Zaal et al. "Multimodal pilot control behavior in combined target-following disturbance-rejection tasks". In: *Journal of guidance, control, and dynamics* 32.5 (2009), pp. 1418–1428.

[37] P. M. T. Zaal et al. "Use of pitch and heave motion cues in a pitch control task". In: *Journal of guidance, control, and dynamics* 32.2 (2009), pp. 366–377.

[38] P. M. T. Zaal et al. "Identification of multimodal pilot control behavior in real flight". In: *Journal of guidance, control, and dynamics* 33.5 (2010), pp. 1527–1538.

[39] P. M. T. Zaal et al. "Comparing multimodal pilot pitch control behavior between simulated and real flight". In: *Journal of guidance, control, and dynamics* 35.5 (2012), pp. 1456–1471.

[40] P. M. T. Zaal et al. "Modeling human control of self-motion direction with optic flow and vestibular motion." In: *IEEE transactions on systems, man, and cybernetics* 43.2 (2013), pp. 544–556.

[41] R. S. Bigler. "Automobile driver sensory system modeling". PhD thesis. Cambridge, UK: Cambridge University, 2013.

[42] C. J. Nash, D. J. Cole, and R. S. Bigler. "A review of human sensory dynamics for application to models of driver steering and speed control". In: *Biological cybernetics* 110.2-3 (2016), pp. 91–116.

[43] E. Burdet, D. W. Franklin, and T. E. Milner. "Human robotics: neuromechanics and motor control". Cambridge, MA, USA: MIT Press, 2013.

[44] R. H. S. Carpenter. "Neurophysiology". 4th edition. London, UK: Arnold, 1984.

[45] C. Fernandez and J. M. Goldberg. "Physiology of peripheral neurons innervating semicircular canals of the squirrel monkey. parts i to iii." In: *Journal of neurophysiology* 34.4 (1971), pp. 661–675.

[46] E. Kandel, J. Schwartz, and T. Jessell. "Principles of neural science". 4th edition. New York, NY, USA: McGraw-Hill, 2000.

[47] D. M. Wolpert and Z. Ghahramani. "Computational principles of movement neuroscience." In: *Nature neuroscience* 3 (2000), pp. 1212–1217.

[48] D. M. Wolpert, J. Diedrichsen, and J. R. Flanagan. "Principles of sensorimotor learning". In: *Nature reviews neuroscience* 12 (2011), pp. 739–751.

[49] J. M. Flach. "Control with an eye for perception: precursors to an active psychophysics". In: *Ecological psychology* 2.2 (1990), pp. 83–111.

[50] R. S. Bigler and D. J. Cole. "A review of mathematical models of human sensory dynamics relevant to the steering task". In: *Proceedings of the 22nd IAVSD symposium on the dynamics of vehicles on roads and tracks*. Manchester, UK, 2011.

[51] J. J. Gibson. "The perception of the visual world." Boston, MA, USA: Houghton Mifflin, 1950.

[52] M. Lappe, F. Bremmer, and a. V. Van Den Berg. "Perception of self-motion from visual flow". In: *Trends in cognitive sciences* 3.9 (1999), pp. 329–336.

[53] G. Johansson. "Visual motion perception". In: *Scientific american* 232.6 (1975), pp. 76–88.

[54] S. Ullman. "The interpretation of visual motion." Oxford, UK: MIT Press, 1979.

[55] K. Nakayama. "Biological image motion processing: a review". In: *Vision research* 25.5 (1985), pp. 625–660.

[56] F. Raudies and H. Neumann. "A review and evaluation of methods estimating ego-motion". In: *Computer vision and image understanding* 116.5 (2012), pp. 606–633.

[57] J. Dichgans and T. Brandt. "Visual-vestibular interaction: effects on self-motion perception and postural control". In: *Perception*. Ed. by R. Held, H. W. Leibowitz, and H.-L. Teuber. Berlin, Germany: Springer, 1978, pp. 755–804.

[58] J. J. Koenderink. "Optic flow". In: *Vision research* 26.1 (1986), pp. 161–179.

[59] A. J. Grunwald and S. J. Merhav. "Vehicular control by visual field cues-analytical model and experimental validation". In: *IEEE transactions on systems, man, and cybernetics* 6.12 (1976), pp. 835–845.

[60] J. B. Riemersma. "Visual control during straight road driving". In: *Acta psychologica* 48.1-3 (1981), pp. 215–25.

[61] S. Grossberg, E. Mingolla, and L. Viswanathan. "Neural dynamics of motion integration and segmentation within and across apertures". In: *Vision research* 41.19 (2001), pp. 2521–2553.

[62] E. Mingolla. "Neural models of motion integration and segmentation". In: *Neural networks* 16.5-6 (2003), pp. 939–945.

[63] N. A. Browning, S. Grossberg, and E. Mingolla. "A neural model of how the brain computes heading from optic flow in realistic scenes." In: *Cognitive psychology* 59.4 (2009), pp. 320–356.

[64] G. L. Zacharias, A. K. Caglayan, and J. B. Sinacori. "A model for visual flow-field cueing and self-motion estimation". In: *IEEE transactions on systems, man, and cybernetics* SMC-15.3 (1985), pp. 385–389.

[65] D. A. Gordon. "Static and dynamic visual fields in human space perception". In: *Journal of the optical society of America* 55.10 (1965), p. 1296.

[66] F. Bremmer and M. Lappe. "The use of optical velocities for distance discrimination and reproduction during visually simulated self motion". In: *Experimental brain research* 127.1 (1999), pp. 33–42.

[67] D. A. Gordon. "Experimental isolation of the driver's visual input". In: *Human factors* 8.2 (1966), pp. 129–138.

[68] F. Soyka et al. "Predicting direction detection thresholds for arbitrary translational acceleration profiles in the horizontal plane." In: *Experimental brain research* 209.1 (2011), pp. 95–107.

[69] F. Soyka et al. "Modeling direction discrimination thresholds for yaw rotations around an earth-vertical axis for arbitrary motion profiles." In: *Experimental brain research* 220.1 (2012), pp. 89–99.

[70] D. Shinar, E. D. Mcdowell, and T. H. Rockwell. "Eye movements in curve negotiation". In: *Human factors* 19.1 (1977), pp. 63–71.

[71] M. F. Land and D. N. Lee. "Where we look when we steer." In: *Nature* 369.6483 (1994), pp. 742–744.

[72] E. Boer. "Tangent point oriented curve negotiation". In: *Proceedings of conference on intelligent vehicles*. Tokyo, Japan, 1996, pp. 7–12.

[73] F. I. Kandil, A. Rotter, and M. Lappe. "Driving is smoother and more stable when using the tangent point". In: *Journal of vision* 9.1 (2009), pp. 11.1–11.

[74] F. I. Kandil. "Car drivers attend to different gaze targets when negotiating closed vs. open bends". In: *Journal of vision* 10.4 (2010), pp. 24.1–11.

[75] M. F. Land. "The visual control of steering". In: *Vision and action*. Ed. by L. R. Harris and M. Jenkin. Cambridge, UK: Cambridge University Press, 1998, pp. 163–180.

[76] F. Mars. "Driving around bends with manipulated eye-steering coordination." In: *Journal of vision* 8.11 (2008), pp. 10.1–11.

[77] K. D. Robertshaw and R. M. Wilkie. "Does gaze influence steering around a bend?" In: *Journal of vision* 8.4 (2008), pp. 18.1–13.

[78] O. Lappi et al. "Beyond the tangent point: gaze targets in naturalistic driving". In: *Journal of vision* 13.13 (2013), pp. 11.1–18.

[79] M. Chattington et al. "Eye–steering coordination in natural driving". In: *Experimental brain research* 180.1 (2007), pp. 1–14.

[80] M. F. Land and B. W. Tatler. "Steering with the head". In: *Current biology* 11.15 (2001), pp. 1215–1220.

[81] E. Lehtonen et al. "Look-ahead fixations in curve driving." In: *Ergonomics* 56.1 (2013), pp. 34–44.

[82] M. Land and J. Horwood. "Which parts of the road guide steering?" In: *Nature* 377 (1995), pp. 339–340.

[83] J. Steen et al. "A review of visual driver models for system identification purposes". In: *Proceedings of 2011 IEEE international conference on systems, man, and cybernetics*. Anchorage, AK, USA, 2011, pp. 2093–2100.

[84] A. J. Benson, M. B. Spencer, and J. R. Stott. "Thresholds for the detection of the direction of whole-body, linear movement in the horizontal plane." In: *Aviation space and environmental medicine* 57 (1986), pp. 1088–1096.

[85] A. J. Benson, E. C. Hutt, and S. F. Brown. "Thresholds for the perception of whole body angular movement about a vertical axis." In: *Aviation space and environmental medicine* 60 (1989), pp. 205–213.

[86] L. Grabherr et al. "Vestibular thresholds for yaw rotation about an earth-vertical axis as a function of frequency." In: *Experimental brain research* 186.4 (2008), pp. 677–681.

[87] H. Kingma. "Thresholds for perception of direction of linear acceleration as a possible evaluation of the otolith function". In: *BMC ear, nose and throat disorders* 5.5 (2005).

[88] C. Gianna, S. Heimbrand, and M. Gresty. "Thresholds for detection of motion direction during passive lateral whole-body acceleration in normal subjects and patients with bilateral loss of labyrinthine function". In: *Brain research bulletin* 40.5-6 (1996), pp. 443–447.

[89] A. M. Bronstein and J. Derrick Hood. "The cervico-ocular reflex in normal subjects and patients with absent vestibular function". In: *Brain research* 373.1-2 (1986), pp. 399–408.

[90] R. M. Mallery et al. "Human discrimination of rotational velocities." In: *Experimental brain research* 204.1 (2010), pp. 11–20.

[91] Y. Valko et al. "Vestibular labyrinth contributions to human whole-body motion discrimination". In: *Journal of neuroscience* 32.39 (2012), pp. 13537–13542.

[92] A. Einstein. "Über die möglichkeit einer neuen prüfung des relativitätsprinzips". In: *Annalen der physik* 328.6 (1907), pp. 197–198.

[93] L. R. Young and J. L. Meiry. "A revised dynamic otolith model". In: *Aerospace medicine* 39.6 (1968), pp. 606–608.

[94] R. J. A. W. Hosman. "Pilot's perception and control of aircraft motions". PhD thesis. Delft, The Netherlands: Delft University of Technology, 1996.

[95] R. J. Telban and F. Cardullo. "Motion cueing algorithm development: human-centered linear and nonlinear approaches". Tech. rep. NASA, 2005.

[96] C. Fernandez and J. M. Goldberg. "Physiology of peripheral neurons innervating otolith organs of the squirrel monkey. parts i to iii." In: *Journal of neurophysiology* 39.5 (1976), pp. 970–984.

[97] W. Steinhausen. "Über die beobachtung der cupula in den bogengangsampullen des labyrinths des lebenden hechts". In: *Pflügers archiv für die gesamte physiologie des menschen und der tiere* 232.1 (1933), pp. 500–512.

[98] L. R. Young and C. M. Oman. "Model for vestibular adaptation to horizontal rotation." In: *Aerospace medicine* 40.10 (1969), pp. 1076–1080.

[99] D. F. Collins et al. "Cutaneous receptors contribute to kinesthesia at the index finger, elbow, and knee." In: *Journal of neurophysiology* 94.3 (2005), pp. 1699–1706.

[100] U. Proske and S. C. Gandevia. "The kinaesthetic senses". In: *The journal of physiology* 587.17 (2009), pp. 4139–4146.

[101] D. Vaitl et al. "Shifts in blood volume alter the perception of posture: further evidence for somatic graviception". In: *International journal of psychophysiology* 44.1 (2002), pp. 1–11.

[102] P. Sainio. "Non-visual information in vehicle handling". Licenciate of science thesis. Helsinki, Finland: Helsinki University of Technology, 2007.

[103] R. E. Poppele and R. J. Bowman. "Quantitative description of linear behavior of mammalian muscle spindles." In: *Journal of neurophysiology* 33.1 (1970), pp. 59–72.

[104] M. G. Maltenfort and R. E. Burke. "Spindle model responsive to mixed fusimotor inputs and testable predictions of beta feedback effects." In: *Journal of neurophysiology* 89.5 (2003), pp. 2797–2809.

[105] M. P. Mileusnic et al. "Mathematical models of proprioceptors. i. control and transduction in the muscle spindle." In: *Journal of neurophysiology* 96.4 (2006), pp. 1772–1788.

[106] J. A. Houck and W. Simon. "Responses of golgi tendon organs to forces applied to muscle tendon." In: *Journal of neurophysiology* 30.6 (1967), pp. 1466–1481.

[107] A. Prochazka. "Quantifying proprioception". In: *Progress in brain research* 123 (1999), pp. 133–142.

[108] M. P. Mileusnic and G. E. Loeb. "Mathematical models of proprioceptors. ii. structure and function of the golgi tendon organ." In: *Journal of neurophysiology* 96.4 (2006), pp. 1789–1802.

[109] R. C. Fitzpatrick. "Probing the human vestibular system with galvanic stimulation". In: *Journal of applied physiology* 96.6 (2004), pp. 2301–2316.

[110] M. Hämäläinen et al. "Magnetoencephalography—theory, instrumentation, and applications to noninvasive studies of the working human brain". In: *Reviews of modern physics* 65.2 (1993), pp. 413–497.

[111] F. Soyka, H. H. Bülthoff, and M. Barnett-Cowan. "Temporal processing of self-motion: modeling reaction times for rotations and translations". In: *Experimental brain research* 228.1 (2013), pp. 51–62.

[112] P. B. Matthews. "Evidence from the use of vibration that the human long-latency stretch reflex depends upon spindle secondary afferents." In: *The journal of physiology* 348.1 (1984), pp. 383–415.

[113] W. Trojaborg and E. H. Sindrup. "Motor and sensory conduction in different segments of the radial nerve in normal subjects". In: *Journal of neurology, neurosurgery & psychiatry* 32.4 (1969), pp. 354–359.

[114] W. W. Wierwille, J. G. Casali, and B. S. Repa. "Driver steering reaction time to abrupt-onset crosswinds, as measured in a moving-base driving simulator." In: *Human factors* 25.1 (1983), pp. 103–116.

[115] O. Kawakami et al. "Visual detection of motion speed in humans: spatiotemporal analysis by fMRI and MEG". In: *Human brain mapping* 118 (2002), pp. 104–118.

[116] K. Lam et al. "Magnetic response of human extrastriate cortex in the detection of coherent and incoherent motion". In: *Neuroscience* 97.1 (2000), pp. 1–10.

[117] S. T. Aw, M. J. Todd, and G. M. Halmagyi. "Latency and initiation of the human vestibuloocular reflex to pulsed galvanic stimulation." In: *Journal of neurophysiology* 96.2 (2006), pp. 925–930.

[118] S. Tabak et al. "Gain and delay of human vestibulo-ocular reflexes to oscillation and steps of the head by a reactive torque helmet". In: *Acta oto-laryngologica* 117.6 (1997), pp. 785–795.

[119] M. Barnett-Cowan. "Vestibular perception is slow: a review." In: *Multisensory research* 26.4 (2013), pp. 387–403.

[120] M. Barnett-Cowan et al. "Reaction time and event-related potentials to visual, auditory and vestibular stimuli". In: *Journal of vision* 10.7 (2010), p. 1400.

[121] M. Barnett-Cowan and L. R. Harris. "Perceived timing of vestibular stimulation relative to touch, light and sound." In: *Experimental brain research* 198.2-3 (2009), pp. 221–231.

[122] P. Gawthrop et al. "Intermittent control: a computational theory of human control". In: *Biological cybernetics* 104.1-2 (2011), pp. 31–51.

[123] T. A. Johns and D. J. Cole. "Measurement and mathematical model of a driver's intermittent compensatory steering control". In: *Vehicle system dynamics* 53.12 (2015), pp. 1811–1829.

[124] E. G. Boring. "A chart of the psychometric function". In: *The American journal of psychology* 28.4 (1917), p. 465.

[125] H. Levitt. "Transformed up-down methods in psychoacoustics". In: *The journal of the acoustical society of America* 49.2B (1971), pp. 467–477.

[126] E. Weber. "Annotationes anatomicae et physiologicae". CF Koehler, 1834.

[127] E. Groen et al. "Motion perception thresholds in flight simulation". In: *AIAA modeling and simulation technologies conference*. Reston, VA, USA, 2006, e6254.

[128] E. Todorov. "Stochastic optimal control and estimation methods adapted to the noise characteristics of the sensorimotor system." In: *Neural computation* 17.5 (2005), pp. 1084–1108.

[129] B. de Bruyn and G. A. Orban. "Human velocity and direction discrimination measured with random dot patterns". In: *Vision research* 28.12 (1988), pp. 1323–1335.

[130] L. dos Santos Buinhas et al. "Modeling coherence zones in flight simulation during yaw motion". In: *AIAA modeling and simulation technologies conference*. Reston, VA, USA, 2013.

[131] A. Nesti et al. "Self-motion sensitivity to visual yaw rotations in humans". In: *Experimental brain research* 233.3 (2014), pp. 861–869.

[132] J. Monen and E. Brenner. "Detecting changes in one's own velocity from the optic flow". In: *Perception* 23.6 (1994), pp. 681–690.

[133] C. N. Authié and D. R. Mestre. "Path curvature discrimination: dependence on gaze direction and optical flow speed". In: *PLOS one* 7.2 (2012), e31479.

[134] G. E. Legge and F. Campbell. "Displacement detection in human vision". In: *Vision research* 21.2 (1981), pp. 205–213.

[135] A. Nesti et al. "Human sensitivity to vertical self-motion". In: *Experimental brain research* 232.1 (2014), pp. 303–314.

[136] F. Soyka et al. "Does jerk have to be considered in linear motion simulation?" In: *AIAA modeling and simulation technologies conference*. Reston, VA, USA, 2009, pp. 1381–1388.

[137] R. J. A. W. Hosman and J. C. Van Der Vaart. "Vestibular models and thresholds of motion perception: results of tests in a flight simulator". Tech. rep. Delft, The Netherlands: Delft University of Technology, 1978.

[138] H. Heerspink et al. "Evaluation of vestibular thresholds for motion detection in the simona research simulator". In: *AIAA modeling and simulation technologies conference*. Reston, VA, USA, 2005, e6502.

[139] A. R. Naseri and P. R. Grant. "Human discrimination of translational accelerations." In: *Experimental brain research* 218.3 (2012), pp. 455–464.

[140] A. C. Newberry, M. J. Griffin, and M. Dowson. "Driver perception of steering feel". In: *Proceedings of the institution of mechanical engineers, part D: journal of automobile engineering* 221.4 (2007), pp. 405–415.

[141] A. Samji and L. D. Reid. "The detection of low-amplitude yawing motion transients in a flight simulator". In: *IEEE transactions on systems, man, and cybernetics* 22.2 (1992), pp. 300–306.

[142] E. L. Groen and W. Bles. "How to use body tilt for the simulation of linear self motion." In: *Journal of vestibular research: equilibrium & orientation* 14.5 (2004), pp. 375–385.

[143] P. Pretto et al. "Variable roll-rate perception in driving simulation". In: *Driving simulation conference*. Paris, France, 2014, pp. 1–7.

[144] L. Zaichik et al. "Acceleration perception". In: *AIAA modeling and simulation technologies conference*. Reston, VA, USA, 1999, e4334.

[145] V. Rodchenko, S. Boris, and A. White. "In-flight estimation of pilots' acceleration sensitivity thresholds". In: *AIAA modeling and simulation technologies conference*. Reston, VA, USA, 2000, e4292.

[146] A. Valente Pais et al. "Modeling human perceptual thresholds in self-motion perception". In: *AIAA modeling and simulation technologies conference*. Reston, VA, USA, 2006, e6626.

[147] D. M. Pool et al. "Identification of nonlinear motion perception dynamics using time-domain pilot modeling". In: *Journal of guidance, control, and dynamics* 35.3 (2012), pp. 749–763.

[148] A. R. Valente Pais et al. "Pitch motion perception thresholds during passive and active tasks". In: *Journal of guidance, control, and dynamics* 35.3 (2012), pp. 904–918.

[149] H. F. A. M. van der Steen. "Self-motion perception". PhD thesis. Delft, The Netherlands: Delft University of Technology, 1998.

[150] A. R. Valente Pais et al. "Perception coherence zones in flight simulation". In: *Journal of aircraft* 47.6 (2010), pp. 2039–2048.

[151] A. R. Valente Pais et al. "Perception of combined visual and inertial low-frequency yaw motion". In: *AIAA modeling and simulation technologies conference*. Reston, VA, USA, 2010, pp. 1–10.

[152] A. R. Valente Pais et al. "Effect of performing a boundary-avoidance tracking task on the perception of coherence between visual and inertial cues". In: *AIAA modeling and simulation technologies conference*. Reston, VA, USA, 2011, e6324.

[153] K. de Winkel et al. "Visual inertial coherence zone in the perception of heading". In: *AIAA modeling and simulation technologies conference*. Reston, VA, USA, 2010, e7916.

[154] P. R. Grant and P. T. Lee. "Motion-visual phase-error detection in a flight simulator". In: *Journal of aircraft* 44.3 (2007), pp. 927–935.

[155] P. Jonik et al. "Phase coherence zones in flight simulation". In: *AIAA modeling and simulation technologies conference*. Reston, VA, USA, 2011, e6555.

[156] B. J. Correia Grácio et al. "Tuning of the lateral specific force gain based on human motion perception in the Desdemona simulator". In: *AIAA modeling and simulation technologies conference*. Reston, VA, USA, 2010, e8094.

[157] B. J. Correia Grácio et al. "Optimal and coherence zone comparison within and between flight simulators". In: *Journal of aircraft* 50.2 (2013), pp. 493–507.

[158] B. J. Correia Grácio et al. "Perceptual scaling of visual and inertial cues: effects of field of view, image size, depth cues, and degree of freedom." In: *Experimental brain research* 232.2 (2014), pp. 637–646.

[159] J. L. Campos and H. H. Bülthoff. "Multimodal integration during self-motion in virtual reality". In: *The neural bases of multisensory processes*. Ed. by M. Murray and M. Wallace. Boca Raton, FL, USA: CRC Press, 2012. Chap. 30.

[160] R. J. A. W. Hosman and H. Stassen. "Pilot's perception in the control of aircraft motions". In: *Control engineering practice* 7.11 (1999), pp. 1421–1428.

[161] M. O. Ernst and M. S. Banks. "Humans integrate visual and haptic information in a statistically optimal fashion." In: *Nature* 415.6870 (2002), pp. 429–433.

[162] I. Oruç, L. T. Maloney, and M. S. Landy. "Weighted linear cue combination with possibly correlated error". In: *Vision research* 43.23 (2003), pp. 2451–2468.

[163] R. L. Seilheimer, A. Rosenberg, and D. E. Angelaki. "Models and processes of multisensory cue combination". In: *Current opinion in neurobiology* 25 (2014), pp. 38–46.

[164] Y. Gu, D. E. Angelaki, and G. C. Deangelis. "Neural correlates of multisensory cue integration in macaque mstd." In: *Nature neuroscience* 11.10 (2008), pp. 1201–1210.

[165] J. S. Butler et al. "Bayesian integration of visual and vestibular signals for heading". In: *Journal of vision* 10.11 (2010), pp. 23.1–13.

[166] C. R. Fetsch et al. "Dynamic reweighting of visual and vestibular cues during self-motion perception". In: *Journal of neuroscience* 29.49 (2009), pp. 15601–15612.

[167] M. Prsa, S. Gale, and O. Blanke. "Self-motion leads to mandatory cue fusion across sensory modalities." In: *Journal of neurophysiology* 108.8 (2012), pp. 2282–2291.

[168] J. Drugowitsch et al. "Optimal multisensory decision-making in a reaction-time task". In: *eLife* 3 (2014), e03005.

[169] C. R. Fetsch, G. C. Deangelis, and D. E. Angelaki. "Visual-vestibular cue integration for heading perception: applications of optimal cue integration theory." In: *The European journal of neuroscience* 31.10 (2010), pp. 1721–1729.

[170] T. Bayes. "An essay towards solving a problem in the doctrine of chances". In: *Philosophical transactions of the royal society of London* 53 (1763), pp. 370–418.

[171] J. J. Clark and A. L. Yuille. "Data fusion for sensory information processing systems". Norwell, MA, USA: Kluwer Academic Publishers, 1990.

[172] S. V. Vaseghi. "Advanced digital signal processing and noise reduction". 2nd edition. Chichester, UK: John Wiley & Sons, Ltd, 2005.

[173] A. L. Yuille and H. H. Bülthoff. "Bayesian decision theory and psychophysics". In: *Perception as bayesian inference*. Ed. by D. C. Knill and W. Richards. Cambridge, UK: Cambridge University Press, 1996, pp. 123–162.

[174] P. R. MacNeilage et al. "A bayesian model of the disambiguation of gravitoinertial force by visual cues." In: *Experimental brain research* 179.2 (2007), pp. 263–290.

[175] F. Soyka, H. H. Bülthoff, and M. Barnett-Cowan. "Integration of semi-circular canal and otolith cues for direction discrimination during eccentric rotations". In: *PLOS one* 10.8 (2015), e0136925.

[176] K. N. de Winkel et al. "Integration of visual and inertial cues in the perception of angular self-motion." In: *Experimental brain research* 231.2 (2013), pp. 209–218.

[177] A. Nesti et al. "Human discrimination of head-centred visual–inertial yaw rotations". In: *Experimental brain research* 233.12 (2015), pp. 3553–3564.

[178] J. S. Butler et al. "The role of stereo vision in visual-vestibular integration." In: *Seeing and perceiving* 24.5 (2011), pp. 453–470.

[179] J. Carriot, M. Jamali, and K. E. Cullen. "Rapid adaptation of multisensory integration in vestibular pathways". In: *Frontiers in systems neuroscience* 9.59 (2015), pp. 1–5.

[180] R. E. Kalman. "A new approach to linear filtering and prediction problems". In: *Journal of basic engineering* 82.1 (1960), pp. 35–45.

[181] M. S. Grewal and A. P. Andrews. "Kalman filtering: theory and practice using Matlab". 2nd edition. New York, NY, USA: John Wiley & Sons, Inc., 2001.

[182] J. Borah, L. R. Young, and R. E. Curry. "Optimal estimator model for human spatial orientation". In: *Annals of the New York academy of sciences* 545.1 (1988), pp. 51–73.

[183] L. H. Zupan, D. M. Merfeld, and C. Darlot. "Using sensory weighting to model the influence of canal, otolith and visual cues on spatial orientation and eye movements." In: *Biological cybernetics* 86.3 (2002), pp. 209–230.

[184] L. R. Young. "Optimal estimator models for spatial orientation and vestibular nystagmus." In: *Experimental brain research* 210.3-4 (2011), pp. 465–476.

[185] C. Onur. "Developing a computational model of the pilot's best possible expectation of aircraft state given vestibular and visual cues". Master's thesis. Atlanta, GA, USA: Georgia Institute of Technology, 2014.

[186] M. O. Ernst and H. H. Bülthoff. "Merging the senses into a robust percept." In: *Trends in cognitive sciences* 8.4 (2004), pp. 162–169.

[187] S. Deneve, P. E. Latham, and A. Pouget. "Reading population codes: a neural implementation of ideal observers." In: *Nature neuroscience* 2.8 (1999), pp. 740–745.

[188] A. Pouget, P. Dayan, and R. Zemel. "Information processing with population codes." In: *Nature reviews neuroscience* 1.2 (2000), pp. 125–132.

[189] M. J. Barber, J. W. Clark, and C. H. Anderson. "Neural representation of probabilistic information." In: *Neural computation* 15.8 (2003), pp. 1843–1864.

[190] M. O. Ernst and M. Di Luca. "Multisensory perception: from integration to remapping". In: *Sensory cue integration*. Ed. by J. Trommershauser, K. Kording, and M. S. Landy. Oxford, UK: Oxford University Press, 2011, pp. 224–250.

[191] P. Scarfe and P. B. Hibbard. "Statistically optimal integration of biased sensory estimates." In: *Journal of vision* 11.7 (2011), pp. 12.1–17.

[192] J. S. Butler, J. L. Campos, and H. H. Bülthoff. "Optimal visual–vestibular integration under conditions of conflicting intersensory motion profiles". In: *Experimental brain research* 233.2 (2014), pp. 587–597.

[193] M. Kaliuzhna et al. "Learning to integrate contradictory multisensory self-motion cue pairings". In: *Journal of vision* 15.1 (2015), pp. 10.1–15.

[194] K. N. de Winkel, M. Katliar, and H. H. Bülthoff. "Forced fusion in multisensory heading estimation". In: *PLOS one* 10.5 (2015), e0127104.

[195] K. P. Körding et al. "Causal inference in multisensory perception." In: *PLOS one* 2.9 (2007), e943.

[196] M. S. Landy et al. "Measurement and modeling of depth cue combination: in defense of weak fusion". In: *Vision research* 35.3 (1995), pp. 389–412.

[197] J. Burge, A. R. Girshick, and M. S. Banks. "Visual-haptic adaptation is determined by relative reliability". In: *Journal of neuroscience* 30.22 (2010), pp. 7714–7721.

[198] A. Zaidel, A. H. Turner, and D. E. Angelaki. "Multisensory calibration is independent of cue reliability". In: *Journal of neuroscience* 31.39 (2011), pp. 13949–13962.

[199] D. C. Knill. "Robust cue integration: a bayesian model and evidence from cue-conflict studies with stereoscopic and figure cues to slant." In: *Journal of vision* 7.7 (2007), pp. 5.1–24.

[200] A. R. Girshick and M. S. Banks. "Probabilistic combination of slant information: weighted averaging and robustness as optimal percepts." In: *Journal of vision* 9.9 (2009), pp. 8.1–20.

[201] Z. Ghahramani, D. M. Wolpert, and M. I. Jordan. "Computational models of sensorimotor integration". In: *Advances in psychology*. Vol. 119. 1997, pp. 117–147.

[202] I. Rock and J. Victor. "Vision and touch: an experimentally created conflict between the two senses". In: *Science* 143.3606 (1964), pp. 594–596.

[203] A. A. Rader, C. M. Oman, and D. M. Merfeld. "Perceived tilt and translation during variable-radius swing motion with congruent or conflicting visual and vestibular cues". In: *Experimental brain research* 210.2 (2011), pp. 173–184.

[204] L. R. Harris, M. Jenkin, and D. C. Zikovitz. "Visual and non-visual cues in the perception of linear self-motion." In: *Experimental brain research* 135.1 (2000), pp. 12–21.

[205] M. Ohmi. "Egocentric perception through interaction among many sensory systems". In: *Cognitive brain research* 5.1-2 (1996), pp. 87–96.

[206] G. Zacharias and L. Young. "Influence of combined visual and vestibular cues on human perception and control of horizontal rotation". In: *Experimental brain research* 41.2 (1981), pp. 159–171.

[207] M. Ishida et al. "Self-motion perception during conflicting visual-vestibular acceleration". In: *Journal of vestibular research* 18.5-6 (2008), pp. 267–272.

[208] M. Wentink, B. Correia, and W. Bles. "Frequency dependence of allowable differences in visual and vestibular motion cues in a simulator". In: *AIAA modeling and simulation technologies conference*. Reston, VA, USA, 2009, e6248.

[209] G. L. Zacharias. "Motion sensation dependence on visual and vestibular cues". PhD thesis. Massachusetts Institute of Technology, Cambridge, MA, USA, 1977.

[210] W. G. Wright, P. DiZio, and J. R. Lackner. "Vertical linear self-motion perception during visual and inertial motion: more than weighted summation of sensory inputs." In: *Journal of vestibular research* 15.4 (2005), pp. 185–195.

[211] L. Ljung. "System identification: theory for the user". 2nd edition. Upper Saddle River, NJ, USA: Prentice Hall, 1999.

[212] P. M. T. Zaal et al. "Modeling human multimodal perception and control using genetic maximum likelihood estimation". In: *Journal of guidance, control, and dynamics* 32.4 (2009), pp. 1089–1099.

[213] S. D. Keen and D. J. Cole. "Bias-free identification of a linear model-predictive steering controller from measured driver steering behavior". In: *IEEE transactions on systems, man, and cybernetics, part B: cybernetics* 42.2 (2012), pp. 434–443.

[214] A. M. Odhams and D. J. Cole. "Identification of the steering control behaviour of five test subjects following a randomly curving path in a driving simulator". In: *International journal of vehicle autonomous systems* 12.1 (2014), pp. 44–64.

[215] C. J. Nash and D. J. Cole. "Development of a novel model of driver-vehicle steering control incorporating sensory dynamics". In: *The dynamics of vehicles on roads and tracks*. Ed. by M. Rosenberger et al. Graz, Austria: CRC Press, 2016, pp. 57–66.

[216] R. A. Hess. "Analyzing manipulator and feel system effects in aircraft flight control". In: *IEEE transactions on systems, man, and cybernetics* 20.4 (1990), pp. 923–931.

[217] I. Deary and G. Der. "Reaction time, age and cognitive ability: logitudinal findings from age 16 to 63 years in representative population samples". In: *Aging, neuropsychology, and cognition* 12.2 (2005), pp. 187–215.

[218] G. Box and G. Jenkins. "Time series analysis: forecasting and control". San Francisco, CA, USA: Holden-Day Inc., 1970.

[219] J. P. Timings and D. J. Cole. "Vehicle trajectory linearisation to enable efficient optimisation of the constant speed racing line". In: *Vehicle system dynamics* 50.6 (2012), pp. 883–901.

[220] X. Na and D. J. Cole. "Game-theoretic modeling of the steering interaction between a human driver and a vehicle collision avoidance controller". In: *IEEE transactions on human-machine systems* 45.1 (2015), pp. 25–38.

[221] S. Schnelle et al. "A personalizable driver steering model capable of predicting driver behaviors in vehicle collision avoidance maneuvers". In: *IEEE transactions on human-machine systems* (2016), pp. 1–11.

[222] B. S. Repa and P. M. Leucht. "The influence of motion cues on driver-vehicle performance in a simulator". In: *Proceedings of the 17th annual conference on manual control*. 1981.

[223] K. Tagesson and D. Cole. "Advanced emergency braking under split friction conditions and the influence of a destabilising steering wheel torque". In: *Vehicle system dynamics* 55.7 (2017), pp. 970–994.

[224] R. A. Hess. "Modeling pilot detection of time-varying aircraft dynamics". In: *Journal of aircraft* 49.6 (2012), pp. 2100–2104.

[225] P. Zaal and D. M. Pool. "Multimodal pilot behavior in multi-axis tracking tasks with time-varying motion cueing gains". In: *AIAA modeling and simulation technologies conference*. Reston, VA, USA, 2014, e0810.

[226] P. M. Zaal. "Manual control adaptation to changing vehicle dynamics in roll–pitch control tasks". In: *Journal of guidance, control, and dynamics* 39.5 (2016), pp. 1046–1058.

[227] N. Filatov and H. Unbehauen. "Survey of adaptive dual control methods". In: *IEE proceedings - control theory and applications* 147.1 (2000), pp. 118–128.

[228] P. Lakerveld et al. "The effects of yaw and sway motion cues in curve driving simulation". In: *IFAC-PapersOnLine* 49.19 (2016), pp. 500–505.

[229] G. Perantoni and D. J. Limebeer. "Optimal control for a formula one car with variable parameters". In: *Vehicle system dynamics* 52.5 (2014), pp. 653–678.

[230] P. Falcone et al. "Linear time-varying model predictive control and its application to active steering systems: stability analysis and experimental validation". In: *International journal of robust and nonlinear control* 18.8 (2008), pp. 862–875.

[231] M. Gerdts et al. "Generating locally optimal trajectories for an automatically driven car". In: *Optimization and engineering* 10.4 (2009), pp. 439–463.

[232] S. M. Erlien, S. Fujita, and J. C. Gerdes. "Shared steering control using safe envelopes for obstacle avoidance and vehicle stability". In: *IEEE transactions on intelligent transportation systems* 17.2 (2016), pp. 441–451.

[233] J. Edelmann et al. "A passenger car driver model for higher lateral accelerations". In: *Vehicle system dynamics* 45.12 (2007), pp. 1117–1129.

[234] C. J. Nash and D. J. Cole. "Modelling the influence of sensory dynamics on linear and nonlinear driver steering control". In: *Vehicle system dynamics* (2017).

[235] H. B. Pacejka and E. Bakker. "The magic formula tyre model". In: *Vehicle system dynamics* 21.S1 (1992), pp. 1–18.

[236] J. Hartikainen, A. Solin, and S. Särkkä. "Optimal filtering with Kalman filters and smoothers - a manual for the Matlab toolbox EKF/UKF". Espoo, Finland, 2011.

[237] J. M. Maciejowski. "Predictive control: with constraints". Harlow, UK: Pearson Education, 2002.

[238] R. C. McLane and W. W. Wierwille. "The influence of motion and audio cues on driver performance in an automobile simulator". In: *Human factors* 17.5 (1975), pp. 488–501.

[239] D. E. Newland. "An introduction to random vibrations, spectral & wavelet analysis". 3rd edition. Essex, UK: Longman Scientific & Technical, 1993.

[240] T. D. Gillespie. "Fundamentals of vehicle dynamics". Warrendale, PA: SAE International, 1992.

[241] B. D. O. Anderson and J. B. Moore. "Linear optimal control". Englewood Cliffs, NJ, USA: Prentice-Hall, 1971.

[242] N. Lally, B. Frendo, and J. Diedrichsen. "Sensory cancellation of self-movement facilitates visual motion detection". In: *Journal of vision* 11.14 (2011), pp. 5.1–9.

[243] P. M. Bays, J. R. Flanagan, and D. M. Wolpert. "Attenuation of self-generated tactile sensations is predictive, not postdictive". In: *PLOS biology* 4.2 (2006), pp. 281–284.

[244] H. Cathcart et al. “A mathematical occupant model for investigating discomfort during transient longitudinal acceleration”. In: *Proceedings of the 23rd IAVSD symposium on the dynamics of vehicles on roads and tracks*. Qingdao, China, 2013, pp. 1–8.

[245] A. Wills and B. Ninness. “QPC - quadratic programming in C”. Newcastle, Australia, 2009.

[246] IBM. “CPLEX optimizer”. 2009.

[247] A. Wächter and L. T. Biegler. “On the implementation of an interior-point filter line-search algorithm for large-scale nonlinear programming”. In: *Mathematical programming* 106.1 (2006), pp. 25–57.

Appendix A

Driver model derivation and summary

Throughout this thesis a new model of driver steering control is developed, incorporating human sensory dynamics. In Chapters 3 to 6 the major aspects of the development of the model are discussed, however full mathematical derivations are sometimes omitted for the sake of brevity. Various changes made to the model are presented in separate chapters, to maintain the chronology of the development and application of the model. For clarity, a full mathematical description and summary of the new driver model is presented in this appendix. **An amended version of this appendix has been published as a journal paper [234].**

A.1 Linear driver model

Vehicle steering control can be thought of as a combined target-following and disturbance-rejection task [6], as shown in Figure A.1. The driver must follow a target path of curvature f_κ while reacting to disturbances f_v and f_ω on the lateral and angular velocities of the vehicle. The target-following component is generally a feedforward control task, as the driver can 'preview' the upcoming target path in order to plan future steering control inputs. However in Chapters 3 and 4 experiments were carried out where the driver could not preview the upcoming target, allowing delays in the driver's visual system to be measured.

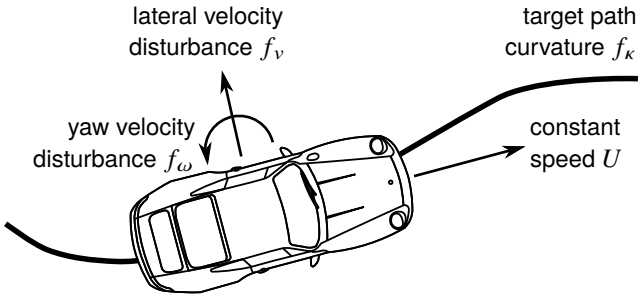

Figure A.1: Representation of steering control task in new driver model

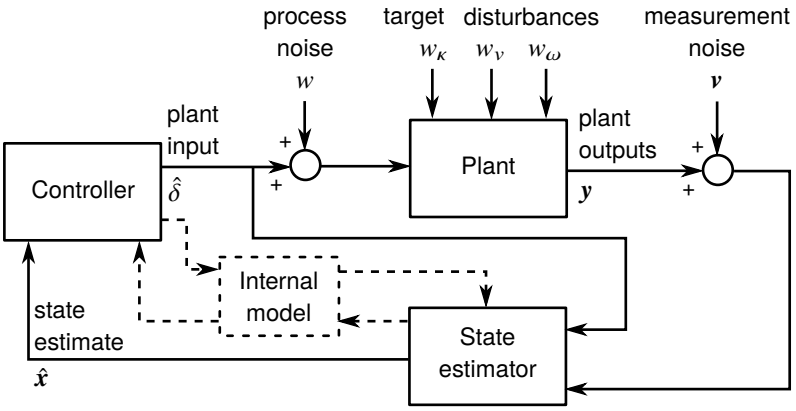

Figure A.2: Overall structure of new driver model

The disturbance-rejection component is a feedback task, as the driver cannot perceive disturbances until after they have occurred.

The structure of the new driver-vehicle control model is shown in Figure A.2. The model uses optimal control theory to represent a driver who has learned to steer as well as possible on average based on the information available to them. The model consists of three main components: a plant, a controller and a state estimator. The dynamics of the vehicle and the driver are described by the plant, which is perturbed by target and disturbance white noise representations w_κ, w_v and w_ω, and process noise w. The plant equations are derived in Section A.1.1. The plant outputs $\boldsymbol{y}$ represent the outputs of the driver's sensory systems, and these are perturbed by measurement noise $\boldsymbol{v}$. A state estimator calculates an estimate $\hat{\boldsymbol{x}}$ of the plant states, using an internal model of the plant to reduce the uncertainty in the noisy sensory measurements. The state estimator is described in Section A.1.2. Finally, a controller uses this state estimate and the internal model to calculate an optimal plant input $\hat{\delta}$, as discussed in Section A.1.3.

A.1.1 Plant

The plant describes the open-loop dynamics of the driver-vehicle system. In addition, the driver has an internal model of the plant which is used by the controller and state estimator [47, 48]. It is possible to define the internal model separately from the plant to represent errors in the driver's understanding of the system dynamics, however in most cases drivers have been found to learn an accurate internal model (see Chapters 3 to 5). A block diagram of the plant is shown in Figure A.3.

The plant is implemented as a state-space system, in discrete time with sample period T_s so that delays can be modelled explicitly. All continuous transfer functions $H(s)$ are converted to discrete state-space matrices ($\mathbf{A}$, $\mathbf{B}$, $\mathbf{C}$, $\mathbf{D}$) with states $\boldsymbol{x}$, with subscripts

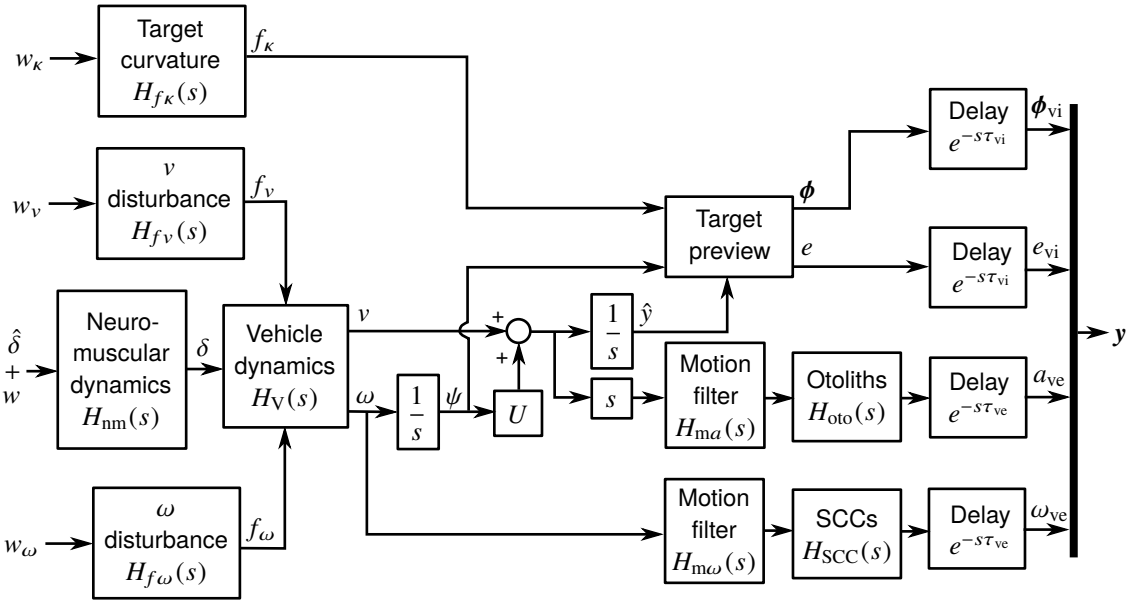

Figure A.3: Block diagram of plant describing the dynamics controlled by the driver, including the vehicle dynamics, driver's neuromuscular and sensory dynamics, and motion and forcing function filters.

matching the transfer function. Discretisation is carried out using a zero-order hold method. In some cases this is approximated in the form $\mathbf{A} = \mathbf{I} + T_\mathrm{s}\mathbf{A}_\mathrm{c}$, $\mathbf{B} = T_\mathrm{s}\mathbf{B}_\mathrm{c}$, where $\mathbf{A}_\mathrm{c}$ and $\mathbf{B}_\mathrm{c}$ are continuous-time state-space matrices.

The driver's neuromuscular dynamics $H_{\mathrm{nm}}(s)$ shape the plant input $\hat{\delta}$ (plus process noise w) to give the steering angle δ:

$$\begin{aligned} \boldsymbol{x}_{\mathrm{nm}}(k+1) &= \mathbf{A}_{\mathrm{nm}}\boldsymbol{x}_{\mathrm{nm}}(k) + \mathbf{B}_{\mathrm{nm}}(\hat{\delta}(k) + w(k)) \\ \delta(k+1) &= \mathbf{C}_{\mathrm{nm}}\boldsymbol{x}_{\mathrm{nm}}(k) + \mathbf{D}_{\mathrm{nm}}(\hat{\delta}(k) + w(k)) \end{aligned} \tag{A.1}$$

The steering angle is included as a state to allow the plant to be adapted more easily for a nonlinear vehicle (see Section A.2).

The target and disturbance forcing function filters $H_{f\kappa}(s)$, $H_{fv}(s)$ and $H_{f\omega}(s)$ are written in discrete state-space form. The target curvature f_κ is given by:

$$\begin{aligned} \boldsymbol{x}_{f\kappa}(k+1) &= \mathbf{A}_{f\kappa}\boldsymbol{x}_{f\kappa}(k) + \mathbf{B}_{f\kappa}w_\kappa(k) \\ f_\kappa(k) &= \mathbf{C}_{f\kappa}\boldsymbol{x}_{f\kappa}(k) + \mathbf{D}_{f\kappa}w_\kappa(k) \end{aligned} \tag{A.2}$$

and the lateral velocity disturbance f_v and angular velocity disturbance f_ω are found similarly, where w_κ, w_v and w_ω are Gaussian white noise inputs with RMS magnitudes W_κ, W_v and W_ω.

The vehicle $H_{\mathrm{V}}(s)$ takes as inputs the steering angle δ and the disturbances f_v and f_ω,

and its outputs are the vehicle lateral velocity v and angular velocity ω:

$$\begin{aligned} \boldsymbol{x}_{\mathrm{V}}(k+1) &= \mathbf{A}_{\mathrm{V}}\boldsymbol{x}_{\mathrm{V}}(k) + \mathbf{B}_{\mathrm{V}}\left\{\delta(k) \;\; f_v(k) \;\; f_\omega(k)\right\}^{\mathrm{T}} \\ \left\{v(k) \;\; \omega(k)\right\}^{\mathrm{T}} &= \mathbf{C}_{\mathrm{V}}\boldsymbol{x}_{\mathrm{V}}(k) + \mathbf{D}_{\mathrm{V}}\left\{\delta(k) \;\; f_v(k) \;\; f_\omega(k)\right\}^{\mathrm{T}} \end{aligned} \tag{A.3}$$

which expands to:

$$\begin{aligned} \boldsymbol{x}_{\mathrm{V}}(k+1) &= \mathbf{A}_{\mathrm{V}}\boldsymbol{x}_{\mathrm{V}}(k) + \mathbf{B}_{\mathrm{V}(:,1)}\delta(k) + \mathbf{B}_{\mathrm{V}(:,2)}\mathbf{C}_{fv}\boldsymbol{x}_{fv}(k) \\ &\quad + \mathbf{B}_{\mathrm{V}(:,2)}\mathbf{D}_{fv}w_v(k) + \mathbf{B}_{\mathrm{V}(:,3)}\mathbf{C}_{f\omega}\boldsymbol{x}_{f\omega}(k) + \mathbf{B}_{\mathrm{V}(:,3)}\mathbf{D}_{f\omega}w_\omega(k) \\ v(k) &= \mathbf{C}_{\mathrm{V}(1,:)}\boldsymbol{x}_{\mathrm{V}}(k) + \mathbf{D}_{\mathrm{V}(1,1)}\delta(k) + \mathbf{D}_{\mathrm{V}(1,2)}\mathbf{C}_{fv}\boldsymbol{x}_{fv}(k) \\ &\quad + \mathbf{D}_{\mathrm{V}(1,2)}\mathbf{D}_{fv}w_v(k) + \mathbf{D}_{\mathrm{V}(1,3)}\mathbf{C}_{f\omega}\boldsymbol{x}_{f\omega}(k) + \mathbf{D}_{\mathrm{V}(1,3)}\mathbf{D}_{f\omega}w_\omega(k) \\ \omega(k) &= \mathbf{C}_{\mathrm{V}(2,:)}\boldsymbol{x}_{\mathrm{V}}(k) + \mathbf{D}_{\mathrm{V}(2,1)}\delta(k) + \mathbf{D}_{\mathrm{V}(2,2)}\mathbf{C}_{fv}\boldsymbol{x}_{fv}(k) \\ &\quad + \mathbf{D}_{\mathrm{V}(2,2)}\mathbf{D}_{fv}w_v(k) + \mathbf{D}_{\mathrm{V}(2,3)}\mathbf{C}_{f\omega}\boldsymbol{x}_{f\omega}(k) + \mathbf{D}_{\mathrm{V}(2,3)}\mathbf{D}_{f\omega}w_\omega(k) \end{aligned} \tag{A.4}$$

where $\mathbf{M}_{(i,j)}$ indicates the ith row and jth column of matrix $\mathbf{M}$, and ':' represents the entire row or column.

The plant outputs are subjected to visual and vestibular delays τ_{vi} and τ_{ve}, consisting of $N_{\mathrm{vi}} = \tau_{\mathrm{vi}}/T_{\mathrm{s}}$ and $N_{\mathrm{ve}} = \tau_{\mathrm{ve}}/T_{\mathrm{s}}$ time steps. The number of states required to model this can be reduced by applying the delays to v and ω instead, then calculating the plant outputs from these delayed values. Delayed values of v are found using a shift register of length $N_{\mathrm{m}} = \max(N_{\mathrm{vi}}, N_{\mathrm{ve}})$:

$$\begin{Bmatrix} v(k) \\ \vdots \\ v(k-N_{\mathrm{m}}+1) \end{Bmatrix} = \begin{bmatrix} \mathbf{0}_{[1,N_{\mathrm{m}}-1]} & 0 \\ \mathbf{I}_{[N_{\mathrm{m}}-1,N_{\mathrm{m}}-1]} & \mathbf{0}_{[N_{\mathrm{m}}-1,1]} \end{bmatrix} \begin{Bmatrix} v(k-1) \\ \vdots \\ v(k-N_{\mathrm{m}}) \end{Bmatrix} + \begin{bmatrix} 1 \\ \mathbf{0} \end{bmatrix} v(k)$$

$$\begin{aligned} \boldsymbol{x}_{\tau v}(k+1) &= \mathbf{A}_\tau\boldsymbol{x}_{\tau v}(k) + \mathbf{B}_\tau v(k) \\ &= \mathbf{A}_\tau\boldsymbol{x}_{\tau v}(k) + \mathbf{B}_\tau\mathbf{C}_{\mathrm{V}(1,:)}\boldsymbol{x}_{\mathrm{V}}(k) + \mathbf{B}_\tau\mathbf{D}_{\mathrm{V}(1,1)}\delta(k) \\ &\quad + \mathbf{B}_\tau\mathbf{D}_{\mathrm{V}(1,2)}\mathbf{C}_{fv}\boldsymbol{x}_{fv}(k) + \mathbf{B}_\tau\mathbf{D}_{\mathrm{V}(1,2)}\mathbf{D}_{fv}w_v(k) \\ &\quad + \mathbf{B}_\tau\mathbf{D}_{\mathrm{V}(1,3)}\mathbf{C}_{f\omega}\boldsymbol{x}_{f\omega}(k) + \mathbf{B}_\tau\mathbf{D}_{\mathrm{V}(1,3)}\mathbf{D}_{f\omega}w_\omega(k) \end{aligned} \tag{A.5}$$

where $\mathbf{I}$ is the identity matrix, $\mathbf{0}$ is a matrix of zeros, and $\mathbf{M}_{[i,j]}$ is a matrix with i rows and j columns. Delayed values of ω are found similarly:

$$\begin{aligned} \boldsymbol{x}_{\tau\omega}(k+1) &= \mathbf{A}_\tau\boldsymbol{x}_{\tau\omega}(k) + \mathbf{B}_\tau\mathbf{C}_{\mathrm{V}(2,:)}\boldsymbol{x}_{\mathrm{V}}(k) + \mathbf{B}_\tau\mathbf{D}_{\mathrm{V}(2,1)}\delta(k) \\ &\quad + \mathbf{B}_\tau\mathbf{D}_{\mathrm{V}(2,2)}\mathbf{C}_{fv}\boldsymbol{x}_{fv}(k) + \mathbf{B}_\tau\mathbf{D}_{\mathrm{V}(2,2)}\mathbf{D}_{fv}w_v(k) \\ &\quad + \mathbf{B}_\tau\mathbf{D}_{\mathrm{V}(2,3)}\mathbf{C}_{f\omega}\boldsymbol{x}_{f\omega}(k) + \mathbf{B}_\tau\mathbf{D}_{\mathrm{V}(2,3)}\mathbf{D}_{f\omega}w_\omega(k) \end{aligned} \tag{A.6}$$

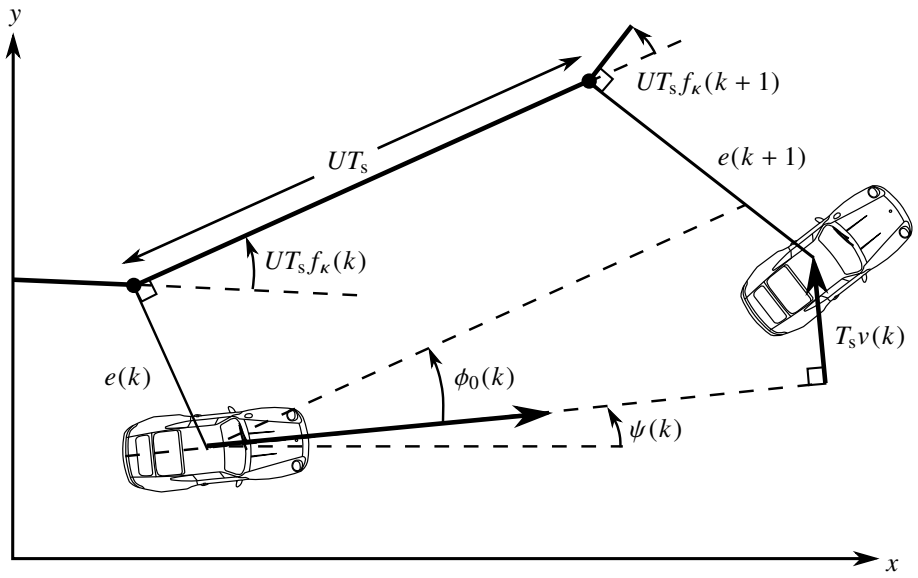

Figure A.4: Visual system measurements. The driver measures the path-following error e, and previewed road angles $\boldsymbol{\phi}$ relative to the yaw angle ψ of the vehicle.

The visual system measurements are delayed by τ_{vi}. For ω this is given by:

$$\omega(k - N_{\mathrm{vi}}) = \begin{bmatrix} \mathbf{0}_{[1,N_{\mathrm{vi}}-1]} & 1 & \mathbf{0}_{[1,N_{\mathrm{m}}-N_{\mathrm{vi}}]} \end{bmatrix} \boldsymbol{x}_{\tau\omega}(k) = \mathbf{C}_{\tau\mathrm{vi}} \boldsymbol{x}_{\tau\omega}(k) \tag{A.7}$$

Similarly, the semi-circular canals (SCCs) take measurements of ω, delayed by τ_{ve}:

$$\omega(k - N_{\mathrm{ve}}) = \begin{bmatrix} \mathbf{0}_{[1,N_{\mathrm{ve}}-1]} & 1 & \mathbf{0}_{[1,N_{\mathrm{m}}-N_{\mathrm{ve}}]} \end{bmatrix} \boldsymbol{x}_{\tau\omega}(k) = \mathbf{C}_{\tau\omega} \boldsymbol{x}_{\tau\omega}(k) \tag{A.8}$$

The otoliths measure the vehicle's lateral acceleration, which is found from:

$$a = \frac{\mathrm{d}v}{\mathrm{d}t} + U\omega \tag{A.9}$$

In discrete time, and delayed by τ_{ve}, this becomes:

$$\begin{aligned} a(k - N_{\mathrm{ve}}) &= \frac{1}{T_{\mathrm{s}}} v(k - N_{\mathrm{ve}} + 1) - \frac{1}{T_{\mathrm{s}}} v(k - N_{\mathrm{ve}}) + U\omega(k - N_{\mathrm{ve}}) \\ &= \begin{bmatrix} \mathbf{0}_{[1,N_{\mathrm{ve}}-2]} & \frac{1}{T_{\mathrm{s}}} & \frac{-1}{T_{\mathrm{s}}} & \mathbf{0}_{[1,N_{\mathrm{m}}-N_{\mathrm{ve}}]} \end{bmatrix} \boldsymbol{x}_{\tau v}(k) + U\mathbf{C}_{\tau\omega} \boldsymbol{x}_{\tau\omega}(k) \\ &= \mathbf{C}_{\tau v} \boldsymbol{x}_{\tau v}(k) + U\mathbf{C}_{\tau\omega} \boldsymbol{x}_{\tau\omega}(k) \end{aligned} \tag{A.10}$$

The visual system of the driver measures the path-following error e and previews the upcoming target angles $\boldsymbol{\phi} = \begin{Bmatrix} \phi_0(k) & \dots & \phi_{N_{\mathrm{p}}}(k) \end{Bmatrix}$ relative to the vehicle, as shown in Figure A.4. This gives a prediction horizon of length $N_{\mathrm{p}} = T_{\mathrm{p}}/T_{\mathrm{s}}$ time steps. The target

angles are stored as states in a shift register, and each angle is related to the previously measured angles by the equation:

$$\phi_n(k+1) = \phi_{(n+1)}(k) - T_\mathrm{s}\omega(k) \tag{A.11}$$

with the most distant previewed angle ϕ_{N_p} given by:

$$\phi_{N_\mathrm{p}}(k+1) = \phi_{N_\mathrm{p}}(k) - T_\mathrm{s}\omega(k) + UT_\mathrm{s}f_\kappa(k+N_\mathrm{p}) \tag{A.12}$$

In matrix form, and delayed by τ_vi:

$$\begin{aligned}\begin{Bmatrix}\tilde{\boldsymbol{x}}_{f\kappa}(k+1)\\ \phi_{N_\mathrm{p}}(k-N_\mathrm{vi}+1)\\ \vdots\\ \phi_0(k-N_\mathrm{vi}+1)\end{Bmatrix} &= \begin{bmatrix}\mathbf{A}_{f\kappa} & \mathbf{0} & \mathbf{0} & \mathbf{0}\\ UT_\mathrm{s}\mathbf{C}_{f\kappa} & 1 & \mathbf{0} & 0\\ \mathbf{0} & 1 & \mathbf{0} & 0\\ \mathbf{0} & \mathbf{0} & \mathbf{I} & \mathbf{0}\end{bmatrix}\begin{Bmatrix}\tilde{\boldsymbol{x}}_{f\kappa}(k)\\ \phi_{N_\mathrm{p}}(k-N_\mathrm{vi})\\ \vdots\\ \phi_0(k-N_\mathrm{vi})\end{Bmatrix} + \begin{bmatrix}\mathbf{B}_{f\kappa}\\ UT_\mathrm{s}\mathbf{D}_{f\kappa}\\ 0\\ \mathbf{0}\end{bmatrix}\tilde{w}_\kappa(k)\\ &\quad + \begin{bmatrix}\mathbf{0}\\ -T_\mathrm{s}\mathbf{1}_{[N_\mathrm{p}+1,1]}\end{bmatrix}\omega(k-N_\mathrm{vi})\\ \boldsymbol{\phi}_\mathrm{vi}(k) = \begin{Bmatrix}\phi_{N_\mathrm{p}}(k-N_\mathrm{vi})\\ \vdots\\ \phi_0(k-N_\mathrm{vi})\end{Bmatrix} &= \begin{bmatrix}\mathbf{0} & \mathbf{I}_{[N_\mathrm{p}+1,N_\mathrm{p}+1]}\end{bmatrix}\boldsymbol{x}_\phi(k)\end{aligned} \tag{A.13}$$

where $\tilde{w}_\kappa(k) = w_\kappa(k+N_\mathrm{p}-N_\mathrm{vi})$, $\tilde{\boldsymbol{x}}_{f\kappa}(k) = \boldsymbol{x}_{f\kappa}(k+N_\mathrm{p}-N_\mathrm{vi})$ and $\mathbf{1}$ is a matrix of ones. This can be written more concisely as:

$$\begin{aligned}\boldsymbol{x}_\phi(k+1) &= \mathbf{A}_\phi\boldsymbol{x}_\phi(k) + \mathbf{B}_\phi\tilde{w}_\kappa(k) + \mathbf{B}_{\phi\omega}\mathbf{C}_{\tau\mathrm{vi}}\boldsymbol{x}_{\tau\omega}(k)\\ \boldsymbol{\phi}_\mathrm{vi}(k) &= \mathbf{C}_\phi\boldsymbol{x}_\phi(k)\end{aligned} \tag{A.14}$$

Assuming ϕ_0 and f_κ are small, based on the geometry in Figure A.4 the path-following error e can be found from:

$$e(k+1) = e(k) + UT_\mathrm{s}\phi_0(k) - T_\mathrm{s}v(k) \tag{A.15}$$

which when delayed by τ_vi becomes:

$$\begin{aligned}e_\mathrm{vi}(k+1) = e(k-N_\mathrm{vi}+1) &= e(k-N_\mathrm{vi}) + UT_\mathrm{s}\phi_0(k-N_\mathrm{vi}) - T_\mathrm{s}v(k-N_\mathrm{vi})\\ &= e(k-N_\mathrm{vi}) + UT_\mathrm{s}\begin{bmatrix}\mathbf{0} & 1\end{bmatrix}\boldsymbol{x}_\phi(k) - T_\mathrm{s}\mathbf{C}_{\tau\mathrm{vi}}\boldsymbol{x}_{\tau v}(k)\end{aligned} \tag{A.16}$$

For the trials without preview the target line is straight, so the driver only sees the vehicle yaw angle ψ. The preview horizon doesn't matter, so let $T_\mathrm{p} = 0$ s. The equations for $\boldsymbol{\phi}_\mathrm{vi}$ become:

$$\begin{Bmatrix} \boldsymbol{x}_{f\kappa}(k+1) \\ \psi(k-N_\mathrm{vi}+1) \\ \phi_0(k-N_\mathrm{vi}+1) \end{Bmatrix} = \begin{bmatrix} \mathbf{A}_{f\kappa} & \mathbf{0} & \mathbf{0} \\ \mathbf{0} & 1 & 0 \\ UT_\mathrm{s}\mathbf{C}_{f\kappa} & 0 & 1 \end{bmatrix} \begin{Bmatrix} \boldsymbol{x}_{f\kappa}(k) \\ \psi(k-N_\mathrm{vi}) \\ \phi_0(k-N_\mathrm{vi}) \end{Bmatrix} + \begin{bmatrix} \mathbf{B}_{f\kappa} \\ 0 \\ UT_\mathrm{s}\mathbf{D}_{f\kappa} \end{bmatrix} \tilde{w}_\kappa(k) + \begin{bmatrix} \mathbf{0} \\ T_\mathrm{s} \\ -T_\mathrm{s} \end{bmatrix} \omega(k-N_\mathrm{vi}) \tag{A.17}$$

$$\begin{aligned} \boldsymbol{x}_\phi(k+1) &= \mathbf{A}_\phi \boldsymbol{x}_\phi(k) + \mathbf{B}_\phi \tilde{w}_\kappa(k) + \mathbf{B}_{\phi\omega}\mathbf{C}_{\tau\mathrm{vi}}\boldsymbol{x}_{\tau\omega}(k) \\ \boldsymbol{\phi}_\mathrm{vi}(k) &= \psi(k-N_\mathrm{vi}) = [\mathbf{0}\ \ 1\ \ 0]\,\boldsymbol{x}_\phi(k) = \mathbf{C}_\phi \boldsymbol{x}_\phi(k) \end{aligned}$$

The visually-perceived path following error e_vi is still found from Equation A.16 as for the trials with preview.

The transfer function between the delayed angular velocity and the angular velocity ω_ve perceived by the SCCs is $H_\omega(s) = H_\mathrm{SCC}(s)H_{\mathrm{m}\omega}(s)$, where $H_\mathrm{SCC}(s)$ is a transfer function representing the dynamics of the SCCs and $H_{\mathrm{m}\omega}(s)$ is the scaling or filtering applied to the yaw motion. The perceived angular velocity is then found from:

$$\begin{aligned} \boldsymbol{x}_\omega(k+1) &= \mathbf{A}_\omega \boldsymbol{x}_\omega(k) + \mathbf{B}_\omega \omega(k-N_\mathrm{ve}) = \mathbf{A}_\omega \boldsymbol{x}_\omega(k) + \mathbf{B}_\omega \mathbf{C}_{\tau\omega}\boldsymbol{x}_{\tau\omega}(k) \\ \omega_\mathrm{ve}(k) &= \mathbf{C}_\omega \boldsymbol{x}_\omega(k) + \mathbf{D}_\omega \omega(k-N_\mathrm{ve}) = \mathbf{C}_\omega \boldsymbol{x}_\omega(k) + \mathbf{D}_\omega \mathbf{C}_{\tau\omega}\boldsymbol{x}_{\tau\omega}(k) \end{aligned} \tag{A.18}$$

The transfer function between the delayed lateral acceleration and the acceleration a_ve perceived by the otoliths is $H_a(s) = H_\mathrm{oto}(s)H_{\mathrm{m}a}(s)$, where $H_\mathrm{oto}(s)$ is a transfer function representing the dynamics of the otoliths and $H_{\mathrm{m}a}(s)$ is the scaling or filtering applied to the lateral acceleration. The perceived lateral acceleration is then found from:

$$\begin{aligned} \boldsymbol{x}_a(k+1) &= \mathbf{A}_a \boldsymbol{x}_a(k) + \mathbf{B}_a a(k-N_\mathrm{ve}) = \mathbf{A}_a \boldsymbol{x}_a(k) + \mathbf{B}_a \mathbf{C}_{\tau v}\boldsymbol{x}_{\tau v}(k) + U\mathbf{B}_a \mathbf{C}_{\tau\omega}\boldsymbol{x}_{\tau\omega}(k) \\ a_\mathrm{ve}(k) &= \mathbf{C}_a \boldsymbol{x}_a(k) + \mathbf{D}_a a(k-N_\mathrm{ve}) = \mathbf{C}_a \boldsymbol{x}_a(k) + \mathbf{D}_a \mathbf{C}_{\tau v}\boldsymbol{x}_{\tau v}(k) + U\mathbf{D}_a \mathbf{C}_{\tau\omega}\boldsymbol{x}_{\tau\omega}(k) \end{aligned} \tag{A.19}$$

Combining Equations A.1 to A.19 gives the complete plant, written in discrete-time state-space form:

$$\begin{aligned} \boldsymbol{x}(k+1) &= \mathbf{A}\boldsymbol{x}(k) + \mathbf{B}\hat{\delta}(k) + [\mathbf{B}\ \ \mathbf{G}_v\ \ \mathbf{G}_\omega\ \ \mathbf{G}_\kappa]\,\{w(k)\ \ w_v(k)\ \ w_\omega(k)\ \ \tilde{w}_\kappa(k)\}^\mathrm{T} \\ \boldsymbol{y}(k) &= \mathbf{C}\boldsymbol{x}(k) \end{aligned} \tag{A.20}$$

where the plant state-space matrices are:

$$\boldsymbol{x} = \left\{ \boldsymbol{x}_{\mathrm{V}} \quad \delta \quad \boldsymbol{x}_{\mathrm{nm}} \quad \boldsymbol{x}_{fv} \quad \boldsymbol{x}_{f\omega} \quad \boldsymbol{x}_{\tau v} \quad \boldsymbol{x}_{\tau\omega} \quad \boldsymbol{x}_{\phi} \quad \boldsymbol{x}_{a} \quad \boldsymbol{x}_{\omega} \quad e_{\mathrm{vi}} \right\}^{\mathrm{T}}$$

$$\mathbf{A} = \begin{bmatrix}
\mathbf{A}_{\mathrm{V}} & \mathbf{B}_{\mathrm{V}(:,\,1)} & \mathbf{0} & \mathbf{B}_{\mathrm{V}(:,\,2)}\mathbf{C}_{fv} & \mathbf{B}_{\mathrm{V}(:,\,3)}\mathbf{C}_{f\omega} & \mathbf{0} & \mathbf{0} & \mathbf{0} & \mathbf{0} & \mathbf{0} & \mathbf{0} \\
\mathbf{0} & 0 & \mathbf{C}_{\mathrm{nm}} & \mathbf{0} & \mathbf{0} & \mathbf{0} & \mathbf{0} & \mathbf{0} & \mathbf{0} & \mathbf{0} & 0 \\
\mathbf{0} & \mathbf{0} & \mathbf{A}_{\mathrm{nm}} & \mathbf{0} & \mathbf{0} & \mathbf{0} & \mathbf{0} & \mathbf{0} & \mathbf{0} & \mathbf{0} & \mathbf{0} \\
\mathbf{0} & \mathbf{0} & \mathbf{0} & \mathbf{A}_{fv} & \mathbf{0} & \mathbf{0} & \mathbf{0} & \mathbf{0} & \mathbf{0} & \mathbf{0} & \mathbf{0} \\
\mathbf{0} & \mathbf{0} & \mathbf{0} & \mathbf{0} & \mathbf{A}_{f\omega} & \mathbf{0} & \mathbf{0} & \mathbf{0} & \mathbf{0} & \mathbf{0} & \mathbf{0} \\
\mathbf{B}_{\tau}\mathbf{C}_{\mathrm{V}(1,\,:)} & \mathbf{B}_{\tau}\mathbf{D}_{\mathrm{V}(1,\,1)} & \mathbf{0} & \mathbf{B}_{\tau}\mathbf{D}_{\mathrm{V}(1,\,2)}\mathbf{C}_{fv} & \mathbf{B}_{\tau}\mathbf{D}_{\mathrm{V}(1,\,3)}\mathbf{C}_{f\omega} & \mathbf{A}_{\tau} & \mathbf{0} & \mathbf{0} & \mathbf{0} & \mathbf{0} & \mathbf{0} \\
\mathbf{B}_{\tau}\mathbf{C}_{\mathrm{V}(2,\,:)} & \mathbf{B}_{\tau}\mathbf{D}_{\mathrm{V}(2,\,1)} & \mathbf{0} & \mathbf{B}_{\tau}\mathbf{D}_{\mathrm{V}(2,\,2)}\mathbf{C}_{fv} & \mathbf{B}_{\tau}\mathbf{D}_{\mathrm{V}(2,\,3)}\mathbf{C}_{f\omega} & \mathbf{0} & \mathbf{A}_{\tau} & \mathbf{0} & \mathbf{0} & \mathbf{0} & \mathbf{0} \\
\mathbf{0} & \mathbf{0} & \mathbf{0} & \mathbf{0} & \mathbf{0} & \mathbf{0} & \mathbf{B}_{\phi\omega}\mathbf{C}_{\tau\mathrm{vi}} & \mathbf{A}_{\phi} & \mathbf{0} & \mathbf{0} & \mathbf{0} \\
\mathbf{0} & \mathbf{0} & \mathbf{0} & \mathbf{0} & \mathbf{0} & \mathbf{B}_{a}\mathbf{C}_{\tau v} & U\mathbf{B}_{a}\mathbf{C}_{\tau\omega} & \mathbf{0} & \mathbf{A}_{a} & \mathbf{0} & \mathbf{0} \\
\mathbf{0} & \mathbf{0} & \mathbf{0} & \mathbf{0} & \mathbf{0} & \mathbf{0} & \mathbf{B}_{\omega}\mathbf{C}_{\tau\omega} & \mathbf{0} & \mathbf{0} & \mathbf{A}_{\omega} & \mathbf{0} \\
\mathbf{0} & 0 & \mathbf{0} & \mathbf{0} & \mathbf{0} & -T_{\mathrm{s}}\mathbf{C}_{\tau\mathrm{vi}} & \mathbf{0} & [\mathbf{0}\ UT_{\mathrm{s}}] & \mathbf{0} & \mathbf{0} & 1
\end{bmatrix}$$

$$\mathbf{B} = \begin{bmatrix} \mathbf{0} & \mathbf{D}_{\mathrm{nm}} & \mathbf{B}_{\mathrm{nm}} & \mathbf{0} & \mathbf{0} & \mathbf{0} & \mathbf{0} & \mathbf{0} & \mathbf{0} & \mathbf{0} & 0 \end{bmatrix}^{\mathrm{T}}$$

$$\mathbf{G}_{v} = \begin{bmatrix} \mathbf{B}_{\mathrm{V}(:,2)}\mathbf{D}_{fv} & 0 & \mathbf{0} & \mathbf{B}_{fv} & \mathbf{0} & \mathbf{B}_{\tau}\mathbf{D}_{\mathrm{V}(1,2)}\mathbf{D}_{fv} & \mathbf{B}_{\tau}\mathbf{D}_{\mathrm{V}(2,2)}\mathbf{D}_{fv} & \mathbf{0} & \mathbf{0} & \mathbf{0} & 0 \end{bmatrix}^{\mathrm{T}}$$

$$\mathbf{G}_{\omega} = \begin{bmatrix} \mathbf{B}_{\mathrm{V}(:,3)}\mathbf{D}_{f\omega} & 0 & \mathbf{0} & \mathbf{0} & \mathbf{B}_{f\omega} & \mathbf{B}_{\tau}\mathbf{D}_{\mathrm{V}(1,3)}\mathbf{D}_{f\omega} & \mathbf{B}_{\tau}\mathbf{D}_{\mathrm{V}(2,3)}\mathbf{D}_{f\omega} & \mathbf{0} & \mathbf{0} & \mathbf{0} & 0 \end{bmatrix}^{\mathrm{T}}$$

$$\mathbf{G}_{\kappa} = \begin{bmatrix} \mathbf{0} & 0 & \mathbf{0} & \mathbf{0} & \mathbf{0} & \mathbf{0} & \mathbf{0} & \mathbf{B}_{\phi} & \mathbf{0} & \mathbf{0} & 0 \end{bmatrix}^{\mathrm{T}}$$

$$\boldsymbol{y} = \left\{ \boldsymbol{\phi}_{\mathrm{vi}} \quad e_{\mathrm{vi}} \quad a_{\mathrm{ve}} \quad \omega_{\mathrm{ve}} \right\}^{\mathrm{T}}$$

$$\mathbf{C} = \begin{bmatrix}
\mathbf{0} & \mathbf{0} & \mathbf{0} & \mathbf{0} & \mathbf{0} & \mathbf{0} & \mathbf{0} & \mathbf{C}_{\phi} & \mathbf{0} & \mathbf{0} & \mathbf{0} \\
\mathbf{0} & 0 & \mathbf{0} & \mathbf{0} & \mathbf{0} & \mathbf{0} & \mathbf{0} & \mathbf{0} & \mathbf{0} & \mathbf{0} & 1 \\
\mathbf{0} & 0 & \mathbf{0} & \mathbf{0} & \mathbf{0} & \mathbf{D}_{a}\mathbf{C}_{\tau v} & U\mathbf{D}_{a}\mathbf{C}_{\tau\omega} & \mathbf{0} & \mathbf{C}_{a} & \mathbf{0} & 0 \\
\mathbf{0} & 0 & \mathbf{0} & \mathbf{0} & \mathbf{0} & \mathbf{0} & \mathbf{D}_{\omega}\mathbf{C}_{\tau\omega} & \mathbf{0} & \mathbf{0} & \mathbf{C}_{\omega} & 0
\end{bmatrix} \tag{A.21}$$

The small-angle assumptions made in this derivation allow a linear simulation to be run, even with large overall angles in the target path and the vehicle dynamics. However, in order to plot the path followed by the vehicle the Cartesian coordinates of the target path and vehicle must be calculated. For the target, the x and y components x_{t} and y_{t} are given by:

$$\begin{aligned}
x_{\mathrm{t}}(k+1) &= x_{\mathrm{t}}(k) + UT_{\mathrm{s}} \cos\left(\sum_{i=0}^{k} UT_{\mathrm{s}} f_{\kappa}(i) \right) \\
y_{\mathrm{t}}(k+1) &= y_{\mathrm{t}}(k) + UT_{\mathrm{s}} \sin\left(\sum_{i=0}^{k} UT_{\mathrm{s}} f_{\kappa}(i) \right)
\end{aligned} \tag{A.22}$$

The position of the vehicle is linearised about the target path as shown in Figure A.4 [219], and is given by finding the point located e away from the target coordinate in a perpendicular direction:

$$\begin{aligned} x(k) &= x_{\mathrm{t}}(k) + e(k)\sin\left(\sum_{i=0}^{k} UT_{\mathrm{s}} f_{\kappa}(i)\right) \\ y(k) &= y_{\mathrm{t}}(k) - e(k)\cos\left(\sum_{i=0}^{k} UT_{\mathrm{s}} f_{\kappa}(i)\right) \end{aligned} \tag{A.23}$$

A.1.2 State estimator

The controller requires the full plant state vector $\boldsymbol{x}$ to calculate the optimal plant input. However, the driver does not have access to all the states, and only measures the outputs $\boldsymbol{y}$ of the plant perturbed by measurement noise $\boldsymbol{v}$. An estimate $\hat{\boldsymbol{x}}$ of the plant states is obtained using a Kalman filter [181], based on an internal model of the plant, a measurement of the noise-free plant input $\hat{\delta}$ and noisy measurements $(\boldsymbol{y}+\boldsymbol{v})$ of the outputs. The statistical properties of the forcing functions and process and measurement noise are described by covariance matrices $\mathbf{Q}_{\mathrm{KF}}$ and $\mathbf{R}_{\mathrm{KF}}$, given by:

$$\begin{aligned} \mathbf{Q}_{\mathrm{KF}} &= \mathrm{diag}\left(\begin{bmatrix} W^2 & W_v^2 & W_\omega^2 & W_\kappa^2 \end{bmatrix}\right) \\ \mathbf{R}_{\mathrm{KF}} &= \mathrm{diag}\left(\begin{bmatrix} V_\phi^2 \mathbf{1}_{[1,N_{\mathrm{p}}+1]} & V_e^2 & V_a^2 & V_\omega^2 \end{bmatrix}\right) \end{aligned} \tag{A.24}$$

where W^2 is the variance of the process noise w, and V_ϕ^2, V_e^2, V_a^2, and V_ω^2 are the variances of the measurement noise added to the plant outputs $\boldsymbol{\phi}_{\mathrm{vi}}$, e_{vi}, a_{ve}, and ω_{ve}. In some implementations $\mathbf{Q}_{\mathrm{KF}}$ is replaced by the covariance of the process noise on the states, given by:

$$\hat{\mathbf{Q}}_{\mathrm{KF}} = \begin{bmatrix} \mathbf{B} & \mathbf{G}_v & \mathbf{G}_\omega & \mathbf{G}_\kappa \end{bmatrix} \mathbf{Q}_{\mathrm{KF}} \begin{bmatrix} \mathbf{B} & \mathbf{G}_v & \mathbf{G}_\omega & \mathbf{G}_\kappa \end{bmatrix}^{\mathrm{T}} \tag{A.25}$$

The optimal state estimate is given by [181]:

$$\hat{\boldsymbol{x}}(k+1) = \mathbf{A}\hat{\boldsymbol{x}}(k) + \mathbf{B}\hat{\delta}(k) + \mathbf{L}(\boldsymbol{y}(k) + \boldsymbol{v}(k) - \mathbf{C}\hat{\boldsymbol{x}}(k)) \tag{A.26}$$

where:

$$\mathbf{L} = \mathbf{A}\mathbf{P}\mathbf{C}^{\mathrm{T}}(\mathbf{C}\mathbf{P}\mathbf{C}^{\mathrm{T}} + \mathbf{R}_{\mathrm{KF}})^{-1} \tag{A.27}$$

and $\mathbf{P}$ solves the discrete Riccati equation:

$$\mathbf{A}^{\mathrm{T}}\mathbf{P}\mathbf{A} - \mathbf{P} - \mathbf{A}^{\mathrm{T}}\mathbf{P}\mathbf{C}(\mathbf{C}^{\mathrm{T}}\mathbf{P}\mathbf{C} + \mathbf{R}_{\mathrm{KF}})^{-1}\mathbf{C}^{\mathrm{T}}\mathbf{P}\mathbf{A} + \hat{\mathbf{Q}}_{\mathrm{KF}} = \mathbf{0} \tag{A.28}$$

This gives a linear time-invariant Kalman filter $\mathbf{H}_{\mathrm{KF}}(s)$, which can be calculated using the Matlab function *kalman*. The state estimate $\hat{\boldsymbol{x}}$ can then be found from the measured plant input and outputs:

$$\hat{\boldsymbol{x}}(s) = \mathbf{H}_{\mathrm{KF}}(s) \begin{Bmatrix} \hat{\delta}(s) \\ \boldsymbol{y}(s) + \boldsymbol{v}(s) \end{Bmatrix} \tag{A.29}$$

A.1.3 Controller

An optimal controller is used to minimise a cost function weighting the path-following error against the driver's steering effort. There are two main implementations of optimal control, a linear quadratic regulator (LQR) and model predictive control (MPC), which have been found to be identical when used under the same conditions [14]. For the linear plant an LQR controller is used since it allows the optimum control input to be found over an infinite control horizon. Target and disturbance inputs beyond the prediction horizon are assumed to be white noise.

The LQR method involves calculating an optimal gain vector $\mathbf{K}_{\mathrm{LQ}}$, which acts on the plant states to give an optimal plant input $\hat{\delta}$ which minimises a cost function J. Additive white noise does not affect the optimal solution, so the white noise inputs w, w_κ, w_v and w_ω can be ignored. The cost function incorporates costs on the tracking error e_{vi} and the plant input $\hat{\delta}$, weighted by q_e and q_δ:

$$\begin{aligned} J &= \sum_{k=0}^{\infty} \left\{ q_e e_{\mathrm{vi}}(k)^2 + q_\delta \hat{\delta}(k)^2 \right\} \\ &= \sum_{k=0}^{\infty} \left\{ \boldsymbol{x}(k)^{\mathrm{T}} \mathbf{Q}_{\mathrm{LQ}} \boldsymbol{x}(k) + \hat{\delta}(k)^{\mathrm{T}} \mathbf{R}_{\mathrm{LQ}} \hat{\delta}(k) \right\} \end{aligned} \tag{A.30}$$

where:

$$\mathbf{Q}_{\mathrm{LQ}} = \mathrm{diag}\left(\begin{bmatrix} 0 & \cdots & 0 & q_e \end{bmatrix} \right) \tag{A.31}$$

$$\mathbf{R}_{\mathrm{LQ}} = q_\delta \tag{A.32}$$

The optimal plant input is [14]:

$$\hat{\delta}(k) = -\mathbf{K}_{\mathrm{LQ}} \boldsymbol{x}(k) \tag{A.33}$$

where:

$$\mathbf{K}_{\mathrm{LQ}} = (\mathbf{B}^{\mathrm{T}} \mathbf{S} \mathbf{B} + \mathbf{R}_{\mathrm{LQ}})^{-1} \mathbf{B}^{\mathrm{T}} \mathbf{S} \mathbf{A} \tag{A.34}$$

and $\mathbf{S}$ solves the discrete Riccati equation:

$$\mathbf{A}^{\mathrm{T}}\mathbf{S}\mathbf{A} - \mathbf{S} - \mathbf{A}^{\mathrm{T}}\mathbf{S}\mathbf{B}(\mathbf{B}^{\mathrm{T}}\mathbf{S}\mathbf{B} + \mathbf{R}_{\mathrm{LQ}})^{-1}\mathbf{B}^{\mathrm{T}}\mathbf{S}\mathbf{A} + \mathbf{Q}_{\mathrm{LQ}} = \mathbf{0} \tag{A.35}$$

The optimal gain $\mathbf{K}_{\mathrm{LQ}}$ can be found in this way using the Matlab function *dlqr*.

A.2 Nonlinear driver model

In this section the linear driver model derived in Section A.1 is extended to control a constant-speed vehicle with nonlinear tyres. Nonlinear optimal control and state estimation are much more difficult than their linear equivalents. However, it is possible to simplify the task by approximating the nonlinear system dynamics. There are various ways in which this can be done, therefore several state estimators and controllers are implemented. The performance of the different methods is compared using simulations in [234], and these results are used to guide the choice of models which are fit to measured experimental data in Chapter 6.

A.2.1 Plant

The only difference between the linear and nonlinear plant is a nonlinear vehicle. The disturbances are added using the linear relationship in Equation A.3, however the dependence on the steering angle and previous states is nonlinear. The vehicle states (v and ω) are therefore found from:

$$\begin{Bmatrix} v(k+1) \\ \omega(k+1) \end{Bmatrix} = A_{\mathrm{V}}\left(\begin{Bmatrix} v(k) \\ \omega(k) \end{Bmatrix}, \delta(k)\right) + \mathbf{B}_{\mathrm{V}(:,2)}\mathbf{C}_{fv}\boldsymbol{x}_{fv} + \mathbf{B}_{\mathrm{V}(:,3)}\mathbf{C}_{f\omega}\boldsymbol{x}_{f\omega} \tag{A.36}$$

where A_{V} is a nonlinear function. The remaining plant states are calculated in the same way as the linear model using Equation A.20, and the same linear output equation is used to find the plant outputs.

To reduce the computational load of the nonlinear controllers, a reduced plant is defined which includes only the states required by the controller. It should be noted that the state estimator still requires the complete plant. The controller minimises a cost function weighting $\hat{\delta}$ against e, therefore any parts of the plant which do not feed into e in Figure A.3 are ignored. This includes the motion filters, sensory dynamics and delays. Furthermore, using an MPC formulation allows the target path to be implemented as a reference without including the preview shift register in the reduced plant. This allows a significant reduction in the number of plant states.

The driver's visual system previews $(N_p + 1)$ path angles, however due to the visual delay N_{vi} of the measured angles are already behind the current position of the vehicle. The controllers described in Section A.2.3 therefore evaluate the reduced plant equations from the current time step k to $(k + N_p - N_{vi} + 1)$.

Equation A.11 can be adapted to find future values of ϕ_0 from the current previewed target angles ϕ_n:

$$\phi_0(k+n) = \phi_n(k) - \hat{\psi}(k+n) \tag{A.37}$$

where $\hat{\psi}$ is the yaw angle of the vehicle, referenced to the current yaw angle so that $\hat{\psi}(k) = 0$. It can be found from:

$$\begin{aligned}\hat{\psi}(k+n+1) &= \hat{\psi}(k+n) + T_s\omega(k+n)\\ &= \hat{\psi}(k+n) + T_s\mathbf{C}_{V(2,:)}\boldsymbol{x}_V(k+n) + T_s\mathbf{D}_{V(2,1)}\delta(k+n)\\ &+ T_s\mathbf{D}_{V(2,2)}\mathbf{C}_{fv}\boldsymbol{x}_{fv}(k+n) + T_s\mathbf{D}_{V(2,2)}\mathbf{D}_{fv}w_v(k+n)\\ &+ T_s\mathbf{D}_{V(2,3)}\mathbf{C}_{f\omega}\boldsymbol{x}_{f\omega}(k+n) + T_s\mathbf{D}_{V(2,3)}\mathbf{D}_{f\omega}w_\omega(k+n)\end{aligned} \tag{A.38}$$

Equation A.15 can then be rewritten to separate the predicted e over the prediction horizon into a controllable part $\hat{y}$ and a reference $\hat{y}_{ref}$:

$$\begin{aligned}e(k+n+1) &= e(k+n) + UT_s\phi_0(k+n) - T_sv(k+n)\\ &= e(k+n) + UT_s\phi_n(k) - UT_s\hat{\psi}(k+n) - T_sv(k+n)\\ &= \hat{y}_{ref}(k+n+1) - \hat{y}(k+n+1)\end{aligned} \tag{A.39}$$

where the reference trajectory is found from:

$$\hat{y}_{ref}(k+n) = \sum_{i=0}^{n-1}(UT_s\phi_i(k)) \tag{A.40}$$

and the controllable part is:

$$\begin{aligned}\hat{y}(k+n+1) &= \hat{y}(k+n) + T_sv(k+n) + UT_s\psi(k+n)\\ &= \hat{y}(k+n) + T_s\mathbf{C}_{V(1,:)}\boldsymbol{x}_V(k+n) + T_s\mathbf{D}_{V(1,1)}\delta(k+n)\\ &+ T_s\mathbf{D}_{V(1,2)}\mathbf{C}_{fv}\boldsymbol{x}_{fv}(k+n) + T_s\mathbf{D}_{V(1,2)}\mathbf{D}_{fv}w_v(k+n)\\ &+ T_s\mathbf{D}_{V(1,3)}\mathbf{C}_{f\omega}\boldsymbol{x}_{f\omega}(k+n) + T_s\mathbf{D}_{V(1,3)}\mathbf{D}_{f\omega}w_\omega(k+n) + UT_s\hat{\psi}(k+n)\end{aligned} \tag{A.41}$$

If the target is close to a straight line, $\hat{y}$ and $\hat{y}_{ref}$ represent the vehicle and target lateral displacements.

The complete reduced plant for a linear vehicle has the same form as Equation A.20,

with state-space matrices:

$$
\begin{aligned}
\boldsymbol{x}_{\mathrm{R}} &= \begin{Bmatrix} \boldsymbol{x}_{\mathrm{V}} & \delta & \boldsymbol{x}_{\mathrm{nm}} & \boldsymbol{x}_{fv} & \boldsymbol{x}_{f\omega} & \hat{\psi} & \hat{y} \end{Bmatrix}^{\mathrm{T}} \\
\mathbf{A}_{\mathrm{R}} &= \begin{bmatrix}
\mathbf{A}_{\mathrm{V}} & \mathbf{B}_{\mathrm{V}(:,1)} & \mathbf{0} & \mathbf{B}_{\mathrm{V}(:,2)}\mathbf{C}_{fv} & \mathbf{B}_{\mathrm{V}(:,3)}\mathbf{C}_{f\omega} & \mathbf{0} & \mathbf{0} \\
\mathbf{0} & 0 & \mathbf{C}_{\mathrm{nm}} & \mathbf{0} & \mathbf{0} & \mathbf{0} & \mathbf{0} \\
\mathbf{0} & \mathbf{0} & \mathbf{A}_{\mathrm{nm}} & \mathbf{0} & \mathbf{0} & \mathbf{0} & \mathbf{0} \\
\mathbf{0} & \mathbf{0} & \mathbf{0} & \mathbf{A}_{fv} & \mathbf{0} & \mathbf{0} & \mathbf{0} \\
\mathbf{0} & \mathbf{0} & \mathbf{0} & \mathbf{0} & \mathbf{A}_{f\omega} & \mathbf{0} & \mathbf{0} \\
T_{\mathrm{s}}\mathbf{C}_{\mathrm{V}(2,:)} & T_{\mathrm{s}}\mathbf{D}_{\mathrm{V}(2,1)} & \mathbf{0} & T_{\mathrm{s}}\mathbf{D}_{\mathrm{V}(2,2)}\mathbf{C}_{fv} & T_{\mathrm{s}}\mathbf{D}_{\mathrm{V}(2,3)}\mathbf{C}_{f\omega} & 1 & 0 \\
T_{\mathrm{s}}\mathbf{C}_{\mathrm{V}(1,:)} & T_{\mathrm{s}}\mathbf{D}_{\mathrm{V}(1,1)} & \mathbf{0} & T_{\mathrm{s}}\mathbf{D}_{\mathrm{V}(1,2)}\mathbf{C}_{fv} & T_{\mathrm{s}}\mathbf{D}_{\mathrm{V}(1,3)}\mathbf{C}_{f\omega} & UT_{\mathrm{s}} & 1
\end{bmatrix} \\
\mathbf{B}_{\mathrm{R}} &= \begin{bmatrix} \mathbf{0} & \mathbf{D}_{\mathrm{nm}} & \mathbf{B}_{\mathrm{nm}} & \mathbf{0} & \mathbf{0} & 0 & 0 \end{bmatrix}^{\mathrm{T}} \\
\mathbf{G}_{v\mathrm{R}} &= \begin{bmatrix} \mathbf{B}_{\mathrm{V}(:,2)}\mathbf{D}_{fv} & 0 & \mathbf{0} & \mathbf{B}_{fv} & \mathbf{0} & T_{\mathrm{s}}\mathbf{D}_{\mathrm{V}(2,2)}\mathbf{D}_{fv} & T_{\mathrm{s}}\mathbf{D}_{\mathrm{V}(1,2)}\mathbf{D}_{fv} \end{bmatrix}^{\mathrm{T}} \\
\mathbf{G}_{\omega\mathrm{R}} &= \begin{bmatrix} \mathbf{B}_{\mathrm{V}(:,3)}\mathbf{D}_{f\omega} & 0 & \mathbf{0} & \mathbf{0} & \mathbf{B}_{f\omega} & T_{\mathrm{s}}\mathbf{D}_{\mathrm{V}(2,3)}\mathbf{D}_{f\omega} & T_{\mathrm{s}}\mathbf{D}_{\mathrm{V}(1,3)}\mathbf{D}_{f\omega} \end{bmatrix}^{\mathrm{T}} \\
\mathbf{G}_{\kappa\mathrm{R}} &= \begin{bmatrix} \mathbf{0} & 0 & \mathbf{0} & \mathbf{0} & \mathbf{0} & \mathbf{0} & \mathbf{0} & 0 & 0 \end{bmatrix}^{\mathrm{T}} \\
\boldsymbol{y}_{\mathrm{R}} &= \hat{y} \\
\mathbf{C}_{\mathrm{R}} &= \begin{bmatrix} \mathbf{0} & 0 & \mathbf{0} & \mathbf{0} & \mathbf{0} & 0 & 1 \end{bmatrix}
\end{aligned}
\tag{A.42}
$$

although for a nonlinear vehicle the vehicle states are calculated using Equation A.36.

For the control calculation at each time step it is necessary to find the reduced state vector $\boldsymbol{x}_{\mathrm{R}}(k)$ and reference trajectory $\hat{\boldsymbol{y}}_{\mathrm{ref}}(k)$ from the full state estimate $\hat{\boldsymbol{x}}(k)$. Most of the states in $\boldsymbol{x}_{\mathrm{R}}(k)$ can be taken directly from the equivalent states in $\hat{\boldsymbol{x}}(k)$, and the yaw angle $\hat{\psi}(k)$ is defined to start at zero. The value of $\hat{y}(k)$ is equal to the negative of the current path-following error $e(k)$. However, only the delayed version $e_{\mathrm{vi}}(k)$ is stored directly in the full state vector. Therefore $\hat{y}(k)$ must be calculated by iterating Equation A.15 using the stored delayed values of v, ω and ϕ_0, giving:

$$
\begin{aligned}
\hat{y}(k) = -e_{\mathrm{vi}}(k) &- UT_{\mathrm{s}} \sum_{n=0}^{N_{\mathrm{vi}}-1} \{\phi_n(k - N_{\mathrm{vi}})\} \\
&+ T_{\mathrm{s}} \sum_{n=-N_{\mathrm{vi}}}^{-1} \{v(k+n)\} + UT_{\mathrm{s}}^2 \sum_{n=-N_{\mathrm{vi}}}^{-2} \{n\omega(k+n)\}
\end{aligned}
\tag{A.43}
$$

Similarly, the reference trajectory depends through Equation A.40 on previewed angles $\phi_n(k)$, however the full state vector contains delayed values $\phi_n(k - N_{\text{vi}})$. The required angles can be calculated by iterating Equation A.11 over the visual delay:

$$\phi_n(k) = \phi_{(n+N_{\text{vi}})}(k - N_{\text{vi}}) - T_{\text{s}} \sum_{i=-N_{\text{vi}}}^{-1} \{\omega(k+i)\} \tag{A.44}$$

A.2.2 State estimators

State estimation for a nonlinear plant can be achieved using an extended Kalman filter, which operates on the same principles as the Kalman filter described in Section A.1.2. Extended Kalman filters approximate the nonlinear plant dynamics by linearisation or similar transformations. Four variations of the extended Kalman filter are implemented using code provided by the EKF/UKF Matlab toolbox [236]. These four extended Kalman filters can also be compared with full state feedback, giving five state estimators in total:

- LKF: Linear Kalman filter. A time-varying implementation of a linear Kalman filter, found by linearising the plant states about zero slip angle. It should give the same results as the time-invariant filter derived in Section A.1.2.
- EKF1: First-order extended Kalman filter. A linearised approximation to the plant states is found at each time step.
- EKF2: Second-order extended Kalman filter. A quadratic approximation to the plant states is found at each time step.
- UKF: Unscented Kalman filter. The nonlinear state covariance functions are approximated at each time step using an unscented transform.
- FSF: Full state feedback. The state estimate $\hat{\boldsymbol{x}}$ is equal to the real states $\boldsymbol{x}$, removing the effects of sensory dynamics.

Detailed derivations of each of the extended Kalman filters are given in [236]. The calculations consist of two stages at each time step: First the *predict* stage in which a new state estimate is predicted from the previous estimate using an internal model of the plant, then the *update* stage where the estimate is updated based on the difference between predicted and measured plant outputs. Unlike the linear Kalman filter, the covariance matrix $\mathbf{P}$ varies with time, and is also predicted and updated in these two steps. The initial covariance matrix $\mathbf{P}_0$ is calculated by finding the steady-state solution for the plant linearised about zero slip angle from Equation A.28, using the Matlab function *kalman*. However, this gives the covariance matrix after the prediction step only, so it must be passed through the update step to ensure compatibility with the extended Kalman filters.

A.2.3 Controllers

Controllers are designed to calculate an optimal plant input $\hat{\delta}$, using an internal model of the reduced plant described in Section A.2.1. True optimal control for a nonlinear plant is computationally intensive, therefore several simplified controllers are implemented which linearise the system dynamics. These linearised controllers are based on MPC, which involves calculating an optimal control sequence $\hat{\boldsymbol{\delta}}$ up to the prediction horizon T_p, then taking the first of these as the next control input $\hat{\delta}$. For a linear plant this gives the same solution as an LQR controller [14].

Ignoring any white noise inputs, the nonlinear reduced plant equations can be written in discrete-time state-space form:

$$\begin{aligned} \boldsymbol{x}_\mathrm{R}(k+1) &= A_\mathrm{R}(\boldsymbol{x}_\mathrm{R}(k)) + \mathbf{B}_\mathrm{R}\hat{\delta}(k) \\ \hat{y}(k) &= \mathbf{C}_\mathrm{R}\boldsymbol{x}_\mathrm{R}(k) \end{aligned} \tag{A.45}$$

The nonlinear function A_R can be linearised about states $\boldsymbol{x}_\mathrm{L}$ with the approximation:

$$A_\mathrm{R}(\boldsymbol{x}_\mathrm{R}(k+n)) \approx A_\mathrm{R}(\boldsymbol{x}_\mathrm{L}(k+n)) + \hat{\mathbf{A}}_n(\boldsymbol{x}_\mathrm{R}(k+n) - \boldsymbol{x}_\mathrm{L}(k+n)) \tag{A.46}$$

where $\hat{\mathbf{A}}_n$ is the Jacobian $\mathrm{d}A_\mathrm{R}/\mathrm{d}\boldsymbol{x}$ evaluated at $\boldsymbol{x}_\mathrm{L}(k+n)$. Five different model predictive controllers are implemented, with varying levels of approximation to the nonlinear plant dynamics as illustrated in Figure A.5:

- L0: Linearisation about zero slip angle, $\boldsymbol{x}_\mathrm{L}(k+n) = \mathbf{0}$. This gives the same result as the LQR controller derived in Section A.1.3.
- LP0: Linearisation about the initial prediction state $\boldsymbol{x}_\mathrm{R}(k)$ [20, 230, 232]. $\hat{\mathbf{A}}$ is constant over the prediction horizon, linearised about $\boldsymbol{x}_\mathrm{L}(k+n) = \boldsymbol{x}_\mathrm{R}(k)$.

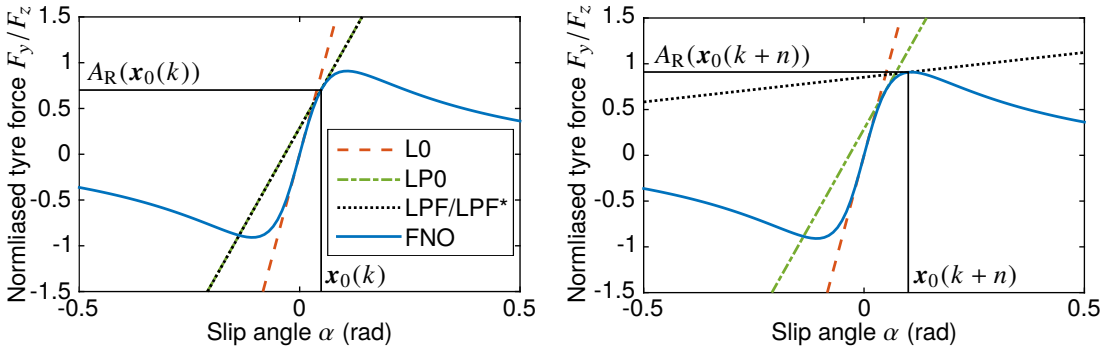

(a) Current time **(b)** Future prediction

Figure A.5: Illustration of linearisation carried out by different nonlinear controllers

- LPF: Linearisation about the full prediction horizon [21, 219]. The solution starts from a nominal control sequence $\hat{\boldsymbol{\delta}}_0$, which is the previous optimal sequence shifted by one time step, with a corresponding state trajectory $\mathbf{X}_{\mathrm{R0}} = \begin{bmatrix}\boldsymbol{x}_{\mathrm{R0}}(k) & \dots & \boldsymbol{x}_{\mathrm{R0}}(k+N_{\mathrm{p}}-N_{\mathrm{vi}}+1)\end{bmatrix}$. The linearised matrix $\hat{\mathbf{A}}_n$ is calculated about each nominal state $\boldsymbol{x}_{\mathrm{L}}(k+n) = \boldsymbol{x}_{\mathrm{R0}}(k+n)$.
- LPF*: LPF constrained to stop the slip angles exceeding the force peak, plus a constraint on the maximum change in $\hat{\boldsymbol{\delta}}$ from the nominal control sequence [7].
- FNO: Full nonlinear optimisation [229, 231]. The full nonlinear equations are used to predict the plant trajectory up to the prediction horizon.

A.2.3.1 Linearised MPC

Four of the controllers simplify the control task by linearising the plant states. They are derived based on the linear MPC method of [14], adapted for a nonlinear plant using methods similar to [21]. For simplicity the control horizon is chosen to equal the prediction horizon. In each case the control sequence $\hat{\boldsymbol{\delta}}$ is replaced with a nominal sequence $\hat{\boldsymbol{\delta}}_0$ plus a small change $\Delta\hat{\boldsymbol{\delta}}$, and similarly for $\hat{\boldsymbol{y}}$. The linearised dynamics then give the approximate relationship $\Delta\hat{\boldsymbol{y}} \approx \boldsymbol{\Theta}\Delta\hat{\boldsymbol{\delta}}$. The aim of the controller is to minimise the cost function:

$$\begin{aligned} J &= \sum_{n=1}^{N_{\mathrm{p}}-N_{\mathrm{vi}}+1} \left\{ q_e e(k+n)^2 + q_\delta \hat{\delta}(k+n)^2 \right\} \\ &= \sum_{n=1}^{N_{\mathrm{p}}-N_{\mathrm{vi}}+1} \left\{ q_e (\hat{y}_{\mathrm{ref}}(k+n) - \hat{y}(k+n))^2 + q_\delta \hat{\delta}(k+n)^2 \right\} \end{aligned} \tag{A.47}$$

Note that unlike Equation A.30 the cost only applies over the finite prediction horizon. Writing the values of $\hat{y}_{\mathrm{ref}}$, $\hat{y}$ and q_δ over the prediction horizon as vectors $\hat{\boldsymbol{y}}_{\mathrm{ref}}$, $\hat{\boldsymbol{y}}$ and $\hat{\boldsymbol{\delta}}$, and removing the $\hat{y}_{\mathrm{ref}}^2$ term which is independent of the control input, Equation A.47 can be written as:

$$J = q_e \hat{\boldsymbol{y}}^{\mathrm{T}}\hat{\boldsymbol{y}} - 2q_e \hat{\boldsymbol{y}}_{\mathrm{ref}}^{\mathrm{T}}\hat{\boldsymbol{y}} + q_\delta \hat{\boldsymbol{\delta}}^{\mathrm{T}}\hat{\boldsymbol{\delta}} \tag{A.48}$$

Replacing the control sequence $\hat{\boldsymbol{\delta}}$ with a nominal sequence $\hat{\boldsymbol{\delta}}_0$ plus a small change $\Delta\hat{\boldsymbol{\delta}}$, and similarly for $\hat{\boldsymbol{y}}$, gives:

$$J = q_e(\hat{\boldsymbol{y}}_0 + \Delta\hat{\boldsymbol{y}})^{\mathrm{T}}(\hat{\boldsymbol{y}}_0 + \Delta\hat{\boldsymbol{y}}) - 2q_e\hat{\boldsymbol{y}}_{\mathrm{ref}}^{\mathrm{T}}(\hat{\boldsymbol{y}}_0 + \Delta\hat{\boldsymbol{y}}) + q_\delta(\hat{\boldsymbol{\delta}}_0 + \Delta\hat{\boldsymbol{\delta}})^{\mathrm{T}}(\hat{\boldsymbol{\delta}}_0 + \Delta\hat{\boldsymbol{\delta}}) \tag{A.49}$$

Multiplying out and removing any independent terms:

$$J = q_e\Delta\hat{\boldsymbol{y}}^{\mathrm{T}}\Delta\hat{\boldsymbol{y}} + 2q_e(\hat{\boldsymbol{y}}_0 - \hat{\boldsymbol{y}}_{\mathrm{ref}})^{\mathrm{T}}\Delta\hat{\boldsymbol{y}} + q_\delta\Delta\hat{\boldsymbol{\delta}}^{\mathrm{T}}\Delta\hat{\boldsymbol{\delta}} + 2q_\delta\hat{\boldsymbol{\delta}}_0^{\mathrm{T}}\Delta\hat{\boldsymbol{\delta}} \tag{A.50}$$

and with the linearised dynamics $\Delta\hat{\boldsymbol{y}} = \boldsymbol{\Theta}\Delta\hat{\boldsymbol{\delta}}$:

$$J = \Delta\hat{\boldsymbol{\delta}}^{\mathrm{T}}(q_e\boldsymbol{\Theta}^{\mathrm{T}}\boldsymbol{\Theta} + q_\delta\mathbf{I})\Delta\hat{\boldsymbol{\delta}} + 2(q_e(\hat{\boldsymbol{y}}_0 - \hat{\boldsymbol{y}}_{\mathrm{ref}})^{\mathrm{T}}\boldsymbol{\Theta} + q_\delta\hat{\boldsymbol{\delta}}_0^{\mathrm{T}})\Delta\hat{\boldsymbol{\delta}} \tag{A.51}$$

which is in the form of a quadratic program. If there are no constraints this can be solved using QR decomposition as in [14], however with constraints it can be solved using a dedicated solver. Examples of quadratic program solvers include QPC [245], CPLEX [246], and Matlab's *quadprog* function.

Similarly to the linear MPC derivation in [14], however with linearised matrices $\hat{\mathbf{A}}_n$ predicted n time steps ahead of the current time step k, $\boldsymbol{\Theta}$ is found from:

$$\boldsymbol{\Theta}(k) = \begin{bmatrix} \mathbf{C}_{\mathrm{R}}\mathbf{B}_{\mathrm{R}} & \mathbf{0} & \mathbf{0} & \cdots & \mathbf{0} \\ \mathbf{C}_{\mathrm{R}}\hat{\mathbf{A}}_1\mathbf{B}_{\mathrm{R}} & \mathbf{C}_{\mathrm{R}}\mathbf{B}_{\mathrm{R}} & \mathbf{0} & \cdots & \mathbf{0} \\ \mathbf{C}_{\mathrm{R}}\hat{\mathbf{A}}_2\hat{\mathbf{A}}_1\mathbf{B}_{\mathrm{R}} & \mathbf{C}_{\mathrm{R}}\hat{\mathbf{A}}_2\mathbf{B}_{\mathrm{R}} & \mathbf{C}_{\mathrm{R}}\mathbf{B}_{\mathrm{R}} & \cdots & \mathbf{0} \\ \vdots & \vdots & \vdots & \ddots & \vdots \\ \mathbf{C}_{\mathrm{R}}\left(\prod_{i=1}^{N_{\mathrm{p}}-N_{\mathrm{vi}}}\hat{\mathbf{A}}_i\right)\mathbf{B}_{\mathrm{R}} & \mathbf{C}_{\mathrm{R}}\left(\prod_{i=2}^{N_{\mathrm{p}}-N_{\mathrm{vi}}}\hat{\mathbf{A}}_i\right)\mathbf{B}_{\mathrm{R}} & \mathbf{C}_{\mathrm{R}}\left(\prod_{i=3}^{N_{\mathrm{p}}-N_{\mathrm{vi}}}\hat{\mathbf{A}}_i\right)\mathbf{B}_{\mathrm{R}} & \cdots & \mathbf{C}_{\mathrm{R}}\mathbf{B}_{\mathrm{R}} \end{bmatrix} \tag{A.52}$$

For LPF and LPF*, the nominal control sequence $\hat{\boldsymbol{\delta}}_0$ is the previous optimal control sequence shifted by one time step. The nonlinear plant equations are then evaluated over the prediction horizon to get $\hat{\boldsymbol{y}}_0$. For L0 and LP0, the nominal control sequence $\hat{\boldsymbol{\delta}}_0$ is zero. However the non-zero initial state $\boldsymbol{x}_{\mathrm{R}}(k)$ leads to a non-zero $\hat{\boldsymbol{y}}_0$. For L0, as in [14]:

$$\hat{\boldsymbol{y}}_0 \approx \boldsymbol{\Psi}\boldsymbol{x}_{\mathrm{R}}(k) \tag{A.53}$$

where:

$$\boldsymbol{\Psi} = \begin{bmatrix} \mathbf{C}_{\mathrm{R}}\hat{\mathbf{A}} & \mathbf{C}_{\mathrm{R}}\hat{\mathbf{A}}^2 & \cdots & \mathbf{C}_{\mathrm{R}}\hat{\mathbf{A}}^{(N_{\mathrm{p}}-N_{\mathrm{vi}})} \end{bmatrix}^{\mathrm{T}} \tag{A.54}$$

For LP0:

$$\begin{aligned} \boldsymbol{x}_{\mathrm{R}}(k+1) &= A_{\mathrm{R}}(\boldsymbol{x}_{\mathrm{R}}(k)) \\ \boldsymbol{x}_{\mathrm{R}}(k+2) &= A_{\mathrm{R}}(\boldsymbol{x}_{\mathrm{R}}(k+1)) \approx A_{\mathrm{R}}(\boldsymbol{x}_{\mathrm{R}}(k)) + \hat{\mathbf{A}}(\boldsymbol{x}_{\mathrm{R}}(k+1) - \boldsymbol{x}_{\mathrm{R}}(k)) \\ &= (\mathbf{I} + \hat{\mathbf{A}})A_{\mathrm{R}}(\boldsymbol{x}_{\mathrm{R}}(k)) - \hat{\mathbf{A}}\boldsymbol{x}_{\mathrm{R}}(k)) \end{aligned} \tag{A.55}$$

Over the whole prediction horizon this leads to:

$$\hat{\boldsymbol{y}}_0 \approx \boldsymbol{\Psi}_x\boldsymbol{x}_{\mathrm{R}}(k) + \boldsymbol{\Psi}_A A_{\mathrm{R}}(\boldsymbol{x}_{\mathrm{R}}(k)) \tag{A.56}$$

where:

$$\boldsymbol{\Psi}_x = \begin{bmatrix} \mathbf{0} & -\mathbf{C}_{\mathrm{R}}\hat{\mathbf{A}} & -\mathbf{C}_{\mathrm{R}}(\hat{\mathbf{A}}^2 + \hat{\mathbf{A}}) & \cdots & -\mathbf{C}_{\mathrm{R}}\sum_{i=1}^{N_{\mathrm{p}}-N_{\mathrm{vi}}}(\hat{\mathbf{A}}^i) \end{bmatrix}^{\mathrm{T}} \tag{A.57}$$

and:

$$\boldsymbol{\Psi}_A = \begin{bmatrix} \mathbf{C}_\mathrm{R} & \mathbf{C}_\mathrm{R}(\hat{\mathbf{A}} + \mathbf{I}) & \mathbf{C}_\mathrm{R}(\hat{\mathbf{A}}^2 + \hat{\mathbf{A}} + \mathbf{I}) & \cdots & \mathbf{C}_\mathrm{R} \sum_{i=0}^{N_\mathrm{p}-N_\mathrm{vi}} (\hat{\mathbf{A}}^i) \end{bmatrix}^\mathrm{T} \tag{A.58}$$

A.2.3.2 LPF*

Controller LPF* is the same as LPF, however it includes constraints to limit the solution space to values more likely to give a successful outcome. Firstly, the linearisation assumes that the changes in optimal control strategy $\Delta\hat{\boldsymbol{\delta}}$ are small. However, this is not guaranteed with the controllers described in Section A.2.3.1. Therefore constraints are added to limit these changes, in the form:

$$\begin{aligned} \Delta\hat{\boldsymbol{\delta}} &< \Delta\hat{\delta}_\mathrm{max} \\ -\Delta\hat{\boldsymbol{\delta}} &< \Delta\hat{\delta}_\mathrm{max} \end{aligned} \tag{A.59}$$

The value of $\Delta\hat{\delta}_\mathrm{max}$ must be small enough to stop the optimal solution from moving too far from the nominal solution, however large enough that it does not limit the speed with which the controller can respond to disturbances. Simulations were run with different values of $\Delta\hat{\delta}_\mathrm{max}$, and a value of 0.1 rad* was found to be suitable.

Another potential issue with linearised controllers is that they can become unstable if the linearised force/slip characteristic becomes negative. Therefore, additional constraints are added to limit the slip angles $\boldsymbol{\alpha}_\mathrm{f}$ and $\boldsymbol{\alpha}_\mathrm{r}$ to less than α_max, where α_max is defined to be the maximum of the force-slip curve. For the vehicle models used in this thesis, the slip angles are found from linear functions of the first three plant states:

$$\alpha_\mathrm{f} = -v/U - l_\mathrm{f}\omega/U + \delta/G \tag{A.60}$$

$$\alpha_\mathrm{r} = -v/U + l_\mathrm{r}\omega/U \tag{A.61}$$

therefore the equations for $\boldsymbol{\alpha}_\mathrm{f}$ and $\boldsymbol{\alpha}_\mathrm{r}$ are linearised as:

$$\boldsymbol{\alpha}_\mathrm{f} = \boldsymbol{\alpha}_\mathrm{f0} + \boldsymbol{\Theta}_{\alpha\mathrm{f}}\Delta\hat{\boldsymbol{\delta}} \tag{A.62}$$

$$\boldsymbol{\alpha}_\mathrm{r} = \boldsymbol{\alpha}_\mathrm{r0} + \boldsymbol{\Theta}_{\alpha\mathrm{r}}\Delta\hat{\boldsymbol{\delta}} \tag{A.63}$$

Constraint matrices $\boldsymbol{\Theta}_{\alpha\mathrm{f}}$ and $\boldsymbol{\Theta}_{\alpha\mathrm{r}}$ are calculated using Equation A.52, replacing $\mathbf{C}_\mathrm{R}$ with $\mathbf{C}_{\alpha\mathrm{f}}$ or $\mathbf{C}_{\alpha\mathrm{r}}$, where:

$$\mathbf{C}_{\alpha\mathrm{f}} = \begin{bmatrix} -1/U & -l_\mathrm{f}/U & 1/G & \mathbf{0} \end{bmatrix} \tag{A.64}$$

$$\mathbf{C}_{\alpha\mathrm{r}} = \begin{bmatrix} -1/U & l_\mathrm{r}/U & 0 & \mathbf{0} \end{bmatrix} \tag{A.65}$$

The constraint equations therefore become:

$$\begin{aligned}
\boldsymbol{\Theta}_{\alpha \mathrm{f}} \Delta \hat{\boldsymbol{\delta}} &< \alpha_{\max} - \boldsymbol{\alpha}_{\mathrm{f0}} \\
\boldsymbol{\Theta}_{\alpha \mathrm{r}} \Delta \hat{\boldsymbol{\delta}} &< \alpha_{\max} - \boldsymbol{\alpha}_{\mathrm{r0}} \\
-\boldsymbol{\Theta}_{\alpha \mathrm{f}} \Delta \hat{\boldsymbol{\delta}} &< \alpha_{\max} + \boldsymbol{\alpha}_{\mathrm{f0}} \\
-\boldsymbol{\Theta}_{\alpha \mathrm{r}} \Delta \hat{\boldsymbol{\delta}} &< \alpha_{\max} + \boldsymbol{\alpha}_{\mathrm{r0}}
\end{aligned} \tag{A.66}$$

A.2.3.3 Full nonlinear optimisation

A nonlinear optimiser can be used to find a solution which considers the nonlinear dynamics of the plant in full, without any approximation. Matlab's *fminunc* function is a versatile nonlinear optimiser, although it is much more computationally expensive than the linearised alternatives. Alternative commercial nonlinear optimisers are also available, such as Ipopt [247]. As with the linearised MPC, the optimisation begins from a nominal steering command sequence $\hat{\boldsymbol{\delta}}_0$, which is the previous optimal steering sequence shifted by one time step. The optimiser then iteratively evaluates the cost function for different values of $\Delta\hat{\boldsymbol{\delta}}$, in each case calculating the full nonlinear reduced plant equations over the prediction horizon. Gradient-based optimisers such as *fminunc* use the Jacobian of the cost function to estimate the direction of the optimal solution. Although this can be estimated by the optimiser, it is much faster to calculate the Jacobian explicitly. This can be achieved by linearising the dynamics similarly to the LPF controller. The derivative of the cost function J about $\hat{\boldsymbol{\delta}}$ is equal to the linear term in Equation A.51:

$$\frac{\mathrm{d}J}{\mathrm{d}\hat{\boldsymbol{\delta}}} = 2(q_e(\hat{\boldsymbol{y}} - \hat{\boldsymbol{y}}_{\mathrm{ref}})^{\mathrm{T}}\boldsymbol{\Theta} + q_\delta \hat{\boldsymbol{\delta}}^{\mathrm{T}}) \tag{A.67}$$

A.3 Model parameter values

The performance of the driver model derived in Sections A.1 and A.2 depends on several parameter values and the dynamics of various linear and nonlinear systems. Some of these are properties of the driving conditions, for example the vehicle, motion filters and forcing function spectra and amplitudes. These can be adjusted depending on the conditions being modelled, and the values used in the experiments in Chapters 3 to 7 are given in these chapters. Other values relate to physical properties of the human driver, and work has been carried out throughout this thesis to identify suitable values to match the performance of human drivers.

A review of the literature is undertaken in Chapter 2 to choose appropriate physiological models for the driver's sensory and neuromuscular dynamics. An approximation to drivers'

neuromuscular dynamics can be made using a second order filter [15, 216]:

$$H_{\mathrm{nm}}(s) = \frac{\omega_{\mathrm{nm}}^2}{s^2 + 2\zeta_{\mathrm{nm}}\omega_{\mathrm{nm}}s + \omega_{\mathrm{nm}}^2} \tag{A.68}$$

although the values of parameters ω_{nm} and ζ_{nm} may vary. Transfer functions for the SCCs and otoliths are [95]:

$$H_{\mathrm{SCC}}(s) = \frac{458.4s^2}{(80s + 1)(5.73s + 1)} \tag{A.69}$$

$$H_{\mathrm{oto}}(s) = \frac{0.4(10s + 1)}{(5s + 1)(0.016s + 1)} \tag{A.70}$$

In Chapters 3 to 6, experiments were carried out by human drivers in a driving simulator, and a parameter identification procedure is used to find suitable values of the other driver parameters which fit the model as closely as possible to the measured data. In Chapter 3, the process noise amplitude W is found to be proportional to the RMS steering angle δ, with the relationship:

$$W = \mathrm{RMS}(\delta)/\mathrm{SNR}_W \tag{A.71}$$

where SNR_W is the identified signal-to-noise ratio. Note that the SNR is expressed as the ratio of the RMS values rather than the mean-square ratio more commonly used in communications engineering. Similarly, in Chapter 4 the measurement noise amplitudes are found to be proportional to the equivalent RMS signals, with thresholds η below which the measurement noise remains constant. For example:

$$V_a = \begin{cases} \mathrm{RMS}(a_{\mathrm{ve}})/\mathrm{SNR}_a & \mathrm{RMS}(a_{\mathrm{ve}}) > \eta_a \\ \eta_a/\mathrm{SNR}_a & \mathrm{RMS}(a_{\mathrm{ve}}) < \eta_a \end{cases} \tag{A.72}$$

Similar relationships hold for the measured path-following error e_{vi} and angular velocity ω_{ve}. This is consistent with sensory noise and threshold characteristics measured in previous studies, described in Chapter 2. Measurement noise of variance V_ϕ^2 is added to each previewed visual angle ϕ_{vi}, however the influence of these measurements would vary with the prediction horizon N_{p} if V_ϕ was kept constant. Therefore a combined standard deviation σ_ϕ is defined, with V_ϕ given by:

$$V_\phi = \sigma_\phi \sqrt{N_{\mathrm{p}} + 1} \tag{A.73}$$

In Chapter 4 the value of σ_ϕ is calculated using a signal-dependent relationship similar to Equation A.72, dependent on the RMS value calculated over the whole vector of previewed

Table A.1: Final driver model parameter values

Parameter	SNR_a	SNR_ω	SNR_ϕ	SNR_e	SNR_W	τ_{vi}	τ_{ve}
Units	–	–	–	–	–	s	s
Value	0.390	0.406	1.04	0.901	2.28	0.19	0.23
Parameter	T_{p}	ω_{nm}	ζ_{nm}	η_a	η_ω	η_ϕ	η_e
Units	s	rad/s	–	$\mathrm{m/s^2}$*	rad/s*	rad	m
Value	0.87	14.3	0.537	0.221	0.0235	0.0129	0.0559

angles $\boldsymbol{\phi}_{\mathrm{vi}}$. However, in Chapter 5 it is shown that this can be unreliable for targets with large angles. A better method is to calculate the noise amplitude based on the RMS amplitude of the first previewed angle ϕ_0:

$$\sigma_\phi = \begin{cases} \mathrm{RMS}(\phi_0)/\mathrm{SNR}_\phi & \mathrm{RMS}(\phi_0) > \eta_\phi \\ \eta_\phi/\mathrm{SNR}_\phi & \mathrm{RMS}(\phi_0) < \eta_\phi \end{cases} \tag{A.74}$$

A single set of parameter values is identified in Chapter 4 to fit the results of 51 trials carried out over a range of conditions. Due to the updated description of the signal-dependent relationship for the previewed steering angles given in Equation A.74, it is suggested in Chapter 5 that SNR_ϕ should be reduced by a factor of 1.4. The final set of parameter values identified through the experiments and simulations carried out in this thesis is given in Table A.1.

Two identified parameter values are excluded from Table A.1, as they are only used in specific cases. A lower value of $\mathrm{SNR}_\phi = 0.415$ is identified in Chapter 4 for trials without preview, which is likely to be a result of the unintuitive nature of the visual display. Furthermore, a 'target shift' parameter $T_{\mathrm{t}} = -0.26$ s is identified to account for drivers aligning a part of the vehicle other than the centre of mass with the target. This only becomes significant for a very slow vehicle, as used in the experiment in Chapter 3.

The only other parameter values not shown in Table A.1 are the cost function weights. This is because they are a choice rather than a physical property of the driver. The controller is affected only by the relative values of the weightings, therefore q_e is set to 1 m^{-2}. The relative weights have been found to vary significantly between drivers and trials, therefore separate values of q_δ are identified for each trial in Chapters 4 to 6. Values of q_δ between around 0.1 and 2 rad^{-2}* have been found.

The parameter values shown in Table A.1 can also be used for a nonlinear driver model, although simulations carried out in Chapter 6 indicate that a closer fit to experimental results can be obtained by extending T_{p} slightly to 1 s. This may be due to the control

horizon being equal to T_p for the nonlinear model, unlike the infinite control horizon for the linear model. Drivers have been found to consider the time-varying operating point of the nonlinear vehicle over the prediction horizon, therefore FNO is the best match of the controllers presented in Section A.2.3. However, under many conditions LPF* performs identically to FNO, so can be used in its place [234]. Similarly, all extended Kalman filters are found to perform almost identically, therefore it is sensible to use EKF1 which is the fastest to simulate of the state estimators described in Section A.2.2.

In Chapter 5, an experiment was carried out where the target and disturbance signals were formed from transient events. This conflicts with the driver model which represents all signals as filtered Gaussian white noise. It is found to be difficult to identify a fixed set of parameter values to match driver behaviour for all types of transient signals. However, in most cases for the analysis of driver behaviour it is sufficient, or even desirable, to describe target and disturbance signals in terms of their statistical properties. Various techniques for carrying out reliable simulations with the new driver model are described in Chapter 7. The results of various illustrative simulations are also presented, which highlight the importance of considering sensory dynamics in models of driver steering behaviour.